Evaluating the Stratospheric Pathway of the Arctic-Midlatitude Linkage using a Chemistry Climate Model

A Dissertation

Submitted in Partial Fulfilment of the Requirements for the

Degree of Doctor rerum naturalium (Dr. rer. nat.)

to the Department of Earth Sciences

of Freie Universität Berlin

by

Franziska Schmidt

Berlin, May 2024

Abstract

Arctic amplification is the phenomenon of accelerated warming of the Arctic polar regions in the context of climate change induced by anthropogenic greenhouse gas emissions. A number of recent cold episodes in midlatitudes in winter have raised the question of whether the Arctic amplification has led to the observed midlatitude cooling. The proposed mechanism of this Arctic-midlatitude linkage involves a stratospheric pathway. Accordingly, the horizontal temperature gradients are decreasing due to the enhanced polar warming at the surface. Consequently, the superjacent winds are weakened which results in slower and more meandering polar jet streams. The enhanced planetary waves propagate into the stratosphere, where they induce strong circulation anomalies, referred to as sudden stratospheric warmings (SSWs). These strong disturbances of the stratospheric polar vortex can potentially exert a downward influence on the troposphere, favouring local cold air outbreaks. Investigating this stratospheric pathway in a climate model requires an accurate representation of the middle atmosphere. Therefore, a comprehensive evaluation using the climate-chemistry model ECHAM/MESSy Atmospheric Chemistry (EMAC) was conducted in this thesis, with the additional aim of examining the impact of ozone chemistry on the stratospheric processes. The suggested steps of the stratospheric pathway were examined using a set of transient simulations and timeslice experiments. Although the Arctic amplification signal continued to rise, no cooling trend or cessation of warming was found in the transient simulations. In contrast, the frequency of SSWs has increased significantly under the influence of climate change. This increase could be attributed to a larger planetary wave input from the troposphere. The primary area of enhanced planetary wave propagation was identified as the Northern Pacific and the region spanning the North Atlantic and Europe. Moreover, the number of events corresponding to strong wave input into the stratosphere increased significantly in a warmer climate. The behaviour of the jet streams was evaluated using a jet detection scheme to determine the exact jet positions. The Eurasian region exhibited an increased occurrence of polar jets, showing a wavier path as well. In contrast, the western hemisphere was characterised by a reduced polar jet frequency. A straightforward connection between the wavier jets and temperature gradients in the lower troposphere was not established in this study. While the modifications in the lower layers imply reduced baroclinic instability and fewer atmospheric waves, an enhanced wave generation became evident in the upper troposphere. However, these anomalies coincide with changes in the static stability and in subtropical temperature changes. The release of additional waves into the stratosphere appears to be related to these upper-tropospheric anomalies. The findings of this thesis suggest that the step linking temperature gradients to upper-tropospheric wave propagation requires further clarification. This is critical for validating the stratospheric pathway. Moreover, an evaluation of the downward influence of SSWs was conducted. Despite more frequent SSWs in a warmer climate, no tendency towards more extreme cold events was found in the most affected regions. While significant cooling anomalies still existed after the SSW events, the temperature anomalies are considerably lower. Finally, the representation of ozone chemistry in the model was determined to have an insignificant impact on the results of the stratospheric pathway.

Zusammenfassung

Die arktische Verstärkung beschreibt die beschleunigte Erwärmung der arktischen Polarregionen im Zusammenhang mit dem Klimawandel, der durch anthropogene Treibhausgasemissionen verursacht wird. Eine Reihe jüngster Kälteepisoden in den mittleren Breiten im Winter hat die Frage aufgeworfen, ob die arktische Verstärkung zu diesen Abkühlungen geführt hat. Der vorgeschlagene Mechanismus dieser Kopplung zwischen Arktis und mittleren Breiten umfasst einen stratosphärischen Pfad. Demzufolge verringern sich die horizontalen Temperaturgradienten aufgrund der bodennahen Erwärmung in den Polargebieten. Die überlagerten Winde werden abgeschwächt, was zu einem langsamen und mäandrierenden polaren Strahlstrom führt. Die so gestärkten planetaren Wellen breiten sich bis in die Stratosphäre aus, wo sie massive Zirkulationsanomalien hervorrufen, die sogenannten plötzlichen Stratosphärenerwärmungen (SSWs). Diese Störungen des stratosphärischen Polarwirbels können einen abwärtsgerichteten Einfluss ausüben und zu lokalen Kaltluftausbrüchen führen. Die Untersuchung dieses stratosphärischen Pfades in einem Klimamodell erfordert eine genaue Darstellung der mittleren Atmosphäre. Daher wurde eine umfängliche Studie mit dem Klimachemiemodell ECHAM/MESSy Atmospheric Chemistry (EMAC) durchgeführt, mit dem zusätzlichen Ziel den Einfluss der Ozonchemie auf die stratosphärischen Prozesse genauer zu untersuchen. Die vorgeschlagenen Schritte des stratosphärischen Pfades wurden anhand einer Reihe von transienten Simulationen und Zeitscheiben-Experimenten untersucht. Obwohl das Signal der arktischen Verstärkung weiter ansteigt, konnte kein Trend einer Abkühlung oder ein Stagnieren der Erwärmung festgestellt werden. Im Gegensatz dazu stieg die Häufigkeit der Stratosphärenerwärmungen unter dem Einfluss des Klimawandels signifikant an. Dieser Anstieg konnte einem stärkeren troposphärischen Welleneintrag zugeordnet werden. Die Hauptregionen dieser erweiterten Wellenausbreitung sind der Nordpazifik und die Region im Nordatlantik und Europa. Im Weiteren steigt die Anzahl der starken Wellenereignisse unter wärmeren Klimabedingungen signifikant an. Der genaue Verlauf der Strahlströme wurde mithilfe eines Strahlerkennungsschemas bewertet. Die polaren Strahlströme über Eurasien treten häufiger auf und zeigen einen wellenförmigeren Verlauf. Im Gegensatz dazu zeigen sich weniger polare Strahlströme in der westlichen Hemisphäre. Einen direkten Zusammenhang zwischen wellenförmigen Strahlströmen und den Temperaturgradienten in der unteren Troposphäre konnte in dieser Studie nicht nachgewiesen werden. Die Änderungen in den unteren Schichten deuten zwar auf eine Verringerung der baroklinen Instabilität und verminderter atmosphärischer Wellen hin, jedoch wurde auch eine Zunahme der Wellenanregung in der oberen Troposphäre festgestellt. Diese Anomalien fallen allerdings mit einer Änderung der statischen Stabilität und einer Erwärmung in den Subtropen zusammen. Zudem scheinen die oberen Anomalien für den zusätzlichen Welleneintrag in die Stratosphäre verantwortlich zu sein. Die aufgeführten Ergebnisse dieser Studie legen nahe, dass eine Validierung dieses Schrittes, Verbindung zwischen Temperaturgradienten und wellenförmiger Strahlstrom, notwendig ist, um den stratosphärischen Pfad zu bestätigen. Des Weiteren wurde eine Bewertung des abwärtsgerichteten Einflusses der SSWs durchgeführt. Ungeachtet der Häufung von Stratosphärenerwärmungen in einem wärmeren Klima, konnte keine Tendenz zu kalten Extremereignissen in den sonst üblich betroffenen Regionen festgestellt werden. Die signifikanten Abkühlungssignale treten nach wie vor im Zuge der Stratosphärenerwärmungen auf, jedoch sind diese wesentlich geringer. Letztendlich konnte kein Einfluss der Berücksichtigung der Ozonchemie auf den stratosphärischen Pfad nachgewiesen werden.

Contents

CHAPTER 1

Introduction

Climate change has become increasingly discernible and a matter of growing concern. The warming of the atmosphere induced by anthropogenic emissions of greenhouse gases has progressed steadily and is expected to continue in the coming decades. In contrast to the implication of the term *global warming*, the increase in temperature is not uniformly distributed across the Earth. The Arctic polar region exhibits a warming trend nearly four times larger than the global average, a phenomenon referred to as Arctic amplification. Concurrently, severe cold spells have been observed in some midlatitude regions during the winter season. These extensive cold episodes have given rise to a heavily debated research topic:

Is there a connection between the cold winter weather observed and the enhanced warming in the Arctic?

This counterintuitive idea is also known as the *Arctic-midlatitude linkage* or the *warm Arctic – cold continent* pattern. Although it has been extensively investigated in the literature, a comprehensive understanding of its physical background remains incomplete. Instead, some scientists have been polarised into two factions: supporting or denying the causal relationship between Arctic amplification and severe winter weather.

The proposed mechanism of the Arctic-midlatitude linkage comprises a tropospheric and a stratospheric pathway. The latter utilises the fact that the stratospheric polar vortex is coupled with tropospheric winter weather under certain conditions. A strong disturbance or breakdown of the stratospheric polar vortex is induced by tropospheric planetary waves and is referred to as sudden stratospheric warming (SSW). In the aftermath of these stratospheric events, there is a tendency for local cold air outbreaks in midlatitudes.

In essence, the stratospheric pathway of the Arctic-midlatitude linkage suggests a weakening of the horizontal temperature gradients through Arctic amplification, which results in weaker and wavier jet streams. This is accompanied by increased planetary wave generation in the troposphere. Subsequently, these waves propagate into the stratosphere where they induce SSWs. The downward influence of these stratospheric disturbances favours colder winter weather in certain midlatitude regions. Thus, the stratospheric pathway relates surface polar warming to severe winter weather conditions in a series of steps, in which circulation anomalies are transmitted to the stratosphere and return to the surface. However, the extent to which the stratospheric pathway, in conjunction with the tropospheric pathway, exerts an influence is contentious.

One reason for this controversy arises from diverging findings in observations and climate models (e.g. Cohen et al., 2020). Observational studies have implied a strong relationship between Arctic conditions, specifically sea ice, and winter weather (e.g. Kim et al., 2014). However, the observational record is too short to establish reliable conclusions. On the other hand, model studies evaluating the effect of Arctic amplification suggest either a very small signal (e.g. Kretschmer et al., 2020; Liang et al., 2024) or question the remote impact of Arctic warming (e.g. Blackport and Screen, 2020b,a). Several authors have highlighted the importance of internal variability and the challenge of distinguishing between a significant effect and natural weather fluctuations (e.g. Screen et al., 2014; McCusker et al., 2016).

In the course of the discussion, model deficiencies emerged as an explanation for why the models were unable to accurately reflect the relationship (Cohen et al., 2020). Among the various aspects, the representation of the stratosphere in the model has come into focus (Romanowsky et al., 2019). The model top needs to be sufficiently high to represent stratospheric processes, including the stratosphere and mesosphere. A further improvement in the simulation of stratospheric phenomena is the representation of ozone chemistry in the model. Previous studies have suggested an effect of interactive ozone chemistry on stratospheric dynamics through the modification of the temperature structure (Haase and Matthes, 2019; Oehrlein et al., 2020; Friedel et al., 2022).

Hence, this thesis aims to provide a comprehensive study of the stratospheric pathway using a chemistry-climate model. The model ECHAM/MESSy2 Atmospheric Chemistry (EMAC) was utilised to simulate the historical climate change that has occurred thus far and to provide a realistic projection of future trends. Furthermore, sensitivity experiments were conducted to examine the changes in different time periods and to determine the relevance of stratospheric ozone chemistry.

The following questions should be addressed as opening clarifications:

Q1 Does the outcome of historical model simulations indicate a cessation or cooling trend during winter in midlatitude regions?

Q2 Does climate change leads to an increase in the frequency of stratospheric warmings?

To outline the further procedure of this thesis, a brief preview of the responses to these questions is provided: the answer to the first question is no, while the answer to the second question is yes. From this point in the study, the evaluation is centred on the increased SSW frequency found in EMAC. The first part of this work analyses the changes leading to more SSWs in a warmer climate. The specific research questions regarding the impact of global warming on the atmospheric circulation are as follows:

Q3 Are stratospheric circulation anomalies induced by an enhanced planetary wave input from the troposphere?

Q4 Are tropospheric jet streams becoming weaker and more meandering?

Q5 How is the relationship between horizontal temperature gradients and tropospheric wave generation?

The second set of questions are addressed using a combination of sophisticated methodologies that have not yet been employed in this context. The tropospheric wave input is assessed using an event-based analysis of the 3D Plumb wave activity flux. This provides information about the source region of the enhanced wave propagation into the stratosphere. The tropospheric jet streams are classified using an advanced jet detection algorithm and evaluated for shifts in location, strength, and meridional wind velocities. The effects of changes in temperature gradients are examined with respect to baroclinic instability and the resulting planetary wave anomalies.

In the further course of this thesis, the effects of the increased stratospheric disturbances will be investigated separately from their cause. Climate models show diverging results regarding future changes in SSW frequency. The range of possible outcomes extends from increasing, to no change, towards decreasing. EMAC joins the group of models that show more SSWs in a warmer climate. To date, very little attention has been paid to the impact of more frequent stratospheric warmings on the tropospheric circulation, and this study aims to answer the following question:

Q6 Are more stratospheric warmings in a warmer climate associated with more extreme cold events in midlatitudes, and how severe are the SSW-induced anomalies?

Finally, the results regarding the stratospheric pathway were reviewed in model simulations performed without an interactive chemistry module. Uncertainty remains regarding whether the allowance for feedback between ozone and dynamics significantly influences stratospheric circulation in the northern hemisphere. The final question of this study is as follows:

Q7 Does the consideration of ozone chemistry in the model affect the representation of stratospheric pathway processes?

The remaining parts of this thesis proceed as follows: The second chapter introduces background information about the tropospheric and stratospheric phenomena involved. The third chapter dives into the Arctic-midlatitude linkage literature with a particular focus on the stratospheric pathway. In this section, the diverging perspectives on the topic are elucidated in more detail. A description of the model and the simulations conducted are provided in the fourth chapter, complemented by a model evaluation. The fifth chapter contains a comprehensive declaration of the methods used in this study. The results are presented in the sixth chapter, addressing the aforementioned research questions. A summary of these results and a discussion are outlined in the seventh chapter.

CHAPTER 2

Background

The stratospheric pathway of the Arctic-midlatitude linkage extends across two atmospheric layers, the troposphere and the stratosphere. The processes that lead to a coupling between Arctic warming and severe winter weather are influenced by a variety of dynamical phenomena. In this chapter, background information is provided. In addition to introducing climate change and Arctic amplification, this chapter also covers atmospheric dynamics in the troposphere and stratosphere. The emphasis is on all aspects related to the stratospheric pathway.

2.1 Climate Change

The weather and climate on Earth depend on the following factors: the radation budget, the chemical composition of the atmosphere, the atmospheric circulation, and the hydrological cycle. The different components of the climate system interact with each other and are sensitive to external influences. We are still about to understand this complex system with all of its feedback. Since the input of greenhouse gases to the atmosphere through industrial production, humankind has become one of those external factors affecting the climate system.

2.1.1 Radiation

Before discussing the causes and effects of global warming, a few basic concepts of radiation are introduced. Radiation can be considered as an electromagnetic wave with a certain wavelength λ. All objects warmer than absolute zero emit radiation according to their temperature and other characteristics. To simplify these relations, the concept of a black body can be applied. A black body is an ideal object that absorbs all incident radiation without reflection. Concurrently, it emits the maximum possible radiation in agreement with the Planck's law

$$B_\lambda(T) = \frac{2hc^2}{\lambda^2} \frac{1}{e^{\frac{hc}{\lambda T}} - 1}.$$ (2.1)

The spectral radiance B_λ is determined by the temperature T of the body. The Planck constant is given by h and the speed of light is c. In Figure 2.1a the spectral radiance B_λ is

(a) Spectral radiance
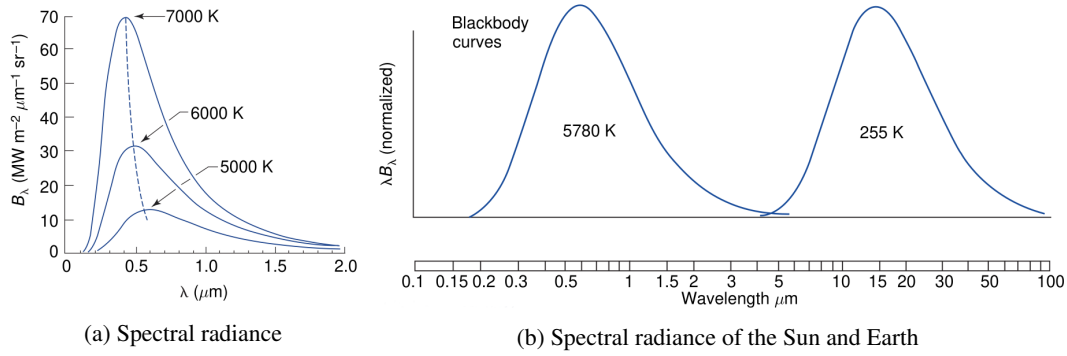
(b) Spectral radiance of the Sun and Earth

Figure 2.1: Spectral radiance of black bodies with different temperatures in a linear scale (a) and of the Sun and the Earth in (b) where the wavelength λ is shown in logarithmic scale and $B_\lambda(T)$ is normalized. Figures adapted from Wallace and Hobbs (2005).

plotted as a function of λ at specific temperatures. A higher temperature of the black body results in a shift in the emission towards shorter wavelengths. Therefore, the emission of the Sun, with a temperature of 5780 K, is called *shortwave radiation*. The Earth has an average temperature of 255 K and emits *longwave radiation* in the infrared domain of the spectrum (see Figure 2.1b).

The peak wavelength of the emitted radiation can be determined by the Wien's displacement law

$$\lambda_{\text{max}} = \frac{a}{T} \qquad \text{with} \quad a = 2897 \, \mu\text{m} \, \text{K}. \tag{2.2}$$

The dashed line in Figure 2.1a indicates the shift of λ_{max} to longer wavelengths as the temperature decreases. The area under the Planck curve obtained by the integration over all wavelengths is given by the Stefan-Boltzmann law

$$B(T) = \sigma T^4. \tag{2.3}$$

The total radiant intensity $B(T)$ of a black body is a function of T^4 with the Stefan-Boltzmann constant $\sigma = 5.67 \cdot 10^{-8} \, \text{W} \text{m}^{-2} \text{K}^{-4}$. The fundamental radiometric quantities given in this section are essential for understanding the global radiative equilibrium of the atmosphere.

2.1.2 Natural greenhouse effect

The energy budget of the Earth is determined by the incoming radiation from the Sun. Approximately one-third of this shortwave radiation is reflected back into space by clouds, the atmosphere, and the Earth's surface. The remainder of the radiation is absorbed and heats the planet.

To maintain a balanced state, the system must release energy as thermal radiation. The Earth and atmosphere can be assumed to be a black body. They emit longwave radiation depending on their temperature. If this longwave radiation completely escapes the Earth's

atmosphere, the mean temperature at the surface would be $-19\,°C$. This value is much lower than the average temperature on Earth.

In fact, the atmosphere traps a certain amount of heat. It contains several trace gases which absorb outgoing infrared radiation. These compounds are known as greenhouse gases (GHGs). The most important GHGs are water vapour (H_2O), carbon dioxide (CO_2), methane (CH_4) and nitrous oxide (N_2O). After absorbing longwave radiation from the Earth, they re-emit radiation in all directions, partly back down to the surface. In accordance with the natural greenhouse effect, the lower layers of the atmosphere are warmed to an average temperature of $14\,°C$ (Baede et al., 2001).

2.1.3 Anthropogenic influence

Since the industrial revolution in the mid-18th century, human activities have released a significant amount of GHGs into the atmosphere and substantially changed its composition. The anthropogenic emissions are mainly caused by the combustion of fossil fuel, agriculture, land use and industrial activities. The fossil fuel burning is known as the major contributor to GHG emissions. As a consequence, the concentration of carbon dioxide increased by more than 40%. Further, methane and nitrous oxide abundances have raised to higher levels. All of these trace gases have a long enough lifetime to become well mixed in our atmosphere.

The enhanced greenhouse effect leads to a warming of the climate system. The influence of global warming is becoming increasingly discernible, and the rise in temperature will continue for many decades. According to the Intergovernmental Panel on Climate Change (IPCC), the global average temperature has reached $1.1\,°C$ above preindustrial levels (IPCC, 2021a).

Global warming leads to more severe heatwaves, accelerated sea ice melting, rising sea levels, and an increase in the frequency of wildfires. In Figure 2.2 the change in the global temperature and the Arctic sea ice area in September clearly demonstrate the effects already occurring (in black and grey) and possible consequences under different scenarios (coloured lines). The projected global change after the Shared Socioeconomic Pathway (SSP) scenarios are estimates of future emissions, economics, and climate policies (Riahi et al., 2017). They range from a very green and sustainable path (SSP1) to a fossil fuel and intense energy-consuming path (SSP5). Under the SSP1 scenario, global warming could be limited to about $1.5\,°C$ until the end of the century. The SSP5 scenario, in contrast, projects a temperature change of nearly $5\,°C$.

The climate system is complex, and several feedback mechanisms must be considered. One example is the response in the Arctic region. By the end of summer, one-third of the Arctic sea ice had already melted currently (Figure 2.2b). In three of the five future scenarios, a practically ice-free Arctic in September is a very probable outcome. The melting of polar sea ice is a key factor in a feedback mechanism that cause the accelerated warming of the Arctic region.

(a) Global surface temperature change relative to 1850–1900
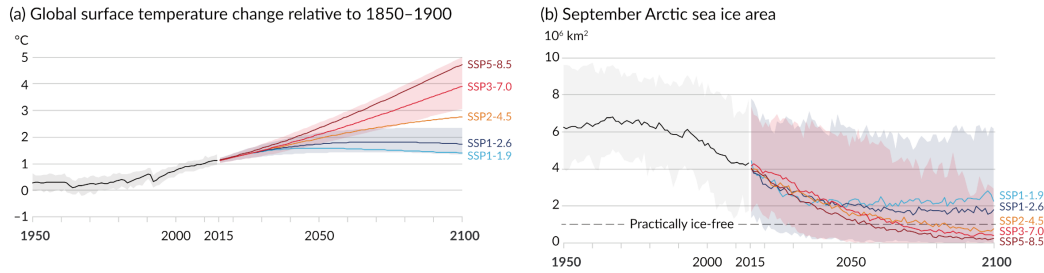
(b) September Arctic sea ice area

Figure 2.2: Historical and future changes of global surface temperature (a) and September Arctic sea ice (b). These changes were obtained from CMIP6 historical simulations (grey) and simulations with different future scenarios (coloured) of projected socioeconomic global changes (SSPs). Very likely ranges (90%) are shown in shaded colours for the historical, SSP1-2.6 and SSP3-7.0 run. Figures adapted from SPM.8 in IPCC (2021b): Summary for Policymakers.

2.1.4 Arctic Amplification

Arctic amplification refers to the phenomenon of enhanced surface warming in the Arctic relative to the rest of the world. Manabe and Wetherald (1975) used a simple general-circulation model to evaluate the effects of a doubling of CO_2 concentrations. Besides a general warming in the lower atmosphere, an amplified temperature increase was particularly notable at high latitudes. At present, we can already witness these accelerated changes in the Arctic. A warming nearly four times stronger than the global mean was recently reported by Rantanen et al. (2022) from observations (1979–2021).

Thus far, much research has been conducted to understand this amplified warming. It was found that the direct radiative forcing of CO_2 is insufficient to fully explain Arctic amplification, and several climate feedback mechanisms must be taken into account. Pithan and Mauritsen (2014) pointed out the dominant role of the temperature feedback. The second important factor is the sea ice-related feedback (Previdi et al., 2021).

Two types of temperature feedback can be distinguished: Planck feedback and lapse rate feedback (e.g. Soden and Held, 2006). The Planck response is based on a vertically uniform warming of the atmosphere. A warmer atmosphere emits more outgoing longwave radiation (OLR) to stabilise the climate system. Following the Stefan-Boltzmann law (Equation 2.3), the OLR depends nonlinearly on temperature (T^4). Accordingly, colder regions must warm up more than warmer regions to compensate for the same radiative forcing.

The lapse rate feedback accounts for the sensitivity of the OLR to the vertical temperature distribution. If the surface warms more than the free atmosphere, such as that prevailing in the Arctic, the radiative flux to space decreases compared to uniform warming. This results in a positive feedback in polar regions. Several studies claimed the lapse rate feedback is the primary cause of Arctic amplification (e.g. Stuecker et al., 2018).

Moreover, the largest temperature response occurs in regions with sea ice loss (Boeke et al., 2021). The melting of sea ice and snow cover plays a crucial role in the amplified Arctic warming. The reduction in the snow-covered areas leads to a substantial decrease in albedo,

due to the large difference between sea ice and open water. As a consequence, an enhanced absorption of incoming solar radiation occurs in ice-free areas during late spring and summer. The additional heat is finally released from the ocean to the atmosphere during the fall and winter. This is consistent with the largest Arctic amplification signal in the dark season, even with little or no sunlight. Pithan and Mauritsen (2014) suggest that this surface albedo feedback is the second main contributor to Arctic amplification.

Furthermore, cloud and water vapour feedback increases the downwelling longwave radiation (e.g. Soden and Held, 2006). A warmer environment is expected to result in lower clouds and a higher concentration of water vapour. Both are linked to sea-ice loss through increased moisture and stronger convection. Clouds and water vapour, in turn, emit downwelling longwave radiation which contributes to the additional warming of the surface.

Besides these local feedback mechanisms, changes in energy transport in the atmosphere and ocean can influence the strength of Arctic amplification. The different insolations at high and low latitudes induce a meridional heating gradient. A compensation is accomplished through the poleward energy transport (PET). Studies have indicated that the PET increases in response to positive radiative forcing (Huang et al., 2017). Nonetheless, PET change and local feedback are tightly coupled, as pointed out in Previdi et al. (2021).

Rapid Arctic warming has a significant influence on the local climate, wildlife, and vegetation. Warmer summer conditions, for example, can lead to a severe change in regional vegetation, which is referred to as *Arctic greening* (Myers-Smith et al., 2020). Further, the environmental transformation drives a change in the Arctic carbon cycle with fire increases and permafrost thaw (Bruhwiler et al., 2021). Another point of concern is the melting of Arctic land ice and the resulting global sea level rise. Finally, a modification of the jet stream with an increased frequency of weather extremes in midlatitudes has been intensively discussed (e.g. Meleshko et al., 2016; Francis and Vavrus, 2015).

2.2 Atmospheric Dynamics

The dynamical meteorology is the study of atmospheric motion. This section presents the basic concepts of atmospheric dynamics. The motions in the atmosphere follow the central laws of the conservation of momentum, mass, and energy.

Fundamental forces

According to Newton's second law of motion, the acceleration of an object is the sum of all acting forces. Relevant atmospheric motions include the pressure gradient force, gravitational force, and viscous force. When spatial variations in pressure exist, a force is exerted from regions of higher to lower pressure. The *pressure gradient force* $\mathbf{F}_p$ per mass unit is given by

$$\frac{\mathbf{F}_p}{m} = -\frac{1}{\rho}\nabla p, \tag{2.4}$$

9

where m denotes the mass, ρ the density, and p the pressure. This is the only force that can initiate air movement. The airflow from high pressure to low pressure reduces the pressure difference. The wind speed is determined by the magnitude of the pressure gradient. However, the wind does not flow from high to low directly because other forces have to be considered in addition.

Newton's law of universal gravitation implies that the attraction of two objects in the universe is proportional to their masses and inversely proportional to the distance between the centres of mass. If the mass of the Earth is considered as M and the distance between the center of the Earth and the atmosphere as $\mathbf{r}$, the *gravitational force* $\mathbf{F}_g$ per mass unit is

$$\frac{\mathbf{F}_g}{m} = -\frac{GM}{r^2}\left(\frac{\mathbf{r}}{r}\right) = \mathbf{g}^*, \tag{2.5}$$

where G denotes the universal gravitational constant ($6.673 \cdot 10^{-11}\,\mathrm{N\,m^2\,kg^{-2}}$). The true gravitational attraction is indicated by $\mathbf{g}^*$. The variation in gravitational forces at higher altitudes due to the larger distance r is negligible, and r is typically approximated by the radius of the Earth.

Finally, the internal friction between molecules in the atmosphere acts to resist the tendency to flow (Holton, 2004). The *frictional force* can be stated as

$$F_r = -\frac{1}{\rho}\frac{\partial \tau}{\partial z} \tag{2.6}$$

where τ represents the vertical component of the shear stress. Friction is most relevant in layers close to the Earth's surface (i.e. the boundary layer), where a large vertical shear occurs.

Apparent forces

Strictly speaking, Newton's second law of motion holds for a fixed reference system. This would be an inertial framework with no acceleration on the system. However, the Earth rotates on its own axis and two additional forces appear in the rotating reference frame. First, the *centrifugal force* pulls all objects outwards from the axis of planetary rotation (Wallace and Hobbs, 2005). The true gravitational attraction $\mathbf{g}^*$ from Equation 2.5 and the small centrifugal force are summed to the effective gravity $\mathbf{g}$. Secondly, an object moving on a rotating plane experiences a deflection of the path. This can be explained by considering an air parcel which is at rest relative to the Earth's surface, and therefore has a certain tangential velocity depending on the latitude of the location. If this air parcel starts moving to the north, it maintains its original speed, but reaches a new latitude with a lower tangential velocity. Thus, the parcel appears to be forced to the east which is also known as the *Coriolis force*. The horizontal component of the Coriolis force $\mathbf{F}_c$ is given by

$$\frac{\mathbf{F}_c}{m} = f\mathbf{k} \times \mathbf{v} \quad \text{with} \quad f = 2\Omega\sin(\varphi)$$

with Coriolis parameter f, the wind vector $\mathbf{v}$, the rotational velocity of the Earth Ω and latitude φ.

2.2.1 Primitive equations

Dynamical processes can be described by the primitive equations. These equations are composed of Newton's second law, the first law of thermodynamics, the continuity equation, and the ideal gas law. Under hydrostatic equilibrium, the equations in pressure coordinates are:

$$\frac{d\mathbf{v}_h}{dt} = -\vec{\nabla}_h\Phi - f\mathbf{k} \times \mathbf{v}_h + \mathbf{F}_r \tag{2.7}$$

$$\frac{\partial \Phi}{\partial p} = -\frac{RT}{p} \tag{2.8}$$

$$\frac{dT}{dt} = \frac{\kappa T}{p}\omega + \frac{J}{c_p} \tag{2.9}$$

$$\frac{\partial \omega}{\partial p} = -\vec{\nabla} \cdot \mathbf{v}_h. \tag{2.10}$$

The horizontal wind velocity is denoted by $\mathbf{v}_h$ and the vertical wind velocity in pressure coordinates by ω. The geopotential is represented by Φ, pressure by p, friction force by $\mathbf{F}_r$ and J is diabatic heating. The temperature is represented by T, R is the specific gas constant, κ is the heat capacity ratio, and c_p is the heat capacity at constant pressure (Wallace and Hobbs, 2005). The above equations are nonlinear partial differential equations. Various simplification methods can be applied, depending on the problem. Nevertheless, the solution to the primitive equations in their original form can only be obtained through an iterative process, a method commonly used in weather prediction and climate models.

2.2.2 Thermal wind relation

The primitive equations encompass a wide range of atmospheric phenomena. Some of these, such as sound waves or friction, are not crucial when investigating large-scale circulation. One simplification broadly applied in synoptic meteorology is the geostrophic approximation. In midlatitudes above the planetary boundary layer, the influence of friction ($\mathbf{F}$) can be neglected. Moreover, the acceleration of the horizontal wind ($\frac{d\mathbf{v}_h}{dt}$) is minimal. Disregarding both terms in Equation 2.7 yields the geostrophic balance of the Coriolis force and the pressure gradient force

$$f\mathbf{k} \times \mathbf{v}_h = -\vec{\nabla}\Phi. \tag{2.11}$$

Rearranging for the horizonal wind gives

$$\mathbf{v}_g = \frac{1}{f}\mathbf{k} \times \vec{\nabla}\Phi, \tag{2.12}$$

11

where $\mathbf{v}_g$ is the geostrophic wind directed along the isolines of the geopotential.

The thermal wind relation is derived by considering the vertical wind shear of the geostrophic wind under hydrostatic conditions. The hydrostatic equilibrium signifies the balance between the gravitational force and the pressure gradient force in the vertical direction. Taking the derivative of the geostrophic wind (Equation 2.12) with respect to the vertical coordinate p and using the hydrostatic equilibrium (Equation 2.8) yields

$$\frac{\partial \mathbf{v}_g}{\partial p} = -\frac{R}{f p} \mathbf{k} \times \vec{\nabla} T = \mathbf{v}_{th} \tag{2.13}$$

the so-called *thermal wind* which does not refer to an actual wind but rather to a variation in wind with altitude. The above equation implies that if a temperature gradient exists on a pressure surface, the geostrophic wind must vary with height. Based on this relationship, the flow can be classified into two categories. In the absence of temperature variations on pressure surfaces, the wind remains constant across all layers. This condition is called *barotrop*. In contrast, a *baroclinic* atmosphere is characterised by a vertical wind shear induced by a temperature gradient on pressure surfaces. For instance, the horizontal temperature difference between the pole and equator is often used to explain the intensification of westerly winds with altitude and the formation of jet streams.

2.2.3 Potential vorticity

The midlatitude dynamics can be characterised using basic state variables from primitive equations (Eq. 2.7 - 2.10) and some approximations, for example the quasi-geostrophic system. An alternative approach for understanding dynamical processes involves the use of a single variable – the potential vorticity (Martin, 2007). In the following, some important dynamical and thermodynamical variables are described to understand the meaning of the potential vorticity (*short*: PV).

Vorticity

Atmospheric motion on Earth occurs on a sphere and exhibits strong rotational patterns. A measure of the local rotation is the curl of the velocity vector; in this case, the wind vector $\mathbf{v}$

$$\vec{\xi} = \vec{\nabla} \times \mathbf{v}. \tag{2.14}$$

The *vorticity* ζ represents the vertical component of this measure given by

$$\zeta = \mathbf{k} \cdot \vec{\nabla} \times \mathbf{v}. \tag{2.15}$$

As atmospheric motions occur on a rotating Earth, the absolute velocity of an air parcel can be separated into a relative and an Earth component

$$\mathbf{v}_a = \mathbf{v}_r + \mathbf{v}_e, \tag{2.16}$$

and consequently, absolute vorticity is composed of both relative vorticity and planetary vorticity

$$\zeta_a = \zeta_r + f. \tag{2.17}$$

The planetary vorticity f is solely induced by the rotation of the Earth and is defined as

$$f = 2\Omega \sin \varphi \tag{2.18}$$

where Ω is the angular velocity of the Earth and φ is the latitude. Relative vorticity ζ_r is positive for cyclonic or counterclockwise rotations in the northern hemisphere (NH). Anticyclones with clockwise rotation indicate a negative vorticity. In the southern hemisphere (SH) this relationship is reversed.

Potential temperature

The potential temperature θ represents the temperature that an air parcel would attain when moving adiabatically from a specific temperature and pressure to a standard pressure p_s, usually 1000 hPa

$$\theta = T \left(\frac{p_s}{p} \right)^{R/c_p}. \tag{2.19}$$

The above equation is also called the *Poisson's equation* and can be derived from the first law of thermodynamics (Equation 2.9). The potential temperature is a useful variable in meteorology. In a stable stratified atmosphere, the potential temperature increases with height and can be employed as a vertical coordinate (isentropic coordinate system). For adiabatic processes, the motion of an air parcel follows a constant θ level.

Static stability

When an air parcel is lifted adiabatically to a higher level, it expands and cools based on the adiabatic lapse rate. If the new surrounding temperature is lower than that in the air parcel, it rises due to the buoyancy force. This condition corresponds to a static unstable stratification and typically results in upward motion with clouds and possible thunderstorms. If the surrounding temperature is higher compared to the air parcel, an oscillation is induced with the frequency

$$N = \sqrt{\frac{g}{\theta} \frac{\partial \theta}{\partial z}} \tag{2.20}$$

where g is the gravitational acceleration, and z is the geometric altitude. N is called the *Brunt-Väisälä* or *buoyancy frequency*, and can be used as a measure of static stability. A high Brunt-Väisälä frequency corresponds to a very stable stratification. A negative term
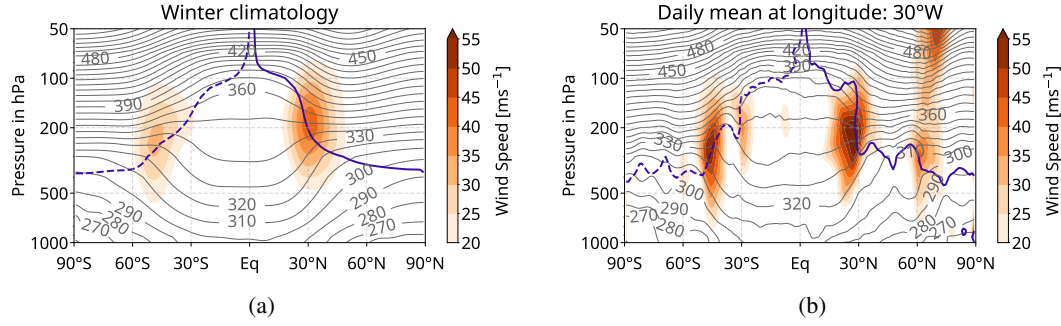
Figure 2.3: Distribution of potential temperature in Kelvin (grey contours) based on the zonal mean winter ERA5 climatology (1979–2021) in (a) and a cross section at 30°W longitude for a specific date (25 January 2003) to show the local structure. The tropopause is represented by the ± 2 PVU isolines of PV in blue (with negative values in the SH). The location of the jet streams is outlined by the wind speed $|\mathbf{v}_h|$ in shaded contours.

under the square root, which only occurs when the potential temperature decreases with altitude, is indicative for an unstable atmosphere.

The ERA5 reanalysis (Hersbach et al., 2020) winter climatology of the potential temperature θ is presented in Figure 2.3a. In general, the potential temperature increase with height in the climatological mean. The distance between the isolines of θ (isentropes) are related to the static stability. At higher altitudes, towards the stratosphere above 100 hPa, the atmosphere becomes more stable (see Section 2.4), resulting in isolines being spaced closer together.

Definition of the potential vorticity

The potential vorticity can be derived from the vorticity equation in isentropic coordinates and the continuity equation. It is defined as

$$q = -g(\zeta_\theta + f)\left(\frac{\partial \theta}{\partial p}\right) \tag{2.21}$$

and combines the dynamical quantity absolute vorticity with the thermodynamical static stability. For adiabatic and frictionless processes, the PV of an air parcel is preserved

$$\frac{\mathrm{d}q}{\mathrm{d}t} = 0, \tag{2.22}$$

implying that the static stability of an air parcel can be transformed into vorticity, and vice versa. The PV is given in *potential vorticity unit* with $1\,\text{PVU} = 1 \cdot 10^{-6}\,\text{m}^2\,\text{s}^{-1}\,\text{K}\,\text{kg}^{-1}$. It is defined positive in the northern hemisphere and negative in the southern hemisphere. In the stratosphere, the absolute values increase rapidly owing to the strong static stability in this region. Applying a value of 2 PVU as a criterion to distinguish between the troposphere and stratosphere is common practice, also referred to as the *dynamical tropopause*. The 2 PVU

isoline is depicted in Figure 2.3 as the climatological zonal mean, and for a specific winter day. In both cases, the ± 2 PVU isolines serve as good indicators of the transition between the troposphere and stratosphere. This transition is also marked by changes in the distance between isentropes.

2.2.4 General circulation

The general circulation is defined as the global-scale atmospheric flow obtained by averaging over a long period. This circulation is driven by differential heating between the pole and the equator. In 1735, George Hadley studied the cause of trade winds and proposed the existence of a thermally direct overturning cell from the equator to the pole.

Hadley described the flow in this cell as follows: The tropics experience higher insolation, leading to the ascent of warm air. At higher altitudes, this flow moves toward the poles and gradually cools. Upon reaching the pole, it descends and then circulates back to the equator at lower levels (Figure 2.4a). The easterly trade winds in the subtropics can be explained by the deflection of the equatorward low-level flow by the Coriolis force.

Subsequently, it became evident from observations and theoretical studies that a single cell per hemisphere could not exist on a rotating planet. The deflection of the flow by the Coriolis force disrupts the formation of a single cell, resulting in a descending flow at the subtropics near latitude 30°. Similar processes induce a thermally direct but weaker meridional cell near the pole. In between in midlatitudes, there is no direct cell to reduce the differential heating. Instead, a certain temperature gradient gives rise to *baroclinic instability*, resulting in the generation of baroclinic waves in midlatitudes. Considering this effect, the general circulation on Earth consists of three meridional cells: the thermally direct Hadley cell in the tropics, the weaker polar cell, and the indirect *Ferrel cell*, induced by midlatitude waves (Figure 2.4b).

Baroclinic instability

The instability of a zonal mean flow implies that a small perturbation can grow rapidly, drawing energy from the mean flow (Holton, 2004). Baroclinic instability arises from a vertical wind shear, and hence from horizontal temperature gradients, and provides an explanation for the formation of extratropical cyclones. These wave-like perturbations of the zonal mean flow are also referred to as baroclinic waves.

The meridional temperature variation between the north and south in the midlatitudes induces a strong vertical wind shear. Above a certain level of wind shear, the flow becomes unstable. The developing baroclinic wave gains potential energy from the mean flow and moves warm air poleward and cold air equatorward. The induced heat flux acts to reduce the temperature gradient, ultimately restoring the system to a stable condition.

The characteristics of the unstable modes of baroclinic instability can be derived by assuming the simplest possible model (outlined in detail in Holton, 2004). This method was
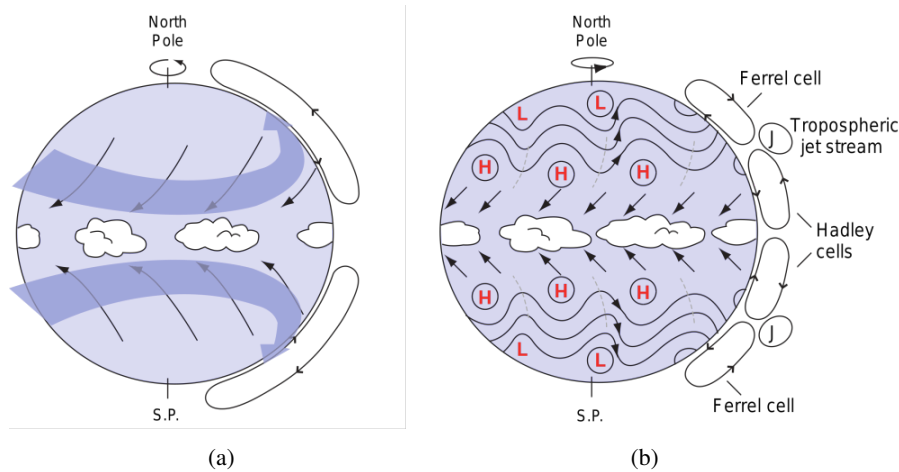
Figure 2.4: Schematic depiction of the general circulation. A single Hadley cell in (a) is unstable on a rotating Earth. A realistic description shown in (b) consists of three cells: the Hadley, Ferrel and polar cells (the latter is not shown in the graph) (from Wallace and Hobbs, 2005).

proposed by Eady in 1949, and is known as the *Eady problem*. The growth rate of the most unstable mode under these assumptions is refered to as the *maximum Eady growth rate* and is given by

$$\sigma_{max} = 0.31 \, \frac{f}{N} \cdot \left| \frac{\partial \mathbf{v}_h}{\partial z} \right|. \tag{2.23}$$

Hoskins and Valdes (1990) showed that the Eady growth rate (EGR) is a suitable measure of baroclinicity. Larger values correspond to higher potential for the development of baroclinic waves. As indicated in Formula 2.23, this potential increases with a larger shear of the horizontal wind or with a reduction in the Brunt-Väisälä frequency N. In other words, low static stability or strong wind shear favours baroclinic instability. Analysing the EGR provides insights into the location and intensity of cyclonic activity.

Jet streams

The jet streams are narrow bands of strong winds at heights of 10 km to 15 km near the tropopause. Jet streams can directly impact surface conditions by steering the weather systems below. Furthermore, a jet stream can meander and develop waves, a crucial feature of the large-scale circulation.

Two main types of jet streams can be distinguished: *subtropical jets* and *polar jets*. They are embedded into the general circulation, as illustrated in Figure 2.5a. The subtropical jet is located at the poleward edge of the Hadley cell. In the upper branch of this cell, the poleward flow is deflected to the east by the Coriolis force. Around 30° latitude, the Hadley cell breaks up, mainly due to the translation of the southerly winds into westerlies. The Coriolis effect along the path from the equator to the subtropics is strong enough to create
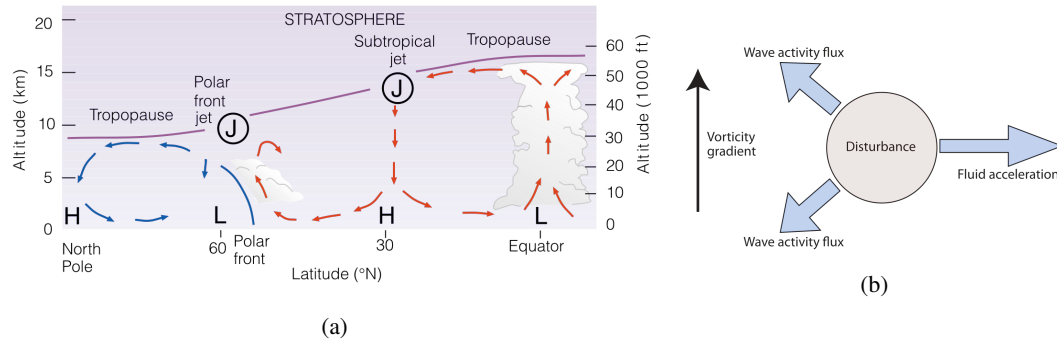
(a)

(b)

Figure 2.5: (a) Average position of subtropical and polar jet streams in the context of general circulation in the northern hemisphere (from Ahrens, 2000). (b) Schematic of wave propagation and acceleration of a zonal flow (from Vallis, 2017).

a high-level westerly wind band. Therefore, the subtropical jet is primarily induced by the conservation of angular momentum in the Hadley cell.

In midlatitudes, the poleward energy transport is archived by baroclinic waves rather than by a thermally driven cell. As midlatitude waves grow due to baroclinic instability, they tend to propagate away from the source. By considering comprehensive wave dynamics (see Vallis, 2017), wave propagation away from the disturbance acts to transport the westerly momentum back to the source region (schematically shown in Figure 2.5b). The acceleration of the zonal flow leads to the development of strong westerlies. Therefore, this polar jet is also referred to as the *eddy-driven jet*. Both jets are more pronounced in the winter hemisphere because of the larger temperature gradient during this season.

The different formation mechanisms give rise to specific jet features. The subtropical jet is stronger than the polar jet and can be considered as a circumpolar wind band, although it may experience disruption at certain latitudes. It is centred around the 30° latitude, manifesting as distinct wind maxima in zonal or temporal averages. On the contrary, the polar jet can emerge anywhere in mid- to high latitudes, typically around 60°, and manifests in various forms.

Figure 2.6 shows the climatological patterns of the wind from the ERA5 reanalysis. The subtropical jet reaches its peak intensity at 200 hPa, clearly emerging as a wind maximum in the time-averaged data at this pressure level (Figure 2.6a) and in the latitude-height cross section of the zonal mean zonal wind (Figure 2.6b). The winter subtropical jet is more intense, as previously noted. In the northern hemisphere, two local wind maxima – east of North America and Asia – are typically observed. These longitudinal asymmetries are primarily induced by large topography and land-ocean heating contrasts.

The presence of a polar jet is not discernible in these climatological maps. The sparse and disrupted nature of the polar jet impedes the evaluation through time or zonal averages. However, when daily wind maps are considered, two distinct jets often occur. A latitude-height cross-section at a specific longitude on a specific date in winter is shown in Figure
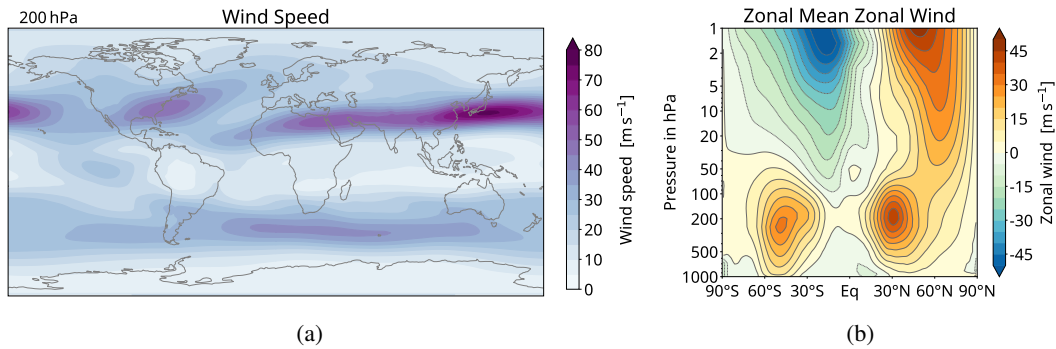
Figure 2.6: Winter (DJF) climatological wind in ERA5 reanalysis (1979–2022): The magnitude of the horizontal wind $|\mathbf{v}_h|$ in the upper troposphere (200 hPa) is demonstrated in (a). A latitude-height cross-section of the zonal mean zonal wind is shown in (b), depicting the troposphere and the middle atmosphere.

2.3 on page 14. In addition to the well-defined subtropical jet, a polar jet emerges at 60°N. The depicted jet maxima are located near the tropopause, as indicated by the 2 PVU contour line. The tropopause typically shows jumps or discontinuities at jet locations. Occasionally, subtropical and polar jets are in close proximity and can be regarded as *merged*. Furthermore, the strength of the subtropical jet can influence the formation of the polar jet (e.g. Liu et al., 2021). Accordingly, the jets are considered to have an interconnected relationship.

2.2.5 Atmospheric waves

A broad spectrum of weather disturbances is linked to atmospheric waves. In general, waves refer to oscillations of field variables, such as velocity or pressure, characterised by various scales in time and space. These waves transmit energy and momentum without a material transport of air. Atmospheric waves can be classified based on their restoring forces. For example, sound waves are a type of longitudinal waves generated by oscillations in the pressure gradient force. Although they represent a solution to the primitive equations, they are considered unimportant for atmospheric dynamics. Consequently, sound waves are typically filtered in numerical models.

Internal *gravity waves* are induced by the buoyancy force acting on a vertically displaced air parcel. The emerging oscillation exhibits a specific frequency known as the Brunt-Väisälä frequency N (see Formula 2.20). Vertical displacement can be initiated by a flow over mountains, convection, or fronts. Gravity waves are small-scale disturbances that propagate horizontally and vertically. They can manifest as lee waves in typical cloud formations. Nevertheless, gravity waves have little effect on large-scale tropospheric weather patterns. However, their crucial role in vertically transporting momentum to higher altitudes is an essential component of the circulation in the middle atmosphere.

(a) Barotropic Rossby wave generation
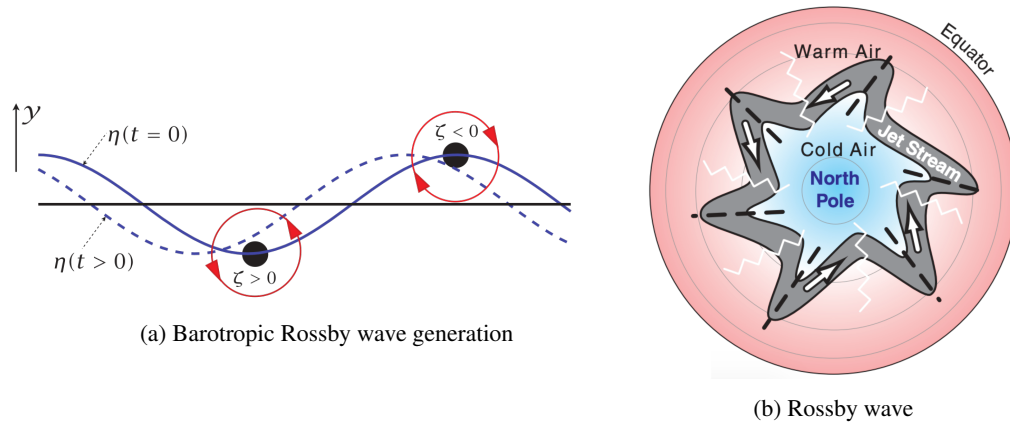

(b) Rossby wave

Figure 2.7: Schematic explanation of Rossby waves: The barotropic generation mechanism is illustrated in (a). The inertial disturbance is indicated by the blue line, the induced velocity field by the red arrows, and the westward phase propagation by the dashed blue line (from Vallis, 2017). (b) A schematic illustration of a Rossy wave in the northern hemisphere: The troughs are marked with black dashed lines and ridges with white zigzag lines. The location of the jet stream is also indicated (from Stull, 2017).

Rossby waves

In midlatitude dynamics, large-scale *Rossby waves* or *planetary waves* play an essential role in shaping the weather. They owe their existence to the rotation of the Earth and can be explained by considering the conservation of potential vorticity (see Formula 2.22). In a simple barotropic perspective, this reduces to the conservation of the absolute vorticity

$$\frac{\mathrm{d}}{\mathrm{d}t}(\zeta + f) = 0. \tag{2.24}$$

In this case, the restoring force is the meridional gradient of planetary vorticity f (see Formula 2.18). If an air parcel is displaced in the meridional direction, planetary vorticity f varies which must be followed by a change in relative vorticity ζ. As illustrated in Figure 2.7a, this leads to the production of relative vorticity, depending on the direction of the displacement. The induced velocities give rise to advection and the disturbance propagates westward, as indicated by the dashed line in Figure 2.7a.

The meridional displacements are preferentially excited after a large orographic topography. This process leads to the generation of stationary Rossby waves in the lee region of the Rocky Mountains and Himalayas. In fact, the northern hemisphere experiences a greater occurrence of these waves due to the presence of larger mountain ranges and a more pronounced land-sea contrast. Rossby waves can be observed on geopotential maps as alternating ridges and troughs around the globe (pictured in Figure 2.7b). They can be characterised by the number of troughs (or ridges) along a latitudinal circle. This dimensionless number is known as the zonal wavenumber. Some common values are presented in Table 2.1. A typical wavenumber of seven is observed during winter in the northern hemisphere. However, weather maps generally do not reveal a single-wave pattern. Instead, Rossby waves

with varying scales can be superimposed. The polar jet stream is often embedded within Rossby waves and occasionally exhibits a distinctive wave-like shape. Although often depicted as horizontal waves, Rossby waves can also propagate vertically and, like gravity waves, transport energy into the middle atmosphere.

2.2.6 Zonal mean circulation

The nature of the general circulation was discussed in Section 2.2.4. It can be understood as large-scale global circulation averaged over a certain time period. However, despite often being depicted as a zonal mean circulation, longitudinal variations play a significant role, especially in midlatitudes. In the following section, a mathematical description of the zonal mean circulation and the influence of waves on this circulation is outlined.

Conventional Eulerian mean equation

To study the general circulation, it is convenient to divide the flow into two components: a zonal mean and a longitudinally dependent *eddy* component (Holton, 2004). Any variable A, depending on longitude λ, latitude φ, pressure p and time t, can be separated into

$$A(\lambda, \varphi, p, t) = \overline{A}(\varphi, p, t) + A'(\lambda, \varphi, p, t) \qquad (2.25)$$

$$\text{with} \qquad (2.26)$$

$$\overline{A}(\varphi, p, t) = \frac{1}{2\pi} \int_0^{2\pi} A(\lambda, \varphi, p, t)\, \mathrm{d}\lambda. \qquad (2.27)$$

The variable $\overline{A}$, averaged across all longitudes, represents the zonal mean state, whereas the eddy term A' reflects the longitudinal deviation from the mean. As this approach is evaluated at fixed spatial coordinates, it is referred to as the *Eulerian mean*.

For the analysis of zonally averaged circulation, it is not sufficient to consider only the zonally symmetric component. The influence of eddies on the average flow must also be considered. Applying the perturbation method (Equation 2.25) to all spatially dependent variables of the primitive equations (Equation 2.7 – 2.10), taking the zonal mean of the entire equations, utilising the quasi-geostrophic approximation and making various simplifications

Table 2.1: Examples of different wavenumbers and their classification.

Wavenumber	Characteristics
0	Pure zonal flow
1 – 3	Large-scale planetary waves
4 – 10	Synoptic-scale disturbances

yield the conventional Eulerian mean equations

$$\frac{\partial \overline{u}}{\partial t} = f_0 \overline{v} - \frac{\partial(\overline{u'v'})}{\partial y} + \overline{X} \tag{2.28}$$

$$\frac{\partial \overline{T}}{\partial t} = -\sigma_p \overline{\omega} - \frac{\partial(\overline{v'T'})}{\partial y} + \frac{\overline{J}}{c_p}, \tag{2.29}$$

with the static stability parameter in pressure coordinates given by

$$\sigma_p = \frac{\kappa \overline{T}}{p} - \frac{\partial \overline{T}}{\partial p}. \tag{2.30}$$

These equations can be derived based on the calculations outlined in Holton (2004) but have been adapted for use in pressure coordinates. The variables $\overline{v}$ and $\overline{w}$ correspond to a mean meridional overturning circulation and the waves are represented by the eddy momentum $(\overline{u'v'})$ and eddy heat flux $(\overline{v'T'})$.

When examining these equations in detail, insights can be gained regarding the impact of different forcings on the zonal mean variables $\overline{u}$ and $\overline{T}$. Thus, the local change in the zonal mean zonal wind $\overline{u}$ is influenced by the following factors:

- The Coriolis term ($f_0 \overline{v}$) indicates that, in the presence of a meridional flow, the change in the local zonal wind is influenced by deflection due to the Coriolis force.

- The divergence of the eddy momentum flux ($\overline{u'v'}$) represents the effect of the eddies on the zonal mean flow.

- The term $\overline{X}$ depicts frictional forces or small-scale eddies.

On the other hand, the zonal mean temperature $\overline{T}$ can be controlled by:

- Adiabatic heating or cooling induced by vertical motions ($\sigma_p \overline{\omega}$).

- The divergence of the eddy heat flux ($\overline{v'T'}$), again representing the effect of the eddies.

- The diabatic term ($\overline{J}$): Despite a small residual, plays an essential role in this context as it is the primary driver of the meridional circulation.

The Eulerian mean equations 2.28 and 2.29 suggest that the zonal wind and temperature are two independent variables. However, under geostrophic conditions, these quantities are connected through the thermal wind balance, given in the zonal mean form as

$$f_0 \frac{\partial \overline{u}}{\partial p} = \frac{R}{p} \frac{\partial \overline{T}}{\partial y}. \tag{2.31}$$

The introduction of a single eddy flux term in Equation 2.28 or 2.29 would disrupt the thermal wind relation. To uphold this relationship, any departure from the geostrophic balance induces an ageostrophic meridional circulation. The divergence of the eddy momentum flux is roughly offset by a poleward flow, while the convergence of the eddy heat flux is countered by adiabatic cooling through downwelling.

In a good approximation, the midlatitude waves generate an ageostrophic mean circulation rather than changing the zonal mean state. The prevalence of geostrophic balance in the atmosphere can be attributed to this geostrophic adjustment process. In practice, Eulerian mean equations can be utilised to assess the mean meridional circulation, explaining the forcings of the Hadley and the Ferrel cell.

Transformed Eulerian Mean Equations

Under certain circumstances, it is necessary to diagnose the net effect of waves on the zonal mean flow. As indicated in Equation 2.28, when neglecting small-scale processes, a variation in the zonal mean wind $\overline{u}$ can only occur because of a small residual or imbalance between the eddy force and meridional circulation. Analogously, the local temperature change is determined by the discrepancy between the divergence of eddy heat flux and adiabatic cooling, or by diabatic effects. Andrews and McIntyre (1976) introduced the *transformed Eulerian mean* (TEM) equations to better diagnose net eddy forcing and to provide a more direct view of mass transport.

In a broad summary, the meridional circulation is transformed into a *residual* meridional circulation. In the first instance, the vertical residual velocity $\overline{\omega}^*$ is defined as the vertical motion whose impact on adiabatic temperature changes remains uncompensated by the divergence of eddy heat flux

$$\overline{\omega}^* = \overline{\omega} + \sigma_p^{-1} \frac{\partial\left(\overline{v'T'}\right)}{\partial y}. \tag{2.32}$$

Considering mass conservation, in accordance with Equation 2.10, the residual meridional velocity $\overline{v}^*$ is given by

$$\overline{v}^* = \overline{v} - \sigma_p^{-1} \frac{\partial\left(\overline{v'T'}\right)}{\partial p}. \tag{2.33}$$

Substituting into the Eulerian mean equations yields the TEM equations

$$\frac{\partial \overline{u}}{\partial t} = f_0 \overline{v}^* + \frac{\partial\left(\overline{u'v'}\right)}{\partial y} + \sigma_p^{-1} \frac{\partial\left(\overline{v'T'}\right)}{\partial p} + \overline{X}, \tag{2.34}$$

$$\frac{\partial \overline{T}}{\partial t} = -\sigma_p \overline{\omega}^* + \frac{\overline{J}}{c_p}. \tag{2.35}$$

Two important statements emerge within the TEM framework. In addition to the diabatic term, the temperature variation is determined by the vertical motion of the residual circulation alone, while the zonal flow is influenced by a combination of the two eddy flux quantities.

Eliassen-Palm flux

The TEM equations provide a better classification of the net effect of eddy fluxes on the zonal mean circulation. Furthermore, the eddy terms in Equation 2.34 can be combined and intepreted as a divergence of a vector

$$\nabla \cdot \mathbf{F} = \frac{\partial (\overline{u'v'})}{\partial y} + \frac{\partial (\sigma_p^{-1} \overline{v'T'})}{\partial p} \tag{2.36}$$

namely the *Eliassen-Palm* (EP) *flux* $\mathbf{F}$ with

$$\mathbf{F} = \overline{u'v'}\,\mathbf{j} + (\sigma_p^{-1}\overline{v'T'})\,\mathbf{k} \tag{2.37}$$

in quasi-geostrophic scaling and with $\mathbf{j}$ as the unit vector in the meridional direction and $\mathbf{k}$ as the unit vector in the vertical direction. Hence, the divergence of the EP flux represents the influence of quasi-geostrophic waves on the mean flow.

$$\frac{\partial \overline{u}}{\partial t} = f_0 \overline{v}^* + \nabla \cdot \mathbf{F} + \overline{X} \tag{2.38}$$

As outlined in Vallis (2017), the zonal mean of the eddy flux of potential vorticity q is equivalent to the divergence of the EP flux

$$\nabla \cdot \mathbf{F} = \overline{v'q'}. \tag{2.39}$$

This relationship indicates that the interaction between the waves and mean flow can be characterised by the poleward flux of PV. Another important feature of the EP flux arises from the Eliassen-Palm relation (Andrews and McIntyre, 1976)

$$\frac{\partial A}{\partial t} + \nabla \cdot \mathbf{F} = D, \tag{2.40}$$

where A denotes the wave activity density and D denotes non-conservative effects. Applying this equation in a conservative scenario and considering a plane wave with a valid dispersion relation, holds

$$\frac{\partial A}{\partial t} + \nabla \cdot (A\mathbf{c}_g) = 0 \quad \text{with} \quad \mathbf{F} = A\mathbf{c}_g \tag{2.41}$$

and $\mathbf{c}_g$ as group velocity of the wave. Under these assumptions, the EP vector shows the direction of wave propagation. The described characteristics of the EP flux make it a widely used tool for illustrating wave propagation and wave-mean flow interaction. Usually, meridional-height cross-sections are presented where EP arrows indicate the direction of wave propagation. The EP flux divergence is shown as contours and refers to wave-mean flow interaction (Edmon et al., 1980). This type of illustration is particularly common for studies of the middle atmosphere and the diagnosis of sudden stratospheric warmings.

2.3 Climate variability

Our climate undergoes several variations on different timescales: seasonal, interannual or decadal. According to the IPCC (2022), the term *climate variability* refers to "the variation of the mean state and other statistics . . . of the climate on all spatial and temporal scales beyond that of individual weather events". When this variability arises spontaneously without external influences, it is termed *natural* or *internal variability*. In contrast, climate change was defined by the UNFCCC[1] as "the change of climate which is attributed directly or indirectly to human activity . . . in addition to natural climate variability". The presence of a large or undervalued internal variability can aggravate the interpretation of climate change studies (e.g. Deser et al., 2010a; Jain et al., 2023). The response to anthropogenic emissions is commonly referred to as *signal*, and internal variability as *noise*. Accurately determining the effects of climate change requires a sufficient signal-to-noise ratio. This can be improved using various methods, including:

- Long time series: Short observational data records may pose challenges.

- Ensemble simulations: Multiple model simulations with identical boundary conditions, but slight variations in initial conditions.

- Evaluation of a multimodel ensemble.

2.3.1 NAO and AO

Internal variability can occur randomly. However, some pronounced repetitive oscillations can be observed in the climate system. In the northern hemisphere, one of the most prominent teleconnection patterns is the North Atlantic Oscillation (NAO). This atmospheric oscillation is characterised by the difference in sea level pressure (SLP) between the Icelandic Low and the Azores High, which serve as centres of action, indicating a north-south oscillation of the atmospheric mass (Hurrell, 2001). The NAO is most active in boreal winter, accounting for one-third of the total variance of SLP over the North Atlantic from December to March.

When the pressure systems over Iceland and Azores are strong, the NAO is in its positive phase. Due to the large pressure gradients, stronger westerly winds prevail in the North Atlantic, transporting warm and moist maritime air into Europe. Meanwhile, the northwestern Atlantic experiences colder weather conditions. The negative phase of the NAO is characterised by a weaker pressure difference between the centres of action, which is associated with opposing signals. For example, this phase often brings colder winter weather to Northern Europe and increases storm activity and precipitation in Southern Europe.

While the NAO is confined to the Atlantic region and surrounding areas, the hemispheric mode of variability is determined by the Arctic Oscillation (AO). This measure is based on the leading mode of pressure variability at various levels, synonymously referring to

---
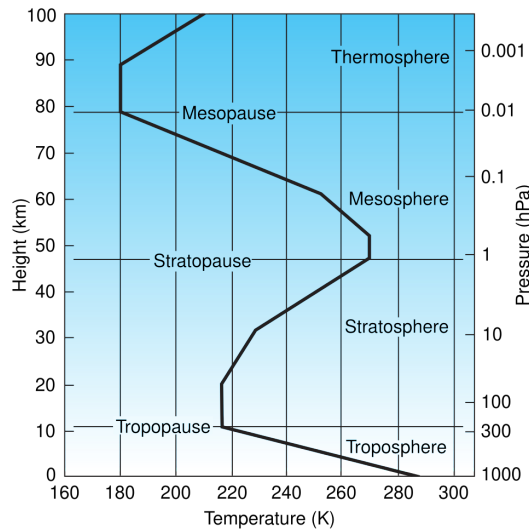
[1]Framework Convention on Climate Change (UNFCCC)

Figure 2.8: Vertical temperature profile typically observed in midlatitudes as represented by the U.S. Standard Atmosphere (from Wallace and Hobbs, 2005).

the Northern Hemisphere Annular Mode (NAM). In contrast to the NAO, the AO extends throughout the entire depth of the troposphere and into the stratosphere. A positive index is associated with strong pressure differences between the North Pole and the midlatitudes. The impacts on European weather are similar to those described for the NAO.

Moreover, the AO in the stratosphere reflects the strength of the polar vortex (see Section 2.4.2). In this context, it is often termed NAM. Baldwin and Dunkerton (2001) calculated the NAM on each pressure level using the first empirical orthogonal function (EOF) of geopotential anomalies north of 20°N. This approach aims to illustrate the troposphere-stratosphere coupling following extreme stratospheric events. Nowadays, it is common to simplify the analysis by applying the area-averaged geopotential height north of 65°N, also known as the *polar cap height* (PCH).

2.4 The Stratosphere

In the preceding sections, various atmospheric phenomena within the troposphere were discussed. Our weather is predominantly shaped in this lowermost layer. On average, the troposphere is typically characterised by decreasing temperatures with altitude (see Figure 2.8). Upon further ascent, the mean temperature profile shows alternating behaviour throughout the full depth of the atmosphere. In general, the sign of the vertical temperature gradient serves as a criterion for classifying atmospheric layers, identified by names ending in *spheres*. The regions marking the transition zones between these layers are referred to as the *pauses*.

The temperature reaches a local minimum at the tropopause, typically occurring between

25

300 hPa and 100 hPa. After remaining relatively constant over a range of altitudes, temperatures begin to increase in the *stratosphere*. This atmospheric layer accounts for approximately 90% of ozone in the atmosphere. Warming in the stratosphere is attributed to the absorption of short-wave radiation by ozone. Subsequently, the temperatures decrease again in the *mesosphere*, reaching an absolute minimum. The stratosphere and mesosphere are also referred to as *middle atmosphere*. The layer above exhibits a temperature increase owing to photoionization and is called *thermosphere*. The following sections provide insight into the features and dynamics of the middle atmosphere.

2.4.1 Stratospheric ozone

Ozone is a molecule composed of three oxygen atoms that naturally form in the atmosphere. More specifically, it is a fundamental compound that makes life on Earth possible by filtering harmful ultraviolet (UV) radiation. The amount of ozone is often quantified using vertically integrated total column ozone (TCO) measured in Dobson units (1 DU).

In 1930, Chapman proposed a mechanism to explain the formation and maintenance of the ozone layer. It involves photodissociation of oxygen molecules O_2 resulting in two oxygen radicals

$$O_2 + hv \longrightarrow O + O. \tag{2.42}$$

Subsequently, ozone O_3 is formed when these atoms combine with another oxygen molecule

$$O + O_2 \longrightarrow O_3. \tag{2.43}$$

On the contrary, ozone can be destroyed by absorbing UV light and decompose into an oxygen molecule and atomic oxygen

$$O_3 + hv \longrightarrow O_2 + O \tag{2.44}$$

or reacts with an oxygen radical

$$O_3 + O \longrightarrow O_2 + O_2. \tag{2.45}$$

These reactions are also referred to as the ozone-oxygen cycle, and the net effect is the conversion of radiation into thermal energy. The distribution of ozone in the stratosphere is basically determined by the balance between these production and removal reactions. Over time, it became clear that the Chapman cycle underestimated the ozone loss, and some additional reactions with free radicals must also be considered. Most ozone production occurs in the tropical stratosphere, where insolation is high. However, early ozone measurements by Dobson et al. (1929) revealed an ozone maximum in the spring in the Arctic. This discrepancy can be explained by the Brewer-Dobson circulation, which is a slow drift of air masses rising in the tropics, moving poleward and descending at the pole.

Ozone depletion

The equilibrium in ozone reactions was upset by chlorofluorocarbons (CFCs), which were widely used for industrial purposes at the beginning of the 20th century. Molina and Rowland suggested in 1974 that these substances break down in the upper stratosphere and release chlorine radicals which can very effectively destroy ozone. Shortly afterwards, Wofsy et al. (1975) demonstrated that bromine radicals released from halon compounds have an even more significant effect on the ozone layer. The most substantial ozone depletion driven by these gas-phase catalytic cycles was expected in the upper stratosphere.

However, unexpected observational evidence has emerged from the lower stratosphere of Antarctica (Farman et al., 1985). An explanation for the rapid ozone depletion at this altitude was given by Solomon et al. (1986). The crucial element in the winter stratosphere over the South Pole is *polar stratospheric clouds* (PSCs) which form only at temperatures below −78 °C. At the surface of the cloud particles, heterogeneous reactions can transform inactive chlorine reservoir species into chlorine gas Cl_2. The return of sunlight in spring induces the formation of chlorine radicals which initiate catalytic reactions. In the following years, it became clear that CFCs and halons could nearly destroy the entire ozone content at certain altitudes, and the term Antarctic *ozone hole* was established. In the Arctic stratosphere, fewer PSCs are formed in winter due to the higher temperatures in this region. While localised heterogeneous ozone depletion has been observed in some years, it is significantly less severe than that in Antarctica.

Ozone recovery

Encouraged by the gravity of the situation and the threat of increased UV radiation, the international community took swift action by implementing the Montreal Protocol and its amendments, which banned most ozone-depleting substances (ODSs). Despite the prolonged lifetimes of these compounds, a decline in the ODS abundance has become evident in the last two decades. Figure 2.9 provides insights into the timeframe for ozone columns to return to 1980 levels, which is a widely used benchmark for assessing ozone recovery. The return date for Antarctic ozone in October is predicted to occur in the second half of this century. Recovery in global-scale ozone, excluding polar regions, is expected around 2040 (World Meteorological Organization (WMO), 2022).

However, the rate of ozone recovery depends on GHG emissions. The ozone layer reveals earlier signs of recovery with increased climate change forcing. Towards the end of the century, the ozone abundance may even exceed their original values. This phenomenon is known as ozone *super recovery*. As pointed out by Langematz (2018), two effects can become important. First, the stratosphere undergoes a cooling trend owing to climate change, leading to slower ozone-depleting reactions in the upper stratosphere. Secondly, the Brewer-Dobson circulation in the middle atmosphere strengthens under global warming (e.g. Oberländer et al., 2013), allowing for more ozone transport from the tropics to the pole.
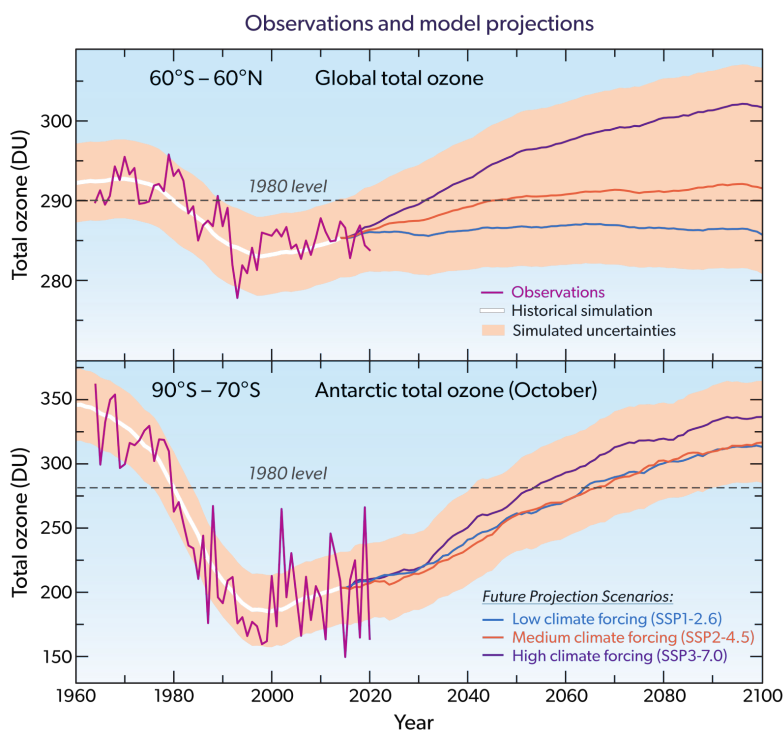
Figure 2.9: Observations of total column ozone (purple) complemented by future projections with Chemistry Climate Models showing possible evolutions of ozone under different GHG scenarios (colours as indicated in the legend). The upper pannel shows gobal ozone without polar regions and the lower panel highlights the trends of ozone over Antarctica (from Salawitch et al., 2023).

2.4.2 Climatological conditions in the stratosphere

The thermal structure of the stratosphere is predominately determined by radiative processes. Nevertheless, the observed temperature distribution reveals some deviations from the theoretical radiative equilibrium state. For example, the polar lower stratosphere is considerably warmer during winter. This discrepancy can be explained by the fluid motion and poleward heat transfer. In contrast to the troposphere, baroclinic instability is largely suppressed by stable stratification in the stratosphere. Hence, circulation in the middle atmosphere is driven mainly by the breaking and dissipation of Rossby and gravity waves propagating from the troposphere (Vallis, 2017).

An overview of the climatological temperature and wind distribution in both solstice seasons is given in Figure 2.10 for ERA5 reanalysis. Two prominent temperature minima stand out: one in the tropical upper troposphere and the other over the winter pole in the stratosphere. In the tropics, deep convection is accompanied by strong vertical motion, and adiabatic cooling associated with this updraft results in a minimum temperature. Over the pole of the winter stratosphere, reduced solar insolation leads to strong radiative cooling. With due
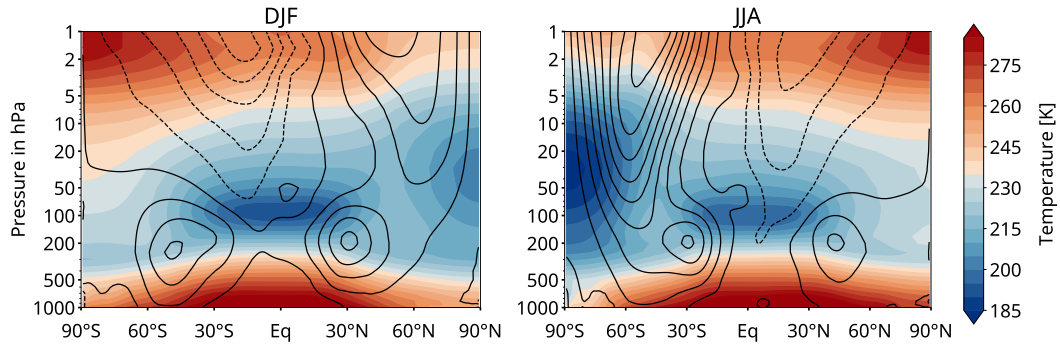
Figure 2.10: Seasonal climatological average of zonal mean temperature and zonal mean zonal wind in ERA5 reanalysis (1979–2021). Temperatures are shown as coloured contours, and zonal wind as black contour lines with contour levels of $10\,\mathrm{m\,s^{-1}}$. Dashed lines represent easterly winds and solid lines westerly winds.

regard to the thermal wind relations (Equation 2.13), specifically

$$\frac{\partial u}{\partial p} = \frac{R}{f\,p}\frac{\partial T}{\partial y},$$

(2.46)

the horizontal temperature gradients between the cold pole and midlatitudes induce strong westerly winds in the winter middle atmosphere, also known as the *polar night jet*. In the summer hemisphere, the reversed horizontal temperature gradients induce prevailing easterly winds (dashed lines in Figure 2.10).

Stratospheric polar vortex

Strong circumpolar westerlies in the winter stratosphere form a belt that encloses an area of extremely cold air. This pronounced low-pressure structure is denoted as the *polar vortex*. The highest wind speeds can reach $100\,\mathrm{m\,s^{-1}}$ in the upper stratosphere, and these strong winds isolate the cold air inside the vortex, thereby preventing its mixing with midlatitude air. Moreover, the temperatures within the polar vortex fall below the threshold required for PSC formation, which is a crucial factor in ozone depletion (see Section 2.4.1).

The polar vortex begins to build up every autumn as the solar heating diminishes over the pole. It typically reaches the maximum strength in January and breaks down in spring when sunlight returns. The Antarctic polar vortex is significantly stronger and colder than its Arctic counterpart. This can be explained by the influence of Rossby waves, leading to deceleration of the polar night jet and subsequent mixing with midlatitude air. The Rossby wave activity is more pronounced in the northern hemisphere (see Section 2.2.5), thus the vortex in this hemisphere is subjected to more frequent disturbances, and mixing.

2.4.3 Sudden stratospheric warmings

During certain winters, the stratospheric circulation undergoes an impressive disruption. In 1952, Richard Scherhag discovered an explosive-type warming in radiosonde measurements conducted at Tempelhof Airport in Berlin. This warming, locally exceeding 50 K, develops in just a few days and is referred to as *sudden stratospheric warming*. With more observations in the following decades, it became evident that the warming is accompanied by disruption or strong displacement of the polar vortex. These events are extreme in terms of their circulation anomaly rather than their temporal incidence, occurring roughly every two years in the northern hemisphere. However, the frequency of SSWs can vary considerably, with only two warming events occurring in the 1990s, followed by more active winters in subsequent decades.

SSW classification

The WMO classification of stratospheric warmings is based on the temperature difference between the pole and midlatitudes, as well as the strength of the zonal wind of the polar night jet. The mid-winter warming events are grouped into *minor* and *major warmings*. A minor warming occurs when the gradient of the zonal mean temperature at 10 hPa between the pole and midlatitudes (60°) is positive

$$\overline{T}_{90°} - \overline{T}_{60°} > 0, \tag{2.47}$$

or in simpler terms if the pole is warmer than the lower latitudes in the middle stratosphere. Note that strictly spreaking $\overline{T}_{90°}$ is not a zonal-mean quantity. Depending on the evaluated data, the grid points closest to the pole may be utilised and averaged.

If the polar vortex is centred directly over the pole and has a circular shape, the maximum wind speed of the westerly polar night jet is typically found at 60° latitude. A major warming is characterized by a reversal of the zonal wind at that latitude and in 10 hPa

$$\overline{u}_{60°} < 0 \tag{2.48}$$

indicating an easterly wind in the zonal mean. This change in direction is often referred to as complete breakdown of the polar vortex. Although this criterion indicates a significant disruption of circulation, the polar vortex does not disappear completely. Instead, the vortex is considerably weakened, sometimes shifts far away from the pole or even splits into two separated vortices. When averaging around the latitude circle, the easterly winds gain predominance. In this study only major wamings are evaluated. These are termed SSWs or simply stratospheric warmings. Examples of a strong polar vortex and a stratospheric warming are shown in Figures 2.11a and b, respectively.

Some alternative classifications of SSWs have been used. Charlton and Polvani (2007) established the commonly used method to identify major warmings, which applies only the zonal wind reversal criterion in Equation 2.48. However, it was shown by Butler and Gerber (2018) that the location and threshold of the WMO and Charlton and Polvani (2007) classification are well suited for identifying SSW events with a significant dynamical impact.
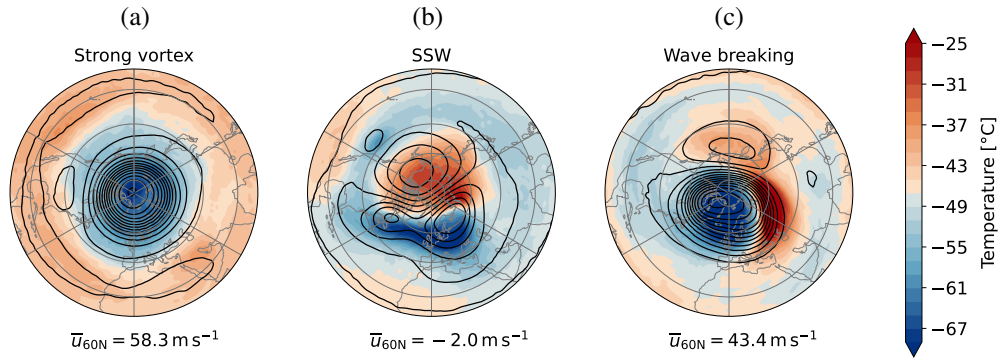
Figure 2.11: Daily mean ERA5 geopotential height (contours) and temperature (shadings) in 10 hPa. A strong and centred polar vortex is shown in (a) for 17 February 2020. A sudden stratospheric warming (SSW) on 2 January 2019 is illustrated in (b). The wave breaking at the vortex edge on 4 Feb 2018 is demonstrated in (c), ultimately leading to an SSW one week later. The contour interval of the geopotential height is 250 m, and the zonal mean zonal wind at 60°N is denoted below.

SSW mechanism

The formation of SSWs can be largely explained by wave-mean flow interactions, although not every aspect is fully understood. The extreme disturbance of the stratospheric circulation can be attributed to the upward propagation and dissipation of Rossby waves from the troposphere. The planetary wave activity is most pronounced during winter, and under suitable conditions, these waves can reach the middle atmosphere. Charney and Drazin (1961) established a criterion restricting the propagation of planetary waves

$$0 < \bar{u} - c < u_{crit} \quad \text{with} \quad u_{crit} \approx \beta(k^2 + l^2). \tag{2.49}$$

The zonal mean background flow is given by $\bar{u}$ and the phase velocity of the wave is denoted by c. The critical velocity u_{crit} depends on the zonal and meridional wavenumber, k and l respectively. This condition implies that the vertical wave propagation is confined to a certain background wind and the size of the wave. Accordingly, only large-scale planetary waves are permitted to propagate upward and solely in westerly winds. Consequently, Rossby waves with wavenumbers of one to three occur in the winter stratosphere. In the summer hemisphere, prevailing easterlies completely suppress wave propagation, resulting in a dynamically undisturbed state in the summer stratosphere.

Charney and Drazin (1961) also concluded that in the absence of dissipation or a critical layer, waves can pass through a mean flow without any acceleration. However, as the waves ascend into the upper atmosphere, they encounter one of two scenarios: either they reach a critical layer or their amplitude increases due to a decrease in density. Consequently, wave breaking ultimately occurs, and the easterly momentum of the Rossby wave decelerates the westerly wind in the polar night jet.

In the quasi-geostrophic framework, the processes that occur during an SSW unfold as follows: Local wave breaking destroys the geostrophic balance between the Coriolis force F_c
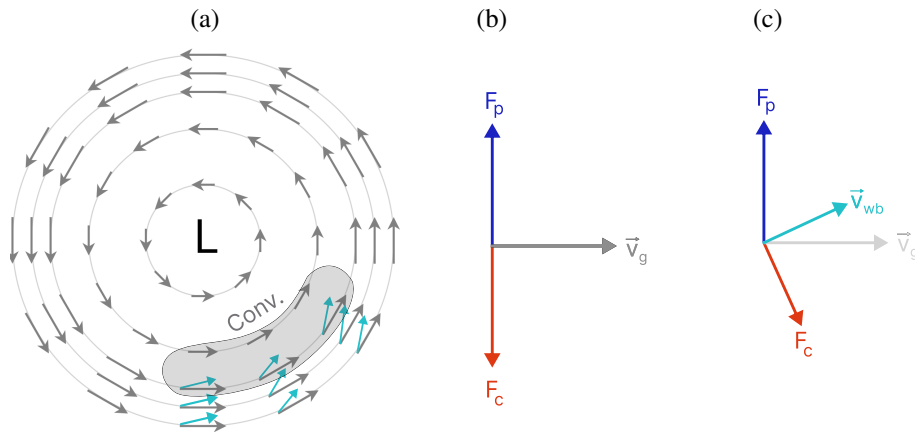
(a) (b) (c)

Figure 2.12: Schematic illustration of wave breaking at the polar vortex edge. (a) A low-pressure system is depicted with isohypses in light grey contours and grey vectors representing the geostrophic wind. Cyan vectors depict the deflected wind resulting from wave breaking, with the grey area highlighting wind convergence. (b) The initial geostrophic balance is demonstrated with the pressure gradient force F_p balanced by the Coriolis force F_c. (c) When the wind is decelerated by wave breaking, the velocity-dependent Coriolis force decreases, disturbing equilibrium. As a results, the wind shifts toward the vortex center (cyan vector).

and the pressure gradient force F_p. As illustrated in Figure 2.12, a weaker wind **v** is associated with a weaker Coriolis force, whereas the pressure gradient remains unchanged. As a result, the wind deflects toward lower pressures which is the vortex centre. This local shift in the wind leads to convergence on the poleward side of the wave breaking. This convergence induces a strong descent of air to lower levels. This downwelling becomes apparent as a strong local temperature rise due to adiabatic warming. An example in reanalysis is given in Figure 2.11c indicating wave breaking at the vortex edge over Siberia. The actual explosive-type of warming, already observed by Scherhag (1952), is caused by this downwelling. Consequently, the polar vortex is weakened by the waves because the induced poleward mass flow reduces the pressure gradient toward lower latitudes. On the other hand, the vortex experiences a push away from the location of the wave breaking and ends up being displaced from the pole.

It became evident that a single wave event alone is insufficient to trigger such an extreme disturbance as an SSW. Palmer (1981) proposed the concept of the polar vortex needing to be *preconditioned*, and it is now widely accepted that an accumulated wave forcing, spanning approximately over a month, is required for SSWs to occur. Furthermore, a discussion arises if extraordinary wave input from the troposphere is required for the formation of SSWs (summarised in Baldwin et al., 2021). It is possible that climatological mean forcing alone is adequate, but the passage of these waves is influenced by the state of the stratosphere.

Downward influence of SSWs

Stratospheric warmings represent a remarkable phenomenon in the middle atmosphere, and its occurrence is often mentioned in weather reports. The large media interest in a circulation anomaly occurring at such high altitudes stems from its potential impact on our surface weather and its capability to favour cold air outbreaks.

Figure 2.13 outlines the downward propagation of the SSW signal towards the troposphere. Composite anomalies centred on the onset date of SSW events are illustrated. The graph in (a) reveals that the pronounced warming of the polar cap migrates downward to the lower stratosphere over time, followed by a cooling at upper levels. The downward influence towards the troposphere is also visible in the polar cap pressure in (b) by 'dripping' down anomalies. Baldwin et al. (2021) justify the lumpiness of the pressure signal to the relatively small number of SSW events averaged. Note that the changes in the lower stratosphere and troposphere persist much longer than those in the upper stratosphere. Therefore, the largest influence on the surface is expected one or two months after the onset date.

The weakening of the tropospheric polar vortex following SSWs can result in significant changes in weather patterns as highlighted by Butler et al. (2017). The surface composite anomaly for 60 days after the event is illustrated in Figure 2.14. The increase in the surface pressure over the pole is evident in (a). Simultaneously, a significantly lower pressure over the Atlantic and Europe is visible, indicating a negative NAO configuration (see Section 2.3.1). Moreover, marked cooling over Eurasia is discernible when examining the temperature anomalies in (b). Additionally, there is warming over Eastern Canada, coinciding with cooling in the eastern United States. The shift of the tropospheric pressure patterns increases the chances of cold air outbreaks from the Arctic, thereby raising the risk of severe winter weather in midlatitudes (e.g. Kolstad et al., 2010). Finally, Figure 2.14c reveals wetter conditions in Southern Europe and decreased precipitation in Scandinavia. In summary, SSWs are often followed by a weakened tropospheric pressure gradient between the pole and midlatitudes, resulting in colder winter weather in distinct regions of the northern hemisphere.

The exact mechanisms of the dynamical coupling between the stratosphere and troposphere are not fully understood. As synthesised in Baldwin et al. (2021), possible dynamical theories include the following:

- remote effects of stratospheric wave driving and the induced meridional circulation, also known as *downward control*,

- planetary wave absorption and reflection,

- direct effects on baroclinicity and baroclinic eddies, and

- remote effects of stratospheric PV anomalies.

Although these processes have been discussed in literature, their precise physical mechanisms remain uncertain.
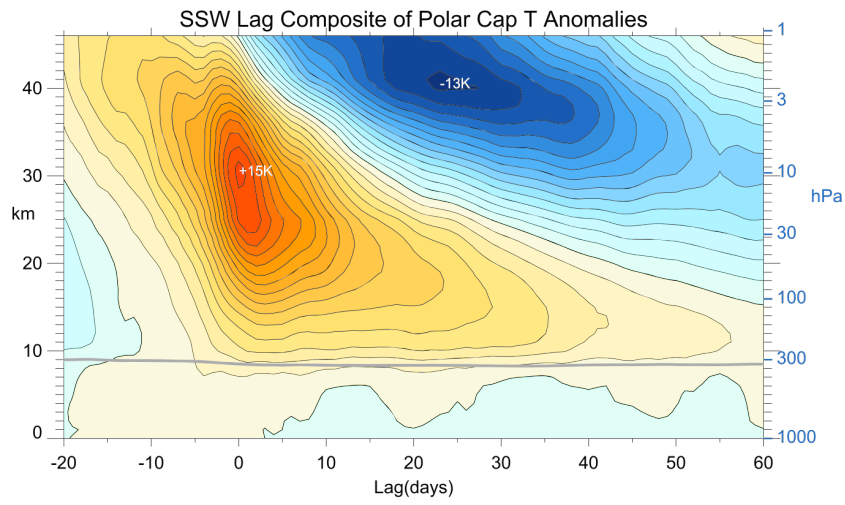
(a) Temperature anomaly
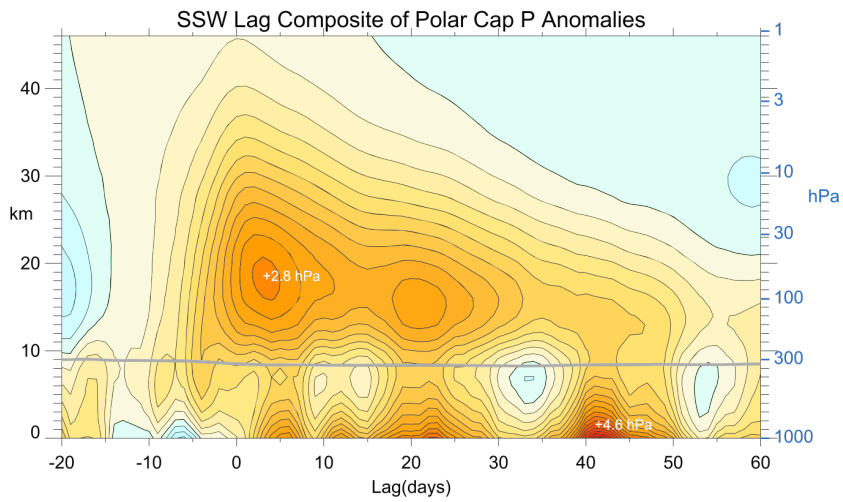
(b) Pressure anomaly

Figure 2.13: Lag-composite anomalies of polar cap (65° to 90°N) mean temperature (a) and pressure (b). The composites include 36 SSW from 1958 to 2015 obtained from JRA-55 reanalysis. SSWs were classified by applying the criteria from Charlton and Polvani (2007). Contour intervals are 1 K in (a) and in (b) 0.25 hPa (from Baldwin et al., 2021).
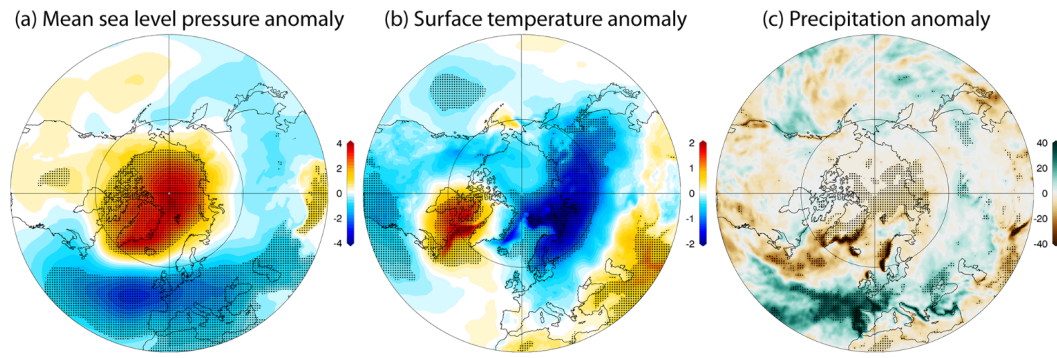
Figure 2.14: Composites anomalies of the 60 days after SSW events from JRA-55 reanalysis for (a) mean sea level pressure in hPa, (b) surface temperature in K and (c) precipitation in mm. Stippling regions marks significant variation from climatological values at 95% level (from Butler et al., 2017).

Another aspect relevant to both the generation of planetary waves in the troposphere and the potential downward influence, is atmospheric blocking. On the one hand, these large-scale anticyclones, often stationary over several days or even weeks, can cause vertically propagating Rossy waves of sufficient duration to trigger SSW events (e.g. Martius et al., 2009; White et al., 2019). On the other hand, a more frequent occurence of blockings has been observed after SSWs (e.g. Labitzke, 1965; Davini et al., 2014), coinciding with persistent cold winter weather in the respective region.

Given the relatively slow tropospheric response to SSWs, troposphere-stratosphere coupling has the potential to enhance the subseasonal to seasonal weather forecast. SSWs can be predicted to occur approximately 10 to 15 days in advance (Domeisen et al., 2020b). Furthermore, Domeisen et al. (2020a) demonstrated that forecast skill improves when the stratosphere and its coupling are appropriately considered.

Sudden warmings in a changing climate

The frequency of sudden warmings, determined from ERA5 reanalysis spanning from winter 1957/58 to 2022/23, and classified according to Charlton and Polvani (2007), is 6.4 events per decade. The distribution of SSWs in this observational time frame is demonstrated in Figure 2.15. The occurrence of SSWs clearly shows fluctuations arising from a combination of internal and external variabilities. Some external drivers are the quasi-biennial oscillation (QBO), El-Niño Southern Oscillation (ENSO), the Madden-Julian oscillation (MJO), and recently discussed, Arctic sea ice or Siberian snow cover. Investigating these forcings within the short-term observational record is challenging because the simultaneous occurrence of these factors is relatively rare.

Another crucial point to address is the influence of climate change on the stratospheric variability. It remains unclear whether the frequency of SSWs will change in the future. The evaluation of SSW occurrence across two different multi-model intercomparison projects,
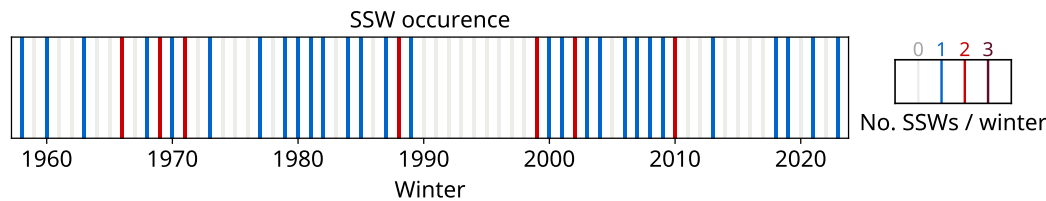
Figure 2.15: Occurrence of major sudden stratospheric warmings (SSWs) in the extended winter season (NDJFM) in ERA5 renanalysis spanning from 1957 to 2023. Events are classified following Charlton and Polvani (2007) and the occurrence is depicted in the legend showing the number of events per season. The years are labeled for January of each season.

the Chemistry-Climate Model Initiative (CCMI) and the Coupled Model Intercomparison Project 6 (CMIP6) by Ayarzagüena et al. (2018) and Ayarzagüena et al. (2020) respectively, has revealed a lack of consensus regarding the significance and even the sign of changes in SSW frequency. The findings for CCMI models and reanalyses are shown in Figure 2.16a. Only three of 12 models showed a significant increase in SSW occurrence in the future. Moreover, the variations in climatological frequency point to large discrepancies in the basic state of the model, and some frequencies are rather unrealistic. The ambiguity is even larger in CMIP6 models, as shown in Figure 2.16b, demonstrating the full range of possible future scenarios. As stated in Baldwin et al. (2021), uncertainties may arise from unknown aspects of SSW dynamics and the biases in the models.

An alternative method for classifying SSWs was employed by Li et al. (2023), focussing on local warming rather than circulation anomalies. Their findings suggest a significant increase in the intensity and duration of SSWs in the recent past (1980 – 2021). Although no changes in frequency were observed, these results could provide an initial indication of increased wave breaking in the stratosphere.

The middle atmosphere has been neglected for a long time in weather forecasting as well as in climate models used for the study of tropospheric dynamics. However, over the last few decades, it has become evident that incorporating these higher altitudes can lead to improvements, particularly in forecasting severe winter weather. Moreover, some tropospheric phenomena are influenced by the coupling of the troposphere and stratosphere. The Arctic-midlatitude linkage could be one of them because it is assumed to involve a stratospheric pathway.
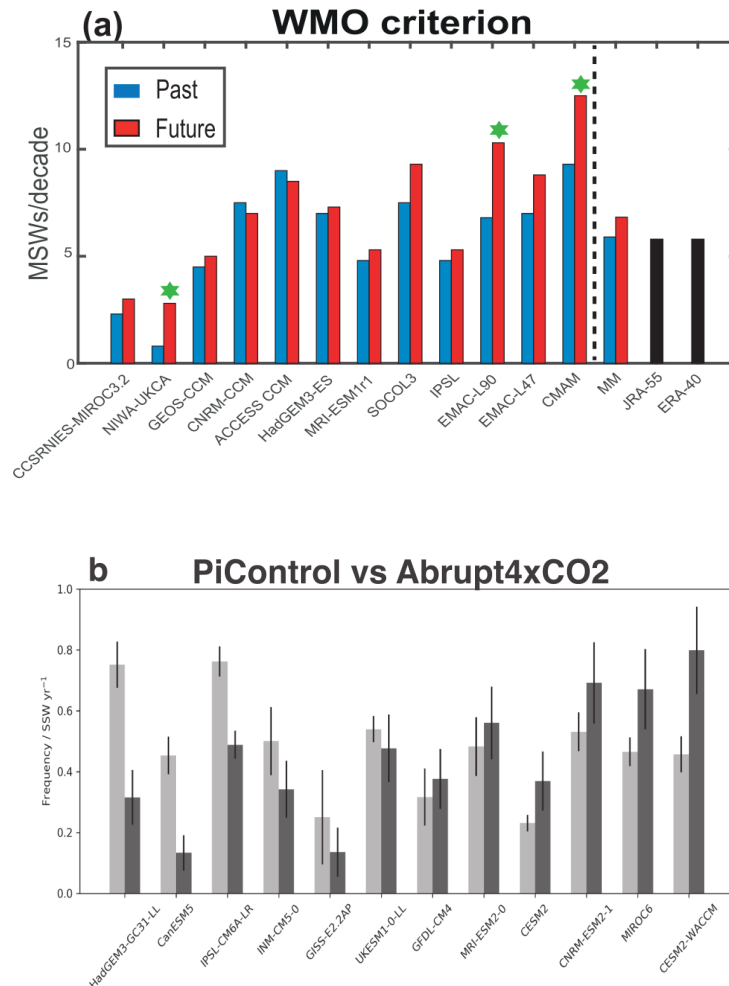
Figure 2.16: Mean frequency of major sudden stratospheric warmings (denoted as MSW or SSW) in two multimodel intercomaparision projects. (a) MSWs per decade for the past (1960 – 2000) and the future (2060 –2100) across 12 CCMI models running a RCP6.0 scenario (Meinshausen et al., 2011), as well as the multi-model mean (MM) and reanalyses JRA-55 and ERA-40. Events were classified according to the WMO criteria. The green bar denotes a significant change in SSW frequency in the future at the 95% confidence level (Ayarzagüena et al., 2018). (b) SSWs per year for a preindustrial (piControl, light grey bars) and abrupt4xCO_2 simulation (dark grey bars) of CMIP6 models. Black lines show 95% confidence interval for each estimate (Ayarzagüena et al., 2020).

CHAPTER 3

Arctic-Midlatitude Linkage

Evidence of global warming induced by GHGs has become increasingly apparent in recent decades. As detailed in Section 2.1.4, one of the climate change symptoms is an accelerated temperature increase in the Arctic region (Arctic amplification). This pronounced warming contributes to a substantial decline in Arctic sea ice, which, in turn, reinforces atmospheric warming. Conversely, midlatitude winters experienced significant cold spells in the 2000s. This sparked the beginning of a controversial debate: whether the warming of the Arctic could paradoxically result in colder winter weather.

This chapter provides an overview of the scientific literature. It is worth noting that a considerable number of articles have been published on the subject to date. The subsequent sections prioritise the exploration of initial concepts, proposed mechanisms with a particular focus on stratospheric contributions, and an overview of the lively debate that has unfolded in recent years.

3.1 Early work

Research into the impact of Arctic amplification on winter circulation began in the late 2000s, motivated by observed sea ice minima and coinciding midlatitude cold waves in winter. The first studies focussed on sea ice reduction in summer and autumn and its influence on early winter circulation.

Honda et al. (2009) found evidence for a large-scale circulation change due to autumn sea ice loss using reanalysis and an atmosphere general circulation model (AGCM). The observed cold anomalies in Eastern Asia have been attributed to the generation of a stationary Rossby wave. The anomalous sea ice cover in the Barents-Kara Sea (BKS or BK Sea) was linked to an anomalous heat flux, which in turn thermally drives a Rossby wave. They reported intensification of the Siberian high, which was responsible for the colder winter conditions in Eastern Asia.

Petoukhov and Semenov (2010) examined the impact of the BK sea ice on the cold winter 2005/2006. By conducting AGCM simulations with prescribed sea-ice concentrations, the analysis indicated that lower-tropospheric heating over the BKS may result in strong anti-cyclonic anomalies. Additionally, they noted a threefold increase in the likelihood of cold

winter extremes and emphasised that the severe winters during that period were not contra-dictory to global warming, but rather indicative of a realignment of circulation patterns.

In the following years, the scientific community has explored many possible correlations and mechanisms associated with sea ice loss. The BKS region and Siberia have received considerable attention. For example, Inoue et al. (2012) concluded that the decline in BK sea ice leads to reduced baroclinicity, which prevents cyclones from travelling eastward, and consequently results in anticyclonic anomalies. Cohen et al. (2012) outlined that the Arctic amplification contributes to an enhanced snow cover in Eurasia and thereby leading to a winter cooling.

However, the research has not been restricted to the Eurasian continent. A heated debate was sparked by the work of Francis and Vavrus (2012). They proposed strong evidence linking Arctic amplification to extreme weather events in North America enabled by larger and slower Rossby waves. This hypothesis promptly drew the attention of the media, but also encountered resistance from the scientific community (e.g. Wallace et al., 2014; Fischer and Knutti, 2014; Kintisch, 2014). At that time, bringing the recent cold weather extremes in North America into alignment with global warming had the potential to strengthen the argument against the denial of global warming. Nevertheless, discussions have emerged regarding the methodology of the study (Barnes, 2013; Screen and Simmonds, 2013) and the challenge of separating remote responses from natural internal variability (Screen et al., 2014).

First review – Cohen et al. (2014)

The first overview on the topic was published by Cohen et al. (2014). While this review highlighted some pitfalls, such as the short data record and failure of climate models to re-produce the linkage, its primary focus was to identify a potential mechanism. They grouped atmospheric responses into three dynamical frameworks:

1. the modification of the storm tracks predominantly in the North Atlantic sector,

2. alteration in characteristics of the jet stream, and

3. anomalous planetary wave configurations through regional changes in tropospheric circulation.

It has been pointed out that these features are occasionally highly interconnected and, there-fore, not without imperfections. Figure 3.1 illustrates the interaction between various forc-ings and midlatitude winter weather. The main conclusions from Cohen et al. (2014) are summarised as follows:

▪ Variability in sea ice may impact the phase and amplitude of the North Atlantic Os-cillation (NAO) or the Arctic Oscillation (AO), thereby influencing storm tracks. Al-though observational studies have indicated significant correlations, model studies have presented ambiguous findings.
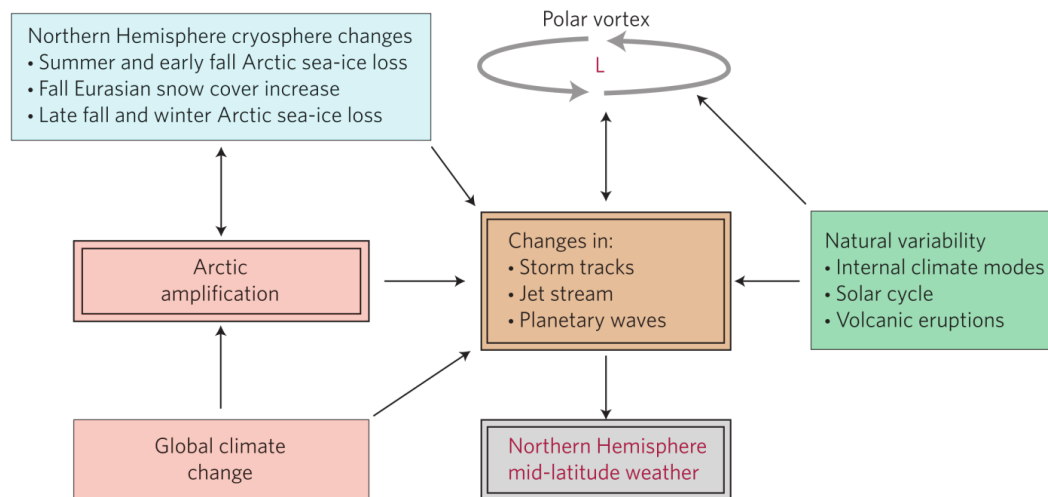
Figure 3.1: Schematic of influence factors of NH midlatitude weather. The proposed dynamical features are shown in the brown box. Bidirectional arrows denote positive and negative feedback between the elements. The stratospheric polar vortex is represented by cyclonic flow and L (from Cohen et al., 2014).

- Arctic amplification has an impact on the tropospheric wave activity and the jet stream in mid- and high-latitudes:

  - *directly* by a modification of the meridional temperature gradient (Arctic Amplification box) and

  - *indirectly* through a feedback with changes in sea ice and snow cover (light blue box).

- Other forcings, not involving Arctic amplification, are also mentioned:

  - natural modes of variability and

  - the influence of global warming (without Arctic amplification) on the general circulation.

- The authors synthesised the cryospheric forcing as follows:

  - Sea ice loss and enhanced snow cover in Siberia in autumn favours mid-tropospheric ridging in the BKS region and troughing over East Asia.

  - This planetary wave configuration favours greater upward wave propagation into the stratosphere.

  - Stratospheric warmings can occur which favour cold air outbreaks several weeks later in midlatitudes.

Hence, the stratosphere has become a part of the mechanism, and the next section delves into studies conducted on this interaction in more detail.

3.2 Stratospheric pathway

Several studies on the tropospheric pathway of the Arctic-midlatitude linkage suggested a modification of planetary wave activity in response to Arctic warming. Considering the troposphere-stratosphere coupling, it was evident that a potential stratospheric contribution to this mechanism was investigated. Jaiser et al. (2013) extented their study of the sea ice influence on the tropospheric circulation (Jaiser et al., 2012) into the stratosphere. ERA-Interim reanalysis data spanning 1979 to 2012 were categorised into high sea ice conditions (1980–2000) and low sea ice conditions (2001-2012). The following signals emerged as indicative of low sea-ice concentrations:

  ▪ a negative AO pattern,

  ▪ enhanced upward EP fluxes, and

  ▪ a weaker stratospheric polar vortex.

Additionally, a maximum covariance analysis (MCA) was performed. Evaluating the influence of the August/September sea ice cover on the winter (DJF) circulation revealed positive geopotential height anomalies over the North pole at 500 hPa and 10 hPa which correspond to a negative NAO/AO pattern.

Kim et al. (2014)

Another study conducted by Kim et al. (2014) also applied ERA-Interim data complemented by sensitivity simulations using the CAM5 model. A similar classification of low sea ice conditions was performed with a focus on the area-averaged sea ice cover over the BKS. The years marked with a red dot in Figure 3.2a are averaged to create a low-sea ice composite. A comparison of these composite means to the entire dataset (1979–2012) reveals the *warm Arctic-cold continent* (WACC) pattern in early winter (ND), as shown in Figure 3.2c. Furthermore, stratospheric conditions were diagnosed by the EP flux and PCH anomaly. The authors linked a weaker polar vortex accompanied by an enhanced vertical EP flux to reduced sea ice conditions. Simulations with prescribed sea ice concentrations confirmed the signals observed in the reanalysis, although with reduced magnitude.

However, the main conclusions of these two early studies were drawn from relatively short reanalysis data records. The assessment of the low sea-ice period only encompassed ten to eleven years. It is conceivable that the sea ice cover and stratospheric polar vortex have been influenced by other processes, or may have aligned by chance. Although the results from model simulations from Kim et al. (2014) matched their findings in the reanalysis, a comprehensive confirmation from climate models was still lacking.

In those days, various model studies have focussed on the isolated effect of melting sea ice on the atmosphere. A typical approach was to exploit sensitivity experiments with AGCMs. In these studies, the boundary conditions were kept fixed, commonly in the present-day state. The only variations arose from the prescribed sea ice concentrations, often comparing
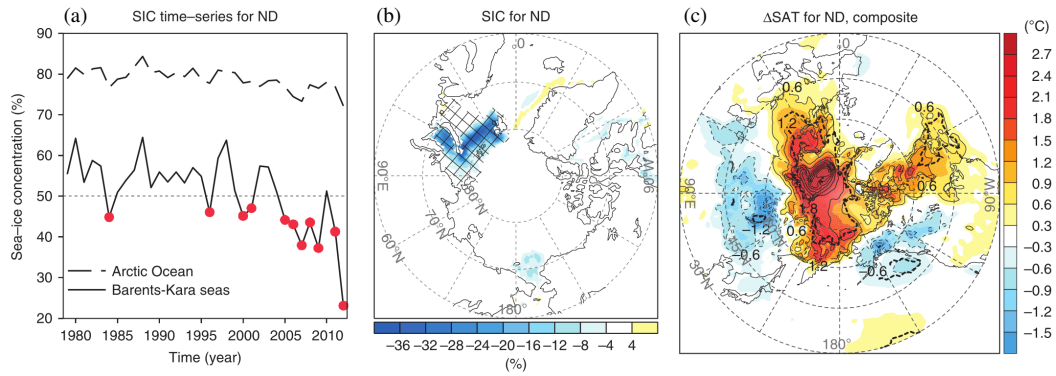
Figure 3.2: (a) Area averaged time series of sea ice cover (SIC) for the BKS (solid) and the entire Arctic Ocean (dashed) during early winter (ND). (b) SIC composite mean of years with BK sea ice lower than 50%, indicated by the red dots in (a). (c) Composite anomaly of surface air temperature (SAT) in early winter. Anomalies are defined as departures from climatology for the period (1979–2012) (from Kim et al., 2014).

present conditions with future scenarios. Given the agreement in GHG concentrations, the discrepancies in these simulations stem only from the impact of sea ice. It is worth noting that atmosphere-ocean feedbacks are not considered in these atmosphere-only models.

Peings and Magnusdottir (2014) used the CAM4 model for sensitivity experiments. According to their simulations, moderate sea ice loss (2007-2012) forces a remote response: weakening of the polar vortex and cooling in midlatitudes in winter. In contrast, a future, and hence stronger, sea ice forcing (2080-2099) revealed weaker and insignificant signals. Cai et al. (2012), on the other hand, found no robust stratospheric response to sea ice changes, besides a weak strengthening in November.

Sun et al. (2015)

In a study employing the WACCM model, Sun et al. (2015) proposed an explanation for the divergent model results. In addition to present and future sea ice conditions, they also conducted simulations prescribing sea ice changes only in the BKS/Atlantic and Pacific regions, respectively. Once again, the stratospheric signal with an overall sea-ice forcing was not found to be significant (Figure 3.3a). The authors demonstrated that the polar vortex weakened under reduced sea ice in the BKS region and strengthened with melting sea ice in the North Pacific (Figure 3.3b and c). In the full forcing case, these changes add up and cancel each other. They elucidated the phenomenon using the linear wave interference theory (e.g. Nishii et al., 2009). Thus, if a forced response is in phase with the climatological planetary wave, upward propagation into the stratosphere will be enhanced. As outlined in Sun et al. (2015), this applies specifically to the BKS forcing. The Pacific forcing tends to suppress wave propagation into the stratosphere through destructive interference with the climatological wave. Nevertheless, contradictions were also evident in this study. They repeated their experiments with the low top version of their model (CAM4) and found an
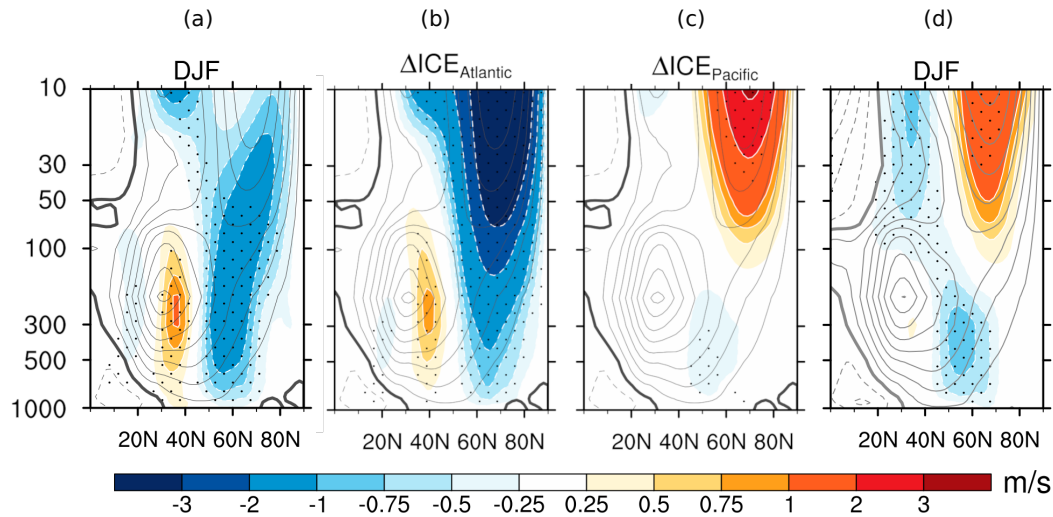
43

Figure 3.3: Zonal mean zonal wind respose (shading) in winter (DJF) for different sea ice forcings and model versions. Climatological zonal wind from the reference period (1980-1999) are depicted with grey contours in an interval of $5\,\mathrm{m\,s^{-1}}$. (a) Wind anomalies relative to the reference period for simulations with WACCM prescribing climatological sea ice for 2080-2099. (b) and (c) same as (a) but with sea ice forcing only in BKS/Atlantic and Pacific region, respectively. Subfigure (d) shows the same as in (a) but for the low top model version CAM4 (from Sun et al., 2015).

opposite stratospheric signal for the full sea ice forcing (Figure 3.3d). This discrepancy was attributed to the lack of a well-resolved stratosphere in CAM4 and the differences in wave propagation.

Idealized model approach

A different approach for assessing the stratospheric pathway was accomplished by Wu and Smith (2016) and Zhang et al. (2017). Several perturbation experiments with imposed near-surface heating were performed using an idealised AGCM. The perturbation was realised as a zonal mean heating source in Wu and Smith (2016) and in different regions and seasons in Zhang et al. (2017). In the latter study, a persistent winter circulation response was found for an all-season additional heating in the BKS region. Specifying this heating only in November and December revealed a prolonged effect on both the stratosphere and troposphere until the end of January. According to this study, applying a nudging method to the stratosphere was thought to distinguish between the tropospheric and stratospheric pathways. The stratospheric pathway was demonstrated to be responsible for a persistent circulation response in midwinter and amplified cooling in central Asia. Enhanced planetary wave propagation with constructive interference in the case of the BKS forcing accounted for the weakening of the stratospheric polar vortex. According to these idealised simulations, the stratosphere plays a central role in the Arctic-midlatide linkage and the warming in the BKS is most effective modifying the wave propagation.
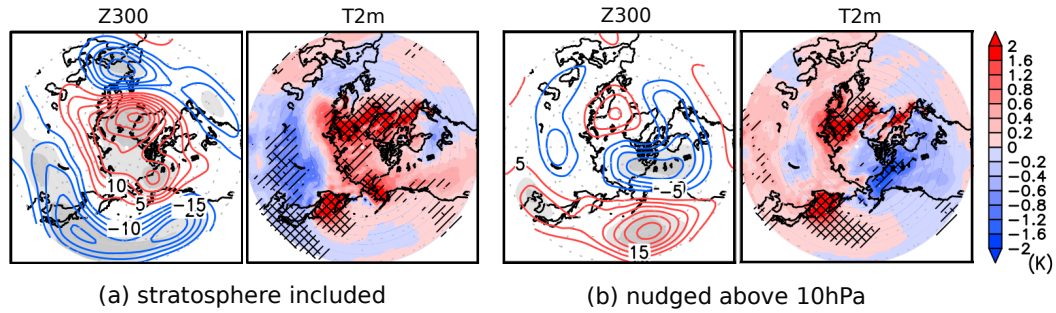
Figure 3.4: Winter (DJF) averaged anomalies calculated as difference between low sea ice conditions (2005–2009) and high sea ice period (1979–1983) and simulated with two different model setups. (a) Anomalies of geopotential height in 300 hPa and 2-meter temperature with the full stratosphere presented in the model. In (b), the stratospheric pathway was suppressed by nudging towards climatological values above 10 hPa. The use of light and heavy grey shades signifies a statistical significance of greater than 95% and 99%, respectively. Hatching (cross-hatching) indicates statistical significance greater than 95% (99%) (from Nakamura et al., 2016).

The isolated effects of sea ice reduction or warming in the BKS are insightful, for example, in understanding the precursors of stratospheric disturbances. At present, the BKS region is among the regions most affected by sea ice loss. However, as suggested by Sun et al. (2015), forcings from other Arctic regions may have offset this impact. This is in accordance with Screen (2017a), who found a significant remote circulation response from isolated sea ice forcing in the BKS region, but did not detect midlatitude cooling in response to pan-Arctic sea ice loss. Therefore, it is difficult to establish a significant stratospheric pathway from an isolated warming in a specific region.

Nakamura et al. (2016) conducted experiments with the AGCM AFES using the widely applied strategy: comparing two different sea ice conditions, in this instance between an early period (1979–1983) and a late period (2005–2009). The authors also evaluated the stratospheric contribution using model runs with a nudged stratosphere, similar to the approach in Zhang et al. (2017). They concluded that the observed decline in sea ice resulted in a negative AO-like response (see Figure 3.4a), with the stratosphere playing a significant role in this mechanism. Specifically, turning off the stratospheric influence resulted in the complete breakdown of the AO signal and even prevented significant cooling in Central Asia, as shown in Figure 3.4b.

The question arises as to whether the stratosphere is a decisive factor, or whether experimental design or natural variability may bias the results. The approach of switching off the stratospheric pathway by nudging the stratosphere towards climatological values encounters some difficulties. In the studies previously mentioned, the nudged simulations revealed significantly weaker signals compared with some references including stratospheric variability. The authors concluded that there was a substantial stratospheric influence on this process. However, the nudged simulations present a world without SSWs and without any SSW impact on the troposphere. Because sea ice is not the only factor inducing SSWs,

it remains unclear whether the discrepancies arise from the stratospheric pathway of the Arctic-midlatitude linkage or the absence of SSWs in general.

This effect was mitigated to some degree in a study by Zhang et al. (2018). Here, the specified chemistry version of the WACCM4 with a well-resolved stratosphere was utilised to perform experiments with a prescribed climatological cycle of BK sea ice for the reference period (1980–1999), in contrast to future projected sea ice (2080–2099). Simulations with a suppressed stratospheric pathway were conducted by nudging the time-evolving zonal mean state in the stratosphere. This povides the occurrence of SSWs, but changes in sea ice can no longer induce these events. According to the results, the cold Siberian pattern could be attributed to the loss of sea ice in the BKS region, mainly through the stratospheric pathway. The authors emphasised the significance of accurately representing the stratosphere in climate models, as several studies have utilised low-top climate models to assess this relationship.

Causal network approach

An alternative method to assess this topic was introduced by M. Kretschmer and co-authors. In Kretschmer et al. (2016), an innovative type of time series analysis, the causal effect network (CEN), was applied to ERA-Interim and observational data to study Arctic drivers of winter midlatitude circulation. An illustration of all considered factors and their relationship are shown in Figure 3.5. In this regards, the BK sea ice was found to be an important external forcing factor. The CEN analysis confirmed the proposed stratospheric pathway: BK sea ice was found to influence sea level pressure in the Ural region, which in turn can alter the upward planetary wave propagation and result in a weakening of the polar vortex. Coupling back to the troposphere occurs instantaneously. Moreover, the CEN indicates a direct effect of the BK sea ice on the AO, which was in agreement with Petoukhov and Semenov (2010).

In a subsequent study based on a cluster analysis with reanalysis data, Kretschmer et al. (2018) demonstrated that the polar vortex tended towards a weaker condition over the last four decades. In accordance with Zhang et al. (2018), the Eurasian cooling trend was largely attributed to stratospheric variability. Furthermore, Kretschmer et al. (2020) applied their causal network approach to historical simulations and future projections of CMIP5 models. In the historical multi-model ensemble, the link between the BK sea ice and the stratospheric polar vortex was determined to be very small relative to the natural variability. Hence, the model results could not confirm the findings from reanalyses. The authors highlighted the challenge of establishing a statistically significant relationship between the actors and pointed out discrepancies in the different CMIP5 models.

A Perspective from Screen et al. (2018)

What has just been described appears to follow a pattern in the literature: a relatively clear relationship in observations contrasted with diverging results from climate models. A detailed discussion, along with all of its controversies, was provided by Screen et al. (2018).
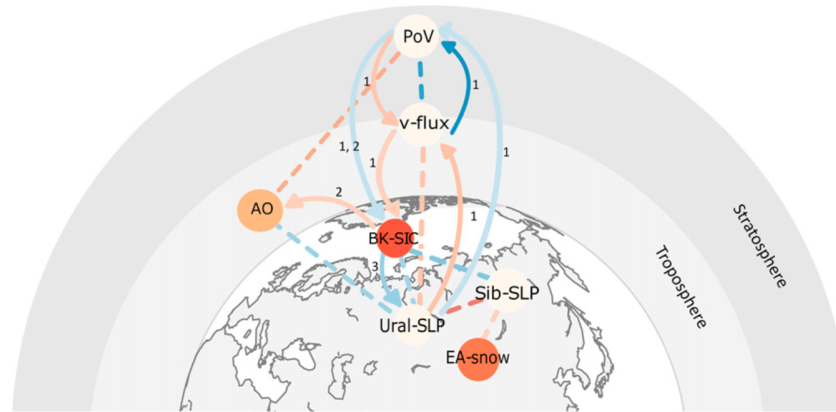
Figure 3.5: Schematic illustration of a causal effect network (CEN) based on monthly mean data. The local actors include BK sea ice, Ural and Siberia sea level pressure (SLP), Eurasian snow cover, Arctic Oscillation (AO), vertical wave propagation (v-flux), and polar vortex (PoV). Only significant links are displayed with arrows, accompanied by the associated time lag in terms of the number of months. The arrow colours represent the standardised regression coefficient β indicating the strength of the relationship. The node colours follow the same scheme, representing the influence of the variables on themselves. Instantaneous links are depicted by dashed lines (more details in Kretschmer et al., 2016).

One key focus of this study was the exploration of sea-ice forcings in sensitivity experiments. In summary, the known sources of discrepancies in the model experimental design are as follows:

1. The extent and geographical distribution of sea ice decline

2. Ice thickness
   - Several models use a constant sea ice thickness, a better specification could improve the results.

3. Treatment of new open water
   - Prescribed sea surface temperature (SST) values differ in these regions.

4. Stratospheric representation
   - The troposphere-stratosphere coupling cannot be accurately represented in low-top models.

5. Ocean
   - Coupled ocean–atmosphere models including interactions among the ocean, sea ice, land and atmosphere are essential.

6. Background state
   - The model mean background state could differ between models and alter the response.

7. Model physics
   - Differences in parameterisations
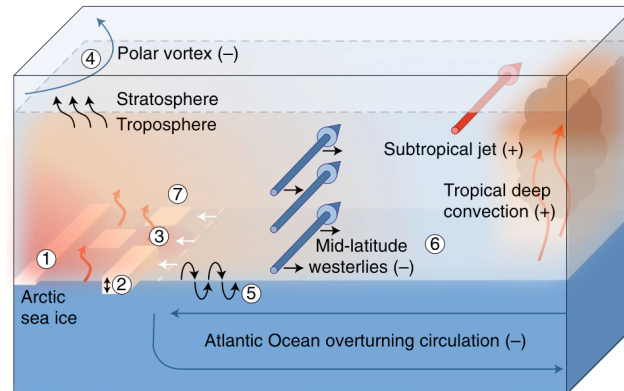
Figure 3.6: Illustration of the potential climate response to Arctic sea ice loss. Red shading indicates regions with the greatest warming. Blue arrows with minus signs represent features that are weakened by Arctic sea ice loss, whereas red arrows with plus signs represent those that are strengthened. The circled numbers stand for sources of disagreement in model experiments as outlined in the text (from Screen et al., 2018).

These arguments are illustrated in Figure 3.6. The authors mainly concentrated on the interaction between the ocean and atmosphere, highlighting the limitations of sea-ice perturbation experiments with atmosphere-only models. They suggested the application of coupled ocean-atmosphere models, but also emphasised some challenges associated with the used forcing approaches.

Tug-of-war

Furthermore, Screen et al. (2018) pointed to another important aspect: in addition to the rising temperatures of the Arctic lower troposphere, a second warming hotspot was observed in the upper tropical troposphere. In simulations involving realistic climate change conditions, such as CMIP studies like Kretschmer et al. (2020), both influences could counteract each other. This phenomenon is known as *tug-of-war*. For example, the Atlantic jet is assumed to shift equatorward in response to sea ice loss, whereas under the influence of tropical warming, a poleward shift of the jet is expected. This could result in a small net response, thereby adding another factor that complicates interpretation. The polar stratosphere can also play a modulating role in the North Atlantic tug-of-war (Peings et al., 2019). In conclusion, the authors recommended coordinated experiments with different models which were eventually realised through the Polar Amplification Model Intercomparison Project (PAMIP).

Second review – Cohen et al. (2020)

It wasn't long before J. Cohen and co-authors published a second review, which highlighted the divergent consensus between observations and model experiments (Cohen et al., 2020). It was shown that the warming of Arctic amplification is often too shallow in models compared with reanalysis. The authors argued that the surface warming might be insufficient to

disrupt the polar vortex. Other model studies support this idea and suggest that deeper Arctic warming must be taken into account (Xu et al., 2019; Labe et al., 2020; He et al., 2020). Moreover, an additional dynamical pathway for the generation of planetary waves has been indicated: atmospheric blockings. There are indications that Ural blockings often precede SSWs (Peings, 2019; Peings et al., 2023), but whether these blockings are influenced by changes in sea ice or increase in frequency under climate change remains an open question.

Once again, the authors highlighted the large natural variability, expected signal-to-noise ratio, and importance of including stratospheric processes in the models. They emphasised model studies which simulated a weaker polar vortex in response to sea ice forcing (Mori et al., 2014; Hoshi et al., 2019; Screen, 2017a). While this review discusses various perspectives and studies, the reasons for the contradictions tended to be attributed to deficiencies in the models.

Dynamical feedback to stratospheric ozone

Given the ongoing debate, all possible sources of interference or model shortcomings have been scrutinised. Stratospheric ozone was determined as a potential factor. The majority of models utilised thus far to study the linkage use prescribed climatological ozone values. Calculating ozone interactively in the model is computationally expensive and large ensembles with hundreds of members are practically impossible. Romanowsky et al. (2019) used a simplified chemistry module SWIFT with the ECHAM6 model and performed the well known sea perturbation experiments with and without their simplified interactive ozone chemistry. The results demonstrated improvements in the stratosphere-troposphere coupling when considering advanced ozone concentrations. Specifically, the NAO response resembled the reanalysis signal when including a chemistry module. Moreover, Haase and Matthes (2019) and Oehrlein et al. (2020) found that the representation of interactive chemistry improves the coupling between the troposphere and stratosphere, and the dynamical feedback on the stratospheric mean state and variability. Another study by Friedel et al. (2022) demonstrated a considerable influence of ozone depletion on the tropospheric circulation, albeit their results refer to the spring season.

Liang et al. (2024)

Before delving into further contentious research, a recent study of the stratospheric pathway based on PAMIP simulations conducted by Liang et al. (2024) should be carefully examined. Sensitivity experiments were performed using the WACCM6 and IPSL-CM6A-LR model, each with a coupled ocean and subject to three nudged sea ice forcings: preindustrial, present, and future, each timeslice with 200 members. The radiative forcing was held fixed at its year 2000 level. The authors have summarised their findings as follows:

- The stratospheric polar vortex experiences a significant weakening as a consequence of the reduction in sea ice.
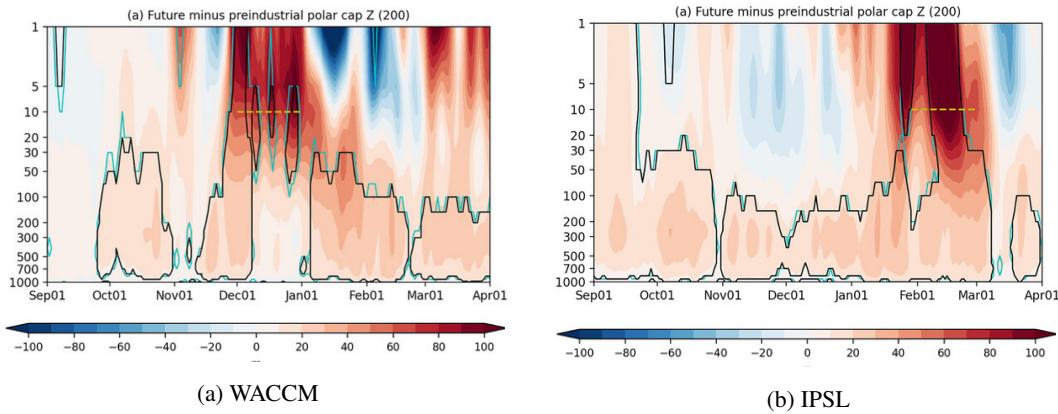
(a) WACCM   (b) IPSL

Figure 3.7: Evolution of polar cap-averaged geopotential height (PCH) response for future sea ice conditions relative to a preindustrial state. The shading represents the PCH response in metre. Black contours denote field significance and cyan contours denote local significance at the 5% level (from Liang et al., 2024). Note that the PCH is typically depicted normalized by its standard deviation at each pressure level, a practice which was not employed in this study.

- ▪ The coupled stratospheric-tropospheric response intensifies during late winter and early spring, leading to a negative NAO pattern in the lower troposphere.

- ▪ Similiar experiments with a second climate model also indicate tighter stratosphere-troposphere coupling although with a different timing.

After a comprehensive review of the results, the following aspects require discussion. The WACCM ensemble mean anomaly of the time-evolving PCH exhibits only short-term stratospheric signals that achieve statistical significance and they occur in December only (shown in Figure 3.7a). The interpretation of such illustrations can be complicated by the following effects: A typical disturbance of circulation in the stratosphere occurs anytime between December and February and manifests as a positive anomaly in the visualisation. The weakening of the polar vortex is sometimes followed by a period of a stronger vortex (negative PCH anomalies) because tropospheric waves fail to reach the upper levels. Consequently, events that do not coincide within a specific timeframe offset each other by averaging. The NAM index for model simulations used in this study is illustrated for single years in Figures A.1 to A.3 in the appendix. The NAM index is derived from the PCH but displays with an opposing sign. Strong disturbances of the polar vortex occur in different months and with various strengths, as depicted by blue shading. It is evident that some exceptionally strong events can bias the long-term average leading to the noisy picture also shown in Liang et al. (2024).

Another aspect complicating the interpretation of Figure 3.7 is the absence of PCH normalisation, which is generally performed when considering both the troposphere and stratosphere together. Although an anomaly of over 100 m in the upper stratosphere appears very high in the graph, it must be considered in the context of a significantly larger geopotential height in upper layers.
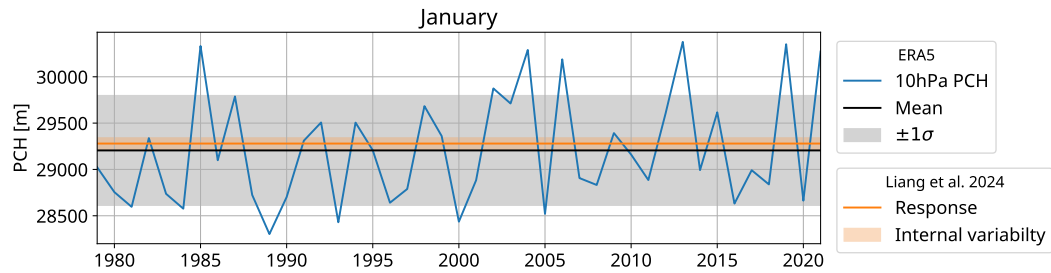
Figure 3.8: Time evolution of January mean ERA5 geopotential height averaged poleward of 65°N (PCH) at 10 hPa and from 1979 to 2021 (blue line). The mean and standard deviation are indicated in the legend. Additionally, the response to a future sea ice forcing (74 ± 61 m) from Liang et al. (2024) is superimposed on the mean ERA5 value (depicted in orange) to provide magnitude comparison.

Liang et al. (2024) detected a statistical significant rise in January-February geopotential height in 50 hPa and 500 hPa, and an increase of sea level pressure in regions with the strongest warming. It was noted that tropospheric changes might arise from a tropospheric pathway or direct thermal effects, but the proportions were not discussed in detail. Instead, the anomalies were attributed to the troposphere-stratosphere coupling alone.

The results from the IPSL model suggest a vortex weaking only in February which was denoted as a different timing (see Figure 3.7b). Examining all seven figures depicting the PCH anomalies in this study (across the two models and different background states), the timing of the response appears highly erratic with no apparent explanation. It is plausible that certain exceptionally strong SSWs, in addition to the aforementioned averaging problem, are associated with this pattern. However, the occurrence of SSWs was not addressed in the discussion at any point in this study.

The stratospheric response was estimated for the January mean 10 hPa PCH (see dashed yellow line in Figure 3.7a). These values were set to the most significant area on seasonal average. The evaluation quantifies the response to future sea-ice conditions (relative to preindustrial levels) as 74 ± 61 m. The magnitude of the response was compared with the uncertainty, revealing a relatively small signal-to-noise ratio of 1.18. The uncertainty was estimated using a bootstrapping method, calculated as twice the standard deviation of a resampled distribution. This analysis yielded the aforementioned value of 61 m, which was further termed natural variability. The resampling was roughly described, but a statistical hypothesis and more detailed explanations were not provided. The value of the natural variability appears to be very low. In contrast, the standard deviation of the ERA5 monthly mean January PCH in 10 hPa is 592 m. The variability of the January ERA5 PCH and the sea ice response of Liang et al. (2024) are illustrated in Figure 3.8, indicating a marginal effect on mid-stratospheric conditions.

Overall, the initially proposed mechanism of the stratospheric pathway encompasses strong disturbance events – namely SSWs. The detailed mechanism of how these extreme circulation anomalies impact the tropospheric weather is not yet fully understood (e.g. Baldwin

et al., 2021). Therefore, it is worth discussing the idea of a stratospheric pathway based on minor variations in stratospheric geopotential height, as indicated by Liang et al. (2024).

3.3 Critical exploration of the topic

The preceding sections provide an overview of studies aimed at identifying connections between Arctic warming and winter circulation patterns. Concurrently, another perspective on the topic has evolved that questions the causal relationship. As previously noted, some authors have raised doubt on the argument made by Francis and Vavrus (2012) regarding changes in Rossby wave behaviour. By contrast, no robust trends could be detected in reanalysis in Barnes (2013) and Screen and Simmonds (2013). Both studies emphasised the methodology of quantifying the properties of Rossby waves.

The relationship between the sea ice response and internal variability was explicitly investigated by Screen et al. (2014). Sea ice perturbation experiments were conducted using two AGCMs, reflecting the prevailing sea ice loss until 2009. This study primarily examined natural variability, leading to ensemble sizes of up to 100 for most of the experiments. The results revealed that a response in midlatitude circulation is likely masked by atmospheric internal variability. They determined that a minimum ensemble size of 50 members is required to detect the effects of Arctic sea ice loss. This number also has implications in the interpretation of observational studies. In those days, a 31 year period of ERA-Interim data was analysed (1979-2009) which is below the proposed suitable number of years. For example, the observed trends in the sea level pressure did not align with the model mean response. The authors pointed out that the observed trends represent only one realisation (effectively one ensemble member), and as such, may not necessarily match the simulated ensemble response. This perspective underscores the challenges of drawing conclusions from reanalyses alone, and emphasises the need to support the findings using model studies.

In this manner, McCusker et al. (2016) found no evidence of the impact of sea ice on Eurasian cooling in AGCM perturbation experiments. Moreover, a large ensemble of 50 realisations of the recent past was conducted using an ocean-atmosphere GCM. While the BK sea ice concentrations appear realistic, only one member exhibited a cooling of magnitude similar to the observations. They concluded that the observed cooling over Eurasia was not influenced by Arctic sea ice conditions but rather by internally generated circulation patterns.

A different perspective on cold air outbreaks (CAOs) was evaluated by Ayarzagüena and Screen (2016). A sensitivity experiment with two AGCMS and transient historical and future runs with coupled versions of these models was used to study the expected change in CAOs. No evidence was found for an increase in CAO frequency or duration in the long-term. On the contrary, the results suggested that future sea ice decline reduces the severity of CAOs in midlatitudes (see Figure 3.9). Figure 3.9 shows that the majority of CAOs in
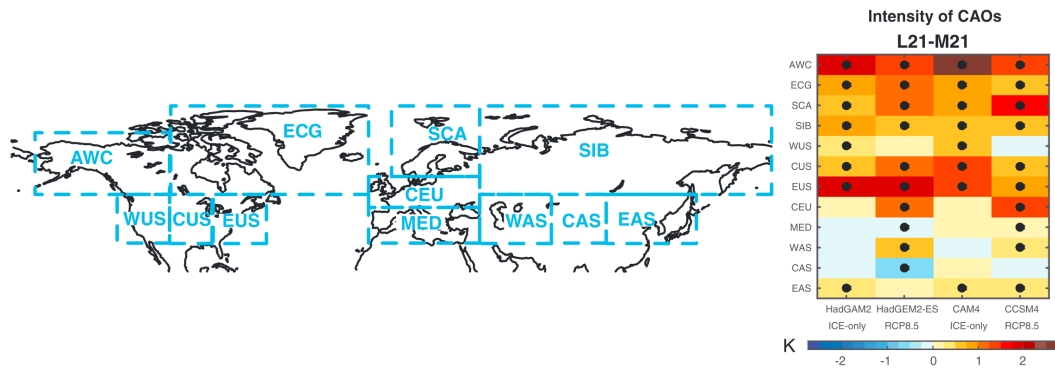
Figure 3.9: Changes of intensity of CAOs, in each region indicated on the left, in response to sea ice loss alone (labelled as ICE-only) and in RCP8.5 transient simulations. The changes were calculated as differences between the 2080–2099 (L21) and 2030–2049 (M21) time periods. Dots denote statistically significant changes at a 95% confidence level (from Ayarzagüena and Screen, 2016).

a warmer climate in different regions and model simulation become less servere which is indicated by higher temperature anomalies. While the circulation structures associated with CAOs events remain unaffected, the local advection of warmer polar air eventually leads to less severe cold episodes in midlatitudes. The analysis was performed thoroughly, focusing on the extremes identified relative to the mean climate of the respective time frame.

In the following years, several critical studies, largely contributed by J. Screen and R. Blackport, were published. Screen (2017b) explored the influence of sea ice changes on the NAO and European winter weather with AGCM perturbation experiments. These results indicate an intensification of the negative phase of the NAO. However, Northern Europe was not affected by cooling because thermal effects prevailed over circulation changes. Moreover, Blackport et al. (2019) found marginal impact of reduced sea ice on winter temperatures in midlatitudes. This study, based on ERA-Interim and two coupled ocean-atmosphere climate models, implies that the atmosphere can be considered as a driver for sea ice loss. Another study by Sun et al. (2022) pointed out that the tropospheric response could be obscured by the large internal variability of the stratosphere.

Moreover, the timing of sea ice forcing was reassessed. The general minimum of the Arctic sea ice extent emerges in September, and most early studies considered autumn sea ice. However, it became clear that the Arctic amplification signal is most pronounced in winter when the additional heat absorbed in summer is released back into the atmosphere (e.g. Deser et al., 2010b). Blackport and Screen (2019) proposed that the circulation response is primarily driven by sea ice loss in winter rather than in autumn. This hypothesis appears reasonable for the stratospheric pathway as well. Planetary waves effectively propagate into the upper levels only from early winter onwards. Moreover, wave propagation and mean flow interactions are nearly instantaneous. Consequently, autumn sea ice cannot directly affect the stratosphere, a type of reservoir would be required. Blackport and Screen (2019) argue once more, that the oberserved correlation between autumn sea ice and winter circu-
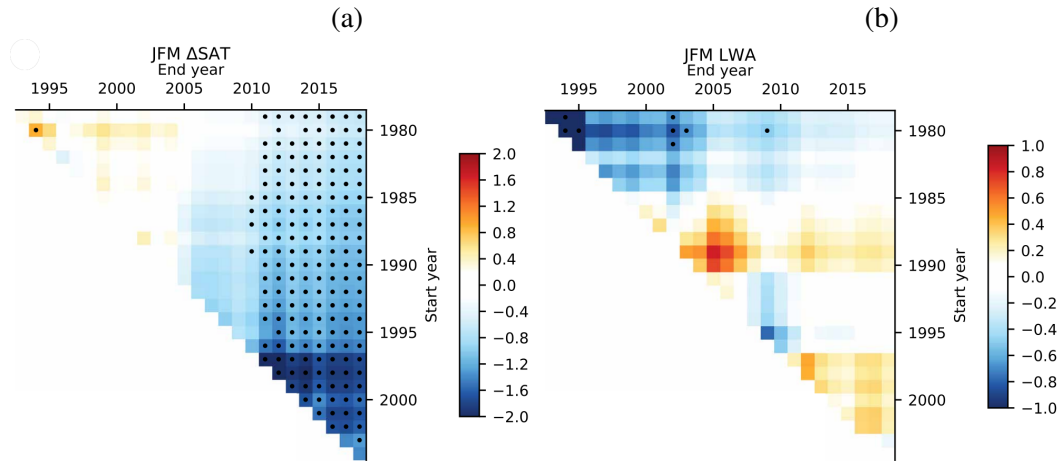
Figure 3.10: Trends of the winter (JFM) meridional near-surface temperature gradient (a) determined as 2-metre temperature difference between midlatitudes (30°N – 50°N) and Arctic (north of 65°N) of ERA-Interim reanalysis. The trends are depicted as a function of the start and end years, with a minimum of 15 years in total. The point in the upper-right corner of the illustration represents the trend in the complete dataset, with fewer years considered as one moves further away from this point. The trends of the waviness diagnosed by LWA averaged over midlatitudes (40°N – 60°N) are similarly shown in (b). The dots denote statistically significant trends at the 95% confidence level. The trend units are °C per decade in (a) and standardised LWA per decade in (b) (from Blackport and Screen, 2020a).

lation could be noncausal and arises due to a common driver.

A further aspect questioned by Blackport and Screen (2020a) was the change in the waviness of atmospheric circulation. Using ERA-Interim data, the trend of the waviness metric LWA (local wave activity, Chen et al. (2015)) was compared to the trend of the temperature gradient between the Arctic and midlatitudes, and hence Arctic amplification. In addition, the start and end years of the trend analysis were adjusted with reference to the short-term trends analysed in previous studies. In winter (JFM), the temperature gradient significantly weakened for all time periods ending after 2010 (see Figure 3.10a). Conversely, the trend of LWA did not exhibit consistency throughout the entire time period. Positive trends were observed from approximately 1990 to 2005, coinciding with the period when early studies drew their conclusions (Figure 3.10b). Blackport and Screen (2020a) emphasised that there is no justification for neclecting the early years in trend calculation as commonly applied by some studies. Neither observations nor models have detected significant impacts of Arctic amplification on atmospheric waviness in this study. Although the westerlies weaken slightly in response to Arctic warming, the proposed chain suggested by Francis and Vavrus (2012) was found to be inconsistent. The authors commented that wave amplitudes were primarily influenced by other factors such as baroclinicity or moisture. It is worth noting that the absence of wave modification would directly undermine the stratospheric pathway, as wave propagation is a key factor in this mechanism.

Finally, a compelling argument was made in a correspondance from Blackport and Screen

(2020b). A set of relevant variables spanning 1980 to 2020 was examined to illustrate recent trends (see Figure 3.11). While Arctic amplification and sea ice loss have continued as expected, the short-term tendencies of other variables have not continued over the past decades. The authors stated that the updated trends align more closely with the modelled response, challenging the argument regarding model deficiencies, as suggested in Cohen et al. (2020). Their conclusion underscores the weakened evidence of the proposed linkage and once again attributed the observed short-term trends to natural variability.

3.4 Discussion

The last section presents an overview of the divergent findings documented in previous studies over the past two decades. Despite all the disagreements, recent literature converges on one point: the large internal variability and, if present, a relatively small signal from Arctic amplification. From the current standpoint, the hypothesis that midlatitude winters will experience more cold extremes in the future has been virtually refuted. In general, the thermodynamic effects of sea ice decline and GHG-induced global warming are expected to shift the winter weather to warmer conditions.

A third review on the topic, focussing only on the aspect of Eurasian cooling in the early 21st century, was carried out by Outten et al. (2023). This study provides a comprehensive and balanced summary of the current state of knowledge and attempts to reconcile the viewpoints *ice-driven* and *internal variability*. The authors pointed out that conflicting conclusions may arise from different interpretations of the results and argued that the interplay between sea ice and internal variability could influence the propability of strong regional cooling. This study was very well elaborated, however, the discussion of stratospheric contributions was brief.

Over time, the stratospheric pathway underwent the full range of implications: from being a major mechanism responsible for Eurasian cooling (e.g. Zhang et al., 2018) to a source that obscures the tropospheric response to sea ice decline (Sun et al., 2022). The stratosphere will experience significant changes owing to climate change. The question of whether Arctic amplification will emerge as a factor influencing stratospheric circulation remains open. The key factor in this pathway are planetary waves generated in the troposphere, a subject further examined in this work. How possible modifications of the jet stream are connected to changes in planetary waves and their propagation into the stratosphere has not yet been fully classified.
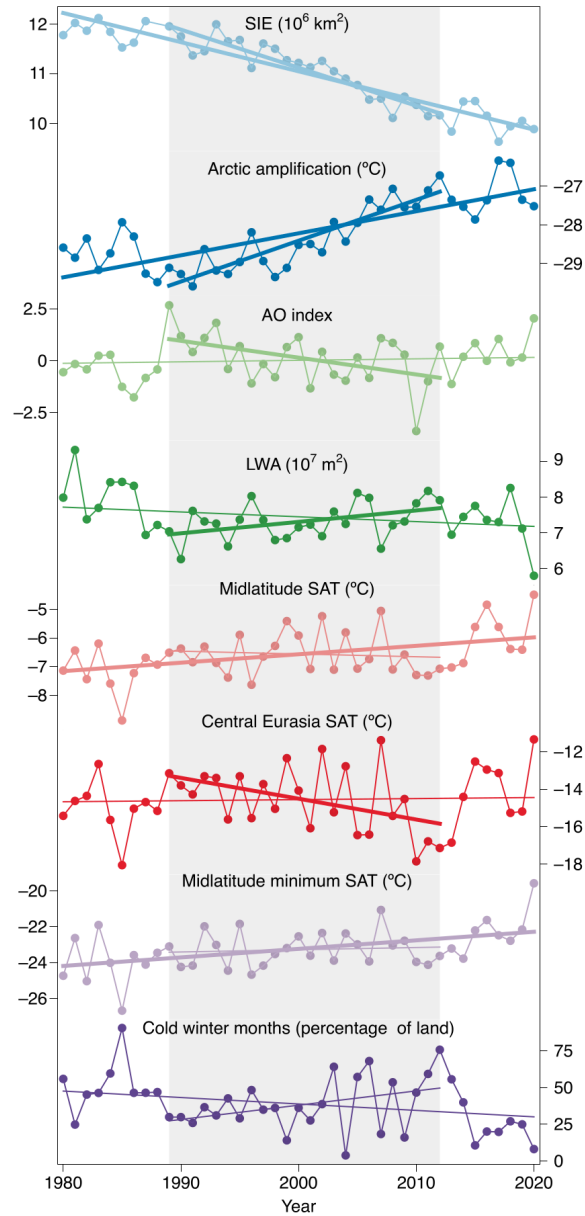
Figure 3.11: Signals of Arctic change and its potential effect on midlatitudes. The time series are labeled in the graph. The Arctic sea-ice extent (SIE; light blue) and Arctic amplification (dark blue) are averaged for September to February, where the Arctic amplification is deetermined as the difference between Arctic (65–90°N) and northern hemisphere (0–90°N) surface air temperature (SAT). The following indices are shown as December to February mean. The waviness is characterised by the local wave activity (LWA) averaged over midlatitudes (40–60°N). The midlatitude (30–60°N) land surface air temperature is depicted in light red and central Eurasia (40–60°N; 60–120°E) in dark red. The figure shows the minimum daily SAT for midlatitude regions in light purple, while the percentage of midlatitude land experiencing at least one cold winter month (1 standard deviation below the average) is depicted in dark purple. Two time periods, 1979/80 to 2019/20 and 1988/89 to 2011/12, are depicted with linear trends, with the latter period being highlighted by grey shading. A significant trend at 95% confidence level is marked with a thicker line. More information and data sources are given in Blackport and Screen (2020b).

Model and Simulations

This study investigates the potential relationships within the dynamical framework of the Arctic-midlatitude linkage using a climate model. These models can simulate realistic climate conditions and integrate complex feedback mechanisms. As discussed in the previous chapter, conclusions drawn from observational data alone may be considered insufficient due to the low signal-to-noise ratio. Long-term or ensemble model simulations can help to better distinguish climate change signals from natural variability.

4.1 Coupled climate models

An atmospheric general circulation model (AGCM) is a comprehensive model of the atmosphere used for weather prediction and climate studies. It is based on a dynamical component that resolves discretised physical equations on a specific grid, which is also known as the *dynamical core*. In addition, all subgrid processes must be represented by physical parameterisations. Examples of small-scale phenomena are radiation, friction, or convection. In an AGCM, ocean conditions are prescribed as boundary parameters. Consequently, the atmosphere can respond to the state of the ocean but not vice versa. If we are interested in interactions between the atmosphere and the ocean, or processes derived from these interactions, a coupled atmosphere-ocean GCM must be employed. The representation of the ocean is accomplished using a comprehensive ocean GCM, which functions similarly to an AGCM. The coupling between these models is achieved by the exchange of related variables such as heat flux, wind stress, and freshwater flux. In addition, the distribution and modification of sea ice are considered, including a sea ice model that simulates thermodynamics, dynamics, and interactions with the ocean and atmosphere. The fully coupled atmosphere-ocean GCM (AOGCM) represents a sophisticated and advanced model of the climate system and has been widely used in climate change studies.

Another factor that influences atmospheric dynamics and radiation budgets is the chemical composition of the atmosphere, which is important for investigating stratospheric phenomena. A chemistry climate model (CCM) represents atmospheric chemistry and its feedback by utilising chemical mechanisms containing various atmospheric reactions that are important for tropospheric or stratospheric chemistry. These models are commonly applied in studies assessing ozone depletion and play a crucial role in enhancing our understanding of

stratospheric dynamics, particularly when considering interactions with chemical composition.

4.1.1 The EMAC model

Both components complementing the climate system play a role in the Arctic-midlatitude linkage, atmosphere-ocean and atmosphere-chemistry via the stratospheric pathway. Thus, the coupled CCM ECHAM/MESSy Atmospheric Chemistry (EMAC, Jöckel et al., 2006, 2010) is used in this study. EMAC is based on the 5th generation European Centre Hamburg general circulation model (ECHAM5, Roeckner et al., 2006). ECHAM5 employs a spectral dynamical core that represents variables using a truncated series of spherical harmonics. The horizontal spectral resolution used in this study is T42, indicating that spherical harmonics are included for wavenumbers up to 42. This corresponds to a Gaussian grid of 64×128 grid points or approximately $2.8° \times 2.8°$ in latitude/longitude space. Model levels are vertically distributed using a hybrid sigma-pressure system. In the lower layers, sigma coordinates are employed to account for Earth's orography, whereas isobars are adopted for the upper layers. An intermediate transition smoothly connects these two systems. With a configuration of 47 levels spanning from the surface to 0.01 hPa in the upper mesosphere, the model resolution applied in this study is specified as T42L47MA.

The base model ECHAM5 is coupled to various submodels via the second version of the Modular Earth Submodel System (MESSy2, Jöckel et al., 2010), which serves as an interface for implementing and integrating codes from multiple institutions. Thus, the flexible module MECCA (Module Efficiently Calculating the Chemistry of the Atmosphere) is coupled to the base model. It includes 224 gas-phase reactions for ozone, hydrogen, nitrogen, carbon, fluorine, chlorine, bromine, and sulphur chemistry (Sander et al., 2005, 2011).

Numerous chemical reactions in the atmosphere involve photolysis, a process wherein molecules dissociate when exposed to sunlight. The rate coefficients of these photolysis reactions are termed *J values*. The submodule JVAL provides an online calculation of these photolysis rate coefficients after Landgraf and Crutzen (1998), considering the solar zenith angle, cloud water and ice content, aerosols, or ozone concentrations. The latest version JVAL-14, was utilised, and details can be found in Sander et al. (2014).

The photolysis reactions of ozone absorb solar radiation in the ultraviolet and visible spectra. The original shortwave radiation scheme of ECHAM5 includes only four spectral bands: one for the visible and UV range and three for the near-infrared region (Roeckner et al., 2006). However, a higher resolution in the UV and visible (UV-VIS) bands is required for ozone absorption, which has been implemented at FU Berlin within the FUBRAD module (Nissen et al., 2007; Kunze et al., 2014). FUBRAD replaces the single UV-VIS band, in altidudes from 70 hPa to 0.01 hPa, with various bands spanning from the Lyman-α line (121.5 nm), across the Schuhmann-Runge bands and continuum (125.5 nm–205 nm), the Herzberg continuum (206.2 nm –243.9 nm), the Hartley bands (243.9 nm–277.8 nm), the Huggins bands (277.8 nm–362.5 nm), to the Chappuis bands (407.5 nm–690 nm). The number of bands in this domain can be adapted in the module, and 81 bands were used in this

study. In the latest MESSy version, the FUBRAD module was integrated into the radiation submodel RAD (see Jöckel et al., 2016).

While the gas-phase chemical reactions are implemented within the MECCA module, the heterogeneous chemistry is calculated using the submodel Multi-phase Stratospheric Box Model (MSBM). Heterogeneous reactions are responsible for rapid ozone depletion and are often related to polar stratospheric clouds (PSC) in the lower stratosphere (outlined in Section 2.4.1). The MSBM submodel simulates the properties of stratospheric background aerosols and PSC cloud particles. It also calculates the reaction rate coefficients of the heterogeneous chemistry occurring on the surface of these particles.

As stated in Jöckel et al. (2016), the so-called *CCMI-base-02* mechanism includes 310 reactions of 115 species divided into 224 gas-phase reactions, 74 photolysis reactions, and 12 heterogeneous reactions. This setup was designed to accommodate a wide range of research applications. However, approximately 50% of these 310 reactions occur exclusively in the troposphere. Since most tropospheric chemical processes are negligible for stratospheric studies, various reactions are excluded in an adapted and compact *CCMI-base-02c* mechanism, developed by T. Spiegl as part of the Solar contribution to climate change on decadal to centennial timescales (SOLCHECK) project. Specifically, tropospheric carbon and nitrogen chemistry were removed. Reactions occurring solely in the middle atmosphere or spanning both the troposphere and the middle atmosphere remain unaffected. This also applies to all heterogeneous reactions and those associated with very short-lived substances (VSLS), which could potentially impact stratospheric ozone depletion. Altogether, the number of reaction rates was reduced to 166, involving 98 chemical species. This modification effectively halves the model run time, which is a highly significant improvement in designing the model experiments in this study. Overall, when considering all described coupled submodels, EMAC transforms into a complete CCM.

Furthermore, the ocean in the model is represented using the Max-Planck institute global ocean/sea ice model (MPIOM, Marsland et al., 2003). Coupling was accomplished within the MESSy interface as detailed in Pozzer et al. (2011). An evaluation of the model performance regarding global sea ice cover revealed a slight overestimation of approximately 8% and a larger interannual variability in the model compared to observations. Nevertheless, the model could reproduce the sea ice decline that occurred after 1950. Hence, the coupled EMAC-MPIOM model serves not only as an atmosphere-ocean GCM but also incorporates comprehensive atmospheric chemistry. Additionally, it allows the exchange of chemical species between the ocean and the atmosphere. For simplicity, this coupled model is referred to as 'EMAC' only throughout the remainder of this study.

4.2 Simulations

Several EMAC simulations were performed within the scope of this thesis. The EMAC model was employed as a fully ocean-coupled CCM for transient ensemble simulations from 1850 to 2100. Moreover, three timeslice simulations with fixed boundary conditions

for a specific year were conducted. These simulations were performed in collaboration with T. Spiegl and the SOLCHECK project. Additionally, timeslice simulations were replicated in an AOGCM configuration, with all chemical submodels deactivated.

4.2.1 Model configuration

The most important model components, such as the integration of the ocean and stratospheric chemistry, are outlined in Section 4.1.1. For the sake of completeness, the full model configuration, encompassing all enabled submodels, is presented in Figure 4.1. Submodels are briefly introduced in Table 4.1. It is worth noting that the simulations analysed in this study were also utilised for other research purposes, and not all components are essential for the evaluation of the Arctic-midlatitude linkage.

Table 4.1: MESSy configuration and description of enabled submodels in the applied model setup.

Module	Module description
A2O	Two-way exchange between ocean and atmosphere for physical coupling
AIROPT	Aerosol optical properties
AIRSEA	Two-way exchange of chemical tracers between ocean and atmosphere
CLOUD	ECHAM5 cloud scheme
CLOUDOPT	Cloud optical properties
CONVECT	Convection parameterisations
CVTRANS	Transport of tracers caused by convection
DDEP	Gas phase and aerosol tracer dry deposition
GWAVE	Non-orographic gravity waves
H2O	Stratospheric water vapour and feedback
HD	Riverine freshwater input into the ocean
JVAL	Photolysis rates
LNOX	Lightning NOx production
MECCA	Atmospheric chemistry
MPIOM	Ocean general circulation model
MSBM	Multi-phase Stratospheric Box Model for heterogeneous chemistry
O3ORIG	Identification of production areas of ozone
OFFEMIS	Prescribed emissions of trace gases and aerosols
ONEMIS	Online calculated emissions of trace gases and aerosols
ORBIT	Earth orbit calculation
PTRAC	Definition of additional prognostic tracers
QBO	Newtonian relaxation of the quasi-biennial oscillation
RAD	ECHAM5 radiation scheme with sub-submodel FUBRAD
SCALC	Simple calculations with channel objects
SEDI	Sedimentation of aerosol particles
SURFACE	Calculation of different surface temperatures
TBUDGET	Calculation of budgets of reactive compounds

Table4.1 – continued from previous page	
Module	**Module description**
TNUDGE	Newtonian relaxation of species as pseudo-emissions
TREXP	Tracer release experiments from point sources
TROPOS	Diagnostic of the tropopause according to various definitions
UBCNOX	Parametrization of energetic particle influence on NO_x
VISO	Isosurfaces and maps

In addition to this comprehensive list, it is important to mention the modules relevant to stratospheric processes. Small-scale gravity waves play a crucial role in driving a mean meridional circulation in the middle atmosphere. The ECHAM5 model incorporates a parameterisation based on the work of Lott and Miller (1997) to represent orographic gravity waves, while the GWAVE module is used to parameterise non-orographic gravity waves. Furthermore, the tropical stratospheric zonal wind oscillation QBO is not generated internally at the applied model resolution. To ensure realistic tropical winds, the QBO is nudged towards observed values in the relevant region during the observational period and towards a recurring QBO cycle in the future.

4.2.2 Transient ensemble simulation

Transient simulations were conducted under changing atmospheric conditions to assess the potential impact of Arctic warming on winter circulation. These simulations span the preindustrial conditions in 1850 throughout the entire observational period and extend into the future until 2100. The boundary conditions for the past (until 2016/2017) were derived from observations, whereas the future scenario follows the specific projected shared socioeconomic pathway SSP-3.70 (Meinshausen et al., 2020). This pathway is a medium-high GHG scenario marked by regional rivalry between countries and has the second-highest warming potential in this framework. Figure 4.2 demonstrates the concentrations of the most important GHGs for the different SSP scenarios. The anticipated warming for the chosen scenario is estimated to be approximately 3.6°C by the end of the 21st century (IPCC, 2021a). Additionally, it is essential to specify the concentrations of ozone-depleting substances. In this study, the baseline scenario for ODS as defined by Carpenter et al. (2018) was applied.

The transient simulation spans 250 years, allowing for the evaluation of gradual changes in climate over time. However, natural variability can obscure small signals arising in the context of the Arctic-midlatitude linkage, as discussed in Chapter 3. To address this issue, an ensemble of six transient simulations was conducted, totaling 1500 model years, the maximum feasible number given the computational effort. This ensemble size represents a significant improvement for a coupled CCM, although it may not rival the hundreds of ensembles usually produced by AGCMs.
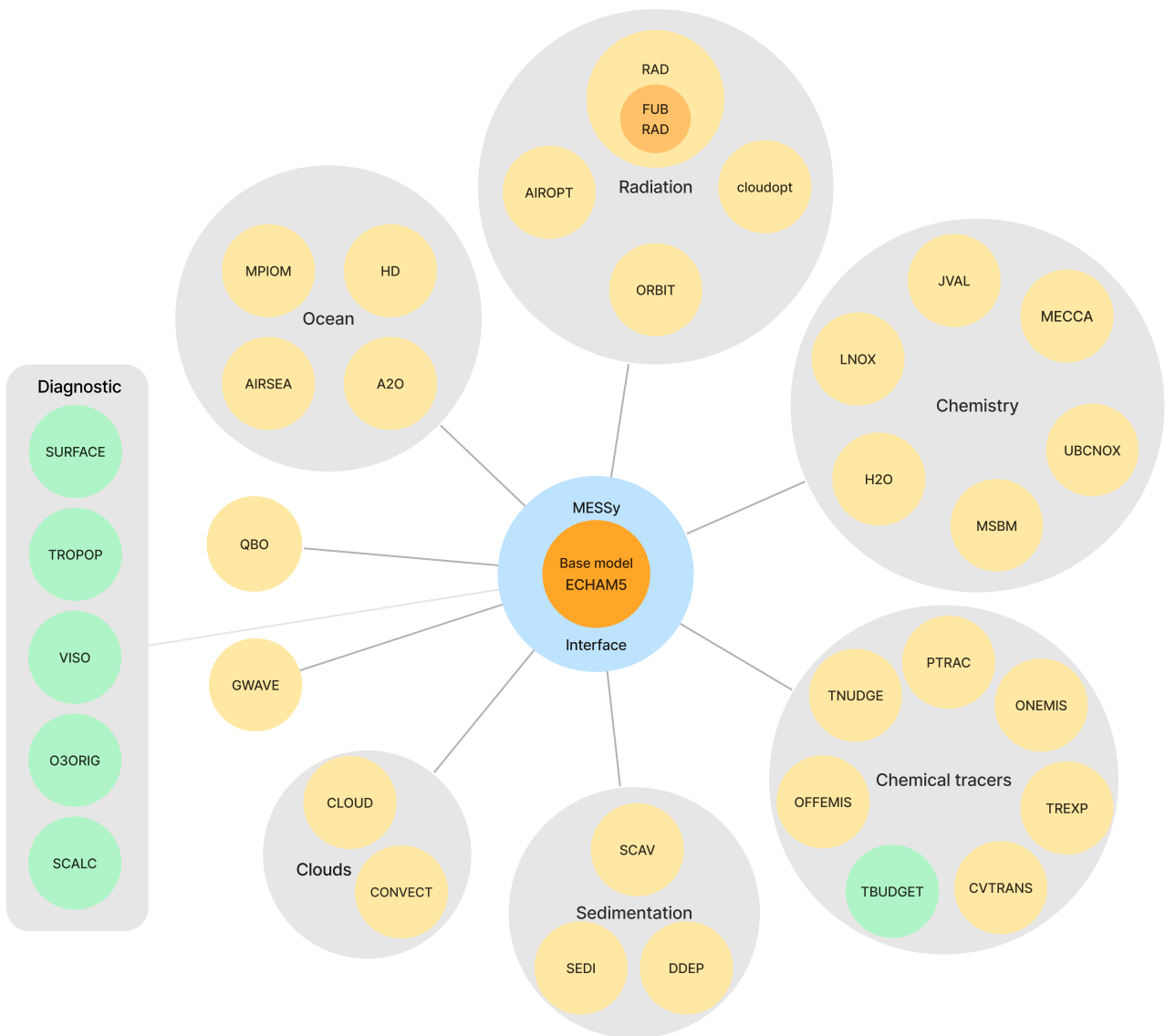
Figure 4.1: MESSy configuration for EMAC simulations with all enabled submodels. The base model ECHAM5 is coupled within the MESSy interface to various submodels or model components (illustrated in yellow). Green submodels indicate diagnostic tools. Some components are grouped under the same theme (grey area), but information exchanges can also extend beyond those borders.
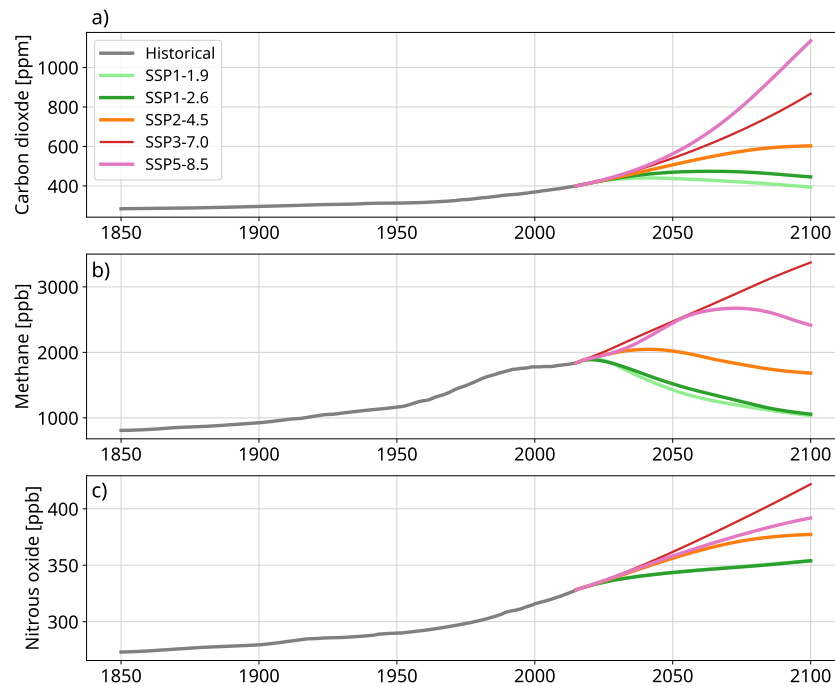
Figure 4.2: Global annual mean concentrations of carbon dioxide (a), methane (b), and nitrous oxide (c) in different SSP scenarios. The historical period extends from 1850 to 2014 and is depicted in grey. Beyond this year, future scenarios diverge, as indicated by the coloured lines. In this study, the SSP3-7.0 scenario is used (shown in red), which exhibits the largest increase in methane and nitrous oxide (data published in Meinshausen et al., 2020).

The ensemble of transient model runs will provide valuable insights into:

- the progression of Arctic Amplification,

- temperature trends across various regions, and

- the response of the stratosphere to climate change.

Model evaluation

Transient runs are well suited for evaluating the model against observations. Figure 4.3 compares Arctic sea ice to the HadISST1 dataset. The winter sea ice distribution in the Arctic simulated by EMAC closely matches observational data, as demonstrated in (a) and (b) of Figure 4.3. The HadISST1 time series in (c) for BK sea ice falls within the statistical range of the EMAC ensemble. Collectively, these findings provide confidence in EMAC's performance regarding Arctic sea ice. Furhermore, an evaluation of the simulated SSTs is presented in Figure 4.4. Overall, both the spatial distribution and temporal trends of SSTs in EMAC show a high level of agreement with observations, reflecting a robust model performance.

Moreover, an assessment of the stratospheric representation in EMAC was conducted. The climatological geopotential height and temperature in the middle stratosphere are presented in Figure 4.5 and compared with the ERA5 reanalysis. The alignment of the low-pressure system is consistent between the model and observations. In EMAC, the polar vortex exhibites a minimal increase in strength and lower temperatures. A slightly stronger warming signal is apparent over Eastern Eurasia in ERA5. This may be attributed to the higher occurrence of SSWs in the observations, as discussed in the next paragraph.

Figure 4.6 illustrates the SSW occurrence in EMAC together with ERA5. The appearance of SSW events exhibits irregular patterns, with some periods marked by annual recurrences, while other decades experience no SSW events. The number of SSWs per decade in the period of 1958 until 2023 spans from 4.4 to 6.7 in transient EMAC simulations. The frequency of SSWs in the ensemble mean is 5.6, which is lower than the ERA5 frequency of 6.4 SSWs per decade. Considering the irregularity of SSW occurrences, as demonstrated in Figure 4.6, this does not necessarily indicate a deviation in the model. Instead, when regarding ERA5
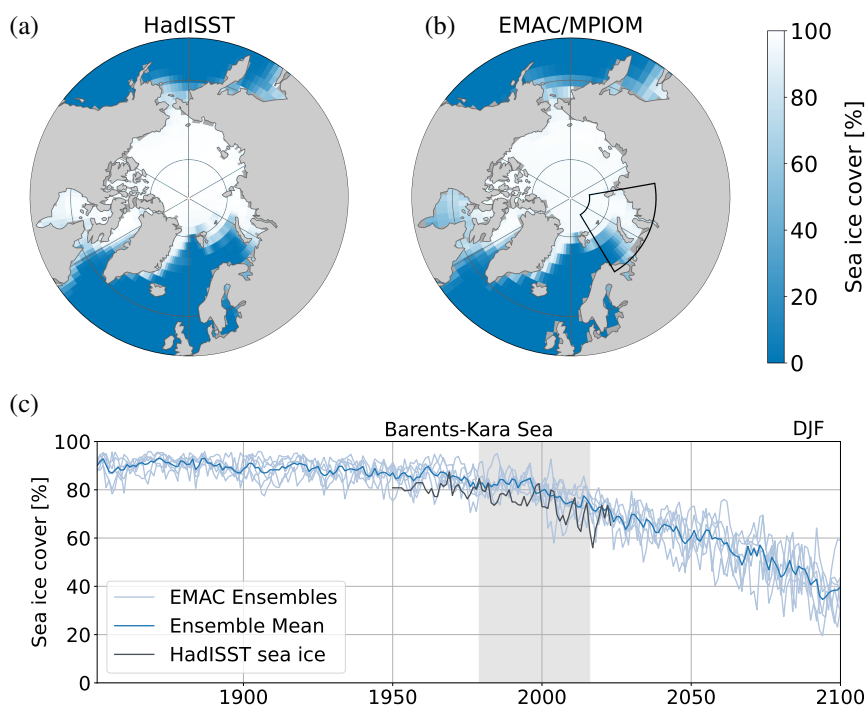
Figure 4.3: Model evaluation of Arctic sea ice. The climatological winter mean (DJF) sea ice cover is compared between the observational dataset HadISST1 (a) and the ensemble mean of EMAC simulations (b). The climatological average is taken over the period from 1979 to 2016, a period characterised by reliable observations and boundary conditions from observations in EMAC simulations. The time series of the SIC over the Barents-Kara Sea (DJF) is shown in (c). The time period used in (a) and (b) are marked by the grey area in (c). The BKS region, delineated by the black lines in (b), is defined within the coordinates of 68°N – 85°N and 31°E – 100°E. The HadISST1 data is described in Rayner et al. (2003).
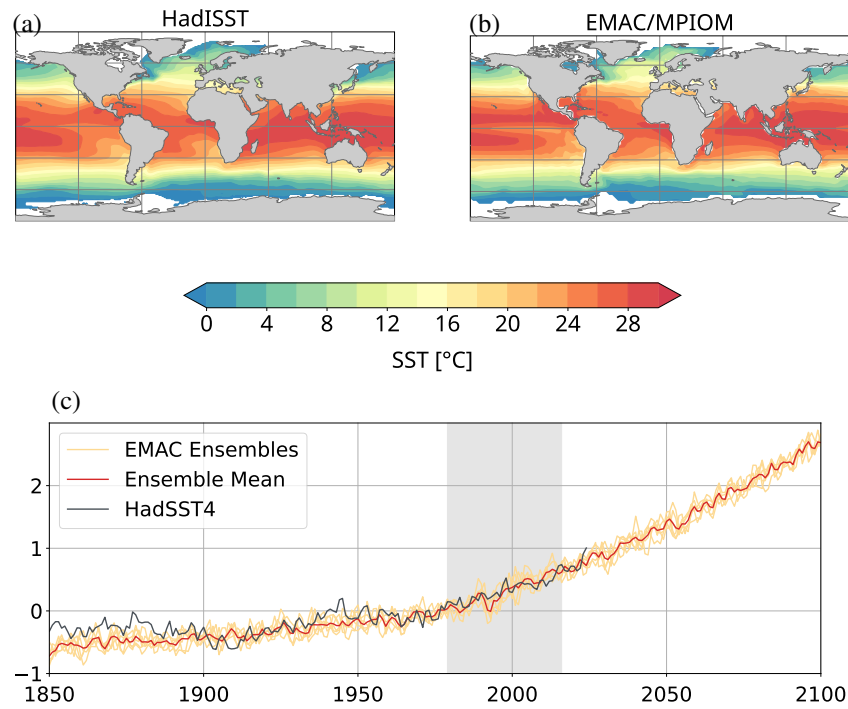
Figure 4.4: Model evaluation of sea surface temperatures (SST). The climatological mean SSTs (1979–2016) are shown for observations (HadISST1) in (a) and the ensemble mean of the EMAC simulations in (b). The time series of the annual global mean SSTs in (c) is presented as anomalies for the 1961–1990 reference period. This figure utilises the HadSST4 dataset, which incorporates enhancements in dataset quality (Kennedy et al., 2019). The time period used in (a) and (b) are marked by the grey area in (c).
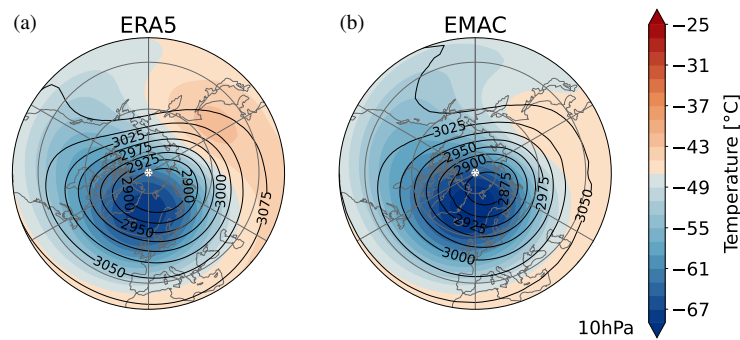
Figure 4.5: Model evaluation of the polar vortex. The climatological winter (DJF) mean of the geopotential height [dm] and temperature in 10 hPa are depicted for ERA5 (a) and the ensemble mean of EMAC simulations (b). The climatological period, as specified in Figure 4.3, encompasses the years 1979 to 2016.
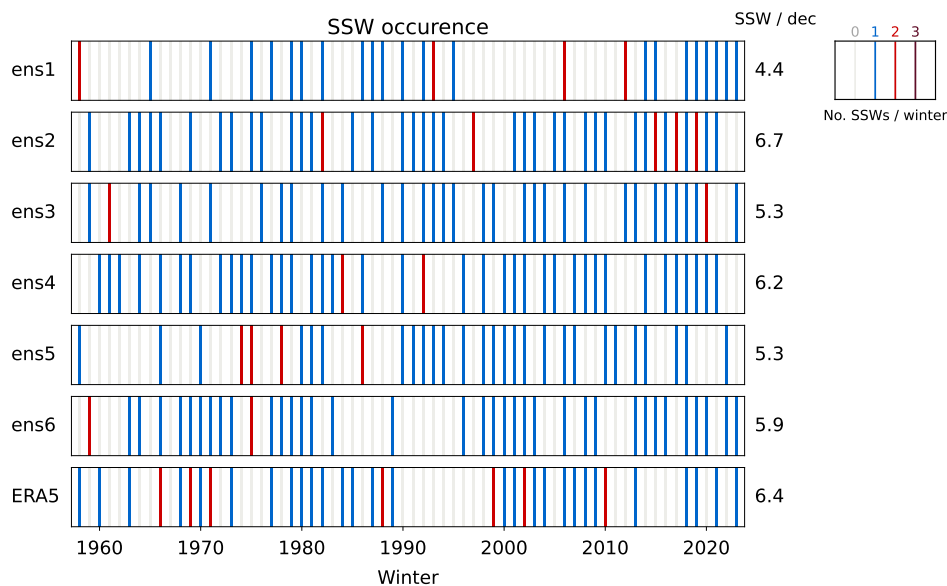
Figure 4.6: The occurrence of major sudden stratospheric warmings (SSWs) in the extended winter season (NDJFM) in ERA5 renanalysis and transient EMAC ensemble simulations, denoted as ens1 – ens6, spanning from 1957 to 2023. Events were classified following the WMO classification for EMAC and Charlton and Polvani (2007) for ERA5. The occurrence is illustrated as the number of events per season (see legend). The number of SSWs per decade is indicated on the left-hand side of the figure. The years are labeled for January of each season.

as one realisation, it falls within the statistical range of the EMAC ensemble. This perspective underscores the advantages of ensemble simulations. Given the limited observational data available, the statistics of the transient EMAC ensemble suggest a reasonably accurate simulation of stratospheric dynamics.

In summary, the model evaluation reflects the good performance of EMAC. Specifically, climate models may struggle to accurately represent sea ice or stratospheric dynamics, which are two major components when analysing the stratospheric pathway of the Arctic-midlatitude linkage. In this context, it was demonstrated that these features were highly satisfactory in EMAC simulations.

4.2.3 Timeslice simulations

Although transient simulations are valuable for analysing evolving changes over time, separating these changes from internal variability can be challenging. In a statistical sense, more accurate assessments can be made using timeslice simulations. In these simulations, the boundary conditions, such as the concentrations of GHGs and ODSs, remain constant. Therefore, a specific year can be simulated repeatedly. This method improves the estimation of internal variability and enhances the statistical robustness of the findings when comparing two different timeslice simulations.

Three timeslice experiments have been carried out in this study: preindustrial, present and future. Each experiment consists of 150 model years. The boundary conditions are configured as follows:

- The simulation for the preindustrial period operates under the conditions of the year 1850, prior to major anthropogenic emissions.

- The present simulation prescribes constant surface mixing ratios based on 2020 levels from the SSP3.70 scenario.

- The future simulation is based on GHG levels from the year 2100 of the respective scenario.

The timeslice simulations were branched off in the respective years within one of the transient runs. The rest of the model configuration remained unchanged from that used in the transient simulations.

According to the design of model experiments, the present and future timeslices are not strictly equivalent to a repetition of the year 2020 and 2100, respectively. Constant GHG concentrations did not result in the immediate cessation of the upward temperature trend. Indeed, the warming has progressed over several decades. An overview of the near-surface global annual mean temperatures in all simulations is given in Figure 4.7. The temperature increase in transient ensemble simulations, shown in blue, reaches approximately 4.5°C under the SSP3.7.0 scenario at the end of the 21st century, which falls in the very likely range of the CMIP6 models (IPCC, 2021a).

Further, the temperature profiles for the timeslice simulations are demonstrated in Figure 4.7. The initial objective was to run the model until achieving an equilibrium state, and to analyse a period of 150 years during which temperatures remain stable. In the present simulation (yellow), a positive temperature trend persisted for several decades, but a balanced state was eventually obtained. In contrast, the future timeslice (red) exhibits a warming trend over hundreds of years. In fact, the warming does not cease completely. However, the simulation could not be continued because of computational costs, and a weak temperature trend in this simulation had to be accepted.

Considering these aspects, it is necessary to refine the interpretation of the timeslice simulations. Rather than regarding them as repetitive simulations of a specific year, they represent the anticipated state with constant GHG concentrations emitted thus far until that year. This approach accounts for the warming progression after maintaining constant GHG levels, and subsequently selects a (nearly) balanced state for analysis. The timeslice temperature anomalies, as shown in the boxplots in Figure 4.7, are approximately 2 K for the present and 6 K for the future timeslice, which is considerably higher than the projected temperature anomalies for the specific years 2020 or 2100.
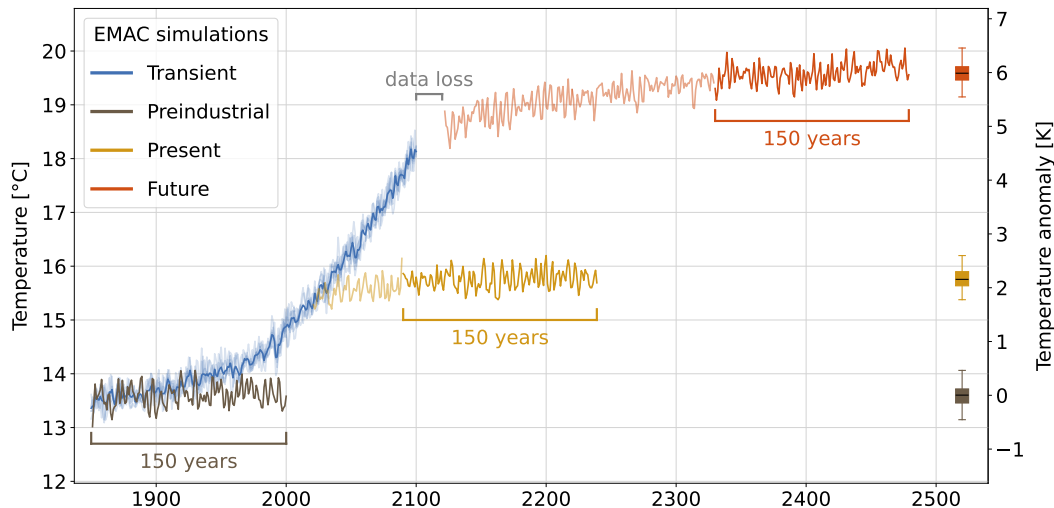
Figure 4.7: Global annual mean near-surface temperature in EMAC simulations. The 150 years used for the timeslice simulation are highlighted. Spinup periods for present and future experiments are depicted in lighter colours. The temperature anomaly relative to the preindustrial timeslice mean is indicated on the right *y*-axis, and the timeslice statistics are represented in boxplots.

4.2.4 Timeslices in an AOGCM configuration

The majority of Arctic-midlatitude linkage studies are based on GCMs. In this study, a comprehensive evaluation using a CCM was accomplished. To analyse the effects of interactive chemistry in the model, preindustrial, present, and future timeslice simulations were replicated in an AOGCM configuration. The ozone concentrations were prescribed as 3D monthly climatology based on the CCM timeslice counterpart. In these simulations, it can be assessed whether accounting for ozone chemistry affects stratospheric dynamics and potentially enhances the downward signal of SSWs into the troposphere. To conclude this chapter, an overview of the EMAC simulations is given in Table 4.2.

Table 4.2: Transient and timeslice simulations conducted with EMAC.

Experiment	GHGs	Time period	Ocean	Ozone	Number of years	Ensembles
transient	SSP3.7.0	1850–2100	MPI-OM	interact.	250	6
timeslice	1850	preindustrial	MPI-OM	interact.	150	–
	2020	present	MPI-OM	interact.	150	–
	2100	future	MPI-OM	interact.	150	–
timeslice no-chem	1850	preindustrial	MPI-OM	clim	150	–
	2020	present	MPI-OM	clim	150	–
	2100	future	MPI-OM	clim	150	–

CHAPTER 5

Methodology

In this thesis, the stratospheric pathway is examined based on various EMAC simulations. The suggested cause-effect chain is illustrated in Figure 5.1 and can be summarized as follows:

Step 1: Arctic amplification leads to pronounced warming in the polar regions compared to the moderate temperature increase observed in midlatitudes.

Step 2: Enhanced polar warming weakens the strong temperature gradients between the cold Arctic and milder midlatitudes. Moreover, the thermal wind balance links the horizontal temperature gradient to changes in wind with altitude.

Step 3: A weaker temperature gradient reduces superjacent winds which could relate to a weaker tropospheric polar jet. Several authors have suggested that this could result in a wavier path for the jet stream.

Step 4: A meandering of the jet stream can be associated with Rossby waves. These tropospheric planetary waves propagate vertically into the stratosphere.

Step 5: Enhanced wave activity reaching the middle atmosphere induces stronger disturbances of the stratospheric polar vortex and more frequent SSWs.

Step 6: The downward influence of SSWs can alter tropospheric circulation, leading to local cold air outbreaks and potentially severe winter weather.
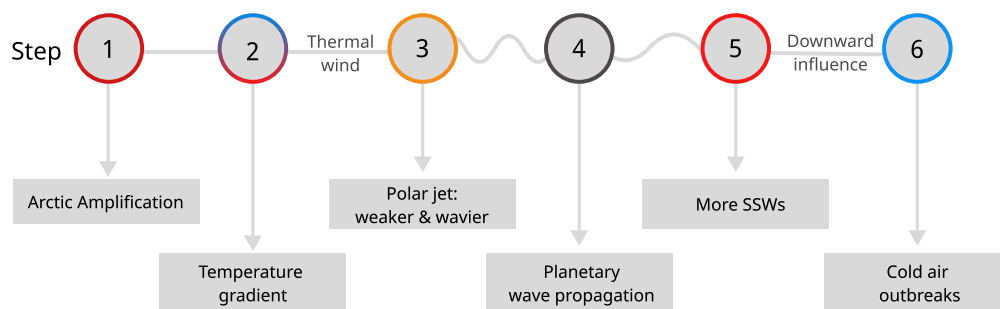
Figure 5.1: Schematic of the proposed steps in the stratospheric pathway of the Arctic-midlatitude linkage. The numbered steps are outlined in the text.

In this chapter, all metrics and methods used for the analysis of the stratospheric pathway are introduced. The description of the analysis follows the sequence of the mechanism.

5.1 Eady growth rate

The second step of the proposed mechanism involves the horizontal temperature gradient and the thermal wind relation. From this perspective, the polar jet stream could be directly affected by a reduction in the temperature gradient via a weakening of the vertical wind shear. Furthermore, a modification of the baroclinic instability is also worth considering. A decrease in vertical wind shear, as anticipated with Arctic amplification, would dampen the development of baroclinic waves. As these waves drive the polar (or eddy-driven) jet, this could also result in a weakening of the jet stream.

As outlined in Section 2.2.4, the maximum Eady growth rate (EGR) is a metric that determines the strength of baroclinic instability and the potential for baroclinic wave growth. The EGR is defined as

$$\sigma_{max} = 0.31 \frac{f}{N} \cdot \left| \frac{\partial \mathbf{v}_h}{\partial z} \right|. \tag{5.1}$$

It is important to derive the EGR from synoptic data, as discussed in Simmonds and Lim (2009). A calculation based on seasonal means would lead to underestimation owing to nonlinearities and covariances. Moreover, some studies used zonal wind shear alone rather than the combined zonal and meridional wind shear. In this respect, the EGR definition is inconsistent in the literature. This study uses daily mean data for the computation of EGR and the full horizontal shear, as indicated in Formula 5.1. The applied method is consistent with Hoskins and Valdes (1990). Furthermore, the EGR was calculated for all model levels, with central differences for the vertical derivatives.

5.2 Jet axis

Step 3 of the stratospheric pathway is related to the strength and waviness of the tropospheric polar jet. There are several strategies for assessing the behaviour of the jet stream. The methods range from a rather simple evaluation of the zonal or seasonal means of the zonal wind to more sophisticated calculations to determine the waviness of the jet stream. In this thesis, the advanced jet detection algorithm developed by Spensberger et al. (2017) is applied. This approach enables the precise identification of jet stream locations, also referred to as the *jet axis*. These jet axes are characterised by high wind speeds and strong horizontal wind shear. As discussed in Section 2.2.4, two jet streams exist in each hemisphere, underlying different formation mechanisms. The subtropical jet is stronger and more persistent than the polar jet, and is usually the dominant structure. In this work, jet streams are detected using the method described in the following section. Subsequently, these jets are separated into subtropical and polar jets. Further, an evaluation is conducted

to analyse their climatological positioning as well as changes in wind speed and zonal and meridional wind components.

5.2.1 Detection algorithm

This section provides a more detailed description of the jet detection algorithm elaborated by Spensberger et al. (2017). In simple terms, this method identifies high wind speed bands in the upper troposphere, where jet maxima are expected. In addition, these wind bands must satisfy certain conditions.

The wind is evaluated at the 2 PVU surface, which is an altitude level based on a specific isosurface of the potential vorticity (PV). The dynamical troposphere is typically characterized by a value of 2 PVU (see Section 2.2.3). As demonstrated in Figure 2.3b, the centers of the subtropical and polar jets can be found at different pressure or isentropic levels. In contrast, the 2 PVU isosurface is located in the vicinity of both jet maxima.

The objective of this algorithm is to determine the location of local wind maxima at this level. Figure 5.2 shows an example of the wind conditions in Europe. In (a), the wind speed U is illustrated, defined by the equation

$$U = \sqrt{u^2 + v^2} \tag{5.2}$$

where u and v represent zonal and meridional wind components, respectively. The depicted date is marked by a curved jet over the North Atlantic and a subtropical jet at approximately 30°N.

The jet detection scheme is based on wind shear in natural coordinates. These coordinates are orthogonal vectors that are oriented parallel and orthogonal to the horizontal velocity at each grid point (Holton, 2004). The unit vector **n** is normally oriented toward the flow and consequently perpendicular to the wind direction. The wind shear σ in natural coordinates is definded as

$$\sigma = \frac{\partial U}{\partial n}. \tag{5.3}$$

Since the data is provided in *x-y* grid space, the wind shear is transformed to the cartesian coordinate formulation given by

$$\sigma = \vec{\nabla} U \cdot \mathbf{n} = \vec{\nabla} U \cdot \frac{1}{U}(\mathbf{k} \times \mathbf{v}) \tag{5.4}$$

$$= -\frac{v}{U}\frac{\partial U}{\partial x} + \frac{u}{U}\frac{\partial U}{\partial y}. \tag{5.5}$$

The wind shear for the example date is shown in Figure 5.2b. It is evident that the jet maxima coincide with the zero shear lines. Hence, a first criterion for determining the location of the jet axis is given by $\sigma = 0$, as applied in Berry et al. (2007). Spensberger et al. (2017) identified these locations with a linear interpolation between gridpoints of opposing signs.
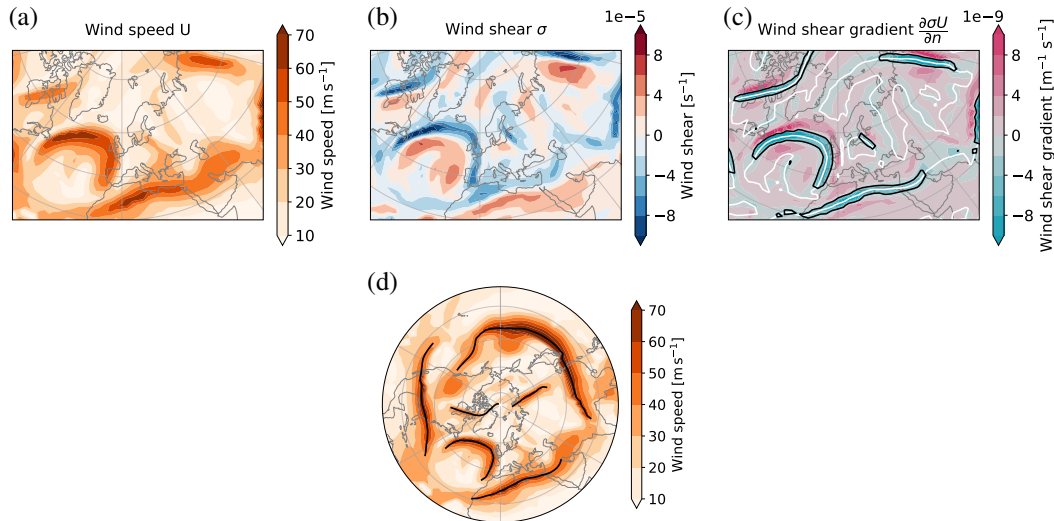
Figure 5.2: The jet detection scheme is presented using an example date from EMAC simulations (February 13 in the present timeslice). The wind speed over Europe is illustrated in (a) and the wind shear σ in natural coordinates in (b). To detect a jet, the first criterion is a change in the sign of wind shear. Therefore, the white contour line in (c) represents the zero-shear line. In addition, the wind shear gradient, which is the second criterion for jet locations, is delineated in (c). The gradient must be lower than the threshold K, which is represented by the black contour line. All locations of the white lines within the black contours are considered as jet locations. The detected jets (black lines) for the provided example date are shown in (d), covering the entire northern hemisphere.

In this study, a more efficient method using a graphical approach is applied to determine the coordinates of the zero-shear lines. These lines are depicted in Figure 5.2c as white contour lines. Evidently, the absence of shear is not exclusive to jet locations. Therefore, a second criterion is necessary. A common and straightforward approach involves the use of a wind speed threshold of $30\,\mathrm{m\,s^{-1}}$. However, Spensberger et al. (2017) argued that this method also detects jets that lack clear spatial boundaries. The exclusion criterion was improved using the equation

$$K \leq \frac{\partial \sigma U}{\partial n} = \sigma^2 + U\frac{\partial \sigma}{\partial n} \tag{5.6}$$

which ensures the detection of jets characterised by a well-defined structures only. The variable K is a negative threshold that essentially comprises the product of wind speed U and shear gradient $\frac{\partial \sigma}{\partial n}$. This criterion allows the detection of jets with wind speeds lower than $30\,\mathrm{m\,s^{-1}}$, as long as they have a well-defined structure. On the other hand, jets with a higher wind speed can be excluded if they miss this structure.

The threshold K depends on the spatial and temporal resolution of the data. In Spensberger et al. (2017), values for ERA-Interim data with spectral resolution T84 were provided with a time resolution of 6-hourly, weekly, monthly, and yearly intervals. If the resolution decreases, either spatially or temporally, the jets become broader, which is accompanied by a

reduction in $\frac{\partial \sigma}{\partial n}$. The K value for 6-hourly data was identified as $K = -6.1 \cdot 10^{-9} \, \mathrm{s}^{-2}$ sub-jectively in Spensberger et al. (2017) which corresponds to the 12.5th percentile of the shear gradient $\frac{\partial \sigma U}{\partial n}$. This percentile was used to determine the threshold for all other time resolutions. For the analysis in EMAC simulations with T42 and daily mean data this threshold has been calculated on the basis of the shear gradient statistics of the preindustrial timeslice which results in
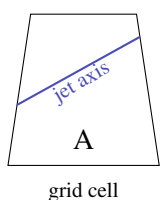
$$K = -3.16 \cdot 10^{-9} \, \mathrm{s}^{-2}. \tag{5.7}$$

There were slight variations in this value in the other timeslice experiments. However, small adjustments to the K threshold only affect the detection sensitivity at the edges of the jet. Thus, in this study, a single value of K was used for all EMAC simulations to ensure methodological consistency.

Finally, any jet axis shorter than 2000 km is excluded. For instance, the jet over the Baltic region in Figure 5.2 fulfils both detection criteria, but is not considered because of its short length. The full picture of the detected jets of the northern hemisphere at the specific date is shown in Figure 5.2d.

5.2.2 Jet axis distribution

The jet detection algorithm provides the exact positions of the jet streams. To analyse the changes in jet behaviour, it is useful to transform it back to grid space. In Spensberger and Spengler (2020), the variable *jet axis distribution* γ is introduced as

$$\gamma = \frac{1}{A} \sum_{i=1}^{N} l_i, \tag{5.8}$$

where A is the area of the grid cell and l is the length of the segment of the jet within that cell. In simpler terms, the jet axis distribution corresponds to the length of the jet axis passing through a grid cell normalised by its area. In this regard, the unit is expressed in km per $1000 \, \mathrm{km}^2$. This variable is calculated using daily data, but meaningful insights can be derived about the climatological behaviour of the jet axis distribution.

The winter climatology for the present EMAC timeslice and ERA-Interim (1979–2018) are depicted in Figure 5.3. Although the present timeslice, with its boundary conditions, cannot be directly compared to the ERA-Interim period (1979–2018), the climatological jet patterns are similar. The local maxima of the jet stream signals are located over the western Pacific and western Atlantic. Moreover, the pathway of the enhanced jet occurrence follows a spiral shape around the northern hemisphere, with the open end located over the eastern Atlantic. The similarity in the jet axis distributions between EMAC and observations provides confidence in the performance of the model with respect to the jet streams.

(a) Timeslice 150 years
daily mean data

(b) ERA-Interim 1979 – 2018
6-hourly instantaneous
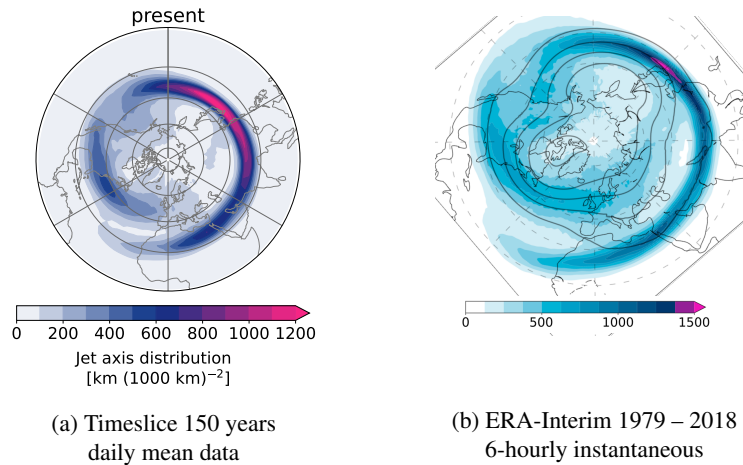
Figure 5.3: Winter climatology of jet axis distributions for the present EMAC timeslice in (a) and ERA-Interim in (b). The datasets have varying spatial and temporal resolutions, as well as slightly different colour bars, but they share the same units. The figure for ERA-Interim (b) was taken from Spensberger and Spengler (2020).

5.2.3 Separation of polar and subtropical jet

The subtropical jet is a prominent trait of climatological jet axis distribution, as shown in Figure 5.3. This jet occurs regularly within a preferred latitudinal band. In contrast, polar jets are sporadic in nature and not limited to a specific latitude. Consequently, the signal of the polar jet is represented by very light blue colours in Figure 5.3 and may be obscured by the subtropical jet. In this respect, the same dilemma arises as with many other jet evaluation methods used in the literature: the subtropical jet is the dominant feature in the results. Nevertheless, when analysing the polar jet, it is essential to ensure that the signals from the subtropical jet are not mistakenly considered.

Spensberger et al. (2023) developed a method to distinguish between subtropical and polar jet. They applied their detection algorithm to identify the locations of both jets in ERA5 3-hourly data. Subsequently, the wind speed and potential temperature θ at these jet locations are evaluated using a two-dimensional histogram. These histograms were applied in separated regions as shown in Figure 5.4. In this phase space, there are two accumulations, shown as dark blue areas, which occur at different θ levels. The polar jets are typically situated at lower θ levels, ranging from 300 K to 330 K. Subtropical jets are represented by an upper maximum above 340 K. The illustration aligns with our understanding of jet behaviour in the shown regions. Polar jets predominate in the northern Atlantic (b) and subtropical jets are rare. The most pronounced separation of both jets can be found over Asia, as shown in (c). The North Pacific, illustrated in (d), is characterised by strong subtropical jets with high wind speeds. Although the jets in the North Pacific are often considered as merged, a distinct polar jet is evident in this evaluation.
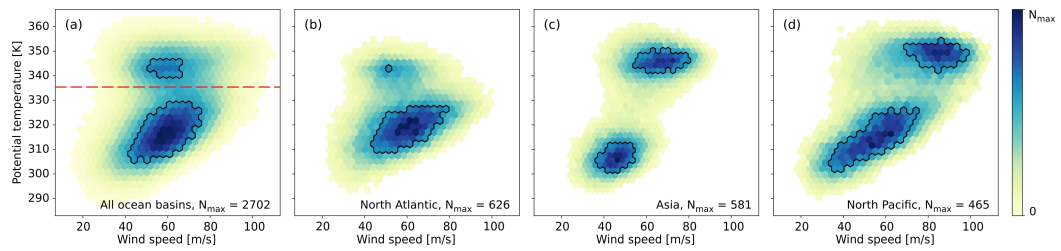
Figure 5.4: Two-dimensional histograms of the jet occurence in ERA5 within potential temperature/wind speed space for winter (DJF). The sum of all ocean sectors is shown in (a), the North Atlantic in (b), Asia in (c), and the North Pacific in (d). The chosen threshold of 335 K for distinguishing between jets is depicted by the red dashed line in (a). Figure adapted from Spensberger et al. (2023).

Spensberger et al. (2023) examined some frequently used metrics for distinguishing jets, such as the potential temperature, the jet latitude, lower tropospheric winds, and vertical wind shear. The results indicate that the potential temperature is suitable for jet classification due to its distinct bimodality in phase space, as illustrated in Figure 5.4. A threshold value of 335 K was determined to be optimal for distinguishing between the two jets, as also proposed in Christenson et al. (2017). This threshold is denoted by the red dashed line in Figure 5.4a. Furthermore, the authors pointed out that the widely used low-level winds (Woollings et al., 2010) exhibit high variability and may not be suitable for jet separation. After classifying the jets, they can be analysed for their behaviour and impacts of global warming.

Adaption of the θ-threshold

Spensberger et al. (2023) and Christenson et al. (2017) applied the θ-threshold method on reanalysis data for the observational time period spanning the last few decades. However, the potential temperature is sensitive to the overall temperature change caused by global warming. The applied temperature of 335 K may not be suitable for future scenarios. Therefore, the θ-threshold was adapted for EMAC timeslice simulations. Using the same approach as described in Spensberger et al. (2023), two-dimensional histograms similar to those shown in Figure 5.4 were evaluated. The authors differentiated between ocean basins and illustrated some notable differences. The specification of θ-thresholds in EMAC was refined by applying a threshold for each longitude.

Some example histograms are demonstrated in Figure 5.5 for longitudes located in Europe, Far East Russia, and North America. The θ-thresholds, indicated by the red lines, were determined subjectively for each longitude and timeslice separately. A clear distinction between the jets is evident in certain regions, such as the Western Pacific, as shown in (b). However, in other regions, a separation threshold is difficult to determine, as over North America depicted in (c). Additionally, the mean latitude of the bins was used as a guide to define the θ values. According to Spensberger et al. (2023), latitude is a reliable variable

(a) Europe: Longitude 14°E

(b) Far East Russia: Longitude 155°E

(c) North America: Longitude 110°W
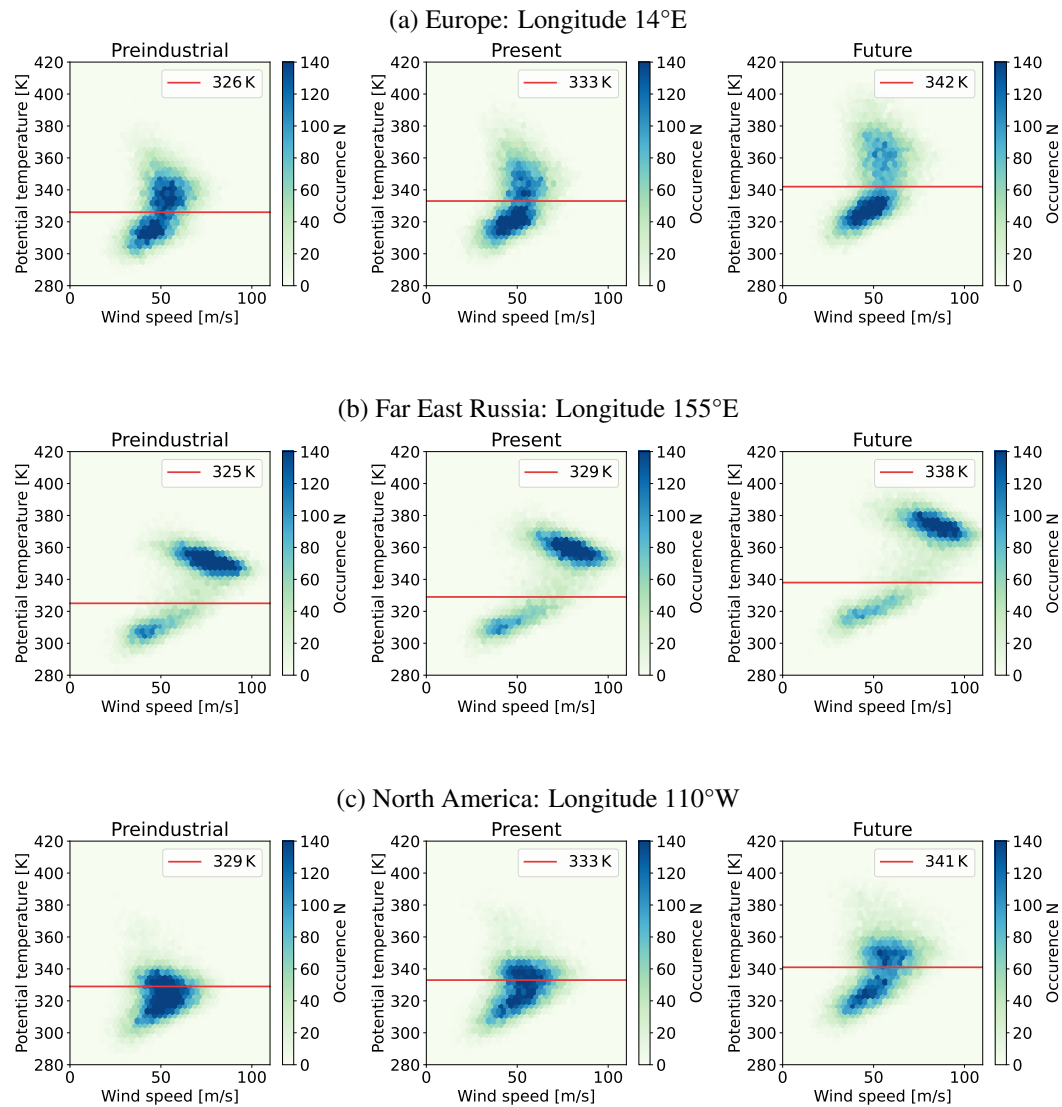
Figure 5.5: Two-dimensional histogram of jet occurrence in θ-U-phase space for three specific longitudes shown for different EMAC timeslice simulations. The θ-threshold was determined for each longitude and in all timeslice experiments separately. The red line marks these thresholds along with the values indicated in the legend.
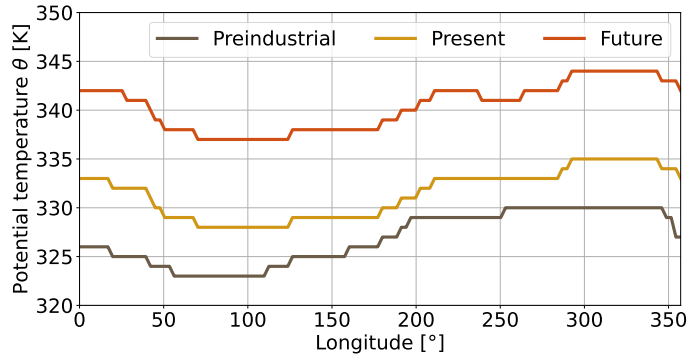
Figure 5.6: Selected θ-thresholds for jet separation as a function of longitude for EMAC timesclice simulations.

for the categorisation of jets. The θ-threshold corresponds roughly to the 40°N latitude in this study.

The manually selected θ-thresholds are illustrated in Figure 5.6. These values exhibit a variation of approximately 7 K within each timeslice, thereby justifying their precise definitions. Furthermore, there is a notable difference of over 13 K in the mean between the preindustrial and future timeslice simulations.

In many regions, this separation approach is efficient. Nonetheless, establishing a definitive boundary poses considerable challenges for North America. Unexpectedly, the Pacific region exhibits two distinguishable jet streams instead of the often-assumed merged jet structure. They may be located close to each other, but show different potential temperature levels and wind speeds. This outcome was already discussed in Spensberger et al. (2023). In contrast, the behaviour of the North American jet was not included in this study.

In summary, the separation algorithm appears to be suitable for the research question addressed in this study. As demonstrated in the results, atmospheric waves that propagate vertically into the stratosphere originate primarily from a region spanning from the Atlantic eastward to the Pacific. In these terms, misinterpretations over America may be tolerated but must be kept in mind.

5.3 Wave fluxes

During Step 4 of the stratospheric pathway, increased planetary wave activity reaches the stratosphere, leading to a deceleration of the polar night jet through wave breaking. This section introduces some metrics to describe wave propagation and the impact of waves on the mean flow. Moreover, a detailed classification of the wave input into the stratosphere, with a specific focus on its spatial distribution, is presented.

5.3.1 Eliassen-Palm flux

The Eliassen-Palm (EP) flux arises in the TEM framework, as delineated in Section 2.2.6. On the one hand, this variable can be interpreted as a vector in the meridional-vertical plane indicating the direction of planetary waves. On the other hand, the divergence of this vector signifies the influence of waves on the mean flow. The EP flux in pressure coordinates on a sphere is defined as

$$
\mathbf{F} = \begin{pmatrix} F_\varphi \\ F_p \end{pmatrix} = a\cos\varphi \begin{pmatrix} -\overline{u'v'} + \overline{u}_p \dfrac{\overline{v'\theta'}}{\overline{\theta}_p} \\ \left(f - \dfrac{1}{a\cos\varphi}\dfrac{\partial \overline{u}\cos\varphi}{\partial \varphi} \right) \dfrac{\overline{v'\theta'}}{\overline{\theta}_p} - \overline{u'\omega'} \end{pmatrix}
\tag{5.9}
$$

using ageostrophic adjustments (Andrews et al., 1983). Most of the variables have been introduced previously. Specifically, the radius of the Earth is represented by a, latitude in radians by φ, vertical velocity in pressure coordinates by ω and the index p denotes the derivative with respect to pressure. The overbars denote the zonal mean of a variable and prime the derivation from the zonal mean. The derivatives were calculated using the central finite differences or forward or backward differences at the grid edges. The divergence of the EP vector is given in Andrews et al. (1983) as

$$
\nabla \cdot \mathbf{F} = \frac{1}{a\cos\varphi}\frac{\partial F_\varphi \cos\varphi}{\partial \varphi} + \frac{\partial F_p}{\partial p}.
\tag{5.10}
$$

The calculation of the EP flux and its divergence is based on daily data, which may then be averaged for further evaluation. An important graphical convention was suggested by Edmon et al. (1980) using the mass-weighted EP flux

$$
\begin{pmatrix} \hat{F}_\varphi \\ \hat{F}_p \end{pmatrix} = \frac{2\pi}{g} a\cos^2\varphi \begin{pmatrix} F_\varphi \\ a \cdot F_p \end{pmatrix}
\tag{5.11}
$$

to display the vectors in the meridional-height cross-section. The EP flux can be considered the main diagnostic for planetary wave properties, but a consensus on how to display these vectors in a plot has been missing for a long time. Jucker (2021) shed some light into the topic and proposed a straightforward graphical convention. For plots in pressure coordinates with a logarithmic scaling of the y-axis the components of the EP flux are transformed to

$$
F_x = \hat{F}_\varphi \cdot \frac{X/Y}{(\varphi_1 - \varphi_0)\pi/180},
\tag{5.12}
$$

$$
F_y = \hat{F}_p \cdot \frac{1}{p\ln(p_1/p_0)}.
\tag{5.13}
$$

The figure aspect ratio is denoted by X/Y. The left latitude is given by φ_0 and the right latitude by φ_1 in degrees. The bottom pressure limit is denoted by p_0 and the top pressure limit is denoted by p_1. This scaling ensures that the EP vectors appear nondivergent only for conditions with $\nabla \cdot \mathbf{F} = 0$ while accounting for the logarithmic decrease in pressure in the y-axis.

5.3.2 Plumb flux

The EP flux is a zonally averaged quantity that indicates wave propagation and mean-flow interactions in a zonal mean sense. An enhanced upward EP flux points to wave activity at a certain height and latitude but does not provide information about the longitudinal distribution of the waves. To objectively evaluate the Arctic-midlatitude linkage, it is beneficial to assess the precise location of the waves. Therefore, the three-dimensional wave activity flux developed by Plumb (1985) is applied in this study. This flux is derived for linear quasi-geostrophic disturbances and is also referred to as the *Plumb flux*. The implementation is derived from Formula (5.7) in Plumb (1985) but has been modified for the use in pressure coordinates

$$\mathbf{F}_s = \cos \varphi \begin{pmatrix} \frac{1}{2a^2 \cos^2 \varphi} \left[\left(\frac{\partial \psi'}{\partial \lambda} \right)^2 - \psi' \frac{\partial^2 \psi'}{\partial \lambda^2} \right] \\ \frac{1}{2a^2 \cos \varphi} \left(\frac{\partial \psi'}{\partial \lambda} \frac{\partial \psi'}{\partial \varphi} - \psi' \frac{\partial^2 \psi'}{\partial \lambda \partial \varphi} \right) \\ \frac{2\Omega^2 \sin^2 \varphi}{\sigma_p^2 a \cos \varphi} \left(\frac{\partial \psi'}{\partial \lambda} \frac{\partial \psi'}{\partial p} - \psi' \frac{\partial^2 \psi'}{\partial \lambda \partial p} \right) \end{pmatrix} \quad \text{with} \quad \psi' = f^{-1}(\overline{\Phi} - \Phi), \tag{5.14}$$

where ψ represents the stream function and Φ is the geopotential. Averaging the Plumb flux over all longitudes yields the EP flux. This flux has been widely used in studies interested in the 3D behaviour of planetary waves, for instance, for the analysis of wave reflection in the stratosphere.

Case examples of wave flux

Typical wave conditions in winter are illustrated in Figure 5.7. In the first example, the EP flux and the Plumb flux represent a quiescent state, as shown in (a) and (b). Some horizontal wave activity is apparent but without significant vertical propagation. In the second example in (c), the EP vectors point upward through the upper troposphere and lower stratosphere, depicting a typical wave propagation scenario. These waves originate in the troposphere and propagate upward until they either dissipate or are reflected, often towards the equator. In (d), the source regions of the upward-propagating waves can be identified as red-shaded areas. In this example, the main source regions are located over Siberia and the Western Pacific.

An example of a wave reflection event is shown in (e) and (f). The Plumb flux exhibits pronounced upward wave propagation over the Pacific, followed by downward propagation in close proximity to the east. In this example, no significant wave activity near the tropopause is characterised by the EP flux in (e) because positive and negative fluxes cancel each other when averaged along longitudes. The EP flux alone indicates a significant wave activity in the stratosphere with no apparent wave propagation originating from the troposphere. These findings would support the argument that SSWs may not require tropospheric wave forcing, as mentioned in Section 2.4.3 and discussed in Baldwin et al. (2021). When considering the Plumb flux, it becomes clear that there is wave activity originating from the troposphere, but it is concealed in the EP framework.
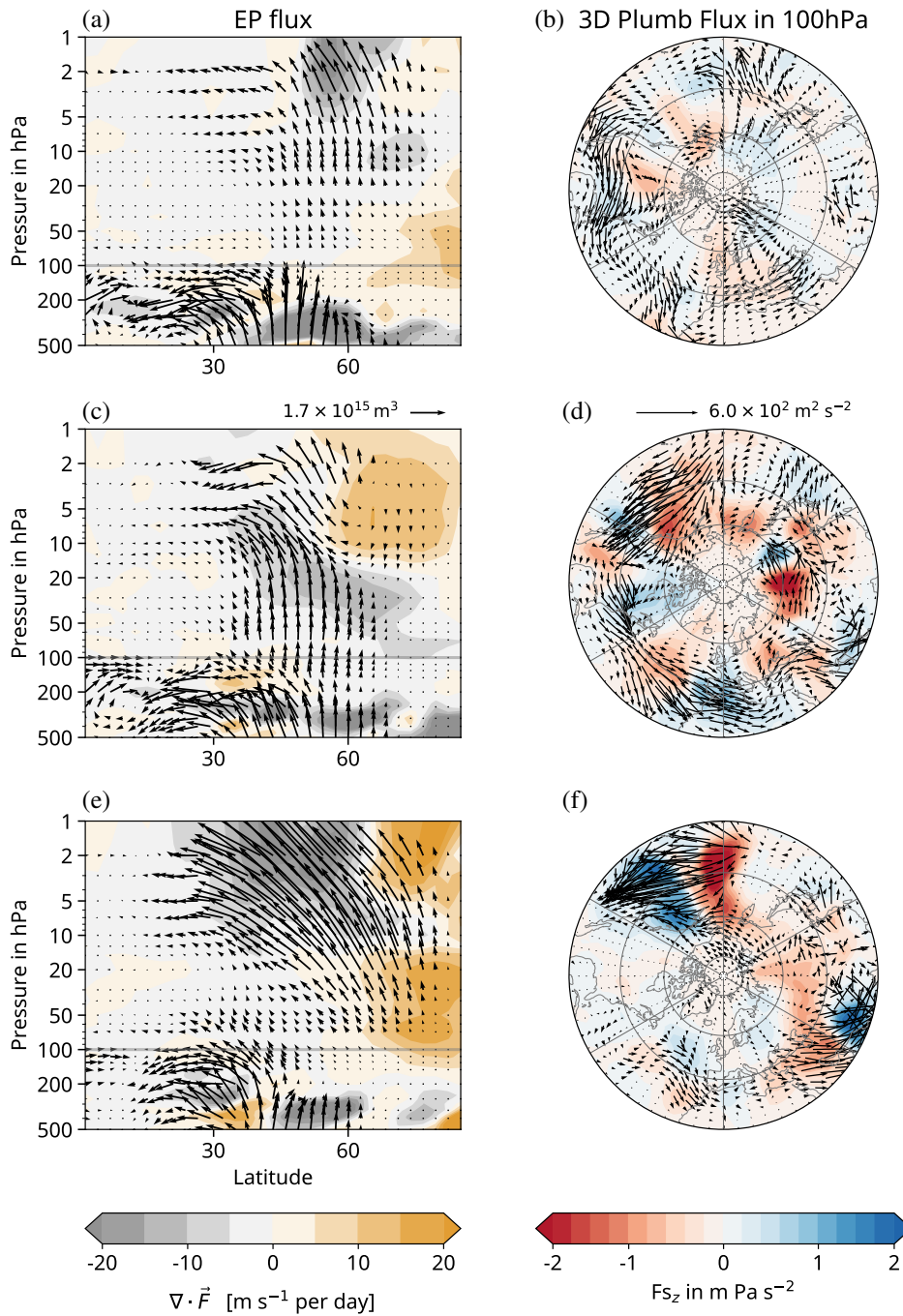
Figure 5.7: Daily EP flux $\vec{F}$ (left column) and 3D Plumb flux F_s (right column) of three example dates in winter in EMAC timeslice simulations. The EP vectors are shown in the meridional-height cross-section, scaled in accordance with Edmon et al. (1980) and Jucker (2021). The 3D Plumb flux for the same day and in 100 hPa is shown on the right. The horizontal components are illustrated as black vectors and the vertical components as shaded contours, with the red areas indicating upward propagation. The 100 hPa levels are marked by a grey line in the meridional-height cross-sections in a), c), and e).

Furthermore, the EP vectors magnify in the upper stratosphere, indicating the expected growth in amplitude. This increase was often suppressed by alternative vector scaling, but represents the more accurate physical behaviour of the waves. In this thesis, both the EP flux and the 3D Plumb flux are applied to analyse the change in wave activity in a warmer climate.

5.3.3 Vertical wave events

As outlined in the previous section, the 3D Plumb flux is used to supplement the EP flux in identifying where upward wave propagation occurs and to avoid concealing wave events related to wave reflection. Tropospheric waves propagate into the stratosphere and can cause stratospheric warmings. This study examines the input of tropospheric waves into the stratosphere using an event-based analysis.

The typical pressure level representing the tropospheric wave input is 100 hPa. At mid- and higher-latitudes, this level is already positioned within the lower stratosphere. Nevertheless, it is deemed suitable for classifying waves that propagate further into the middle atmosphere. The objective of this analysis is to find the locations of the upward wave propagation. As explained in the case example in Figure 5.7, the red areas in (d) and (f) represent a negative vertical component of the Plumb flux indicating a wave input into the stratosphere. Negative values indicating upward propagation arise due to the representation in pressure coordinates.

A categorisation is applied based on whether a grid point exeeds a specified threshold of upward wave propagation strength. This condition is typically fulfilled by adjacent grid points, and these areas are classified as *vertical wave event* (VWE). It is important to note that only upward-directed events were captured.

The threshold values were determined by evaluating the daily conditions preceding the SSWs to ascertain the necessary strength of the tropospheric wave input. Daily maps were analysed individually for this purpose. A threshold of $-1\,\mathrm{m\,Pa\,s^{-1}}$ was found to be convenient for classifying the boundaries of vertical wave events. A second criterion was applied to ensure that only the strongest wave events were classified. The wave events found with the first threshold must exceed the second threshold of $-2\,\mathrm{m\,Pa\,s^{-1}}$ for at least one grid point at one time step during the event.

An example of an event over Eurasia is shown in Figure 5.8. The VWE develops over Western Russia on day 1, extends over a wide range from Finland towards the Ural region by day 5, and decays after day 7. On days 3 and 4, the sufficient condition is met. It has been found that a minimum area or duration condition are not required in this case. Wave events that exceed the second threshold are potentially capable of inducing SSWs regardless of their spatial extent or duration. Hence, no additional restrictions are applied to the aforementioned two conditions. For further evaluation, all grid points within the black contours were identified as a vertical wave event.
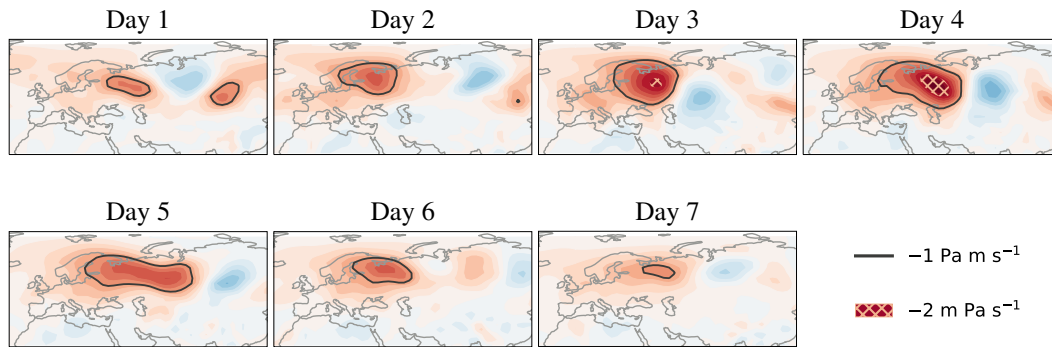
Figure 5.8: Example of vertical wave event classification in EMAC simulations. The vertical component of the Plumb flux in $\mathrm{m\,Pa\,s^{-1}}$ is depicted in colour with red shading as negative values (upward directed). The necessary condition for a vertical wave event is illustrated by a black line as the contour for $-1\,\mathrm{m\,Pa\,s^{-1}}$. For at least one grid point and one time step during the event, the sufficient condition has to be fulfilled, exceeding $-2\,\mathrm{m\,Pa\,s^{-1}}$, as marked by the crossed area.

Statistical reflection of VWE thresholds

The estimated thresholds are further classified based on their statistical occurrence. Figure 5.9 shows a histogram of the vertical Plumb flux in $100\,\mathrm{hPa}$ for all winter days and in the northern hemisphere ($20°\mathrm{N} - 80°\mathrm{N}$). The small differences in timeslice experiments indicate a modification of wave propagation. Nevertheless, changes at the edge of the distribution were small. When merging the three datasets together, the 2.5th quantile of the distribution holds $-0.99\,\mathrm{m\,Pa\,s^{-1}}$. Thus, the first threshold for classifying vertical wave events corresponds to the 2.5th quantile of all the grid points in the key region which seems to be a reasonable assumption. Applying the same analysis to every grid point in this area reveals that some regions are more prone to wave events than others. The spatial distribution of the value of the 2.5th quantile is shown in Figure 5.9b. The minimum value is $-1.91\,\mathrm{m\,Pa\,s^{-1}}$,
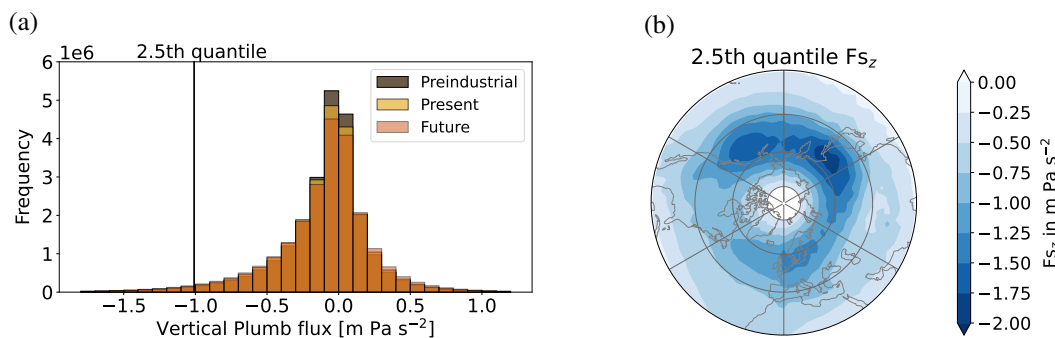
Figure 5.9: (a) Histogram of daily vertical components of the Plumb flux in $100\,\mathrm{hPa}$ for winter days (DJF). All grid points between $20°\mathrm{N}$ to $80°\mathrm{N}$ were used. The EMAC timeslice simulations are presented as shown in the legend. The 2.5th quantile of the merged distribution is indicated in the plot. (b) The spatial distribution of the 2.5th quantile of the merged dataset for three timeslices. The statistics depicted in (a) are area-weighted values.

which is close to the second classification threshold. The classification thresholds were originally established based on an estimate of the wave input strength required to trigger SSW events. In retrospective, the statistical evaluation of these thresholds confirmed their application.

Evaluation of vertical wave events

After determining the vertical wave events on a daily basis in winter and classifying each grid point with a Boolean value, further evaluation can be performed. The variables utilised are listed in Table 5.1. In this way, VWEs can also be assessed for their alterations in area, intensity, duration, and frequency.

Table 5.1: List of VWE variables analysed for the EMAC timeslice experiments.

Variable	Description	Resolution
Spatial frequency	- The number of days per winter for each grid point characterised by the occurrence of an event. - The interpretation of this variable is similar to a blocking frequency, for example.	- Frequency per winter on a spatial grid - If applicable seasonal mean
Mean area of events	- Mean area calculated for every single event - For example: the areas inside the black contours in Figure 5.8 are determined for every day and then averaged over the whole period (7 days in the given example).	- List of values corresponding to all events
Mean intensity of events	- The area-weighted mean of the vertical Plumb flux of every single event - Similar to area: calculation of area-weighted mean each day and then averaged over the whole period.	- List of values corresponding to all events
Duration of events	- Duration of every event - 7 days in the example in Figure 5.8	- List of values corresponding to all events
Number of events per winter	- Absolute events per winter - Events can occure simultaneously in different locations.	- List of values corresponding to all winters

5.4 SSW Composites

The disruption of the polar stratospheric vortex in midwinter can lead to significant changes in tropospheric weather. A commonly used approach to quantify changes following stratospheric warmings is to collect data in a time period after SSWs and compare the mean of this period to the overall average. These SSW composites are analysed for the EMAC timeslice simulations in this study.

5.4.1 Surface variables

Typical variables characterising the surface influence of SSWs are the 2-metre temperature, sea level pressure, and precipitation. The computations described below are applied to each grid point of the data. The surface variables are transformed into anomalies from a daily climatology of the respective timeslice simulation. The SSW onset dates are derived based on the WMO classification, as described in Section 2.4.3. This classification is based on changes in the circulation in the middle stratosphere. Subsequently, the anomalies typically propagate downward over the subsequent month. Therefore, the anomalies of the surface variables are averaged for all days within 30 to 60 days after the SSW onset date. This corresponds to surface changes one month after the SSWs. The SSW composites include all SSWs during December, January and February, ensuring the selection of midwinter warmings only.

5.4.2 NAM composite

Furthermore, the NAM index can be used to evaluate the Arctic circulation anomalies over time. An example of polar cap pressure anomalies was shown in Figure 2.13b to illustrate the downward influence of SSWs. In this study, the NAM index based on the geopotential height Z is computed as outlined in Gerber et al. (2010) and Oehrlein et al. (2020). The subsequent steps are implemented:

1. The zonal mean of the daily timeseries of geopotential height Z is computed.

2. For every timestep and pressure level, the global mean $\overline{Z}_{\text{global}}(t, p)$ is removed. This step reduces the signal due to global warming.

3. The anomalous height $\overline{Z}_{\text{anom}}$ is derived by subtracting the climatological mean $\overline{Z}_{\text{clim}}$ for every time step, latitude and pressure level.

4. The polar cap average north of 65°N is computed for every day and pressure level which gives the NAM index.

5. To maintain consistency with prior studies, the NAM index is multiplied by -1. Therefore, a higher pressure over the pole corresponds to a negative NAM index.

6. The NAM index is normalised by its standard deviation at each pressure level.

After deriving the NAM from daily data in EMAC timeslice experiments, SSW composites are created using a method similar to that described previously. In contrast to the surface

variables, the NAM index is averaged on a daily basis relative to the onset date. For example, all NAM values for the first day of all SSW events were grouped together and averaged, followed by the second day and so forth. This composite covers the time period from 30 days prior to the SSW onset date to 60 days after.

5.5 Statistical hypothesis testing

Statistical tests were performed to determine the significance of the results. The standard hypothesis tests are briefly introduced in this section. In addition, more detailed information regarding the Monte-Carlo simulation conducted to test the significance of the SSW composites is provided.

5.5.1 Two sample independent t-test

This statistical test, commonly known as the Student's t-test, determines whether the means of two independent groups are significantly different. It assumes that the samples are normally distributed and have equal variance. Two examples of the application of t-tests are shown in Figure 5.10. The test statistic determines whether the means (depicted as dashed lines in the examples) are significantly different. Therefore, the p-value of the test is evaluated which quantifies the probability that two samples are drawn from the same population. If the p-value is lower than the significance level, it can be assumed that the means of the samples are statistically different. A significance level of 5% is used in this study, which means that the threshold for the p-value is 0.05.

(a)   (b)
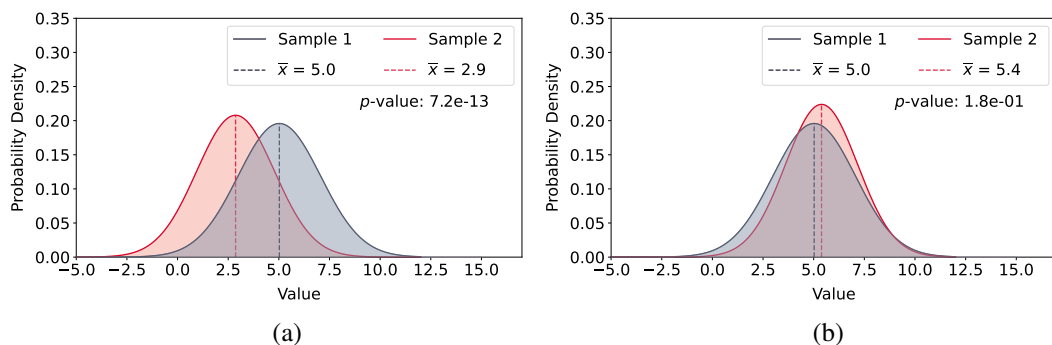
Figure 5.10: Student's t-test illustrated using idealised normal distributed samples. Plot (a) shows a significant difference between the samples, whereas the distributions in (b) show no statistical difference. A significance level of 5% is used and the p-value of the test statistic is indicated in each plot.
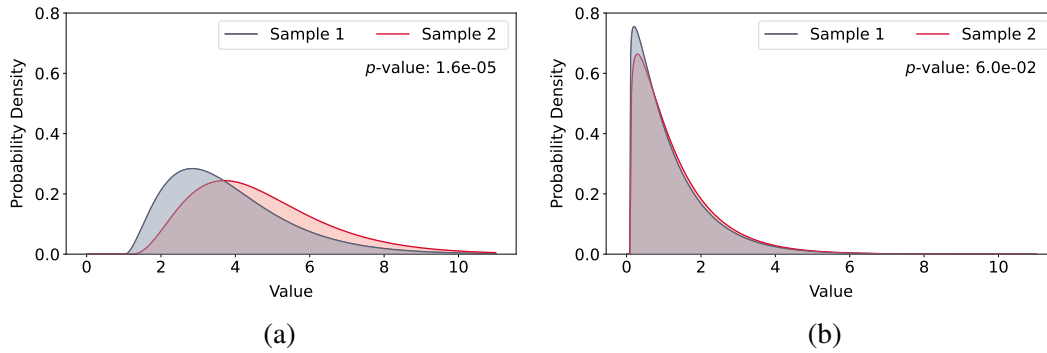
Figure 5.11: Mann-Whitney U test illustrated using idealised non-normal examples. The plot in (a) shows a significant difference between the samples, whereas the distributions in (b) exhibit no statistical difference. A significance level of 5% is used and the *p*-value of the test statistic is indicated in each plot.

5.5.2 Mann-Whitney U test

If the assumptions for conducting a Student's t-test are not met, such as when the data are not normally distributed, the Mann-Whitney U test can be used. This nonparametric test determines whether two samples are drawn from the same population. An example is shown in Figure 5.11 which reflects an idealised illustration of samples of the seasonal mean of the jet axis distribution on specific grid points. In certain regions, jet occurrence is infrequent, leading to skewed and bounded distributions, as shown in Figure 5.11b. The grid points with more frequent jet occurrences, as shown in (a), display a distribution that is more Gaussian in nature. The Mann-Whitney U test is appropriate for all grid points in this example, as it does not require any assumptions regarding the distribution of the data.

5.5.3 Chi-square test

The chi-squared or χ^2 test of independence can be utilised to assess whether two samples of categorical data originate from the same population. This test is applied to determine whether the frequencies of SSW events significantly differ in the timeslice simulations. When considering the occurrence of SSWs in a specific month, either one or none is generally given in a single year. Thus, there are two categories: 1 and 0. A contingency table is used to compare the frequencies of two experiments with each other. Table 5.2 presents contingency tables depicting the occurrence of SSWs in December within EMAC timeslice simulations. The chi-squared test calculates the expected frequency under the assumption of the null hypothesis, which posits that there is no significant relationship between the two experiments. This implies that the samples are drawn from the same population. The value for the expected frequency E is given by

$$E = \frac{R \cdot C}{N},$$

Table 5.2: Contingency table for the chi-square test for SSW occurrence in December in EMAC timeslice simulations. The *p*-value is denoted at the top indicating the probability of the null hypothesis stating that there is no association between experiments and SSW occurrence.

(a) *p*-value = 0.243

Experiment	SSW occurrence		
	0	1	Total
Preindustrial	132	17	149
Present	124	25	149
Total	256	42	**298**

(b) *p*-value = 0.028

Experiment	SSW occurrence		
	0	1	Total
Preindustrial	132	17	149
Future	117	32	149
Total	249	49	**298**

where R is the sum of the row in the contingency table, C is the sum of the column and N is the total number (in bold). The test statistic χ^2 is determined by

$$\chi^2 = \sum \frac{(O-E)^2}{E}$$

where O is the observed frequency. When the observed and expected frequencies exhibit strong deviations, the value of χ^2 will be large. The null hypothesis can be rejected if a critical value is exceeded which is derived from a χ^2 distribution. The test outcome can be assessed using the *p*-value, as previously described for other hypothesis testing. The preindustrial and present timeslices in Table 5.2a demonstrate a *p*-value larger than 0.05 and the null hypothesis cannot be rejected, indicating that both experiments underlie the same population and do not differ significantly. By contrast, the future timeslice in (b) can be assumed to be different from the preindustrial timeslice because the null hypothesis can be rejected.

5.5.4 Monte-Carlo statistics

Simple hypothesis testing cannot be directly applied to SSW composites. A significant composite mean anomaly would suggest a difference between the SSW-associated days and climatology. However, it is necessary to establish a threshold at which the anomalies can be considered significant. A Monte-Carlo simulation is carried out for this purpose. The method is based on random sampling of data to obtain a probability distribution. The significance levels of SSW composites can be derived from these probability distributions. The Monte-Carlo simulation is implemented as follows:

1. The onset dates of SSWs are used for each timeslice experiment. For example, we can assume that 50 SSWs were identified in an experiment that lasted 150 years.

2. A new composite is created by selecting 50 different SSW onset dates, keeping the day and month of each SSW but randomly changing the years.

3. The new composite with 50 random onset dates is averaged according to the choice

of variable, surface variable or NAM index. The result is one new composite mean value.

4. Step 2 and 3 are repeated *N* times to obtain a distribution of composite means. The value *N* is set to 5000 in this study.

5. The 2.5th and 97.5th quantile of the distribution of 5000 composite means are taken as upper and lower significance levels, respectively. Therefore, it is a two-tailed test with a 5% significance level.

6. When the actual composite mean exceeds these signifcant levels, it can be considered statistically different.

The outlined computation is applied to each grid point for the surface variables or for each relative day and pressure level for the NAM index. An idealised sample is shown in Figure 5.12, exemplary for the 2-metre temperature at one grid point. The distribution depicted in grey is derived from the Monte-Carlo simulation. The 2.5th and 97.5th quantiles of this distribution are −0.57 K and 0.55 K, respectively. The actual SSW composite temperature anomaly at the grid point is classified according to these thresholds. Values within the blue or red areas are considered significantly different. For instance, a negative temperature anomaly of −0.6 K is considered significant, whereas an anomaly of −0.5 K falls within the grey area and is classified as not significant.
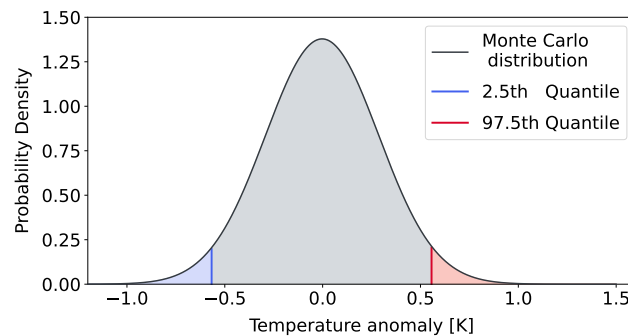
Figure 5.12: Idealised distribution illustating an example of Monte-Carlo simulation for one grid point showing the temperature anomalies. See text for explanations.

CHAPTER 6

Results

This chapter evaluates the Arctic-midlatitude linkage based on EMAC simulations. Given the emphasis on the stratospheric pathway, a fully coupled ocean chemistry climate model is employed, incorporating both ocean-atmosphere interactions and potential ozone feedback on stratospheric dynamics. Transient EMAC simulations provide insights into the slowly evolving changes in the climate system induced by global warming. In contrast, timeslice experiments allow for a better quantification of small signals and their statistical classification. Furthermore, EMAC timeslice experiments without interactive ozone chemistry are utilised to estimate the influence of a realistic representation of ozone on dynamical processes in the model.

The Arctic-midlatitude linkage has a long history of being evaluated using sensitivity experiments. Frequently, the focus has been on the isolated effects of Arctic amplification on atmospheric circulation. For instance, this has been achieved by removing sea ice in AGCMs or introducing an additional warming in idealised models. Often, these modifications take place in a world that is otherwise unaffected by climate change. This approach can be useful for examining the isolated impacts of regional warming. However, because we are interested in changes across a broad range of atmospheric levels, it may not provide a complete picture.

An example is provided, which assumes an influence on the generation of tropospheric waves. In terms of the stratospheric pathway, these waves must propagate into the stratosphere and induce stratospheric warmings, which subsequently exert their influence on surface weather. This scenario could yield different outcomes if the additional wave travels through a warmer troposphere, encounters a stratosphere affected by climate change, and subsequently interacts under different conditions with lower atmospheric layers.

This study assesses the impacts of climate change on the troposphere and the stratosphere using EMAC simulations based on increased GHG emissions. Consequently, a comprehensive evaluation of the entire scope can be achieved. A drawback of this approach is that it is impossible to isolate the sole effect of Arctic amplification. For instance, the assessment in this study cannot directly attribute a signal to changes in Arctic sea ice. However, it can indicate what transformation can be expected in a changing climate when all effects are taken together.

6.1 Transient simulations

The ensemble of transient EMAC simulations, covering the period from 1850 to 2100, are used to evaluate the extent of climate change that has occurred and will continue in the future. Given the lively discussion on the topic, the following simple and obvious question arises:

Q1 Does the outcome of historical model simulations indicate a cessation or cooling trend during winter in midlatitude regions?

The strength of the Arctic amplification and time series of some regional near-surface temperatures are shown in Figure 6.1 for the winter season. Arctic amplification continues to rise until the end of the 21st century in EMAC simulations, as shown in (a). The Arctic mean temperature in (b) includes the temperatures over both land and ocean. This region will warm by approximately 10 K in the SSP3.70 scenario. When comparing the observational time period to ERA5 data, strong agreement is evident. Conversely, the NH mean in (c) exhibits some deviations, with higher temperatures in the model. The average overestimation of NH temperatures is 0.6 K and arises mainly from discrepancies in the tropics and lower latitudes (not shown).

In contrast, the midlatitude land temperatures in (d) are aligned with ERA5 temperature levels. The model results do not suggest a reversal or halt of the midlatitude warming trend. The low temperatures around the year 2010 in observations are situated in the ensemble range of EMAC simulations. As already discussed in Blackport and Screen (2020b) and shown in Figure 3.11, the trends observed in the two decades leading up to 2012 have not continued in recent years. Similarly, the mean ERA5 temperature in Central Asia, as depicted in (e), exhibits a distinct decrease around the year 2010, a tendency not reproduced by EMAC. In this region, EMAC generally shows slightly higher temperature levels than ERA5. McCusker et al. (2016) found that the Eurasian cooling was an event at the edge of the possible internal variability. Taking into account the slight overestimation of temperature in EMAC, this statement may also apply when comparing EMAC with ERA5 in Central Asia. In this regard, there is no need to consider the difference between observations and EMAC in this region as a deficiency of the model in simulating Eurasian cooling.

This point marks a crucial junction in interpreting the results. Either the models have a limited ability to simulate an Arctic-midlatitude linkage or the observed Eurasian cooling can be associated with natural variability. The latter assumption will be maintained for the remainder of this study, particularly due to the fact that the cooling has not perstisted during the last few years.

By examining the temperature time series, it appears that the internal variability can be roughly estimated with six ensemble simulations. The answer to the question posed at the beginning of this section is:

A1 A cooling trend or halt of near-surface temperatures is not evident in EMAC model simulations under a SSP3.70 scenario.

As previously discussed, this statement is based on model simulations using GHG forcing. Therefore, the results indicate that warming will continue, even during winter in midlatitudes and in Central Asia. Numerous studies have challenged the idea that winter weather is becoming colder due to climate change. However, the evaluation of the Arctic-midlatitude linkage should not be concluded at this point. As this study focuses on the stratospheric pathway, it is important to examine the changes in the stratosphere as well.

6.1.1 SSW occurrence

Stratospheric warmings play a crucial role in the mechanism of the Arctic-midlatitude linkage. Following the logical chain of the stratospheric pathway, enhanced Arctic amplification leads to stronger disturbances of the polar vortex and, consequently, more SSWs. Given the increase in the Arctic amplification signal in transient simulations, as shown in Figure 6.1a, it is reasonable to expect an increase in the SSWs frequency in the future. This gives rise to the question:

Q2 Does climate change leads to an increase in the frequency of stratospheric warmings?

The occurrence of SSW is illustrated in Figure 6.2. The SSW occurrence for EMAC transient runs has been shown before for the observational period (Figure 4.6). The current figure illustrates the full simulation period of 250 years. As discussed previously, the SSW frequency shows irregular patterns. Nevertheless, when examining the ensembles from the left (preindustrial era) to the right (end of the 21st century), it appears that the frequency increases over time. However, the third ensemble represents an exception, and a more thorough evaluation is generally required.

A2a As a first impression, there appears to be a tendency for more SSWs towards the end of the century in EMAC simulations.

As outlined in Section 2.4.3, the model findings regarding future changes in SSW occurrence diverge. They range from an increase to no change, or even a decrease, in SSW frequency. Sticking to the argumentation line of the stratospheric pathway, the projected increase in SSWs is consistent with the increasing Arctic amplification. However, the occurrence of SSW in Figure 6.2 reflects the evolution of a gradually changing climate. Owing to the irregular nature of the event, further analysis of the SSW frequency is carried out using timeslice simulations in the following section.

Summary

The original concept of the Arctic-midlatitude linkage relates a reduction in the meridional temperature gradient to circulation changes that bring colder winter weather to the midlatitudes. As in many previous studies, these coherences could not be found in EMAC simulations. However, a tendency towards more SSWs in the future has been identified. It is possible that Arctic amplification plays a role in the generation of planetary waves and
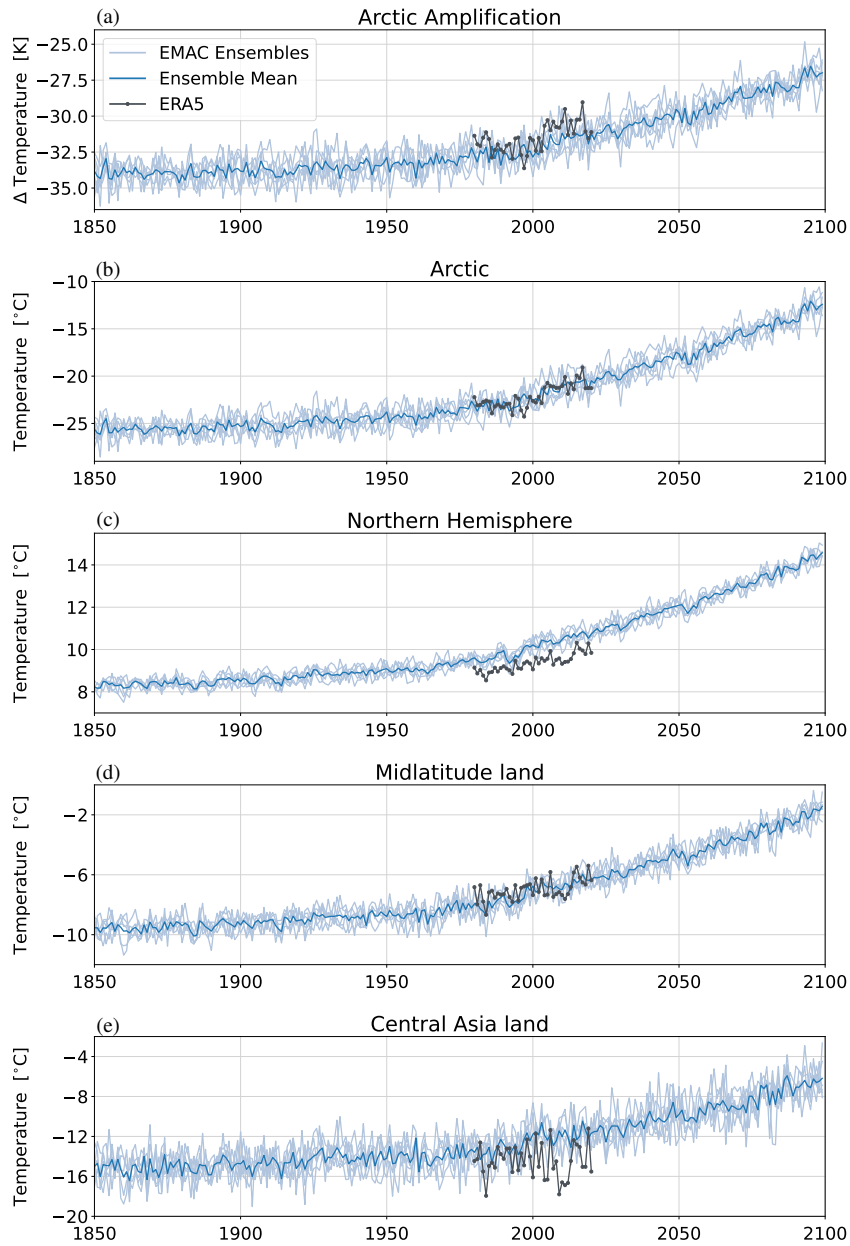
Figure 6.1: Regional near-surface (2 metre) temperature means for transient EMAC simulations (1850 – 2100) in blue and ERA5 (1980 – 2020) in grey. The Arctic amplification in (a) is defined as the difference between the Arctic mean (65°N to 90°N) and the NH mean (0° to 90°N), separately illustrated in (b) and (c). The midlatitude (30°N to 60°N) land temperatures are depicted in (d) and Central Asia (40°N to 60°N, 60°E to 120°E) is shown in (e). All shown averages are area-weighted and winter (DJF) means.
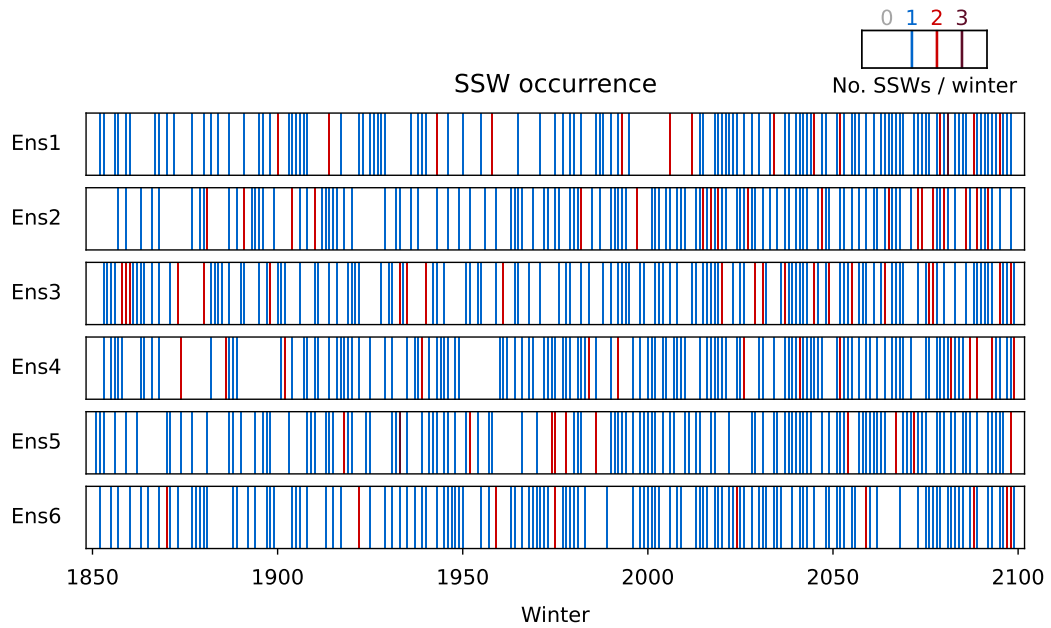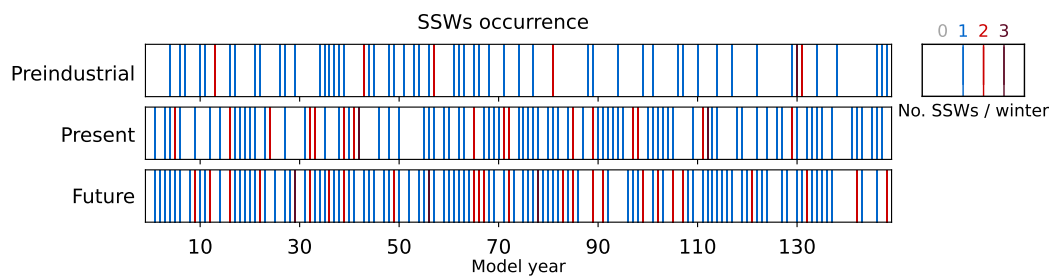
Figure 6.2: Occurrence of major sudden stratospheric warmings (SSW) in the extended winter season (NDJFM) in transient EMAC simulations. Events are classified after the WMO classification and the occurrence is illustrated as the number of events per season (see legend).

partially contributes to changes in the stratosphere without necessarily offsetting the warming trend of climate change. Arctic sea ice is commonly listed as an influencing factor for stratospheric variability, particularly in popular science media. In the course of this thesis, the focus is on the modification of the wave activity, including the tropospheric sources and the effects of the changes in stratospheric circulation.

6.2 Timeslice simulations

In this section, a comprehensive analysis is conducted with EMAC timeslice experiments for the preindustrial, present, and future time periods (see the description in Section 4.2.3). The advantages of timeslice simulations are an improved statistical assessment based on 150 model years of the same condition. In addition, the large climate change signal in the future timeslice has the potential to intensify the effects of Arctic amplification. First, the two main components of the stratospheric pathway are reassessed: Arctic amplification and the occurrence of SSWs. These represent Steps 1 and 5 in the outlined mechanism on page 69. Furthermore, all other proposed steps are thoroughly evaluated in this part of the study.
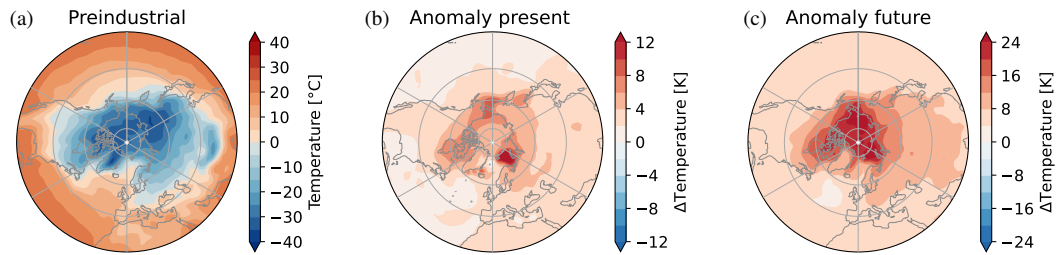
Figure 6.3: Climatological winter mean (DJF) near-surface temperature in the preindustrial timeslice in (a). The temperature anomalies for the present (b) and future (c) timeslices were computed with respect to preindustrial levels. Note that the colour bars in (b) and (c) have different scales. The significance of anomalies was determined using a Student's t-test at a significance level of 5%. The insignificant grid points are marked with dotted hatches, although there are only a few in the present time slice.

6.2.1 Step 1: Arctic amplification

The Arctic amplification signal was evaluated as the difference between the Arctic mean and the NH mean for the transient simulations. Figure 6.3 shows the spatial distributions of temperature changes. The preindustrial mean state of near-surface temperatures during winter is demonstrated in (a), and the anomalies from this basic state are shown in (b) and (c) for present and future, respectively. The Arctic amplification signal becomes evident through larger positive anomalies in the polar region. Calculating the extent of Arctic amplification by taking the difference between the Arctic and NH mean, as illustrated in Figure 6.1, yields a value of approximately $-33\,\mathrm{K}$ for the preindustrial timeslice. This value increases to $-30\,\mathrm{K}$ in the present experiment and to $-23\,\mathrm{K}$ in future experiment. Therefore, Arctic amplification is expected to continue in a climate characterised by extensive warming, as observed in both climate change experiments (present and future).

Figure 6.4 depicts climatological winter sea ice cover. The loss of sea ice in the present timeslice is apparent at the edge of the Arctic, specifically in the Barents and the Bering Sea. This aligns with the temperature anomalies in Figure 6.3, which show the largest signals in these ice loss regions. In the future experiment, the Arctic will no longer have a complete sea ice cover during winter. This simulation experiences dramatic sea ice loss, which explains the substantial temperature anomalies of over $20\,\mathrm{K}$ near the North Pole.

In summary, the present and future timeslices show significant Arctic amplification. This suggests that the simulations would include possible effects on circulation and stratospheric variability.

6.2.2 Step 5: Stratospheric warmings

The stratospheric warmings in EMAC timeslice simulations are demonstrated in Figure 6.5. The chart illustrates an increase in SSW occurrence from the preindustrial era to the present and future timeslices. This increase can be more clearly determined than that in
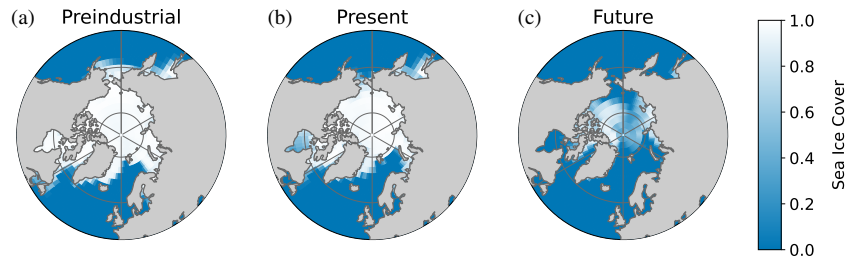
Figure 6.4: Climatological winter mean (DJF) sea ice cover in EMAC timeslice simulations. A sea ice cover of 1 indicates that the gridcell is completely covered with sea ice.

transient simulations. Furthermore, the SSW frequency per decade is depicted in Figure 6.6. There is a significant increase in the general SSW frequency, from 4.4 events per decade in preindustrial times to 7.6 events per decade in the present timeslice. This trend continues and reaches nearly 10 SSWs per decade in the future simulation. The SSW occurrence in Figure 6.5 indicates that winters without stratospheric warmings are still possible in the future, but multiple events per season are more frequent. The increase in SSW frequency is consistent across all months, with the most pronounced rise during early and midwinter.

A2b EMAC timeslice simulations confirm a statistical significant increase of the SSW frequency under the influence of climate change.

The results depicted so far align with the stratospheric pathway, indicating a distinct Arctic amplification (Step 1) and a significant increase in SSW occurrence (Step 5) in climate change experiments. The following sections will examine the steps in between, precisely the wave propagation into the stratosphere, the behaviour of tropospheric jets, and the modification of temperature gradients. This backtracking, starting from the stratospheric signal, may offer insight into the sequence of arguments within the stratospheric pathway mechanism.

Figure 6.5: Occurrence of major sudden stratospheric warmings (SSW) in the extended winter season (NDJFM) in EMAC timeslice simulations. Events are classified after the WMO classification and the occurrence is illustrated as the number of events per season (see legend).
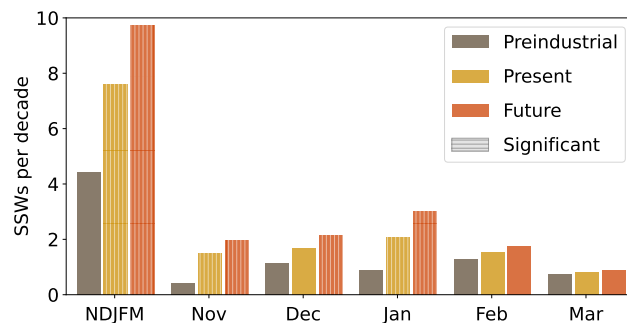
Figure 6.6: SSW frequencies per decade in EMAC timeslice simulations for the extended winter season and for every winter month. The difference was examined using the chi-squared test at a significance level of 5%. Frequencies that are significantly different from the respective preindustrial frequencies are marked with striped bars.

6.2.3 Step 4: Planetary wave propagation

Disturbances in the stratospheric polar vortex are induced by planetary waves propagating from the troposphere into the middle atmosphere. This section aims to answer the following questions:

Q3 Are stratospheric circulation anomalies induced by an enhanced planetary wave input from the troposphere.

EP flux

The evaluation of the EP flux is a common approach for studying atmospheric wave propagation (details see Section 5.3.1). The winter EP flux is illustrated in Figure 6.7a for preindustrial conditions. In the climatological mean, the arrows are upward in the stratosphere, indicating that the waves propagate from the troposphere into the stratosphere and finally break in this layer. The wave breaking manifests as a negative divergence of the EP flux shown in grey. A negative divergence is associated with the deceleration of the polar night jet, which is typically observed before stratospheric warmings. The path of the waves in the climatological mean is as follows:

- Tropospheric waves reaching the upper troposphere are either reflected towards the equator or propagate further up into the stratosphere.

- The input of tropospheric waves into the stratosphere occurs mainly between 45°N and 70°N.

- In the upper stratosphere, the EP flux vectors become larger because the wave amplitudes grow as a result of the decrease in air density.

The vertical component of the EP flux at 100 hPa is commonly used as a metric to specify the tropospheric wave input, typically between 45°N and 75°N. By examining Figure 6.7a,
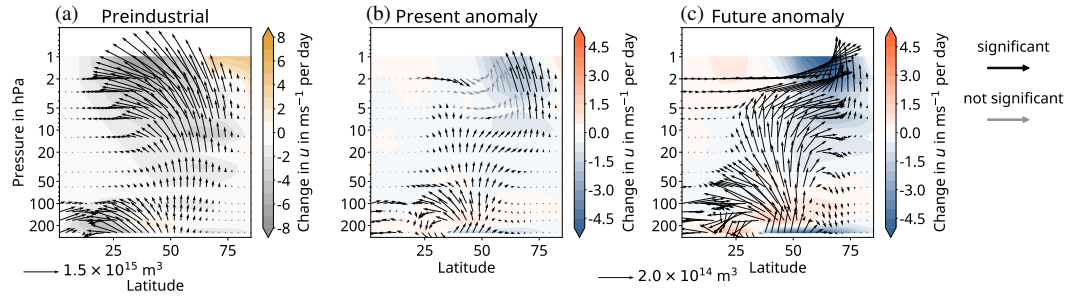
Figure 6.7: Climatological EP flux in the stratosphere in winter (DJF) for the preindustrial run in (a). The EP flux is depicted as a vector, and the divergence of the EP flux as coloured shades with units of $m\,s^{-1}$ per day. The EP vectors are scaled according to Jucker (2021). The anomalies of the present and future experiments with respect to the preindustrial era are shown in (b) and (c), respectively. Note that the vectors in these plots indicate the change, not the direction of wave propagation. The arrow scale is the same in (b) and (c), but different from that in (a) (see legend). Anomaly significance is indicated by the arrow colour, as shown in the legend (specified by the Mann-Whitney U test). At least one component of the EP flux needs to be significantly different to be marked with a black arrow.

this level appears adequate for capturing the upward-moving waves and avoiding the waves that reflect towards the equator.

The difference in the winter climatology of the present and future simulations in relation to the preindustrial state is depicted in (b) and (c) of Figure 6.7. Both experiments show an increase in upward wave propagation originating from the troposphere. The anomalous wave activity enters the upper layers predominantly between 40°N and 60°N. The blue areas in the plots indicate negative EP flux divergence anomalies, revealing enhanced wave breaking. Overall, changes in EP flux quantities imply that the stratosphere is exposed to more planetary waves and enhanced wave breaking under climate change conditions. Although the scale of the anomalous vectors is one magnitude lower than that from climatology, the changes are significant, specifically in the future simulation.

A further assessment of the tropospheric wave input in $100\,hPa$ is given in Figure 6.8. The histograms illustrate the daily heat fluxes, which are the decisive factor in the vertical component of the EP flux, at each latitude between 45°N and 75°N and during winter days. A clear shift towards higher values of the heat flux is evident in comparison to the preindustrial era, accompanied by a reduction in moderate values. The shown distributions are significantly different from each other, given the large sample size of nearly $150\,000$. The results confirm the findings highlighted by the EP flux anomalies in Figure 6.7 and suggest an increase in tropospheric waves entering the stratosphere. This aligns with the enhanced occurrence of SSWs, and the answer to the questions raised before is:

A3 The planetary wave activity is enhanced in present and future experiments, resulting in increased wave breaking in the upper stratosphere.
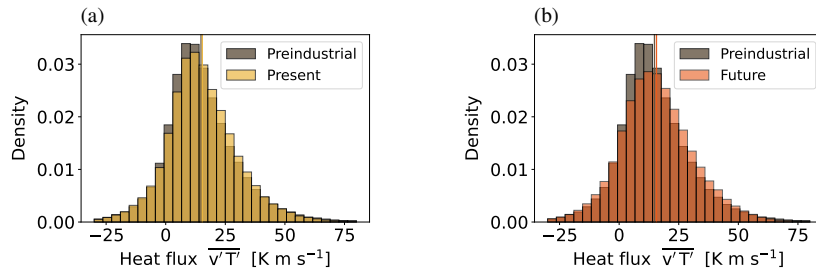
Figure 6.8: Histogram of daily heat flux in $100\,\text{hPa}$ for latitudes between 45°N and 75°N during winter days. Seasonal or spatial averaging was not performed. Each winter day and latitude was individually considered. The mean is indicated by a vertical line in the respective timeslice colour. The preindustrial distribution is identical in both figures and is compared to present and future, respectively. The shown distributions in (a) and (b) are statistically significant to each other, as determined by a Student's t-test with a significance level of 5%.

Vertical wave events

The EP flux diagnosis provides valuable insights into the change in wave activity. However, as discussed in Section 5.3.2, information on the location of these changes is restricted to latitude and altitude. To further evaluate the longitudinal dependence of the anomalies, the 3D Plumb flux is used in addition to answering the following question:

Q3b Where is the origin of the anomalous planetary waves?

The event-based assessment of vertical wave propagation is introduced in Section 5.3.3 and is referred to as a vertical wave event, in short VWE. These events are characterised by strong upward wave propagation, and the evaluation of their occurrence provides a more detailed view of the changes on the local scale. The spatial distribution of the frequency of these events is demonstrated in Figure 6.9, shown as winter climatology. The interpretation of these VWE frequencies is similar to that of other extreme weather metrics, such as blocking or cold air outbreak frequencies. The planetary waves entering the stratosphere originate from a midlatitude ring with the highest occurrence over Far East Russia in the preindustrial simulation. In the present and future simulations, a clear shift towards the Pacific region is evident. In general, an overall frequency increase is apparent in both climate change experiments, while a second but weaker centre of enhanced wave input forms over the North Atlantic and Europe.

The anomalies in the VWE frequency are demonstrated in Figure 6.10, where the findings of the previous illustration can be confirmed.

A3b The results indicate a distinct eastward shift in the location of wave activity over the Pacific and a general increase in frequency over Europe.

Furthermore, these changes are determined to be statistically significant.

An advantage of the event-based evaluation of the vertical wave flux is the assessment of the additional variables mean area, duration, intensity, and the number of events per winter
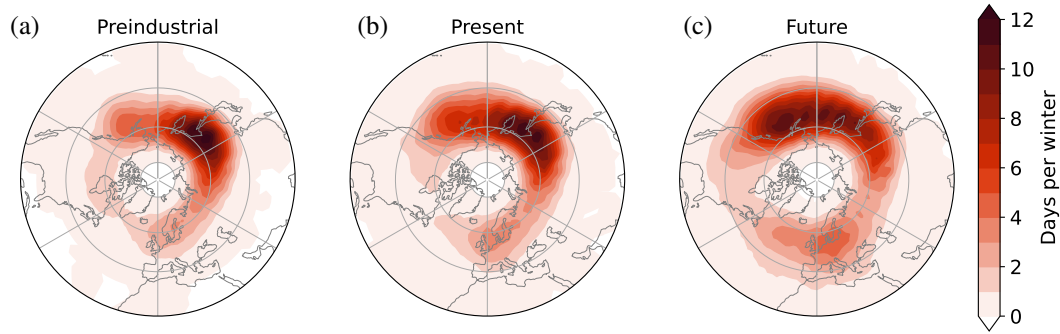
Figure 6.9: Climatological winter (DJF) frequency of vertical wave events in days per winter. A value of five days per winter indicates that, on average, five days out of the 90-day long winter season were classified as VWE at a specific gridpoint. The averages were based on 149 winters at the respective timeslice.
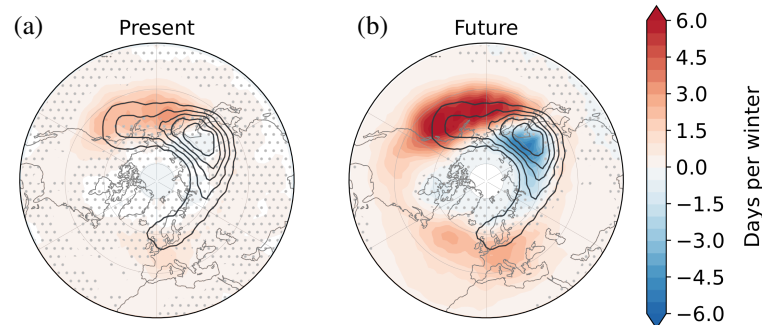
Figure 6.10: Anomalies in the winter frequency of vertical wave events with respect to the preindustrial simulation (depicted as black contours with a contour interval of 2 days). Significance is determined using the chi-squared test at a significance level of 5%. All grid points showing insignificant anomalies are hatched.

(specified in Section 5.3.3). Figure 6.11 indicates that the mean area and duration of the VWEs slightly decrease. This implies that the enhanced wave activity does not stem from events that are spatially larger or last longer. On the other hand, the mean intensity of VWEs exhibits a small rise and the most pronounced change manifests in higher numbers of VWEs per winter. The average number of events doubles from six events per winter in the preindustrial era to 12.7 events in the future timeslice. The positioning of the boxplots in Figure 6.11d suggests a significant difference.

A higher number of wave input events can substantially disturb stratospheric circulation. It is established that SSWs are induced by multiple consecutive wave forcings, also known as preconditioning. Recurring wave breaking at the polar vortex edge leads to successive weakening and can ultimately result in a breakdown of the vortex. Overall, the findings of a general increase in upward wave propagation can be complemented by:
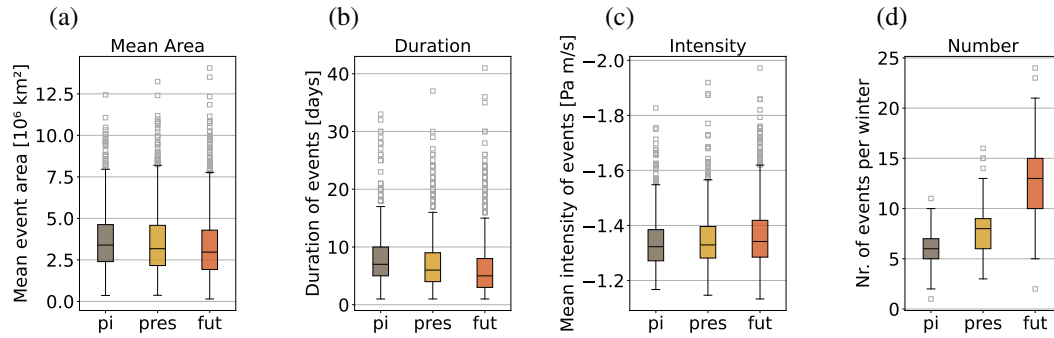
Figure 6.11: Vertical wave event metrics for EMAC timeslice simulations including the mean area, duration, and intensity of VWEs as well as the number of VWEs per winter. A detailed specification of the variables is provided in Section 5.3.3.

A3b An increased frequency of upward propagating wave events has the potential to effectively disturb the stratospheric polar vortex.

The results presented in this section provide a more detailed view of how atmospheric waves change under the influence of global warming. Therefore, the modifications associated with Step 4 of the stratospheric pathway could be confirmed in EMAC model simulations. The next step following the pathway mechanism is Step 3 – the meandering of the polar jet stream.

6.2.4 Step 3: Jet stream

The polar jet stream can be considered as the connecting link between the temperature gradients and planetary waves. It owes its existence to the baroclinic instability in midlatitudes, as outlined in Section 2.2.4. Following the argumentation line of the stratospheric pathway, a weaker temperature gradient between the pole and midlatitudes leads to weaker winds and jet streams, due to the thermal wind relation. Hence, weaker winds in the jet cores could result in greater meandering of the jet.

Subtropical and polar jets are often illustrated from a simplified perspective as two circumpolar high-speed wind bands, as shown in (a) and (b) of Figure 6.12. These illustrations suggest that the polar jet is a continuous band of strong winds around the globe. Although partially correct for the subtropical jet, this does not apply to the polar jet. As shown in (c) to (e), three daily examples of winter days in EMAC simulations suggest a more nuanced perspective. For instance, polar jets display pronounced loops, sometimes only short segments of high wind bands, or they can be absent in larger regions. It becomes evident that assessing the polar jet using seasonal or zonal averages of the wind does not accurately reflect its dynamical behaviour.

Therefore, the jet axes, or jet cores, are determined by the jet detection algorithm described in Section 5.2.1. The precise locations of the wind maxima are illustrated in Figure 6.12 by black lines. The jet axis distributions were determined for all EMAC timeslice simulations
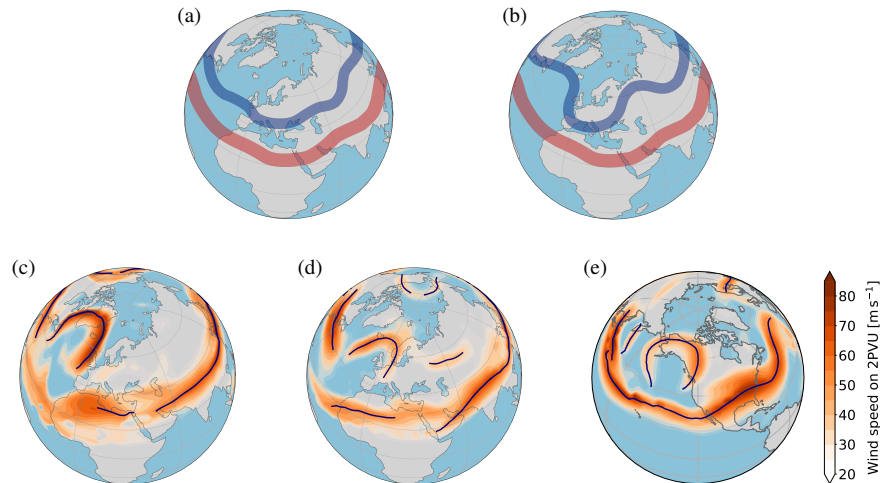
Figure 6.12: Simplified jet illustrations in (a) and (b) are compared to realistic conditions in (c) to (e) in EMAC simulations. In (a) and (b), the subtropical jets are shown as red wind bands and the polar jets as blue wind bands. The second row illustrates wind speed on the 2 PVU level for three specific winter days with jet axes determined by a jet detection algorithm and marked by black lines.

on a daily basis, which can be further evaluated as winter climatologies. One main focus of recent research on jet stream behaviour is the possible shift in jets due to global warming. Hence, before discussing the waviness of the polar jet, a closer look at the climatological jet positions in EMAC timeslice simulations is outlined in the following section.

Changes in jet positions

Figure 6.13 demonstrates the winter climatology of the jet axes. The jet axis distributions are shown as climatological maps to obtain an impression of the magnitude of the changes. The variable *jet axis distribution* indicates the length of the jet path passing through a grid cell. Although not in the same unit, a higher value suggests a greater occurrence or frequency at that grid point. By examining the general location of the jets, the spiral shape stands out. The subtropical jet mainly determines this feature. Further, the ring of strong jet occurrences around the globe exhibits a discontinuity over the Eastern Pacific in the preindustrial era. This interruption appears to become 'closed' in climate change experiments. In essence, subtropical jets become more frequent under the influence of climate change, particularly in the western hemisphere. In contrast to subtropical jets, polar jets lack a uniform ring structure. Instead, polar jets occur more frequently in the western hemisphere in regions where subtropical jets are weak.

The changes can be evaluated more precisely by examining the anomalies for the climate change experiments, as depicted in Figure 6.14. The general impression of an increase in subtropical jet occurrence is confirmed by the significant positive anomalies in (b) and (e). In summary, the main signals of the subtropical jet are:
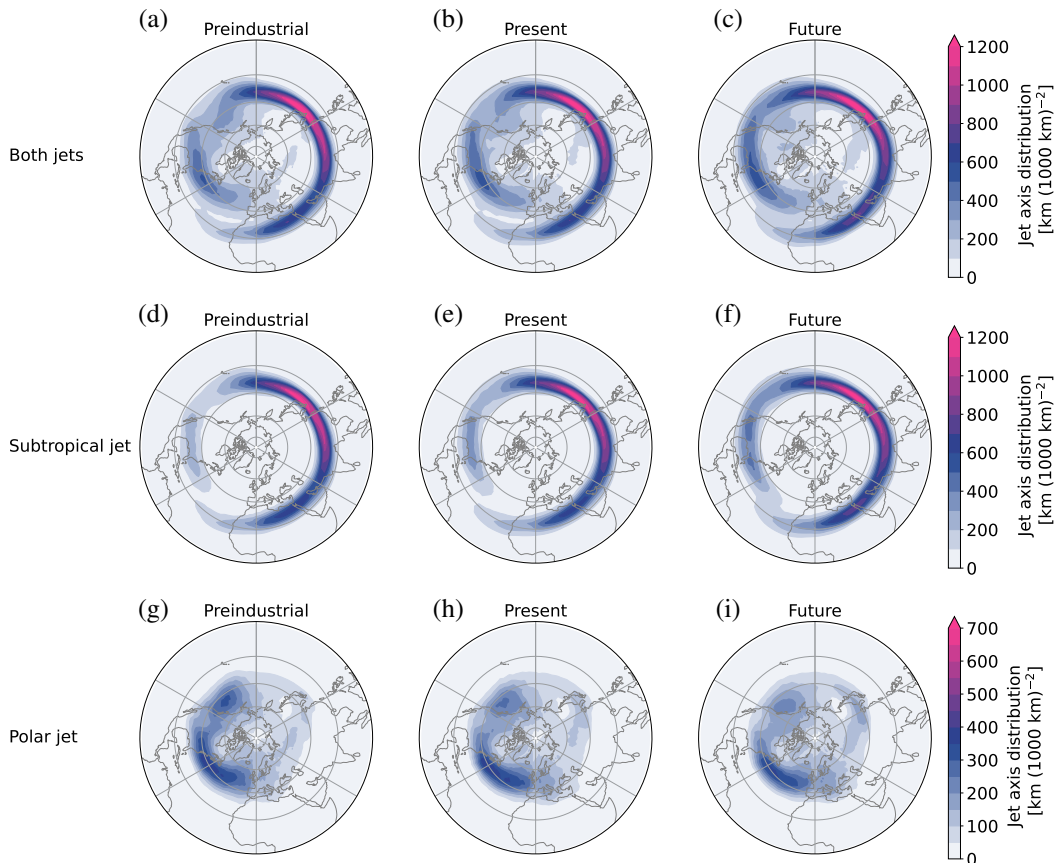
Figure 6.13: Climatological jet axis distribution depicted as winter (DJF) mean in EMAC timeslice simulations. The jet axis distributions for both jet streams are shown in the first row of the subplots. Subtropical and polar jets are separately shown in the second and third rows, respectively. Note that the polar jet has a different colour bar due to its less frequent occurence in general.

- Increased frequency of subtropical jets over the Eastern Pacific and North America, two regions with a lower jet occurence in the past.

- Regional shifts:

  - Equatorward displacement over North Africa and China.

  - Slight poleward shift over the Western Pacific.

The impact of global warming on jet stream location is a widely discussed topic. The shifts in the jets are typically specified as changes in latitude per decade. Zonal mean winds are commonly employed to classify jet locations. For example, Woollings et al. (2023) reported a poleward shift of the subtropical jet in ERA5 and historical CMIP6 simulations based on zonal-mean zonal winds in the entire troposphere. However, no evidence of a poleward shift of the subtropical jet was revealed by Maher et al. (2020) under consideration of tropical expansion and a more sophisticated method using meridional gradients of potential tem-
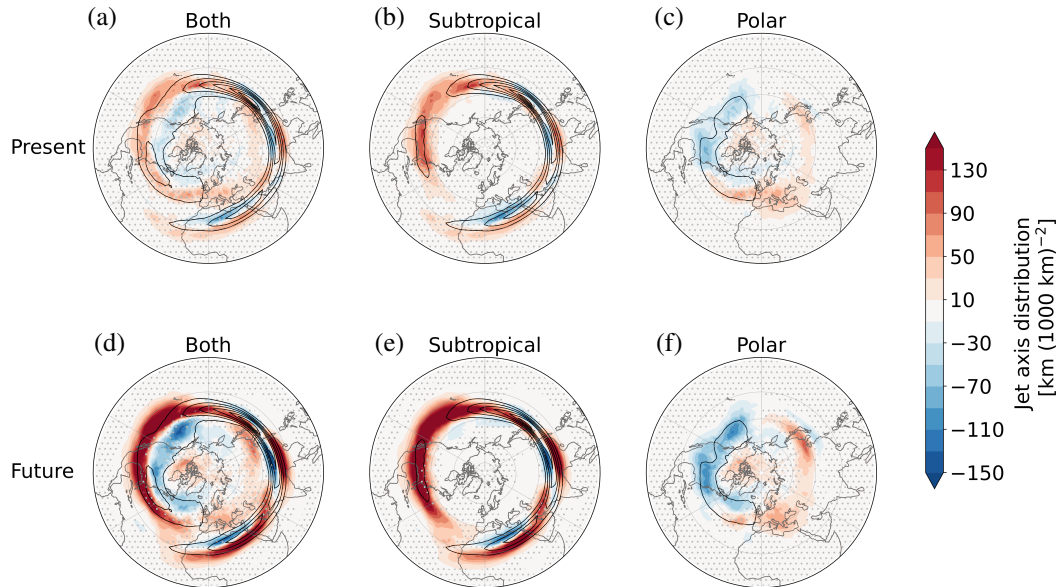
Figure 6.14: Anomalies of winter (DJF) climatological jet axis distribution with respect to preindustrial values (depicted with black contours). Non-significant anomalies are marked with hatchings (specified by a Mann-Whitney U test).

perature at the 2 PVU surface. By analysing the anomalies of the subtropical jet in EMAC depicted in Figure 6.14, it becomes evident that the shifts are regional phenomena. When considering in the zonal mean, the negative anomalies over North Africa and China are masked by strong positive anomalies over the Pacific at the same latitude. Additionally, the spiral shape of the jet complicates the evaluation of zonal mean wind. Although the subtropical jet exhibits a well-defined structure and displays some regional shifts, it is advisable to approach zonal mean variables with caution.

The changes in the polar jet are depicted in (c) and (f) of Figure 6.14. A significant reduction occures over the Eastern Pacific and North America, which are regions associated with a strengthening of the subtropical jet. In contrast, an increase in the occurrence of polar jets is apparent over Europe and Asia. In this regard, referring to shifts in the polar jet may not be the correct term, as there is no preferred latitudinal location in general. An exception is the Atlantic region where polar jets are typically dominant. An equatorward shift is evident in both climate change experiments, although the signals are not consistently significant. These results align with the findings in Screen et al. (2022) who found an equatorward shift of the polar jet in response to sea-ice decline in PAMIP simulations.

The results of EMAC simulations suggest that polar jets will occur more often in the eastern hemisphere and are significantly reduced in the western hemisphere. Interestingly, polar jets are reduced in regions with increasing subtropical jets and vice versa. Hence, this may indicate a coupling of the jets. Investigating the processes leading to changes and shifts in jet location is beyond the scope of this study. In the subsequent section, anomalies in
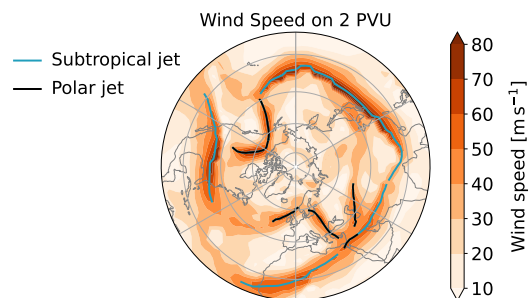
Figure 6.15: Example of jet axes on a specific date showing separated jets.

Simulation	No. of grid points
Preindustrial	1,270,499
Present	1,254,260
Future	1,225,586

Table 6.1: Grid points with polar jets in winter.

the polar jet are evaluated, focussing on their strength and meandering. However, it is not possible to make any statements about jet waviness based solely on the jet axis distribution discussed in this section.

Polar jet – Strength and orientation

In the argumentation line of the stratospheric pathway, a reduced meridional temperature gradient between the pole and midlatitudes is related to weaker and wavier polar jets. After precisely defining the polar jets in the daily data, it is possible to evaluate the wind speed and waviness in a simple manner. Therefore, all grid points with a detected polar jet were assessed in terms of their wind speed U and the zonal and meridional wind components u and v, respectively. An increase in the waviness of the polar jet would manifest as a more pronounced meridional wind. The following section will address the question:

Q4 Are tropospheric jet streams becoming weaker and more meandering?

Figure 6.15 shows the upper tropospheric wind and all detected jet axes for an example date. The detected polar jets are marked by black lines in the plot. For further evaluation, all grid points with polar jets were collected on a daily basis. By assessing all winter days in each timeslice, a large number of grid points can be evaluated, as indicated in Table 6.1.

Figure 6.16 depicts histograms of the wind variables at the polar jet grid points. A general weakening of the polar jet is not evident, as demonstrated by the wind speed U shown in (a) and (d). Weaker polar jets would manifest as a shift in the distribution towards lower wind speeds. Instead, a slight widening of the distribution is evident, indicating a more variable jet core wind speed. However, it should be noted that the changes in wind speed are marginal. The same holds for the zonal wind component u as depicted in (b) and (e), with minor changes and a slight increase in variability.

The meridional wind components v depicted in (c) and (f) indicate the waviness. The bimodal distribution suggests that the polar jet has a meandering nature. Positive or negative values are more frequent than zero meridional winds. A wavier jet would result in higher peaks in the distribution, accompanied by a reduction in low meridional winds. Consider-
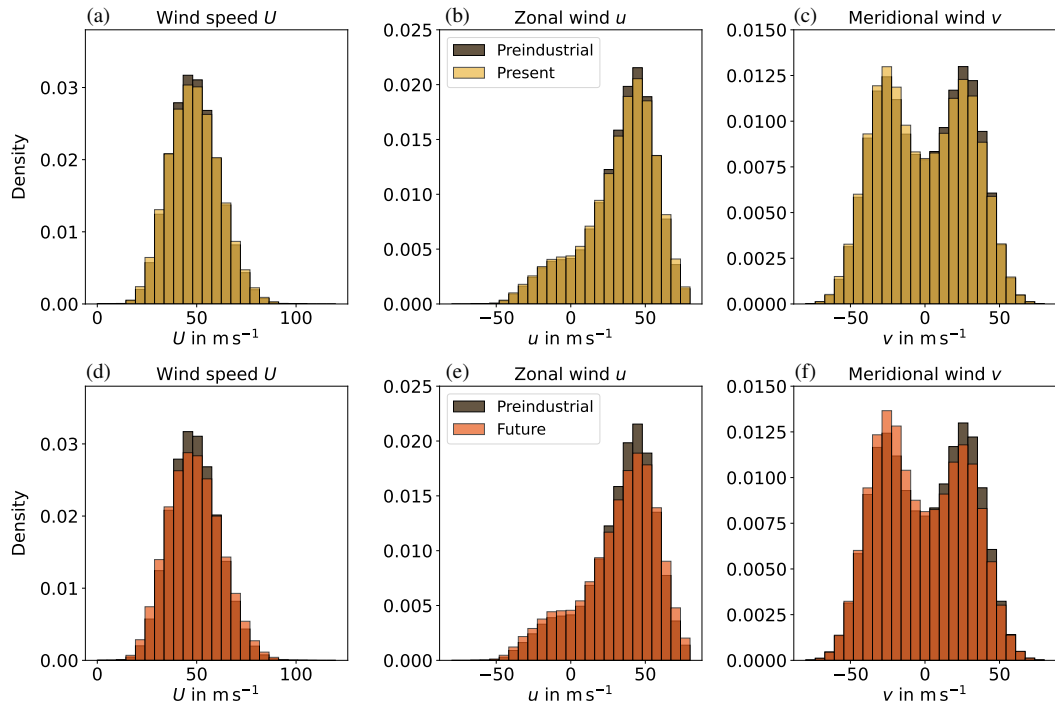
Figure 6.16: Histrograms of wind properties at grid points with a detected polar jet during winter (DJF) days. The preindustrial era is compared to the climate change experiments, respectively.
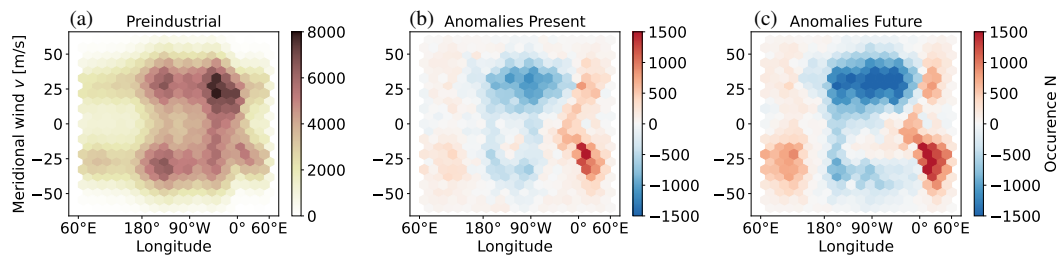
Figure 6.17: Two-dimensional histogram of the meridional wind component of all grid points with a detected polar jet, with respect to longitude. The preindustrial distribution is shown in (a). The anomalies with respect to the preindustrial simulation is indicated in (b) and (c) for present and future experiments.

East Pacific and North America (180°W − 75°W)

North Atlantic (75°W − 360°W)

Eurasia (0°E − 90°E)

East Asia (90°E − 180°E)
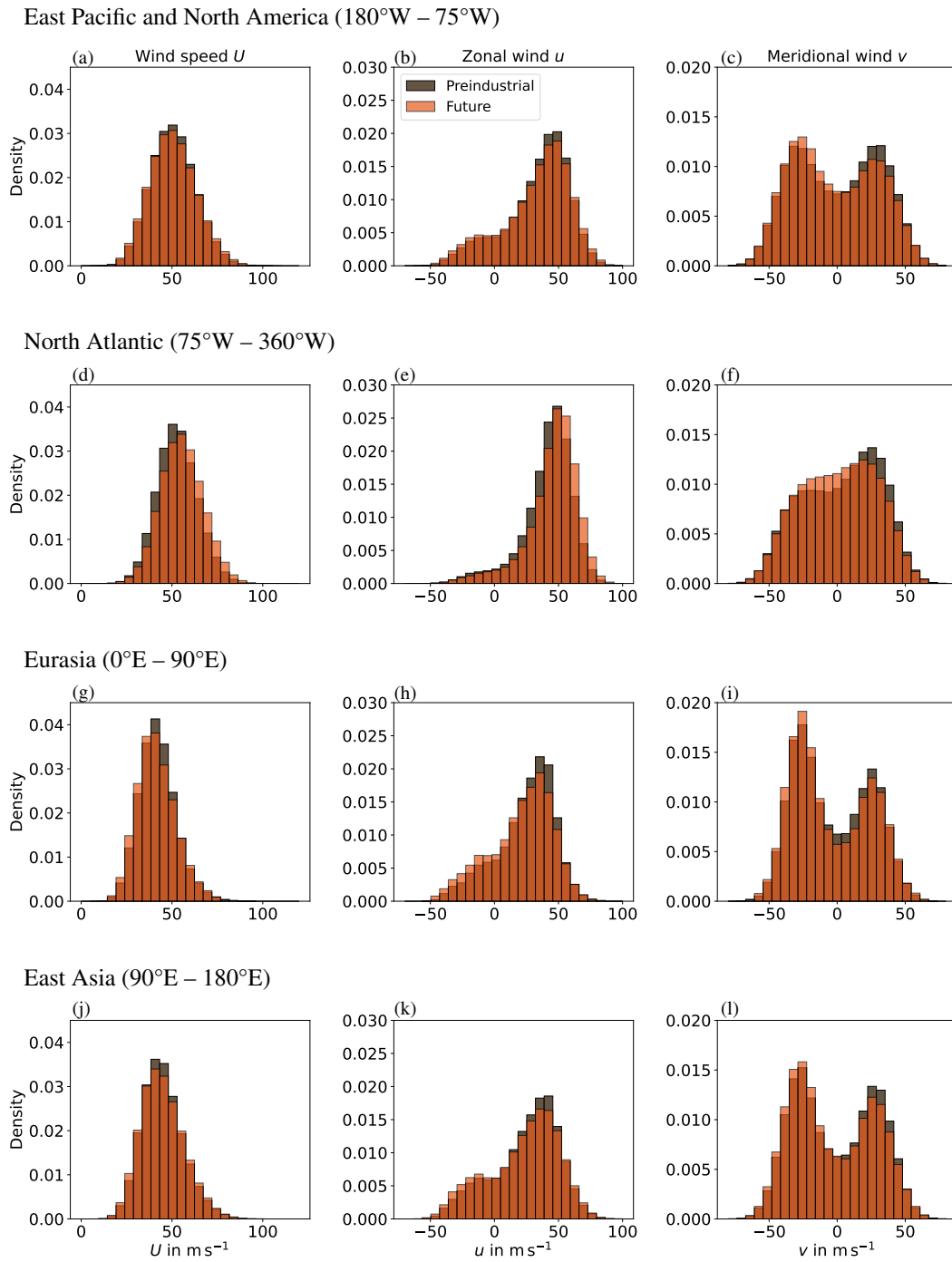
Figure 6.18: Regional histograms of wind properties at grid points with a detected polar jet during winter (DJF) days. The preindustrial era is compared to future experiment only. The corresponding regions are denoted above each row. The first column shows the wind speed U, the second column the zonal wind u and the third column the meridional wind v.

106

ing the changes in the meridional jet winds shown in Figure 6.16, a general increase in jet waviness cannot be concluded. A more frequent occurrence of southward meridional winds (negative values) occurs, but a decrease in the northward components is also apparent.

To further assess the origin of the changes in meridional winds, a two-dimensional histogram is illustrated in Figure 6.17. This 2D version of Figure 6.16 shows the frequency of the meridional wind v depending on the longitude. The preindustrial distribution is depicted in (a), indicating the preferred locations of the north- and southward-directed jets. Both hemispheres exhibit meandering polar jets. The higher numbers in the western hemisphere reflect the larger jet occurrence in this region in general. In the North Atlantic region, a peak in the northward-directed jet is detected.

The anomalies for climate change timeslices reveal the hemispheric differences previously described by the jet axis distribution and depicted in Figure 6.14. The occurrence of the polar jet is reduced in the western hemisphere indicated by the blue areas in Figure 6.17, and the jet frequency increases in the eastern hemisphere (red signal). More specifically, the largest decreasing signal emerges for the northward-directed jets in the western hemisphere. In contrast, a higher occurrence of southward-directed polar jets emerge in Europe. Since Figure 6.17 presents an absolute frequency, it is not feasible to access the alteration of waviness, irrespective of the change in occurrence. Therefore, the histograms for the wind components are divided into different regions of interest in Figure 6.18. These density histograms enable a better assessment of relative changes.

Despite a significant decrease in the overall occurrence in the East Pacific and North American regions, the nature of the polar jets remains alike as shown in (a). Wind speed and zonal wind show only minor changes. However, the negative peak of meridional winds increases at the expense of the positive peak, which was already apparent in the histogram of the entire northern hemisphere (Figure 6.16f). The polar jets in the North Atlantic exhibits a distinct shift towards higher wind speeds and higher zonal winds. The waviness decreases in this region, although there is a slight increase in negative meridional winds as well. Conversely, the jets over Eurasia show weaker winds and, once more, an increase in southward-directed jets. The wind distributions over East Asia exhibit the same signal as over Eurasia, although with a lower magnitude. Thus, a general tendency toward weaker jets can not be established. Only the results for the Eurasian regions suggest weaker polar jets. Furthermore, an enhanced waviness is not evident in general, but all regions exhibit a shift towards southward directed polar jets. This does not indicate a general trend towards more frequent northerlies, but rather suggests that there is an increase in the detection of jets within this range. The answer to the question posed at the beginning of this sections is:

A4 The eastern hemisphere shows an increased polar jet occurrence associated with weaker wind speeds and more southward directed jets. Nevertheless, EMAC simulations do not indicate a general weakening and enhanced meandering of the polar jet.

Summary

Before assessing the next step, the results are recapitulated and interpreted in the context of planetary wave modifications found in Section 6.2.3. The jet streams in the northern hemisphere show complex variations in response to climate change. EMAC simulations do not yield a general indication that the polar jet becomes weaker and more meandering. However, a significant alteration of the jet occurrence was discernable. The western hemisphere is characterised by less polar jets, as indicated by the jet axis distribution in Figure 6.14. Moreover, these jets become slightly more southward-oriented, as discussed in the previous section. Concurrently, the statospheric wave input exhibited a shift in the Pacific region, with positive anomalies in the Eastern Pacific (Figure 6.10). At first glance, this appears contradictory: fewer polar jets occur, but more wave activity reaches the lower stratosphere. There are some possible explanations for this finding:

- The subtropical jet has an influence on the upward planetary wave propagation. This occurrence is enhanced in the relevant region.

- There are polar jets below the detection range of the jet algorithm.

This study does not provide further analysis of these points, which should be addressed in future research.

By contrast, the eastern hemisphere shows a higher occurrence of polar jets in the future simulation, and these jets are slower and wavier. In this case, the results are consistent with the changes in wave propagation. Vertical wave input into the stratosphere was enhanced, particularly over Europe (Figure 6.10). Even if the positive anomalies are weaker over Europe than over the Pacific, these wave modifications could have a significant influence on the stratospheric polar vortex.

An alternative monitoring approach for SSW events was discussed in Li et al. (2023). They employed local warming instead of the widely used zonal mean wind and temperature to identify SSW events. In this manner, the location of the SSW onset was determined during the observational period. The location of the prominent warming is associated with wave breaking and consequently indicates the approximate location of the wave origin. Li et al. (2023) reported that three-quarters of the onset locations of SSWs are located over northern Eurasia (shown in their Figure 10d). These findings suggest that the increase in vertical wave events over Europe and the Atlantic in the EMAC results has the potential to significantly disturb the polar vortex.

6.2.5 Step 2: Temperature gradient

The connecting step between the jet stream and Arctic amplification is the modification of the horizontal temperature gradient and the effect of the thermal wind relation. The formation of polar or eddy-driven jets is attributed to synoptic baroclinic waves, which result from baroclinic instability. The change of baroclinic instability is investigated in EMAC simulations regarding the question:
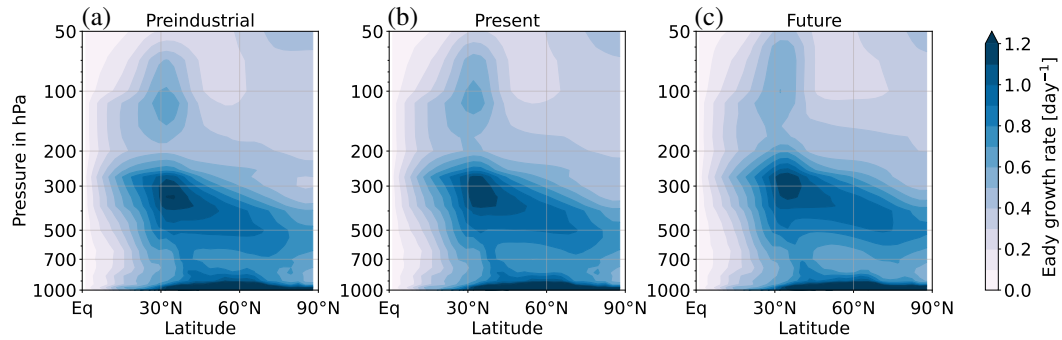
Figure 6.19: Winter (DJF) climatology of the zonal mean Eady growth rate (EGR) for EMAC timeslice simulations.
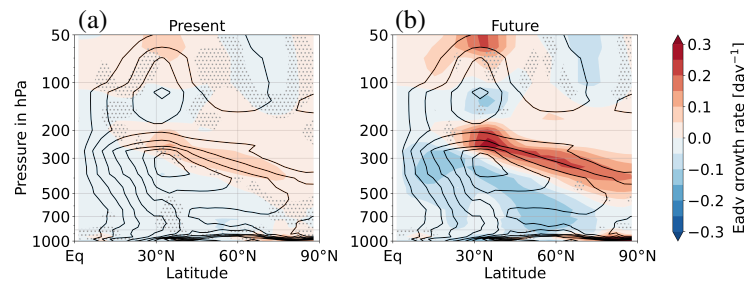
Figure 6.20: Anomalies of the winter (DJF) climatological zonal mean Eady growth rate (EGR) for EMAC timeslice simulations. Non-significant anomalies are marked with hatchings (specified by a Student's t-test and a significance level of 5%).

Q5 How is the relationship between horizontal temperature gradients and tropospheric wave generation?

The Eady growth rate (EGR) is a measure of the baroclinic instability, as introduced in Section 2.2.4 and Section 5.1. Figure 6.19 shows the winter climatology of the Eady growth rate depicted as zonal mean in EMAC timeslice simulations. The maximum EGR is situated in the upper troposphere between the subtropics and the pole. EGR changes in the timeslice experiments are small but significant, as shown in Figure 6.20. The area of high EGR values shifts upward in climate change experiments, with negative anomalies in the middle troposphere and positive anomalies in the upper troposphere.

To complete the picture of zonal mean changes, the EGR anomalies in the upper and middle troposphere are illustrated in Figure 6.21. The negative EGR anomalies in the middle to lower troposphere, as depicted in (e) and (f), are prominent over the ocean basins and Canada. Siberia exhibits negative anomalies, but this region is less affected by a decrease in baroclinicity. However, upper tropospheric changes indicate a rise in baroclinicity over most continents.

The Eady growth rate is composed of two variables, the vertical shear of the horizontal wind
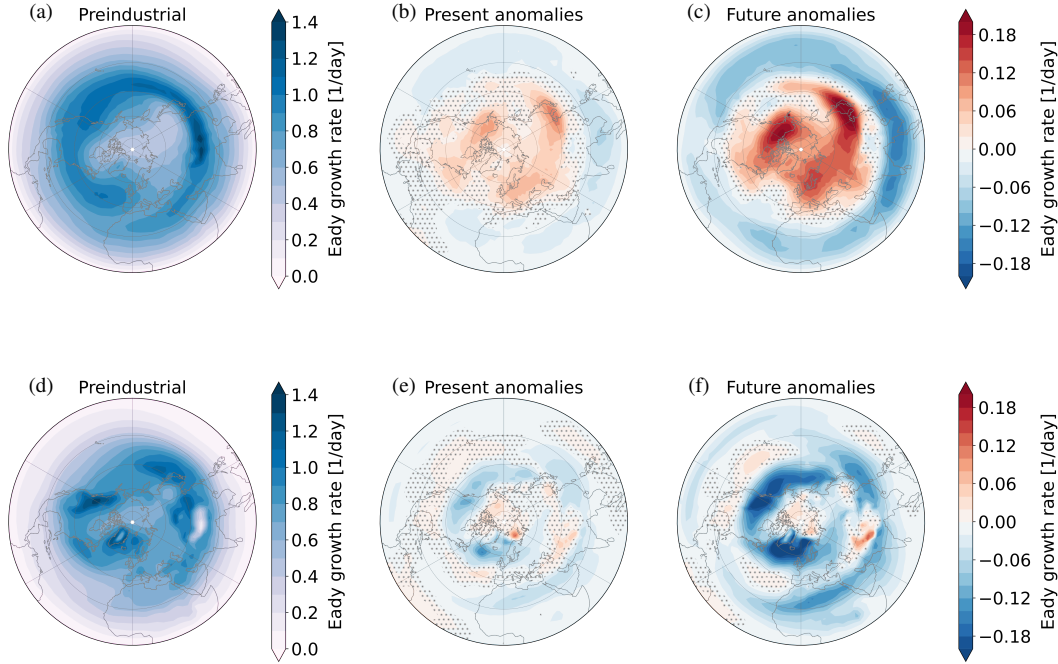
Figure 6.21: Winter (DJF) climatology of the Eady growth rate during the preindustrial era (a) and anomalies for the present (b) and future timeslice (c) averaged from 400hPa to 200hPa. Analogously, the averages from 850hPa to 500hPa are shown in (d) to (f). Significance for the EGR anomalies is determined using a Student's t-test with a 5% significance level, and non-significant anomalies are indicated with hatches.

and the Brunt-Väisälä frequency N

$$\sigma_{max} = 0.31 \frac{f}{N} \cdot \left| \frac{\partial \mathbf{v}_h}{\partial z} \right|.$$

Furthermore, the thermal wind relation links the wind shear and horizontal temperature gradients. Thus, a change in EGR could originate from a modification of the wind shear or changes in static stability. Figure 6.22 presents the EGR anomalies, together with the changes in static stability and thermal wind. The weakening of the horizontal temperature gradients is prominent in midlatitudes and lower troposphere. The anomalies are consistent with negative wind shear, and the results suggest that the reduced baroclinicity in the lower troposphere originates from weakened temperature gradients. Conversely, the increase in EGR in the upper troposphere coincides with a positive anomalies of the temperature gradient in subtropics and a decrease in the Brunt-Väisälä frequency N in midlatitudes. These results provide a more nuanced picture of the changes in EGR. They stem from both the temperature gradient and static stability. The modification of the subtropical temperature gradients between $200\,hPa$ and $300\,hPa$ can be attributed to the upper-tropospheric tropical warming. This warming is 'in competition' with Arctic warming regarding its influence on midlatitude circulation, which is also referred to as the *tug-of-war*. It should be mentioned
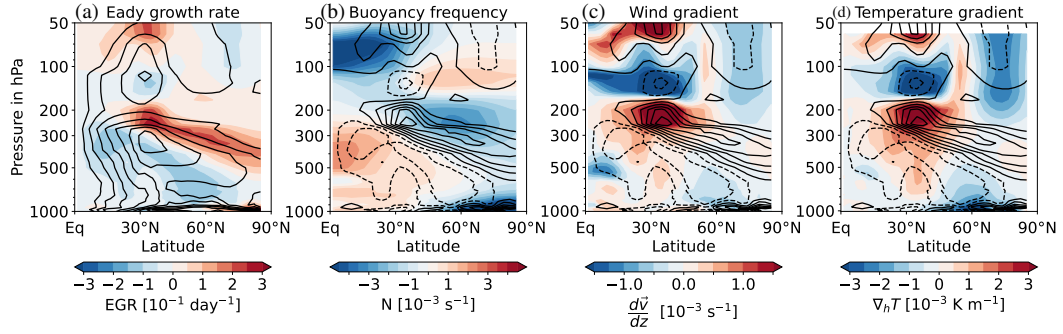
Figure 6.22: Changes of the winter (DJF) zonal mean Eady growth rate, buoyancy frequency, vertical shear of the horizontal wind, and horizontal temperature gradient for the future experiment. The preindustrial EGR is depicted as black contours in (a), and future anomalies as shading. In contrast, in (b)–(d), the EGR future anomalies are marked as black contours for comparison with the respective variable.
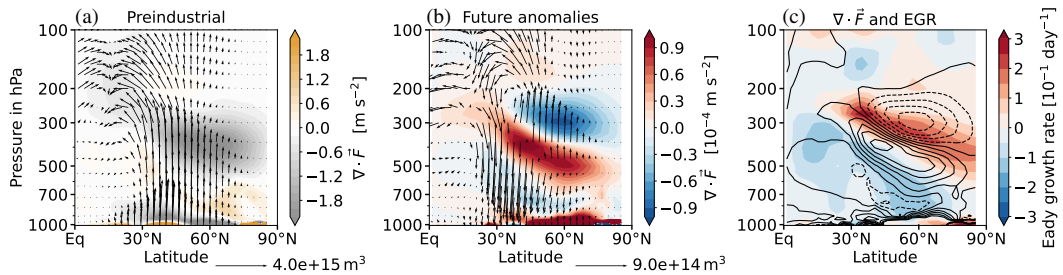
Figure 6.23: Winter (DJF) climatologies of EP flux and its divergence shown for the preindustrial timeslice in (a). The anomalies in the future timeslice with respect to the preindustrial era are indicated in (b). A comparison between the future anomalous EP flux divergence (black contours) and anomalies in the Eady growth rate is illustrated in (c). The contour interval for $\nabla \cdot \vec{F}$ is $0.2 \cdot 10^{-4} \, \mathrm{m \, s^{-2}}$.

that the EGR is assessed in a simple evaluation of climatological winter means, and a more comprehensive analysis of baroclinic instability is needed to dive deeper into the topic.

To conclude this analysis, the changes in EGR are compared to the EP flux in the troposphere, as depicted in Figure 6.23. The climatological winter (DJF) mean of the EP flux and its divergence are shown in (a), representing the tropospheric version of Figure 6.7a. On average, tropospheric waves propagate upward in the troposphere. In this layer, the divergence of the EP flux can also be indicative of a planetary wave source. An area of high convergence is displayed in the upper troposphere (500 hPa to 300 hPa) depicted with grey colours. The future anomalies in (b) provide the following outcomes:

1. Weaker upward wave propagation on average in the lower troposphere as illustrated with downward pointing arrows. Compared with the EGR anomalies in (c), this coincides with the lower baroclinicity in this region. The combination of both signals indicates less wave generation in the lower troposphere.

2. Increased upward wave propagation in the upper troposphere. The lower edge of the area marked by negative anomalies of EP flux divergence coincides with a higher baroclinicity, as shown in Figure 6.23c. Some anomalous planetary waves reach the lower stratosphere at 100 hPa and propagate further into the middle atmosphere, as discussed in the previous sections.

3. The anomalous upward wave propagation in 200 hPa to 100 hPa and between 40°N and 50°N is located above a region with enhanced baroclinicity. According to (b) and (c) in Figure 6.22, the signal in this region arises from the combination of two aspects. First, the alteration of the meridional temperature gradients induced by the upper-tropospheric tropical warming is located below the anomalous wave propagation. This warming is the counterpart of Arctic amplification in the tug-of-war paradigm. On the other hand, the reduction of the static stabilty is also apparent in this upper-tropospheric region.

Upward shift through thermal expansion

Some of the previously presented results exhibit a shift in the signal towards higher altitudes or lower pressure levels. An upward shift in atmospheric structures can occur as a consequence of thermal expansion induced by global warming. Nevertheless, the recently discussed findings suggest an alteration beyond a simple shift. Specifically, the positive EGR anomalies in Figure 6.22a are larger at the top edge than changes at lower layers which indicates some additional changes. A similar upward shift emerges in the anomalies of EP flux divergence in Figure 6.23b. However, the changes in the EP flux vectors are not confined to this region, suggesting a more general change in wave flux.

Discussion

To a certain extent, these findings agree with Steps 2 and 3 of the stratospheric pathway. A distinct weakening of the horizontal temperature gradients in the lower troposphere reduces the baroclinic instability and, consequently, the wave generation in the lower layers. In turn, fewer baroclinic waves lead to a reduced wave flux convergence in the middle troposphere (depicted as red-coloured areas in Figure 6.23b). Theoretically, this implies decreased acceleration of the polar jet stream. Following the arguments of Francis and Vavrus (2012), a weaker zonal flow is associated with higher Rossby wave amplitudes. Indeed, enhanced wave generation can be found in the upper troposphere, which increases stratospheric wave input. On the contrary, the link to weaker winds in the jet cores could not be confirmed in EMAC simulations, as outlined in Section 6.2.4. The results in Figure 6.22b also indicate reduced static stability in areas of intensified baroclinic instability and a signal from the tropical warming at upper levels. These changes spatially agree with the upward EP flux anomalies. From the seasonal and zonal mean perspective it seems plausible that atmospheric conditions favouring wave generation and propagation emerge solely from a modification of the temperature structure in the upper troposphere. At least from the EP flux perspective in Figure 6.23b the changes appear as two separate phenomena. Whether

the Arctic amplification plays a role in the upper tropospheric signals and contributes to these changes must be addressed in further research.

A5 In conclusion, a simple connection between the horizontal temperature gradients in the lower troposphere and the wave generation could not be established. The analysis of Step 2 indicates a more complex picture of physical processes.

6.2.6 Step 6: Downward influence of stratospheric warmings

The last step in the stratospheric pathway is the downward influence of SSWs. EMAC model simulations indicated a significant increase in the frequency of SSW events under the influence of global warming. Regardless of the origin of the wave forcing discussed in the previous sections, another straightforward question is:

Q6 Are more stratospheric warmings in a warmer climate associated with more extreme cold events in midlatitudes and how severe are the SSW-induced anomalies?

Temperature distributions

The first question is not easy to answer simply by calculating CAO frequencies in the usual sense. Large temperature differences in the timeslice experiments imply the need for varying lower thresholds to classify cold events. Typically, this involves setting the threshold to the 10th percentile of the temperature distribution at each grid point. Because the statistical probability of occurrence is the basis for categorising a CAO event, a significant change in frequency using the 10th percentile in each EMAC timeslice is not expected.

In order to get an impression of the 'cold' tail of the temperature distribution, a simple evaluation of the 10th percentile values is assessed instead. Therefore, the near-surface temperatures at each grid point for winter days are normalised to the respective timeslice day-of-the-year climatological mean. Three examples of grid points are shown in Figure 6.24. The first column shows the shift of the original temperature distribution towards higher values as a consequence of global warming. The second column in Figure 6.24 shows the normalised distributions and their 10th percentiles. These percentiles are further evaluated by calculating the difference between climate change experiments and preindustrial simulation

$$\Delta T_{10th} = T_{10th}[\exp] - T_{10th}[\text{pi}].\tag{6.1}$$

An enhanced occurrence of extreme cold events would manifest as a lower 10th percentile value compared to the preindustrial simulations, regardless of general warming. This would result in a negative ΔT_{10th}. Figure 6.25 demonstrates the change in the 10th percentile values in EMAC timeslice experiments. Generally speaking, the northern hemisphere during winter exhibits a positive discrepancy, indicating that cold extremes do not occur more frequently during this season. The locations of the example distributions in Figure 6.24 were placed in areas with cooling anomalies after stratospheric warmings (see Figure 6.26).
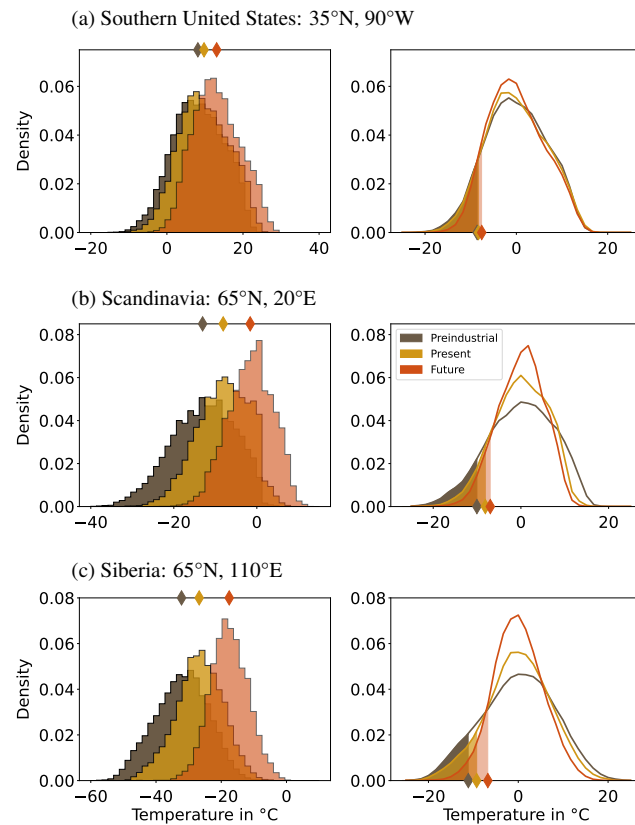
Figure 6.24: Temperature distribution at three specific grid points on winter (DJF) days. The first column shows the change in temperature. The mean values are indicated as a marker at the top. The second column depicts the normalised temperature distribution. The 10th percentile is indicated and marked at the bottom of the graph.

Despite the growing number of SSWs in the climate change experiments, there is no corresponding increase in extreme cold events. In contrast, the distributions become narrower, suggesting less variation in temperature.

A6a EMAC simulations reveal no evidence indicating a shift of the cold tail of the temperature distribution towards more cold extremes.

Impact of stratospheric variability on surface weather

Another point of interest is how stratospheric warmings in a warmer climate affect surface weather. The downward influence of SSWs can be evaluated using a composite analysis, as outlined in Section 5.4. The surface variables were averaged for a period spanning one month after the onset date of SSW events (day 30 to 60).

The composite anomalies are shown in Figure 6.26. Consistent with the composite means from observations, as depicted in Figure 2.14, pronounced cooling is evident over the Arc-
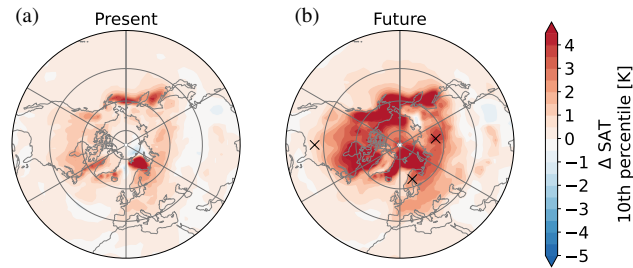
Figure 6.25: Difference of the 10th percentile of the normalised near-surface temperature distribution for winter (DJF) days. The difference is determined with respect to the preindustrial simulation. The calculation is outlined in the text and Equation 6.1. Grid points illustrated in Figure 6.24 are marked by a cross in (b).

tic and Eurasia in the preindustrial simulation shown in (a). The sea-level pressure in (d) is higher over the Arctic and lower over Europe and Asia. These pressure changes are in line with a negative AO or NAO index. Furthermore, the anomalies in precipitation are as expected in EMAC, wetter conditions in Southern Europe, and less precipitation in Greenland and Scandinavia. The majority of the mapped anomalies in the preindustrial experiment agree with the well-known patterns emerging after SSW events.

Furthermore, the climate change experiments in (b) and (c) of Figure 6.26 exhibit the same temperature pattern, albeit with a significantly reduced cooling signal over Eurasia. These outcomes imply that surface temperatures are still coupled to stratospheric circulation anomalies, but the effect of SSWs is significantly reduced. It was tested whether this signal reduction is a result of the higher number of SSWs considered in the climate change experiments. The weaker cooling is a robust signal, even when only subsets of SSWs are considered in composites of climate change experiments.

The sea level pressure anomalies depicted in (d) to (f) remain comparable, with slight variations between the experiments. Moreover, the precipitation signals shown in (g) to (i) decrease in strength in the present and future timeslice. In general, precipitation is highly variable and significant changes occur only in regions with large anomalies. The discrepancy between the temperature and pressure anomalies indicates some explanation for the reduced cooling over Eurasia. While circulation anomalies are still present after SSWs, Arctic air outbreaks are no longer severe as in the preindustrial era. The Arctic air above a closed sea ice sheet is significantly colder than over open water in the future experiment. It is plausible that Arctic amplification leads to the mitigation of cold air outbreaks in polar regions. These results are consistent with the findings of Ayarzagüena and Screen (2016) who demonstrated a reduced severity of CAOs, but no change in frequency or duration in future model simulations.

A6b The findings in EMAC simulations suggest that SSW-induced Eurasian coolings are weaker in a warmer climate and under the influence of Arctic amplification.

To conclude the evaluation of the SSW composites, the NAM index is also assessed in
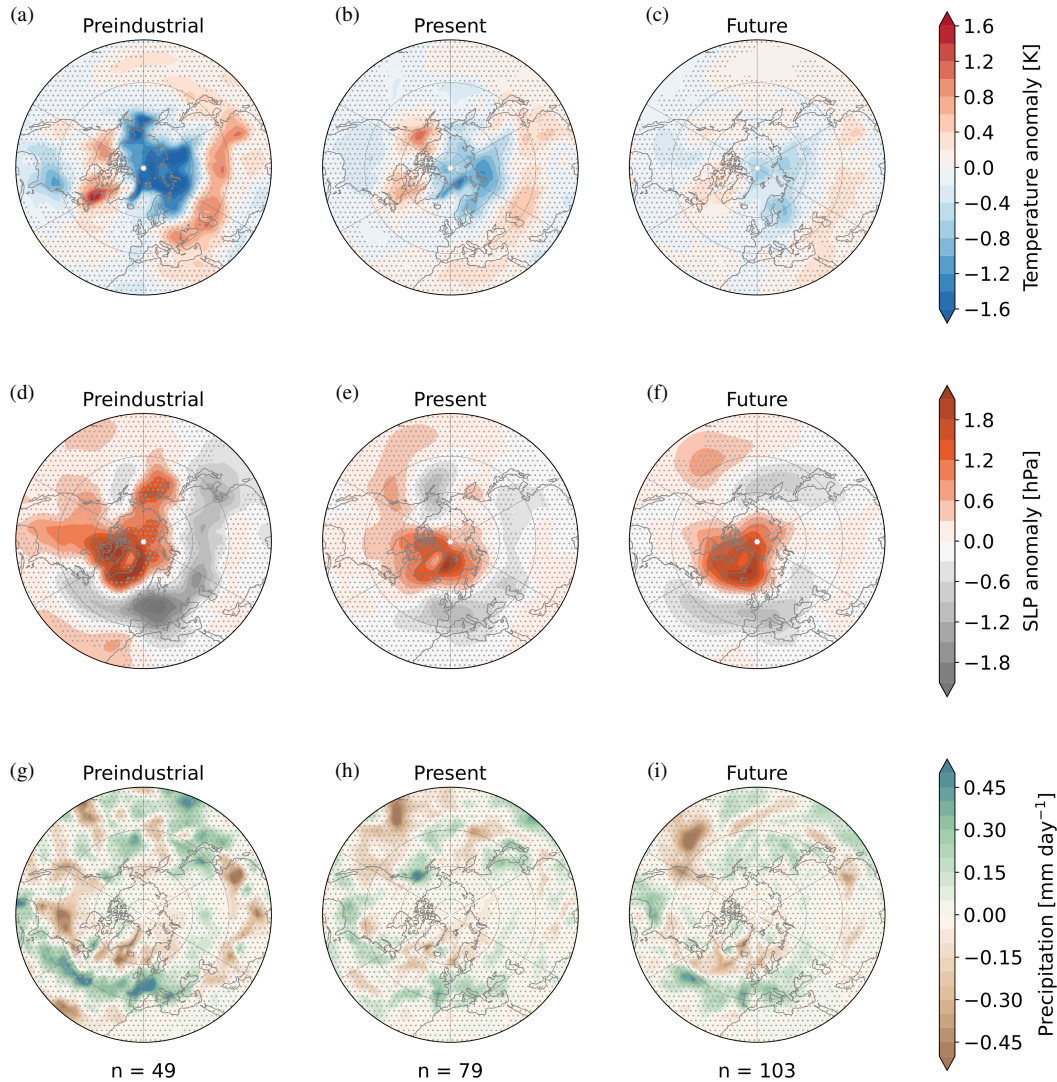
Figure 6.26: SSW composite anomalies of near-surface temperature, sea level pressure (SLP), and precipitation in EMAC timeslice simulations. Significance was determined using a Monte Carlo simulation with $N = 5000$. Non-significant anomalies are illustrated with hatchings. The total number of SSWs used for composite averaging are indicated below.

composite means. Figure 6.27 illustrates the negative NAM anomalies during stratospheric warmings. The preindustrial simulation in (a) exhibits a pronounced NAM signal. The negative NAM index corresponds to a weaker polar vortex and a higher pressure over the poles. However, the strengths of the anomalies diminish in the present and future simulations, as shown in (b) and (c).

Generally, the negative signal persists longer in the lower stratosphere than in the upper stratosphere. In the two months following the onset date, NAM anomalies can descend into the troposphere. However, this behaviour is not consistently observed across all events. The tropospheric anomalies in Figure 6.27a are small compared with stratospheric changes and are not statistically significant. The tropospheric signals are magnified in Figure 6.27b with different shading colours. This illustration demonstrates that the magnitudes of the tropospheric signals in EMAC are comparable to those in other studies, such as Oehrlein et al. (2020) and White et al. (2019). Small significant negative anomalies are evident at the surface in all experiments. These graphs are usually very noisy in the troposphere, as pointed out by Baldwin et al. (2021). The timing of the downward 'dripping' of NAM anomalies can vary considerably. The NAM index of some random single events are shown in Figure A.4 to A.6 in the appendix. The tropospheric responses exhibit highly irregular patterns. The pronounced positive and negative signals tend to cancel each other out when averaging, which results in small and insignificant outcomes. Nevertheless, some strong events or the alignment of events at a specific time lag may have resulted in the dominance of tropospheric negative anomalies in the present timeslice. Given the intermittent pattern, the more pronounced negative NAM signal in the present simulation in (b) is not interpreted as a significant enhancement of the surface impact compared to the other experiments.

Summary

In this section, more frequent stratospheric warmings in EMAC simulations are analysed with respect to their downward influence on surface weather. The occurrence of SSWs in the future simulation doubles compared with the preindustrial timeslice. In contrast, an increase in cold extreme events was not identified by evaluating temperature distributions. Furthermore, the cooling in Eurasia following SSWs is mitigated by climate change, not reaching the intensity ascertain in the preindustrial era. The findings of the EMAC simulations suggest that cold air outbreaks lose strength as a consequence of Arctic amplification.

The evaluation of the NAM index indicates a reduced signal in the stratosphere under the influence of climate change. The calculation of the NAM index includes the background condition, for example the global mean of geopotential hight. It is left for further evaluation if the presented NAM anomalies are a result of a different background state or indicate weaker circulation anomalies during stratospheric warmings. The reduced intensity could lead to weaker coupling between the stratosphere and troposphere, but further research is needed to investigate this topic in more detail.
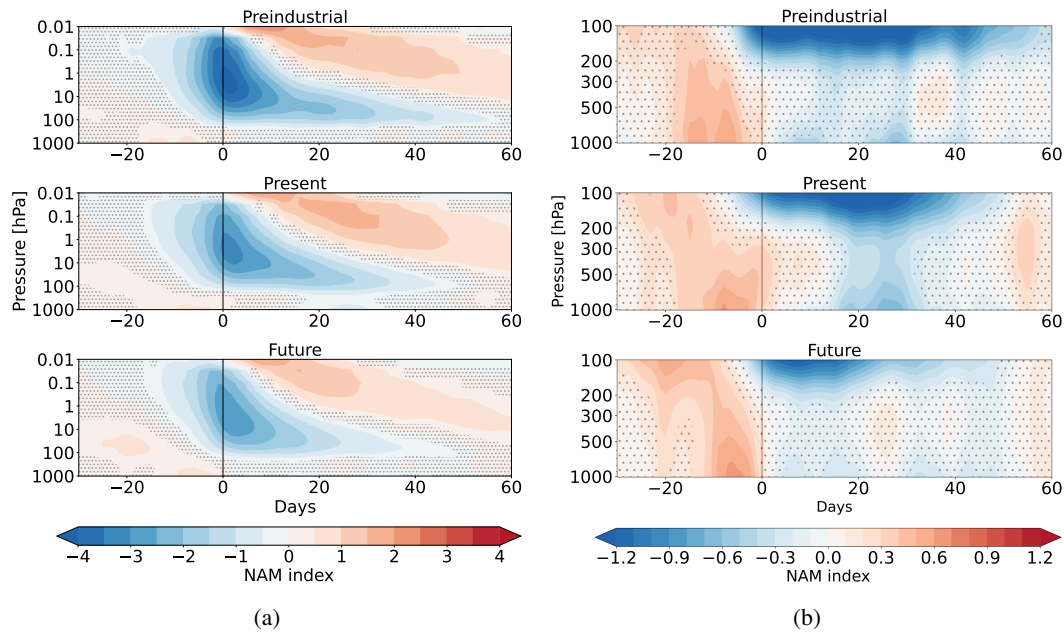
Figure 6.27: SSW composite anomalies of the NAM index for EMAC timeslice simulations, averaged from 30 days before the SSW onset to 60 days after. The troposphere and middle atmosphere are illustrated in (a), and the troposphere only in (b) using different contour levels (see colour bars). The significance was determined by a Monte Carlo simulation with $N = 5000$. Non-significant anomalies are illustrated with hatchings.

6.3 The influence of interactive chemistry

The results presented thus far were obtained using EMAC as a full chemistry-climate model. The ambiguous findings regarding the Arctic-midlatitude linkage in the literature raise the question of whether a climate model which includes stratospheric chemistry provides more accurate results, particularly with respect to the stratospheric pathway. Haase and Matthes (2019) proposed a chemical-dynamical feedback involving a modification of planetary wave propagation through temperature and wind changes, derived from model simulations with and without interactive chemistry. They suggested that low ozone concentrations, which are related to heterogeneous ozone depletion, lead to lower temperatures through radiative feedback. Consequently, the stratospheric winds are affected due to the thermal wind relation which impacts wave propagation. Planetary wave breaking results in mixing of lower-latitude air into the vortex. The Brewer-Dobson circulation is induced by planetary waves, transporting the ozone-rich air pole- and downward into the polar vortex. Haase and Matthes (2019) distinguighed between positive and negative feedback depending of the background strength of the polar vortex. They found fewer SSWs and a stronger climatological polar vortex in simulations with interactive ozone chemistry. A further study by Oehrlein et al. (2020) confirmed a stronger polar vortex in CCM simulations but they reported insignificant changes in SSW frequency in their study. Both studies used the WACCM model, although with different setups.

As a final evaluation, it is investigated whether the interactive chemistry in EMAC has an effect on the results previously discussed in this study. Therefore, the timeslice simulations were replicated in GCM mode, still coupled to an ocean but with prescribed climatological ozone concentrations. In the next section, a modification of the troposphere-stratosphere coupling process is evaluated by comparing timeslice simulations with and without an interactive chemistry module in EMAC to answer the following question:

Q7 Does the consideration of ozone chemistry in the model affect the representation of stratospheric pathway processes?

6.3.1 Climatological mean circulation

Before assessing the different steps in the Arctic-midlatitude mechanism, a general evaluation of the stratospheric circulation change in these sensitivity simulations is outlined. Haase and Matthes (2019) demonstrated a stronger polar vortex in their simulations with interactive chemistry by means of stronger zonal winds and lower temperatures in the middle stratosphere (their Figure 2). EMAC experiments reveal the same signal in the present simulations, as shown in Figure 6.28. In winter, the Arctic region exhibits higher wind speeds and lower temperatures, as evident in (b) and (d). In future simulations, this signal is only pronounced in February, and the preindustrial runs show opposing wind changes in early and late winter. It is reasonable that the expected modification emerges in the present simulations because ozone depletion is most prominent in this time period, including ODS levels of the year 2020. Regarding the climatological change in the polar vortex, the findings of the present EMAC timeslices agree with the results of Haase and Matthes (2019) and Oehrlein et al. (2020). However, the influence of ozone chemistry on the stratospheric circulation in the absence of ozone depletion (preindustrial) and under the impact of extensive global warming (future) has not yet been thoroughly explored. EMAC simulations reveal some significant differences in stratospheric dynamics, but further investigations into the cause of these anomalies are needed. Future research should address this issue, and the following section concentrates on the modification of the stratospheric pathway.

6.3.2 Stratospheric pathway

A modification through interactive chemistry in the model would influence all steps of the mechanism related to the stratosphere. First, the planetary wave propagation in Step 4 is investigated using the daily heat flux at midlatitudes and in 100 hPa. The changes in the probability distributions, as depicted in Figure 6.29, are relatively minor. These findings do not indicate an influence of ozone chemistry on tropospheric wave forcing. However, this ensures that the stratosphere must respond to the same forcing for further evaluation of the subsequent steps.

The results from WACCM discussed in the previous sections suggest a stronger polar vortex in CCM model simulations compared to the GCM mode. In EMAC, the distribution of the zonal mean zonal wind at 10 hPa and 60°N exhibits a small shift toward higher wind speeds

119
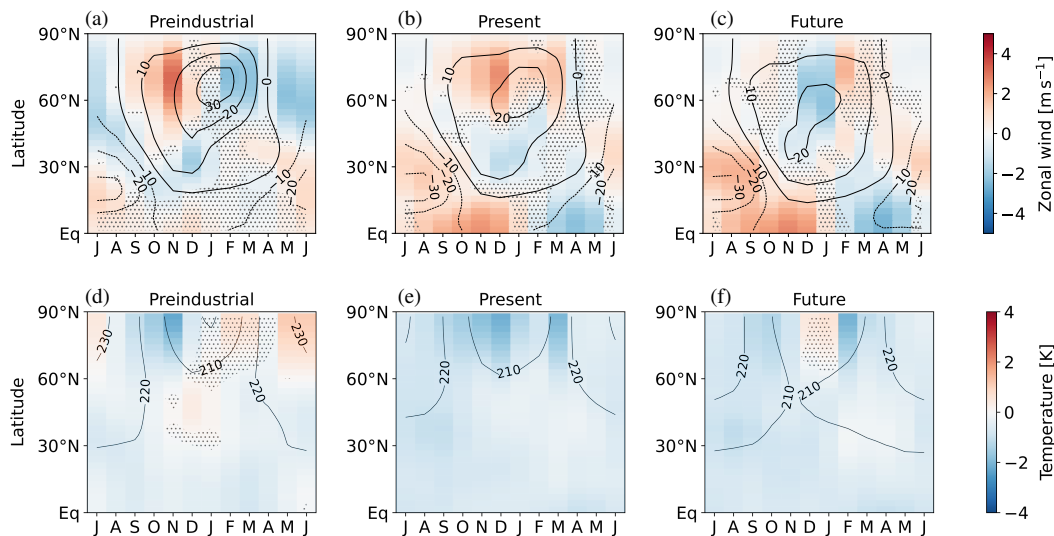
Figure 6.28: Difference between CCM and AOGCM simulations (*chem - nochem*) of monthly mean climatologies. The zonal wind in (a) is shown at 10 hPa and the temperature in (b) at 30 hPa. Contours indicate the non-chemistry version. The significance was determined using the Student's t-test with a significance level of 5%. The non-significant values are marked with hatches.
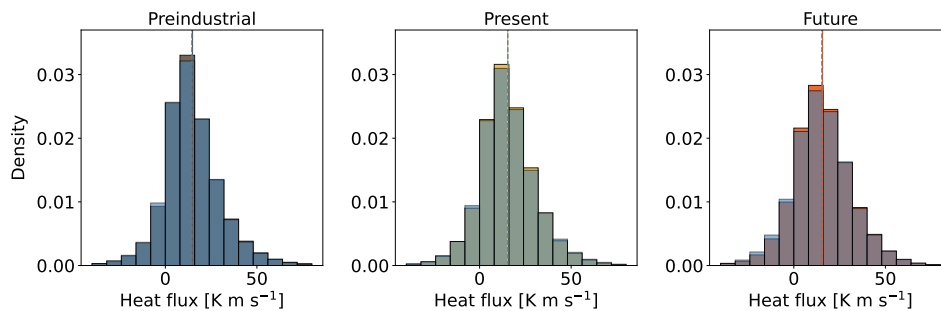
Figure 6.29: Histogram of daily heat flux in 100 hPa for latitudes between 45°N and 75°N during winter days. The non-chemistry version of the model simulation is overlayed in blue, the colors are indicated in the legend of Figure 6.30 The mean is indicated by the vertical line in the respective timeslice color.

in the present simulation, as shown in Figure 6.30b. In contrast, the preindustrial simulations reveal no significant shift, and future simulations indicate a tendency towards lower wind speeds in the chemistry simulation. However, the question arises as to whether these small changes affect the occurrence of stratospheric warmings.

The frequencies of SSWs in EMAC simulations in CCM and AOGCM configurations are shown in Figure 6.31. The climate change-related increase in SSW occurrence in CCM timeslices is discussed in Section 6.2.2 based on Figure 6.6. The SSW frequencies in the non-chemistry version show only minor deviations compared to their chemistry counterpart. Indeed, the winter frequency in the present timeslice is lower in the chemistry version, which is consistent with Haase and Matthes (2019) and Oehrlein et al. (2020). The latter found that the decrease was not statistically significant, which is also the case for EMAC. All differences illustrated in Figure 6.31 were determined to be statistically insignificant. These results indicate that ozone chemistry has no impact on the formation of stratospheric warmings.

Irrespective of the change in SSW frequency, it can also be investigated whether the downward coupling is different in both model setups. To conclude the analysis, the downward impact of SSWs is compared using the composite method. Figure 6.32 shows the temperature composite anomalies for all timeslice simulations. There are minor variations between the CCM and AOGCM simulations. The Siberian cooling in the present timeslice in (d) is slightly stronger in the simulation without interactive chemistry than that in (b). This significant variation is not interpreted as an effect of the switched-off chemistry module. The surface signals after SSWs are not uniform and vary from event to event. In addition, cooling in the Southern United States does not occur at every event, and the variation in this region shown in Figure 6.32 is attributed to the variability instead of being influenced by ozone chemistry in the model.
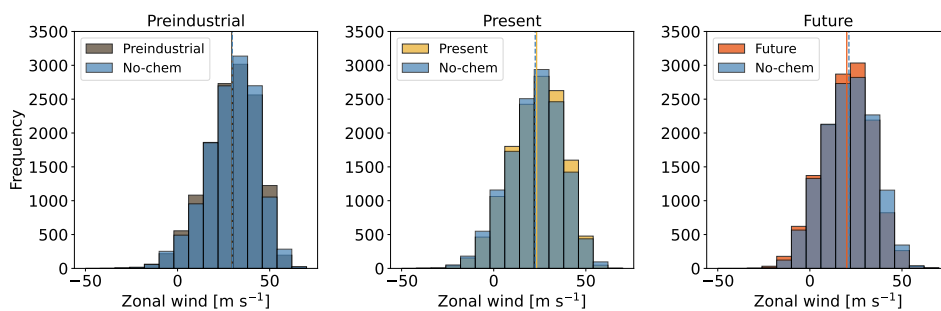
Figure 6.30: Histograms of the daily zonal mean zonal wind at 10 hPa and in 60°N during winter (DJF) in EMAC timeslice simulations. The non-chemistry version of the model simulation is overlaid in blue. The mean is illustrated by the vertical line in the respective timeslice colour.
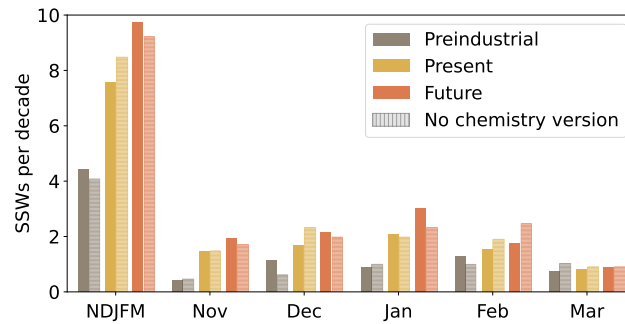
Figure 6.31: SSW frequencies per decade in EMAC timeslice simulations for the extended winter season and for every winter month. The difference between chemistry (plain) and non-chemistry (striped) simulations was examined using the chi-square test at a significance level of 5%. No significant differences between chemistry and non-chemistry version of the simulations were found for any experiment or time period.
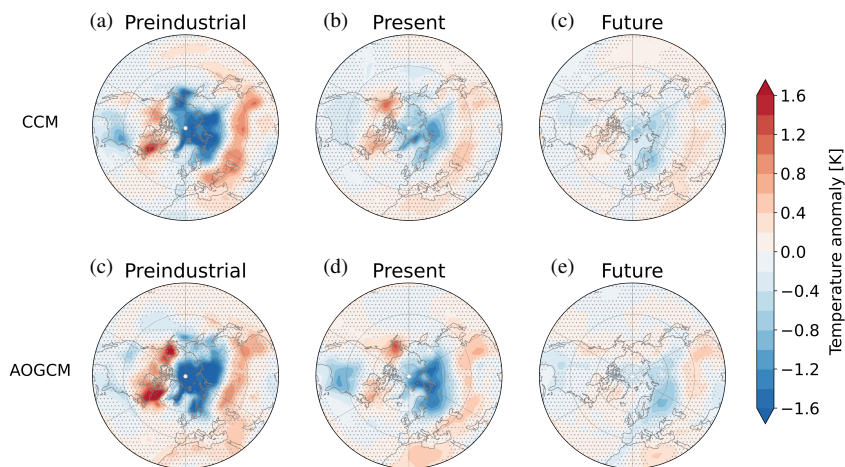
Figure 6.32: SSW composite anomalies of near-surface temperature in EMAC timeslice simulations in CCM and AOGCM configuration. The significance was determined by a Monte Carlo simulation with $N = 5000$. Non-significant anomalies are illustrated with hatchings.

To summarise, the answer to the previously posed question is:

A7 The consideration of ozone chemistry in EMAC had no significant effect on the tropospheric wave input into the stratosphere, the occurrence of stratospheric warmings, nor the downward influence of SSWs.

Most Arctic-midlatitude linkage studies have employed climate models without ozone chemistry. This thesis has investigated the effects of an GHG-increase which is accompanied by a large Arctic amplification. The results of the previous sections highlighted a stronger wave forcing in the stratosphere and significant effects on the stratospheric variability. The findings suggest that taking ozone feedback into account does not substantially improve or bias the results. A slight strengthening of the polar vortex was detected in the CCM simulations, which is consistent with the results of other studies. Nevertheless, a slightly weaker polar vortex in simulations with prescribed ozone concentrations would not inhibit any additional wave forcing related to Arctic amplification based on the findings in the thesis. This evaluation can only assess the effect of the whole climate change on the processes. Given that the isolated effects of Arctic amplification are expected to be considerably weaker, it stands to reason that the stratospheric chemistry would not have a significant impact. In conclusion, the role of interactive chemistry in resolving contradictions regarding Arctic-midlatitude linkage research is not considered a critical element.

CHAPTER 7

Summary

This thesis aimed to analyse the stratospheric pathway of the Arctic-midlatitude linkage in a chemistry-climate model. The controversial debate of whether the accelerated warming in the Arctic is connected to colder winter weather in midlatitudes is still ongoing. For more than two decades, conflicting perspectives have emerged from research in this area. A key point in the discussion is the inability of climate models to reproduce the winter cooling observed in recent decades. Two viewpoints have emerged from this:

1. The models have deficiencies and fail to simulate the linkage correctly.

2. The observed winter cooling occured in the context of natural variability with no causal relationship to Arctic warming.

The integrity of the model was subject to close examination when supporting point 1. The proposed mechanism connecting the enhanced polar warming with remote circulation anomalies involves a stratospheric pathway. The current study investigates this pathway in a CCM, including a realistic representation of the middle atmosphere, and taking into account possible feedback between ozone chemistry and dynamics.

Recent studies have revealed some limitations in sensitivity experiments that prescribe sea ice alone. These experiments do not consider ocean-atmosphere coupling or changes due to warming in other parts of the globe. This thesis presents model simulations that were forced by an increase in GHG concentrations. Thus, the transformation of the entire climate system is assessed instead of the isolated effect of Arctic amplification alone.

In pursuit of this objective, three sets of simulations with the EMAC model were performed. An ensemble of transient simulations, three timeslice simulations for the preindustrial, present, and future time periods, and finally corresponding timeslice simulations without interactive chemistry in the model. The transient simulation spanning the period between 1850 and 2100 represents slowly progressing climate change until the end of the 21st century under a relatively strong GHG scenario. The results from these transient simulations suggest neither a cooling trend nor stability in temperature during winter at midlatitudes. In contrast, while the Arctic amplification continues to rise, warming in the midlatitudes is also progressing steadily.

The stratospheric pathway of the Arctic-midlatitude linkage involves enhanced planetary wave generation under the influence of amplified polar warming. Subsequently, these atmospheric waves can propagate into the middle atmosphere and induce stratospheric warm-

ings. Following the argumentation line of the pathway, it is expected that a warmer climate will lead to an increase in SSW frequency. Transient EMAC simulations indicate such an increase in stratospheric warmings over time. Climate models have shown divergent results regarding future changes in SSW occurrences. However, a detailed explanation of these discrepancies has not yet been provided.

At this point, the thesis leaves the path for establishing a causal link between Arctic warming and midlatitude winter cooling. Instead, the focus is on the increase in SSW events and whether Arctic amplification takes part in causing this increase, without necessarily inducing severe cold winter weather. In the first part of this thesis, the main goal was to examine if the enhanced SSW signal can be traced back towards Arctic amplification, following the outlined steps of the stratospheric pathway mechanism:

- Enhanced wave propagation into the stratosphere,

- Formation of more wave-like polar jet streams,

- Modification of temperature gradients and baroclinic instability.

The analysis is outlined by EMAC timeslice experiments to achieve better statistical evaluations of the results. First, growing Arctic amplification and enhanced SSW frequency were validated in these simulations. The findings of the climate change experiments (present and future) clearly confirmed a significant increase in stratospheric warmings in EMAC timeslice simulations. Furthermore, enhanced planetary wave activity in the stratosphere could be diagnosed by the EP flux, combined with a stronger wave input from the troposphere. These results imply that more frequent SSWs were induced by changes in wave forcing.

The wave input into the stratosphere is realised by local upward moving waves, lasting a few days, and emerging in different preferred locations. Therefore, the 3D Plumb flux was applied to specify the wave source in an event-based analysis. These events of upward propagating atmospheric waves occur mainly between 40°N and 70°N. The preindustrial simulation exhibits an accumulation of vertical wave event frequency over Eastern Siberia and the Western Pacific. The climate change simulations show an increase in that frequency in most parts of the midlatitudes, in addition to a pronounced shift of the high wave input area from Siberia towards the Eastern Pacific region. Another significant increase has occurred over the North Atlantic and Europe. Moreover, the event-based analysis revealed that the general increase can be attributed to more wave events per winter. Changes in the mean area, duration, and intensity of events did not play a decisive role. The concept of preconditioning of the polar vortex before the formation of SSWs makes the increased number of vertical wave events an important factor. Several wave breaking events in succession have the potential to significantly weaken the polar vortex.

The question arises whether the increased wave input into the stratosphere is related to a change in the behaviour of polar jets. For this purpose, a jet detection scheme was applied, which determined the location of the upper troposphere jet cores and accomplished separation of the polar and subtropical jet streams. Changes in jet positioning in the context of global warming provide a complex picture. The subtropical jet revealed local shifts and

126

pronounced strengthening in the western hemisphere. The spiral shape and the locally diverging signals impede a conclusion regarding a general equatorward or poleward shift. The polar jet generally exhibits lower frequencies and, in contrast to the subtropical jet, does not appear in a narrow latitudinal range. With an increase in GHG emissions, polar jets occur less frequently in the western hemisphere, coinciding with areas in which the subtropical jet has strengthened. In contrast, the eastern hemisphere was marked by enhanced polar jet occurrences, specifically over Europe.

Further evaluation of the wind components of the polar jet demonstrated that these enhanced jets become more southward-directed. Francis and Vavrus (2012) suggested a weaker jet stream as a consequence of Arctic amplification. In this study, a general weakening of the wind speed in the jet cores was not confirmed, although a lower wind speed was apparent in the European sector. The modification of the European jets and the amplified upward wave propagation in this region agree with the proposed steps in the stratospheric pathway. Because SSW event onsets preferably occur in the Eurasian sector, these changes can play a crucial role in driving more SSWs. On the contrary, the signals over the North Pacific and America implicate no weakening of the polar jet wind speed . These outcomes highlight that modifications of the jet stream cannot be considered globally but should be assessed on a regional scale. On the other hand, the results for North America have to be treated with caution because a separation in this region could not be guaranteed due to the close vicinity of both jets. However, the results suggest that subtropical jets strengthen locally at the expense of the polar jet, and vice versa. Further research is required to investigate this potential interaction between the jets.

The step connecting Arctic amplification with the behaviour of polar jets is the modification of the temperature gradients. In this study, changes in the temperature structure were evaluated under the lens of baroclinic instability. In theory, a weaker horizontal temperature gradient is associated with lower baroclinic instability and, consequently with fewer baroclinic waves. This relation is evidently present in the lower troposphere in EMAC simulation. The lower signal in the Eady growth rate coincides with the weaker horizontal temperature gradients. Accordingly, Arctic amplification leads to a reduction of baroclinic waves, which could result in less acceleration of the polar jet. Following the argumentation line of the stratospheric pathway and Francis and Vavrus (2012), a slower jet is accompanied by a more meandering path and larger amplitudes of Rossby waves. Some indications of this assertion that jets are becoming slower and wavier, emerge in the European region. However, a comprehensive validation of that hypothesis was not confirmed in this study.

Additionally, an area with stronger baroclinic instability is apparent in the upper troposphere. These anomalies are associated with enhanced wave generation and coincide with a decrease in the static stability and enhanced temperature gradients due to the tropical warming. Consequently, both variables favour vertical wave propagation, resulting in a larger wave input into the stratosphere. A direct link between the temperature gradients in the lower layers and the modifications in the upper troposphere could not be established in this thesis. The increased wave generation could be a result of changes in the upper troposphere without any effects of Arctic amplification. However, several questions remain

unanswered, and a more thorough examination is needed.

In summary, this thesis aimed to trace the steps in the stratospheric pathway mechanism. The increased SSW frequency in climate change simulations could be linked to enhanced planetary wave activity with more wave events and more meridionally oriented polar jets over Eurasia. Reduced baroclinicity and fewer baroclinic waves in the lower troposphere are associated with lower temperature gradients, a consequence of Arctic amplification. However, the link between these temperature gradients and the polar jet stream is a critical point in the theoretical framework, and could not be verified in this study. As long as the evidence is pending, more restraint is recommended when listing Arctic sea ice as one of the main influencing factors for stratospheric variability.

Another focus of this thesis was to investigate the downward influence of more SSWs in a warmer climate. The breakdown of the stratospheric polar vortex is often followed by local cold air outbreaks at midlatitudes. These extreme cold events are not found to increase in EMAC simulations. In contrast, winter temperatures in midlatitudes became less variable in a warmer climate. One major finding in this part of the study is the distinct weakening of the surface cooling after SSW events in the climate change experiments. As already suggested by other studies, cold air outbreaks will likely lose their severity because the advected air will become significantly warmer under the impact of Arctic amplification. In conclusion, a warmer climate could lead to more stratospheric warmings, but these events will forfeit their impact on surface temperatures.

Finally, an evaluation of the influence of interactive chemistry in the model was outlined. General modifications of the temperatures and zonal winds were confirmed in the EMAC present timeslice simulation. The effect of ozone depletion is thought to be the strongest in this timeslice. Despite these small variations in stratospheric variables, no significant influence on the wave forcing, frequency of SSWs, or downward influence was established. These findings suggest that the consideration of ozone chemistry does not significantly impact the results regarding the Arctic-midlatitude linkage.

However, this study raises some research questions that should be addressed further. Why does the number of vertical wave events near the tropopause increase? Can these changes be attributed to anomalies in synoptic structures, or is this a consequence of the modification of the temperature structure in the upper troposphere, or a combination of both? Does reduced synoptic activity in the lower troposphere affect changes in the upper troposphere? This is a critical connecting point in the stratospheric pathway and determines the validity of the proposed framework. In closing, the outcomes of this work do not support the idea of colder winter weather in the course of Arctic amplification. Nevertheless, some aspects of the proposed mechanism have been elucidated from different perspectives. These results suggest the need for a differentiated view of regional changes. Thus, the use of zonal mean variables requires careful consideration. The mechanism believed to facilitate the Arctic-midlatitude linkage is more complex than initially assumed, and broad research is still ongoing. It is important to reflect on the physical processes behind the detected signals and to explore their origins. Keeping this in mind, we may settle the debate and hopefully gain some clarity on this contested research topic.

Bibliography

C. Donald Ahrens. *Essentials of meteorology*. Brooks/Cole/Thomson Learning, Pacific Grove, CA, 3rd ed edition, 2000. ISBN 0534372007.

D. G. Andrews and M. E. McIntyre. Planetary waves in horizontal and vertical shear: The generalized Eliassen–Palm relation and the mean zonal acceleration. *Journal of Atmospheric Sciences*, 33:2031–2048, 1976.

D. G. Andrews, J. D. Mahlman, and R. W. Sinclair. Eliassen-Palm Diagnostics of Wave-Mean Flow Interaction in the GFDL "SKYHI" General Circulation Model. *J. Atmos. Sci.*, 40:2768–2784, 1983. doi:10.1175/1520-0469(1983)040<2768:ETWATM>2.0.CO;2.

B. Ayarzagüena, A. J. Charlton-Perez, A. H. Butler, P. Hitchcock, I. R. Simpson, L. M. Polvani, N. Butchart, E. P. Gerber, L. Gray, B. Hassler, P. Lin, F. Lott, E. Manzini, R. Mizuta, C. Orbe, S. Osprey, D. Saint-Martin, M. Sigmond, M. Taguchi, E. M. Volodin, and S. Watanabe. Uncertainty in the Response of Sudden Stratospheric Warmings and Stratosphere-Troposphere Coupling to Quadrupled CO2 Concentrations in CMIP6 Models. *Journal of Geophysical Research: Atmospheres*, 125(6), March 2020. ISSN 2169-8996. doi:10.1029/2019jd032345.

Blanca Ayarzagüena and James A. Screen. Future Arctic sea ice loss reduces severity of cold air outbreaks in midlatitudes. *Geophysical Research Letters*, 43(6):2801–2809, March 2016. ISSN 1944-8007. doi:10.1002/2016gl068092.

Blanca Ayarzagüena, Lorenzo M. Polvani, Ulrike Langematz, Hideharu Akiyoshi, Slimane Bekki, Neal Butchart, Martin Dameris, Makoto Deushi, Steven C. Hardiman, Patrick Jöckel, Andrew Klekociuk, Marion Marchand, Martine Michou, Olaf Morgenstern, Fiona M. O'Connor, Luke D. Oman, David A. Plummer, Laura Revell, Eugene Rozanov, David Saint-Martin, John Scinocca, Andrea Stenke, Kane Stone, Yousuke Yamashita, Kohei Yoshida, and Guang Zeng. No robust evidence of future changes in major stratospheric sudden warmings: a multi-model assessment from CCMI. *Atmospheric Chemistry and Physics*, 18(15):11277–11287, August 2018. ISSN 1680-7324. doi:10.5194/acp-18-11277-2018.

A. P. M Baede, E. Ahlonsou, Y. Ding, and D. Schimel. The Climate System: an Overview. In J.T. Houghton, Y. Ding, D.J. Griggs, M. Noguer, P.J. van der Linden, X. Dai, K. Maskell, and C.A. Johnson, editors, *Climate Change 2001: The Scientific Basis. Contribution of Working Group I to the Third Assessment Report of the Intergovernmental Panel on Climate Change*, pages 87–98. Cambridge University Press, 2001.

Mark P. Baldwin and Timothy J. Dunkerton. Stratospheric Harbingers of Anomalous Weather Regimes. *Science*, 294(5542):581–584, October 2001. ISSN 1095-9203. doi:10.1126/science.1063315.

Mark P. Baldwin, Blanca Ayarzagüena, Thomas Birner, Neal Butchart, Amy H. Butler, Andrew J. Charlton-Perez, Daniela I. V. Domeisen, Chaim I. Garfinkel, Hella Garny, Edwin P. Gerber, Michaela I. Hegglin, Ulrike Langematz, and Nicholas M. Pedatella. Sudden Stratospheric Warmings. *Reviews of Geophysics*, 59(1), January 2021. ISSN 1944-9208. doi:10.1029/2020rg000708.

Elizabeth A. Barnes. Revisiting the evidence linking Arctic amplification to extreme weather in midlatitudes. *Geophysical Research Letters*, 40(17):4734–4739, September 2013. ISSN 1944-8007. doi:10.1002/grl.50880.

Gareth Berry, Chris Thorncroft, and Tim Hewson. African Easterly Waves during 2004—Analysis Using Objective Techniques. *Monthly Weather Review*, 135(4):1251–1267, April 2007. ISSN 0027-0644. doi:10.1175/mwr3343.1.

Russell Blackport and James A. Screen. Influence of Arctic Sea Ice Loss in Autumn Compared to That in Winter on the Atmospheric Circulation. *Geophysical Research Letters*, 46(4):2213–2221, February 2019. doi:10.1029/2018gl081469.

Russell Blackport and James A. Screen. Insignificant effect of Arctic amplification on the amplitude of midlatitude atmospheric waves. *Science Advances*, 6(8), February 2020a. ISSN 2375-2548. doi:10.1126/sciadv.aay2880.

Russell Blackport and James A. Screen. Weakened evidence for mid-latitude impacts of Arctic warming. *Nature Climate Change*, 10(12):1065–1066, November 2020b. ISSN 1758-6798. doi:10.1038/s41558-020-00954-y.

Russell Blackport, James A. Screen, Karin van der Wiel, and Richard Bintanja. Minimal influence of reduced Arctic sea ice on coincident cold winters in mid-latitudes. *Nature Climate Change*, 9(9):697–704, August 2019. ISSN 1758-6798. doi:10.1038/s41558-019-0551-4.

Robyn C. Boeke, Patrick C. Taylor, and Sergio A. Sejas. On the Nature of the Arctic's Positive Lapse-Rate Feedback. *Geophysical Research Letters*, 48(1):e2020GL091109, 2021. doi:https://doi.org/10.1029/2020GL091109.

Lori Bruhwiler, Frans-Jan W. Parmentier, Patrick Crill, Mark Leonard, and Paul I. Palmer. The Arctic Carbon Cycle and Its Response to Changing Climate. *Current Climate Change Reports*, 7(1):14–34, Mar 2021. ISSN 2198-6061. doi:10.1007/s40641-020-00169-5.

A. H. Butler, J. P. Sjoberg, D. J. Seidel, and K. H. Rosenlof. A sudden stratospheric warming compendium. *Earth System Science Data*, 9(1):63–76, 2017. doi:10.5194/essd-9-63-2017.

Amy H. Butler and Edwin P. Gerber. Optimizing the Definition of a Sudden Strato-
spheric Warming. *Journal of Climate*, 31(6):2337–2344, March 2018. ISSN 1520-0442.
doi:10.1175/jcli-d-17-0648.1.

D. Cai, M. Dameris, H. Garny, and T. Runde. Implications of all season Arctic sea-ice
anomalies on the stratosphere. *Atmospheric Chemistry and Physics*, 12(24):11819–
11831, December 2012. ISSN 1680-7324. doi:10.5194/acp-12-11819-2012.

L. J. Carpenter, J.S. (Lead Authors) Daniel, E.L. Fleming, T. Hanaoka, J. Hu, A.R. Rav-
ishankara, M.N. Ross, S. Tilmes, T. J. Wallington, and D. J. Wuebbles. Scenarios and
Information for P6olicymakers. In Editor(s) of the Ozone Assessment, editor, *WMO
2018 Ozone Assessment*, Global Ozone Research and Monitoring Project–Report No. 58.
World Meteorological Organization, Geneva, Switzerland, 2018.

Andrew J. Charlton and Lorenzo M. Polvani. A New Look at Stratospheric Sudden Warm-
ings. Part I: Climatology and Modeling Benchmarks. *Journal of Climate*, 20(3):449–469,
February 2007. ISSN 0894-8755. doi:10.1175/jcli3996.1.

J. G. Charney and P. G. Drazin. Propagation of planetary-scale disturbances from the lower
into the upper atmosphere. *Journal of Geophysical Research*, 66(1):83–109, January
1961. ISSN 0148-0227. doi:10.1029/jz066i001p00083.

Gang Chen, Jian Lu, D. Alex Burrows, and L. Ruby Leung. Local finite-amplitude wave
activity as an objective diagnostic of midlatitude extreme weather. *Geophysical Research
Letters*, 42(24), December 2015. ISSN 1944-8007. doi:10.1002/2015gl066959.

Croix E. Christenson, Jonathan E. Martin, and Zachary J. Handlos. A Synoptic Climatology
of Northern Hemisphere, Cold Season Polar and Subtropical Jet Superposition Events.
Journal of Climate, 30(18):7231–7246, August 2017. ISSN 1520-0442. doi:10.1175/jcli-
d-16-0565.1.

J. Cohen, X. Zhang, J. Francis, T. Jung, R. Kwok, J. Overland, T. J. Ballinger, U. S. Bhatt,
H. W. Chen, D. Coumou, S. Feldstein, H. Gu, D. Handorf, G. Henderson, M. Ionita,
M. Kretschmer, F. Laliberte, S. Lee, H. W. Linderholm, W. Maslowski, Y. Peings,
K. Pfeiffer, I. Rigor, T. Semmler, J. Stroeve, P. C. Taylor, S. Vavrus, T. Vihma, S. Wang,
M. Wendisch, Y. Wu, and J. Yoon. Divergent consensuses on Arctic amplification in-
fluence on midlatitude severe winter weather. *Nature Climate Change*, 10(1):20–29,
December 2020. ISSN 1758-6798. doi:10.1038/s41558-019-0662-y.

Judah Cohen, James A. Screen, Jason C. Furtado, Mathew Barlow, David Whittleston, Dim
Coumou, Jennifer Francis, Klaus Dethloff, Dara Entekhabi, James Overland, and Justin
Jones. Recent Arctic amplification and extreme mid-latitude weather. *Nature Geoscience*,
7(9):627–637, August 2014. ISSN 1752-0908. doi:10.1038/ngeo2234.

Judah L Cohen, Jason C Furtado, Mathew A Barlow, Vladimir A Alexeev, and Jessica E
Cherry. Arctic warming, increasing snow cover and widespread boreal winter cool-
ing. *Environmental Research Letters*, 7(1):014007, January 2012. ISSN 1748-9326.
doi:10.1088/1748-9326/7/1/014007.

P. Davini, C. Cagnazzo, and J. A. Anstey. A blocking view of the stratosphere-troposphere coupling. *Journal of Geophysical Research: Atmospheres*, 119(19), October 2014. ISSN 2169-8996. doi:10.1002/2014jd021703.

Clara Deser, Adam Phillips, Vincent Bourdette, and Haiyan Teng. Uncertainty in climate change projections: the role of internal variability. *Climate Dynamics*, 38(3–4):527–546, December 2010a. ISSN 1432-0894. doi:10.1007/s00382-010-0977-x.

Clara Deser, Robert Tomas, Michael Alexander, and David Lawrence. The Seasonal Atmospheric Response to Projected Arctic Sea Ice Loss in the Late Twenty-First Century. *Journal of Climate*, 23(2):333–351, January 2010b. ISSN 0894-8755. doi:10.1175/2009jcli3053.1.

Gordon Miller Bourne Dobson, D. N. Harrison, and J. Lawrence. Measurements of the amount of ozone in the Earth's atmosphere and its relation to other geophysical conditions.—Part III. *Proceedings of the Royal Society of London. Series A, Containing Papers of a Mathematical and Physical Character*, 122(790):456–486, 1929. doi:10.1098/rspa.1929.0034.

Daniela I. V. Domeisen, Amy H. Butler, Andrew J. Charlton-Perez, Blanca Ayarzagüena, Mark P. Baldwin, Etienne Dunn-Sigouin, Jason C. Furtado, Chaim I. Garfinkel, Peter Hitchcock, Alexey Yu. Karpechko, Hera Kim, Jeff Knight, Andrea L. Lang, Eun-Pa Lim, Andrew Marshall, Greg Roff, Chen Schwartz, Isla R. Simpson, Seok-Woo Son, and Masakazu Taguchi. The Role of the Stratosphere in Subseasonal to Seasonal Prediction: 2. Predictability Arising From Stratosphere-Troposphere Coupling. *Journal of Geophysical Research: Atmospheres*, 125(2), January 2020a. ISSN 2169-8996. doi:10.1029/2019jd030923.

Daniela I.V. Domeisen, Amy H. Butler, Andrew J. Charlton-Perez, Blanca Ayarzagüena, Mark P. Baldwin, Etienne Dunn-Sigouin, Jason C. Furtado, Chaim I. Garfinkel, Peter Hitchcock, Alexey Yu. Karpechko, Hera Kim, Jeff Knight, Andrea L. Lang, Eun-Pa Lim, Andrew Marshall, Greg Roff, Chen Schwartz, Isla R. Simpson, Seok-Woo Son, and Masakazu Taguchi. The Role of the Stratosphere in Subseasonal to Seasonal Prediction: 1. Predictability of the Stratosphere. *Journal of Geophysical Research: Atmospheres*, 125(2), January 2020b. ISSN 2169-8996. doi:10.1029/2019jd030920.

Howard J Edmon, Brian J Hoskins, and Michael E McIntyre. Eliassen-Palm cross sections for the troposphere. *Journal of the Atmospheric Sciences*, 37:2600–2616, 1980. doi:10.1175/1520-0469(1980)037<2600:EPCSFT>2.0.CO;2.

J. C. Farman, B. G. Gardiner, and J. D. Shanklin. Large losses of total ozone in Antarctica reveal seasonal ClOx/NOx interaction. *Nature*, 315(6016):207–210, May 1985. ISSN 1476-4687. doi:10.1038/315207a0.

Erich M. Fischer and Reto Knutti. Heated debate on cold weather. *Nature Climate Change*, 4(7):537–538, June 2014. ISSN 1758-6798. doi:10.1038/nclimate2286.

Jennifer A. Francis and Stephen J. Vavrus. Evidence linking Arctic amplification to extreme weather in mid-latitudes. *Geophysical Research Letters*, 39(6), March 2012. ISSN 1944-8007. doi:10.1029/2012gl051000.

Jennifer A Francis and Stephen J Vavrus. Evidence for a wavier jet stream in response to rapid Arctic warming. *Environmental Research Letters*, 10(1):014005, January 2015. ISSN 1748-9326. doi:10.1088/1748-9326/10/1/014005.

Marina Friedel, Gabriel Chiodo, Andrea Stenke, Daniela I. V. Domeisen, Stephan Fueglistaler, Julien G. Anet, and Thomas Peter. Springtime arctic ozone depletion forces northern hemisphere climate anomalies. *Nature Geoscience*, 15(7):541–547, July 2022. ISSN 1752-0908. doi:10.1038/s41561-022-00974-7.

Edwin P. Gerber, Mark P. Baldwin, Hideharu Akiyoshi, John Austin, Slimane Bekki, Peter Braesicke, Neal Butchart, Martyn Chipperfield, Martin Dameris, Sandip Dhomse, Stacey M. Frith, Rolando R. Garcia, Hella Garny, Andrew Gettelman, Steven C. Hardiman, Alexey Karpechko, Marion Marchand, Olaf Morgenstern, J. Eric Nielsen, Steven Pawson, Tom Peter, David A. Plummer, John A. Pyle, Eugene Rozanov, John F. Scinocca, Theodore G. Shepherd, and Dan Smale. Stratosphere-troposphere coupling and annular mode variability in chemistry-climate models. *Journal of Geophysical Research: Atmospheres*, 115(D3), February 2010. ISSN 0148-0227. doi:10.1029/2009jd013770.

Sabine Haase and Katja Matthes. The importance of interactive chemistry for stratosphere–troposphere coupling. *Atmospheric Chemistry and Physics*, 19(5):3417–3432, March 2019. ISSN 1680-7324. doi:10.5194/acp-19-3417-2019.

Shengping He, Xinping Xu, Tore Furevik, and Yongqi Gao. Eurasian Cooling Linked to the Vertical Distribution of Arctic Warming. *Geophysical Research Letters*, 47(10), May 2020. ISSN 1944-8007. doi:10.1029/2020gl087212.

Hans Hersbach, Bill Bell, Paul Berrisford, Shoji Hirahara, András Horányi, Joaquín Muñoz-Sabater, Julien Nicolas, Carole Peubey, Raluca Radu, Dinand Schepers, Adrian Simmons, Cornel Soci, Saleh Abdalla, Xavier Abellan, Gianpaolo Balsamo, Peter Bechtold, Gionata Biavati, Jean Bidlot, Massimo Bonavita, Giovanna De Chiara, Per Dahlgren, Dick Dee, Michail Diamantakis, Rossana Dragani, Johannes Flemming, Richard Forbes, Manuel Fuentes, Alan Geer, Leo Haimberger, Sean Healy, Robin J. Hogan, Elías Hólm, Marta Janisková, Sarah Keeley, Patrick Laloyaux, Philippe Lopez, Cristina Lupu, Gabor Radnoti, Patricia de Rosnay, Iryna Rozum, Freja Vamborg, Sebastien Villaume, and Jean-Noël Thépaut. The ERA5 global reanalysis. *Quarterly Journal of the Royal Meteorological Society*, 146(730):1999–2049, June 2020. ISSN 1477-870X. doi:10.1002/qj.3803.

James R. Holton. *An Introduction to Dynamic Meteorology, Volume 88, Fourth Edition (International Geophysics)*. Academic Press, 2004. ISBN 9780123540157.

Meiji Honda, Jun Inoue, and Shozo Yamane. Influence of low Arctic sea-ice minima on anomalously cold Eurasian winters. *Geophysical Research Letters*, 36(8), apr 2009. doi:10.1029/2008gl037079.

Kazuhira Hoshi, Jinro Ukita, Meiji Honda, Tetsu Nakamura, Koji Yamazaki, Yasunobu Miyoshi, and Ralf Jaiser. Weak Stratospheric Polar Vortex Events Modulated by the Arctic Sea-Ice Loss. *Journal of Geophysical Research: Atmospheres*, 124(2):858–869, January 2019. ISSN 2169-8996. doi:10.1029/2018jd029222.

Brian J. Hoskins and Paul J. Valdes. On the Existence of Storm-Tracks. *Journal of the Atmospheric Sciences*, 47(15):1854–1864, August 1990. ISSN 1520-0469. doi:10.1175/1520-0469(1990)047<1854:oteost>2.0.co;2.

Yi Huang, Yan Xia, and Xiaoxiao Tan. On the pattern of CO2 radiative forcing and poleward energy transport. *Journal of Geophysical Research: Atmospheres*, 122(20):10,578–10,593, 2017. doi:https://doi.org/10.1002/2017JD027221.

J.W. Hurrell. *North Atlantic Oscillation (NAO)*, pages 65–72. Elsevier, 2001. doi:10.1016/b978-012374473-9.00263-0.

Jun Inoue, Masatake E. Hori, and Koutarou Takaya. The Role of Barents Sea Ice in the Wintertime Cyclone Track and Emergence of a Warm-Arctic Cold-Siberian Anomaly. *Journal of Climate*, 25(7):2561–2568, March 2012. ISSN 1520-0442. doi:10.1175/jcli-d-11-00449.1.

Intergovernmental Panel on Climate Change (IPCC). *Annex I: Glossary*, pages 541–562. Cambridge University Press, 2022.

IPCC. *Climate Change 2021: The Physical Science Basis. Contribution of Working Group I to the Sixth Assessment Report of the Intergovernmental Panel on Climate Change*, page 2391 pp. Cambridge University Press, Cambridge, United Kingdom and New York, NY, USA, 2021a. doi:10.1017/9781009157896.

IPCC. *Summary for Policymakers*, pages 3–32. Cambridge University Press, Cambridge, United Kingdom and New York, NY, USA, 2021b. doi:10.1017/9781009157896.001.

Shipra Jain, Adam A. Scaife, Theodore G. Shepherd, Clara Deser, Nick Dunstone, Gavin A. Schmidt, Kevin E. Trenberth, and Thea Turkington. Importance of internal variability for climate model assessment. *npj Climate and Atmospheric Science*, 6(1), June 2023. ISSN 2397-3722. doi:10.1038/s41612-023-00389-0.

R Jaiser, K Dethloff, D Handorf, and J Cohen. Impact of sea ice cover changes on the Northern Hemisphere atmospheric winter circulation. *Tellus A: Dynamic Meteorology and Oceanography*, 64(1):11595, 2012. doi:10.3402/tellusa.v64i0.11595.

Ralf Jaiser, Klaus Dethloff, and Dörthe Handorf. Stratospheric response to Arctic sea ice retreat and associated planetary wave propagation changes. *Tellus A: Dynamic Meteorology and Oceanography*, 65(1):19375, December 2013. ISSN 1600-0870. doi:10.3402/tellusa.v65i0.19375.

Martin Jucker. Scaling of Eliassen-Palm flux vectors. *Atmospheric Science Letters*, 22(4), January 2021. ISSN 1530-261X. doi:10.1002/asl.1020.

P. Jöckel, H. Tost, A. Pozzer, C. Brühl, J. Buchholz, L. Ganzeveld, P. Hoor, A. Kerkweg, M. G. Lawrence, R. Sander, B. Steil, G. Stiller, M. Tanarhte, D. Taraborrelli, J. van Aardenne, and J. Lelieveld. The atmospheric chemistry general circulation model ECHAM5/MESSy1: consistent simulation of ozone from the surface to the mesosphere. *Atmospheric Chemistry and Physics*, 6(12):5067–5104, November 2006. ISSN 1680-7324. doi:10.5194/acp-6-5067-2006.

P. Jöckel, A. Kerkweg, A. Pozzer, R. Sander, H. Tost, H. Riede, A. Baumgaertner, S. Gromov, and B. Kern. Development cycle 2 of the Modular Earth Submodel System (MESSy2). *Geoscientific Model Development*, 3(2):717–752, December 2010. ISSN 1991-9603. doi:10.5194/gmd-3-717-2010.

Patrick Jöckel, Holger Tost, Andrea Pozzer, Markus Kunze, Oliver Kirner, Carl A. M. Brenninkmeijer, Sabine Brinkop, Duy S. Cai, Christoph Dyroff, Johannes Eckstein, Franziska Frank, Hella Garny, Klaus-Dirk Gottschaldt, Phoebe Graf, Volker Grewe, Astrid Kerkweg, Bastian Kern, Sigrun Matthes, Mariano Mertens, Stefanie Meul, Marco Neumaier, Matthias Nützel, Sophie Oberländer-Hayn, Roland Ruhnke, Theresa Runde, Rolf Sander, Dieter Scharffe, and Andreas Zahn. Earth System Chemistry integrated Modelling (ESCiMo) with the Modular Earth Submodel System (MESSy) version 2.51. *Geoscientific Model Development*, 9(3):1153–1200, March 2016. ISSN 1991-9603. doi:10.5194/gmd-9-1153-2016.

J. J. Kennedy, N. A. Rayner, C. P. Atkinson, and R. E. Killick. An Ensemble Data Set of Sea Surface Temperature Change From 1850: The Met Office Hadley Centre HadSST.4.0.0.0 Data Set. *Journal of Geophysical Research: Atmospheres*, 124(14):7719–7763, July 2019. ISSN 2169-8996. doi:10.1029/2018jd029867.

Baek-Min Kim, Seok-Woo Son, Seung-Ki Min, Jee-Hoon Jeong, Seong-Joong Kim, Xiangdong Zhang, Taehyoun Shim, and Jin-Ho Yoon. Weakening of the stratospheric polar vortex by Arctic sea-ice loss. *Nature Communications*, 5(1), September 2014. ISSN 2041-1723. doi:10.1038/ncomms5646.

Eli Kintisch. Into the Maelstrom. *Science*, 344(6181):250–253, April 2014. ISSN 1095-9203. doi:10.1126/science.344.6181.250.

Erik W. Kolstad, Tarjei Breiteig, and Adam A. Scaife. The association between stratospheric weak polar vortex events and cold air outbreaks in the Northern Hemisphere: Weak Polar Vortex and Cold Air Outbreaks. *Quarterly Journal of the Royal Meteorological Society*, 136(649):886–893, April 2010. ISSN 0035-9009. doi:10.1002/qj.620.

Marlene Kretschmer, Dim Coumou, Jonathan F. Donges, and Jakob Runge. Using Causal Effect Networks to Analyze Different Arctic Drivers of Midlatitude Winter Circulation. *Journal of Climate*, 29(11):4069–4081, June 2016. ISSN 1520-0442. doi:10.1175/jcli-d-15-0654.1.

Marlene Kretschmer, Dim Coumou, Laurie Agel, Mathew Barlow, Eli Tziperman, and Judah Cohen. More-Persistent Weak Stratospheric Polar Vortex States Linked to Cold Extremes. *Bulletin of the American Meteorological Society*, 99(1):49–60, January 2018. doi:10.1175/bams-d-16-0259.1.

Marlene Kretschmer, Giuseppe Zappa, and Theodore G. Shepherd. The role of Barents–Kara sea ice loss in projected polar vortex changes. *Weather and Climate Dynamics*, 1(2):715–730, November 2020. ISSN 2698-4016. doi:10.5194/wcd-1-715-2020.

M. Kunze, M. Godolt, U. Langematz, J.L. Grenfell, A. Hamann-Reinus, and H. Rauer. Investigating the early Earth faint young Sun problem with a general circulation model. *Planetary and Space Science*, 98:77–92, August 2014. ISSN 0032-0633. doi:10.1016/j.pss.2013.09.011.

Zachary Labe, Yannick Peings, and Gudrun Magnusdottir. Warm Arctic, Cold Siberia Pattern: Role of Full Arctic Amplification Versus Sea Ice Loss Alone. *Geophysical Research Letters*, 47(17), August 2020. ISSN 1944-8007. doi:10.1029/2020gl088583.

Karin Labitzke. On the mutual relation between stratosphere and troposphere during periods of stratospheric warmings in winter. *Journal of Applied Meteorology and Climatology*, 4 (1):91–99, 1965.

J. Landgraf and P. J. Crutzen. An Efficient Method for Online Calculations of Photolysis and Heating Rates. *Journal of the Atmospheric Sciences*, 55:863–878, 1998. doi:10.1175/1520-0469(1998)055<0863:AEMFOC>2.0.CO;2.

Ulrike Langematz. Future ozone in a changing climate. *Comptes Rendus Geoscience*, 350 (7):403–409, November 2018. ISSN 1631-0713. doi:10.1016/j.crte.2018.06.015.

Ying Li, Gottfried Kirchengast, Marc Schwaerz, and Yunbin Yuan. Monitoring sudden stratospheric warmings under climate change since 1980 based on reanalysis data verified by radio occultation. *Atmospheric Chemistry and Physics*, 23(2):1259–1284, jan 2023. doi:10.5194/acp-23-1259-2023.

Yu-Chiao Liang, Young-Oh Kwon, Claude Frankignoul, Guillaume Gastineau, Karen L. Smith, Lorenzo M. Polvani, Lantao Sun, Yannick Peings, Clara Deser, Ruonan Zhang, and James Screen. The Weakening of the Stratospheric Polar Vortex and the Subsequent Surface Impacts as Consequences to Arctic Sea Ice Loss. *Journal of Climate*, 37(1): 309–333, January 2024. ISSN 1520-0442. doi:10.1175/jcli-d-23-0128.1.

Xinhuiyu Liu, Kevin M. Grise, Daniel F. Schmidt, and Robert E. Davis. Regional Characteristics of Variability in the Northern Hemisphere Wintertime Polar Front Jet and Subtropical Jet in Observations and CMIP6 Models. *Journal of Geophysical Research: Atmospheres*, 126(22), November 2021. ISSN 2169-8996. doi:10.1029/2021jd034876.

François Lott and Martin J. Miller. A new subgrid-scale orographic drag parametrization: Its formulation and testing. *Quarterly Journal of the Royal Meteorological Society*, 123 (537):101–127, January 1997. ISSN 1477-870X. doi:10.1002/qj.49712353704.

Penelope Maher, Michael E. Kelleher, Philip G. Sansom, and John Methven. Is the subtropical jet shifting poleward? *Climate Dynamics*, 54(3–4):1741–1759, December 2020. ISSN 1432-0894. doi:10.1007/s00382-019-05084-6.

Syukuro Manabe and Richard T. Wetherald. The Effects of Doubling the CO2 Concentration on the climate of a General Circulation Model. *Journal of Atmospheric Sciences*, 32 (1):3 – 15, 1975. doi:10.1175/1520-0469(1975)032<0003:TEODTC>2.0.CO;2.

S.J. Marsland, H. Haak, J.H. Jungclaus, M. Latif, and F. Röske. The Max-Planck-Institute global ocean/sea ice model with orthogonal curvilinear coordinates. *Ocean Modelling*, 5 (2):91–127, January 2003. ISSN 1463-5003. doi:10.1016/s1463-5003(02)00015-x.

Jonathan E. Martin. *Mid-latitude atmospheric dynamics*. Wiley, Hoboken, NJ [u.a.], 2007. ISBN 978-0-470-86465-4.

O. Martius, L. M. Polvani, and H. C. Davies. Blocking precursors to stratospheric sudden warming events. *Geophysical Research Letters*, 36(14), July 2009. ISSN 1944-8007. doi:10.1029/2009gl038776.

Kelly E. McCusker, John C. Fyfe, and Michael Sigmond. Twenty-five winters of unexpected Eurasian cooling unlikely due to Arctic sea-ice loss. *Nature Geoscience*, 9(11):838–842, October 2016. ISSN 1752-0908. doi:10.1038/ngeo2820.

M. Meinshausen, S. C. B. Raper, and T. M. L. Wigley. Emulating coupled atmosphere-ocean and carbon cycle models with a simpler model, MAGICC6 – Part 1: Model description and calibration. *Atmospheric Chemistry and Physics*, 11(4):1417–1456, February 2011. ISSN 1680-7324. doi:10.5194/acp-11-1417-2011.

Malte Meinshausen, Zebedee R. J. Nicholls, Jared Lewis, Matthew J. Gidden, Elisabeth Vogel, Mandy Freund, Urs Beyerle, Claudia Gessner, Alexander Nauels, Nico Bauer, Josep G. Canadell, John S. Daniel, Andrew John, Paul B. Krummel, Gunnar Luderer, Nicolai Meinshausen, Stephen A. Montzka, Peter J. Rayner, Stefan Reimann, Steven J. Smith, Marten van den Berg, Guus J. M. Velders, Martin K. Vollmer, and Ray H. J. Wang. The shared socio-economic pathway (SSP) greenhouse gas concentrations and their extensions to 2500. *Geoscientific Model Development*, 13(8):3571–3605, August 2020. ISSN 1991-9603. doi:10.5194/gmd-13-3571-2020.

Valentin P. Meleshko, Ola M. Johannessen, Andrey V. Baidin, Tatiana V. Pavlova, and Veronika A. Govorkova. Arctic amplification: does it impact the polar jet stream? *Tellus A: Dynamic Meteorology and Oceanography*, 68(1):32330, December 2016. ISSN 1600-0870. doi:10.3402/tellusa.v68.32330.

Mario J. Molina and F. S. Rowland. Stratospheric sink for chlorofluoromethanes: chlorine atom-catalysed destruction of ozone. *Nature*, 249(5460):810–812, June 1974. ISSN 1476-4687. doi:10.1038/249810a0.

Masato Mori, Masahiro Watanabe, Hideo Shiogama, Jun Inoue, and Masahide Kimoto. Robust Arctic sea-ice influence on the frequent Eurasian cold winters in past decades. *Nature Geoscience*, 7(12):869–873, October 2014. ISSN 1752-0908. doi:10.1038/ngeo2277.

Isla H. Myers-Smith, Jeffrey T. Kerby, Gareth K. Phoenix, Jarle W. Bjerke, Howard E. Epstein, Jakob J. Assmann, Christian John, Laia Andreu-Hayles, Sandra Angers-Blondin, Pieter S. A. Beck, Logan T. Berner, Uma S. Bhatt, Anne D. Bjorkman, Daan Blok, Anders Bryn, Casper T. Christiansen, J. Hans C. Cornelissen, Andrew M. Cunliffe, Sarah C. Elmendorf, Bruce C. Forbes, Scott J. Goetz, Robert D. Hollister, Rogier de Jong, Michael M. Loranty, Marc Macias-Fauria, Kadmiel Maseyk, Signe Normand, Johan Olofsson, Thomas C. Parker, Frans-Jan W. Parmentier, Eric Post, Gabriela Schaepman-Strub, Frode Stordal, Patrick F. Sullivan, Haydn J. D. Thomas, Hans Tømmervik, Rachael Treharne, Craig E. Tweedie, Donald A. Walker, Martin Wilmking, and Sonja Wipf. Complexity revealed in the greening of the Arctic. *Nature Climate Change*, 10(2):106–117, Feb 2020. ISSN 1758-6798. doi:10.1038/s41558-019-0688-1.

Tetsu Nakamura, Koji Yamazaki, Katsushi Iwamoto, Meiji Honda, Yasunobu Miyoshi, Yasunobu Ogawa, Yoshihiro Tomikawa, and Jinro Ukita. The stratospheric pathway for Arctic impacts on midlatitude climate. *Geophysical Research Letters*, 43(7):3494–3501, April 2016. ISSN 1944-8007. doi:10.1002/2016gl068330.

Kazuaki Nishii, Hisashi Nakamura, and Takafumi Miyasaka. Modulations in the planetary wave field induced by upward-propagating Rossby wave packets prior to stratospheric sudden warming events: A case-study. *Quarterly Journal of the Royal Meteorological Society*, 135(638):39–52, jan 2009. doi:10.1002/qj.359.

K. M. Nissen, K. Matthes, U. Langematz, and B. Mayer. Towards a better representation of the solar cycle in general circulation models. *Atmospheric Chemistry and Physics*, 7 (20):5391–5400, October 2007. ISSN 1680-7324. doi:10.5194/acp-7-5391-2007.

Sophie Oberländer, Ulrike Langematz, and Stefanie Meul. Unraveling impact factors for future changes in the Brewer-Dobson circulation. *Journal of Geophysical Research: Atmospheres*, 118(18), September 2013. ISSN 2169-8996. doi:10.1002/jgrd.50775.

Jessica Oehrlein, Gabriel Chiodo, and Lorenzo M. Polvani. The effect of interactive ozone chemistry on weak and strong stratospheric polar vortex events. *Atmospheric Chemistry and Physics*, 20(17):10531–10544, September 2020. ISSN 1680-7324. doi:10.5194/acp-20-10531-2020.

Stephen Outten, Camille Li, Martin P. King, Lingling Suo, Peter Y. F. Siew, Hoffman Cheung, Richard Davy, Etienne Dunn-Sigouin, Tore Furevik, Shengping He, Erica Madonna, Stefan Sobolowski, Thomas Spengler, and Tim Woollings. Reconciling conflicting evidence for the cause of the observed early 21st century Eurasian cooling. *Weather and Climate Dynamics*, 4(1):95–114, January 2023. ISSN 2698-4016. doi:10.5194/wcd-4-95-2023.

Tim N. Palmer. Diagnostic Study of a Wavenumber-2 Stratospheric Sudden Warming in a Transformed Eulerian-Mean Formalism. *Journal of the Atmospheric Sciences*, 38: 844–855, 1981, URLhttps://api.semanticscholar.org/CorpusID: 122676665.

Y. Peings. Ural Blocking as a Driver of Early-Winter Stratospheric Warmings. *Geophysical Research Letters*, 46(10):5460–5468, May 2019. ISSN 1944-8007. doi:10.1029/2019gl082097.

Y. Peings, P. Davini, and G. Magnusdottir. Impact of Ural Blocking on Early Winter Climate Variability Under Different Barents-Kara Sea Ice Conditions. *Journal of Geophysical Research: Atmospheres*, 128(6), March 2023. ISSN 2169-8996. doi:10.1029/2022jd036994.

Yannick Peings and Gudrun Magnusdottir. Response of the Wintertime Northern Hemisphere Atmospheric Circulation to Current and Projected Arctic Sea Ice Decline: A Numerical Study with CAM5. *Journal of Climate*, 27(1):244–264, January 2014. ISSN 1520-0442. doi:10.1175/jcli-d-13-00272.1.

Yannick Peings, Julien Cattiaux, and Gudrun Magnusdottir. The Polar Stratosphere as an Arbiter of the Projected Tropical Versus Polar Tug of War. *Geophysical Research Letters*, 46(15):9261–9270, August 2019. ISSN 1944-8007. doi:10.1029/2019gl082463.

Vladimir Petoukhov and Vladimir A. Semenov. A link between reduced Barents-Kara sea ice and cold winter extremes over northern continents. *Journal of Geophysical Research: Atmospheres*, 115(D21), November 2010. ISSN 0148-0227. doi:10.1029/2009jd013568.

Felix Pithan and Thorsten Mauritsen. Arctic amplification dominated by temperature feedbacks in contemporary climate models. *Nature Geoscience*, 7(3):181–184, Mar 2014. ISSN 1752-0908. doi:10.1038/ngeo2071.

R. Alan Plumb. On the Three-Dimensional Propagation of Stationary Waves. *Journal of Atmospheric Sciences*, 42:217–229, 1985. doi:10.1175/1520-0469(1985)042<0217:OTTDPO>2.0.CO;2.

A. Pozzer, P. Jöckel, B. Kern, and H. Haak. The atmosphere-ocean general circulation model EMAC-MPIOM. March 2011. doi:10.5194/gmdd-4-457-2011.

Michael Previdi, Karen L Smith, and Lorenzo M Polvani. Arctic amplification of climate change: a review of underlying mechanisms. *Environmental Research Letters*, 16(9): 093003, sep 2021. doi:10.1088/1748-9326/ac1c29.

Mika Rantanen, Alexey Yu. Karpechko, Antti Lipponen, Kalle Nordling, Otto Hyvärinen, Kimmo Ruosteenoja, Timo Vihma, and Ari Laaksonen. The Arctic has warmed nearly four times faster than the globe since 1979. *Communications Earth & Environment*, 3(1): 168, Aug 2022. ISSN 2662-4435. doi:10.1038/s43247-022-00498-3.

N. A. Rayner, D. E. Parker, E. B. Horton, C. K. Folland, L. V. Alexander, D. P. Rowell, E. C. Kent, and A. Kaplan. Global analyses of sea surface temperature, sea ice, and night marine air temperature since the late nineteenth century. *Journal of Geophysical Research: Atmospheres*, 108(D14), July 2003. ISSN 0148-0227. doi:10.1029/2002jd002670.

Keywan Riahi, Detlef P. van Vuuren, Elmar Kriegler, Jae Edmonds, Brian C. O'Neill, Shinichiro Fujimori, Nico Bauer, Katherine Calvin, Rob Dellink, Oliver Fricko, Wolfgang Lutz, Alexander Popp, Jesus Crespo Cuaresma, Samir KC, Marian Leimbach, Leiwen Jiang, Tom Kram, Shilpa Rao, Johannes Emmerling, Kristie Ebi, Tomoko Hasegawa, Petr Havlik, Florian Humpenöder, Lara Aleluia Da Silva, Steve Smith, Elke Stehfest, Valentina Bosetti, Jiyong Eom, David Gernaat, Toshihiko Masui, Joeri Rogelj, Jessica Strefler, Laurent Drouet, Volker Krey, Gunnar Luderer, Mathijs Harmsen, Kiyoshi Takahashi, Lavinia Baumstark, Jonathan C. Doelman, Mikiko Kainuma, Zbigniew Klimont, Giacomo Marangoni, Hermann Lotze-Campen, Michael Obersteiner, Andrzej Tabeau, and Massimo Tavoni. The Shared Socioeconomic Pathways and their energy, land use, and greenhouse gas emissions implications: An overview. *Global Environmental Change*, 42:153–168, 2017. ISSN 0959-3780. doi:https://doi.org/10.1016/j.gloenvcha.2016.05.009.

E. Roeckner, R. Brokopf, M. Esch, M. Giorgetta, S. Hagemann, L. Kornblueh, E. Manzini, U. Schlese, and U. Schulzweida. Sensitivity of Simulated Climate to Horizontal and Vertical Resolution in the ECHAM5 Atmosphere Model. *Journal of Climate*, 19(16): 3771–3791, August 2006. ISSN 0894-8755. doi:10.1175/jcli3824.1.

Erik Romanowsky, Dörthe Handorf, Ralf Jaiser, Ingo Wohltmann, Wolfgang Dorn, Jinro Ukita, Judah Cohen, Klaus Dethloff, and Markus Rex. The role of stratospheric ozone for Arctic-midlatitude linkages. *Scientific Reports*, 9(1), May 2019. ISSN 2045-2322. doi:10.1038/s41598-019-43823-1.

Ross J. (Lead Author) Salawitch, Laura A. McBride, Chelsea R. Thompson, Eric L. Fleming, Richard L. McKenzie, Karen H. Rosenlof, Sarah J. Doherty, and David W. Fahey. Twenty Questions and Answers About the Ozone Layer: 2022 Update. Scientific assessment of ozone depletion: 2022, World Meteorological Organization, Geneva, Switzerland, 2023.

R. Sander, A. Kerkweg, P. Jöckel, and J. Lelieveld. Technical note: The new comprehensive atmospheric chemistry module MECCA. *Atmospheric Chemistry and Physics*, 5(2):445–450, February 2005. ISSN 1680-7324. doi:10.5194/acp-5-445-2005.

R. Sander, A. Baumgaertner, S. Gromov, H. Harder, P. Jöckel, A. Kerkweg, D. Kubistin, E. Regelin, H. Riede, A. Sandu, D. Taraborrelli, H. Tost, and Z.-Q. Xie. The atmospheric chemistry box model CAABA/MECCA-3.0. *Geoscientific Model Development*, 4(2): 373–380, May 2011. ISSN 1991-9603. doi:10.5194/gmd-4-373-2011.

R. Sander, P. Jöckel, O. Kirner, A. T. Kunert, J. Landgraf, and A. Pozzer. The photolysis module JVAL-14, compatible with the MESSy standard, and the JVal PreProcessor (JVPP). *Geoscientific Model Development*, 7(6):2653–2662, November 2014. ISSN 1991-9603. doi:10.5194/gmd-7-2653-2014.

R Scherhag. Die explosionsartigen Stratospherenerwarmungen des Spatwinters, 1951-1952. *Ber. Deut. Wetterd. (U.S. Zone)*, 6:51–63, 1952.

James A. Screen. Simulated Atmospheric Response to Regional and Pan-Arctic Sea Ice Loss. *Journal of Climate*, 30(11):3945–3962, May 2017a. ISSN 1520-0442. doi:10.1175/jcli-d-16-0197.1.

James A. Screen. The missing Northern European winter cooling response to Arctic sea ice loss. *Nature Communications*, 8(1), March 2017b. ISSN 2041-1723. doi:10.1038/ncomms14603.

James A. Screen and Ian Simmonds. Exploring links between Arctic amplification and mid-latitude weather. *Geophysical Research Letters*, 40(5):959–964, March 2013. ISSN 1944-8007. doi:10.1002/grl.50174.

James A. Screen, Clara Deser, Ian Simmonds, and Robert Tomas. Atmospheric impacts of Arctic sea-ice loss, 1979–2009: separating forced change from atmospheric internal variability. *Climate Dynamics*, 43(1–2):333–344, June 2014. ISSN 1432-0894. doi:10.1007/s00382-013-1830-9.

James A. Screen, Clara Deser, Doug M. Smith, Xiangdong Zhang, Russell Blackport, Paul J. Kushner, Thomas Oudar, Kelly E. McCusker, and Lantao Sun. Consistency and discrepancy in the atmospheric response to Arctic sea-ice loss across climate models. *Nature Geoscience*, 11(3):155–163, February 2018. ISSN 1752-0908. doi:10.1038/s41561-018-0059-y.

James A. Screen, Rosemary Eade, Doug M. Smith, Stephen Thomson, and Hao Yu. Net Equatorward Shift of the Jet Streams When the Contribution From Sea-Ice Loss Is Constrained by Observed Eddy Feedback. *Geophysical Research Letters*, 49(23), December 2022. ISSN 1944-8007. doi:10.1029/2022gl100523.

Ian Simmonds and Eun-Pa Lim. Biases in the calculation of Southern Hemisphere mean baroclinic eddy growth rate. *Geophysical Research Letters*, 36(1), January 2009. ISSN 1944-8007. doi:10.1029/2008gl036320.

Brian J. Soden and Isaac M. Held. An Assessment of Climate Feedbacks in Coupled Ocean–Atmosphere Models. *Journal of Climate*, 19(14):3354–3360, July 2006. ISSN 0894-8755. doi:10.1175/jcli3799.1.

Susan Solomon, Rolando R. Garcia, F. Sherwood Rowland, and Donald J. Wuebbles. On the depletion of Antarctic ozone. *Nature*, 321(6072):755–758, June 1986. ISSN 1476-4687. doi:10.1038/321755a0.

Clemens Spensberger and Thomas Spengler. Feature-Based Jet Variability in the Upper Troposphere. *Journal of Climate*, 33(16):6849–6871, August 2020. ISSN 1520-0442. doi:10.1175/jcli-d-19-0715.1.

Clemens Spensberger, Thomas Spengler, and Camille Li. Upper-Tropospheric Jet Axis Detection and Application to the Boreal Winter 2013/14. *Monthly Weather Review*, 145 (6):2363–2374, May 2017. ISSN 1520-0493. doi:10.1175/mwr-d-16-0467.1.

Clemens Spensberger, Camille Li, and Thomas Spengler. Linking Instantaneous and Climatological Perspectives on Eddy-Driven and Subtropical Jets. *Journal of Climate*, 36 (24):8525–8537, December 2023. ISSN 1520-0442. doi:10.1175/jcli-d-23-0080.1.

Malte F. Stuecker, Cecilia M. Bitz, Kyle C. Armour, Cristian Proistosescu, Sarah M. Kang, Shang-Ping Xie, Doyeon Kim, Shayne McGregor, Wenjun Zhang, Sen Zhao, Wenju Cai, Yue Dong, and Fei-Fei Jin. Polar amplification dominated by local forcing and feedbacks. *Nature Climate Change*, 8(12):1076–1081, Dec 2018. ISSN 1758-6798. doi:10.1038/s41558-018-0339-y.

Roland Stull. *Practical Meteorology An Algebra-based Survey of Atmospheric Science.* Sundog Publishing, LLC, 2017. ISBN 9780888652836.

Lantao Sun, Clara Deser, and Robert A. Tomas. Mechanisms of Stratospheric and Tropospheric Circulation Response to Projected Arctic Sea Ice Loss*. *Journal of Climate*, 28 (19):7824–7845, September 2015. ISSN 1520-0442. doi:10.1175/jcli-d-15-0169.1.

Lantao Sun, Clara Deser, Isla Simpson, and Michael Sigmond. Uncertainty in the Winter Tropospheric Response to Arctic Sea Ice Loss: The Role of Stratospheric Polar Vortex Internal Variability. *Journal of Climate*, 35(10):3109–3130, May 2022. ISSN 1520-0442. doi:10.1175/jcli-d-21-0543.1.

Geoffrey K. Vallis. *Atmospheric and oceanic fluid dynamics*. Cambridge University Press, Cambridge, second edition edition, 2017. ISBN 9781107588417.

John M. Wallace and Peter V. Hobbs. *Atmospheric Science*. Elsevier, 2005. ISBN 9780127329512.

John M. Wallace, Isaac M. Held, David W. J. Thompson, Kevin E. Trenberth, and John E. Walsh. Global Warming and Winter Weather. *Science*, 343(6172):729–730, February 2014. ISSN 1095-9203. doi:10.1126/science.343.6172.729.

Ian White, Chaim I. Garfinkel, Edwin P. Gerber, Martin Jucker, Valentina Aquila, and Luke D. Oman. The Downward Influence of Sudden Stratospheric Warmings: Association with Tropospheric Precursors. *Journal of Climate*, 32(1):85–108, January 2019. ISSN 1520-0442. doi:10.1175/jcli-d-18-0053.1.

Steven C. Wofsy, Michael B. McElroy, and Yuk Ling Yung. The chemistry of atmospheric bromine. *Geophysical Research Letters*, 2(6):215–218, June 1975. ISSN 1944-8007. doi:10.1029/gl002i006p00215.

Tim Woollings, Abdel Hannachi, and Brian Hoskins. Variability of the North Atlantic eddy-driven jet stream: Variability of the North Atlantic Jet Stream. *Quarterly Journal of the Royal Meteorological Society*, 136(649):856–868, April 2010. ISSN 0035-9009. doi:10.1002/qj.625.

Tim Woollings, Marie Drouard, Christopher H. O'Reilly, David M. H. Sexton, and Carol McSweeney. Trends in the atmospheric jet streams are emerging in observations and could be linked to tropical warming. *Communications Earth & Environment*, 4(1), April 2023. ISSN 2662-4435. doi:10.1038/s43247-023-00792-8.

World Meteorological Organization (WMO). Executive Summary. Scientific Assessment of Ozone Depletion: 2022. Technical Report GAW Report No. 278, WMO, Geneva, Switzerland, 2022.

Yutian Wu and Karen L. Smith. Response of Northern Hemisphere Midlatitude Circulation to Arctic Amplification in a Simple Atmospheric General Circulation Model. *Journal of Climate*, 29(6):2041–2058, March 2016. ISSN 1520-0442. doi:10.1175/jcli-d-15-0602.1.

Xinping Xu, Shengping He, Yongqi Gao, Tore Furevik, Huijun Wang, Fei Li, and Fumiaki Ogawa. Strengthened linkage between midlatitudes and Arctic in boreal winter. *Climate Dynamics*, 53(7–8):3971–3983, April 2019. ISSN 1432-0894. doi:10.1007/s00382-019-04764-7.

Pengfei Zhang, Yutian Wu, and Karen L. Smith. Prolonged effect of the stratospheric pathway in linking Barents–Kara Sea sea ice variability to the midlatitude circulation in a simplified model. *Climate Dynamics*, 50(1–2):527–539, April 2017. ISSN 1432-0894. doi:10.1007/s00382-017-3624-y.

Pengfei Zhang, Yutian Wu, Isla R. Simpson, Karen L. Smith, Xiangdong Zhang, Bithi De, and Patrick Callaghan. A stratospheric pathway linking a colder Siberia to Barents-Kara Sea sea ice loss. *Science Advances*, 4(7), July 2018. ISSN 2375-2548. doi:10.1126/sciadv.aat6025.

Acronyms

AGCM   atmosphere general circulation model

AO   Arctic Oscillation

AOGCM   atmosphere-ocean general circulation model

BKS   Barents-Kara Sea

CAO   cold air outbreak

CCM   chemistry climate model

CCMI   Chemistry-Climate Model Initiative

CFC   chlorofluorocarbon

CMIP6   Coupled Model Intercomparison Project 6

EGR   Eady growth rate

EMAC   ECHAM/MESSy2 Atmospheric Chemistry

EP   Eliassen-Palm

GCM   general circulation model

GHG   greenhouse gas

IPCC   Intergovernmental Panel on Climate Change

NAM   Northern Hemisphere Annular Mode

NAO   North Atlantic Oscillation

NH   northern hemisphere

ODS   ozone-depleting substance

PAMIP   Polar Amplification Model Intercomparison Project

PCH   polar cap height

PSC   polar stratospheric cloud

PV   potential vorticity

PVU   potential vorticity unit

SH   southern hemisphere

SIC   sea ice cover

SLP   sea level pressure

SSP   Shared Socioeconomic Pathway

SST   sea surface temperature

SSW   sudden stratospheric warming

TEM   transformed Eulerian mean

UV   ultraviolet

VWE   vertical wave event

WMO   World Meteorological Organization

List of Figures

150

List of Tables

Appendix

Figure A.1: NAM index for winter of random years in the EMAC preindustrial timeslice. The troposphere and the middle atmosphere are depicted in the left column. The tropospheric conditions of the respective SSW events are shown on the right. The colour bars have different scaling due to the lower signal magnitude in the troposphere.
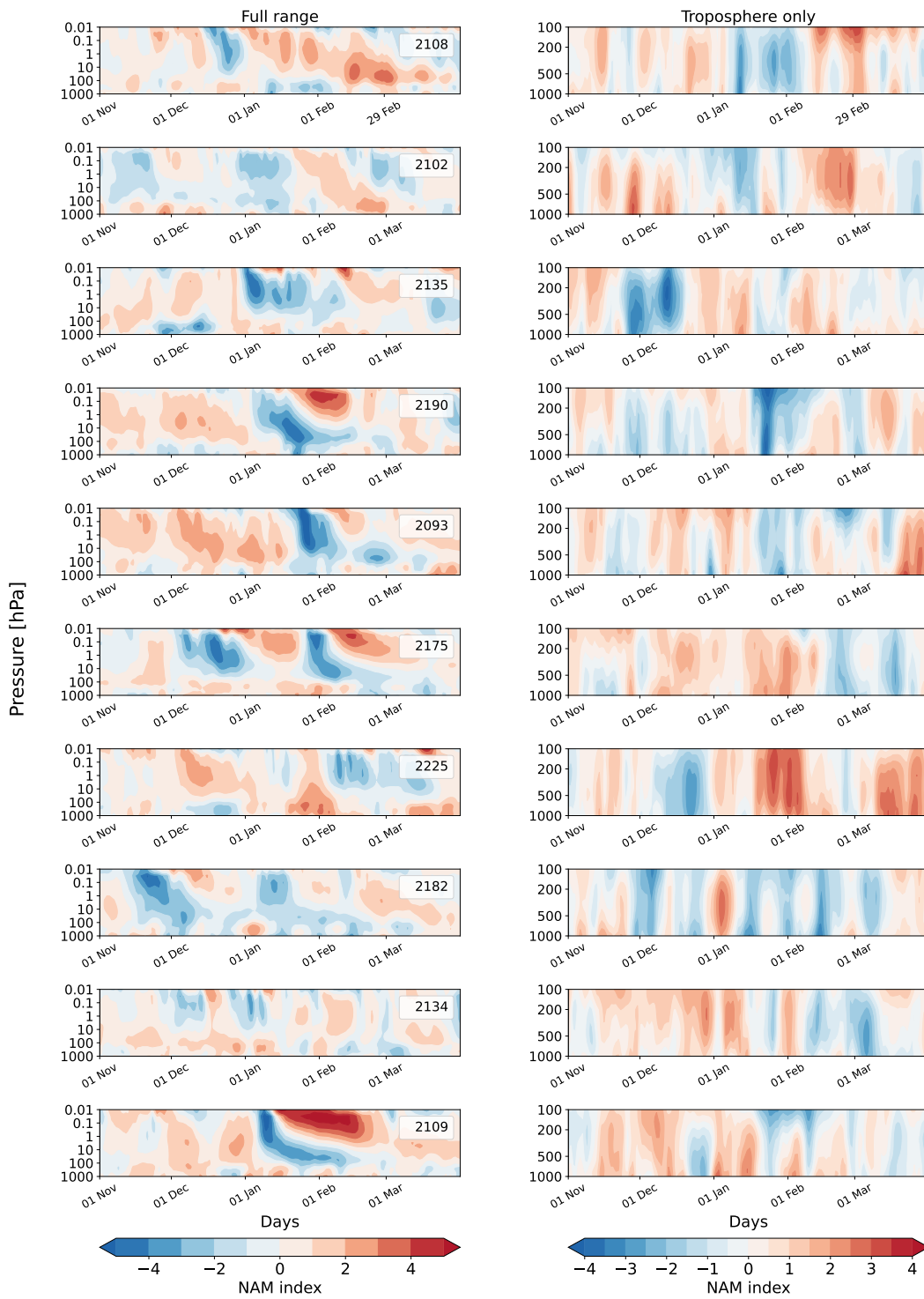
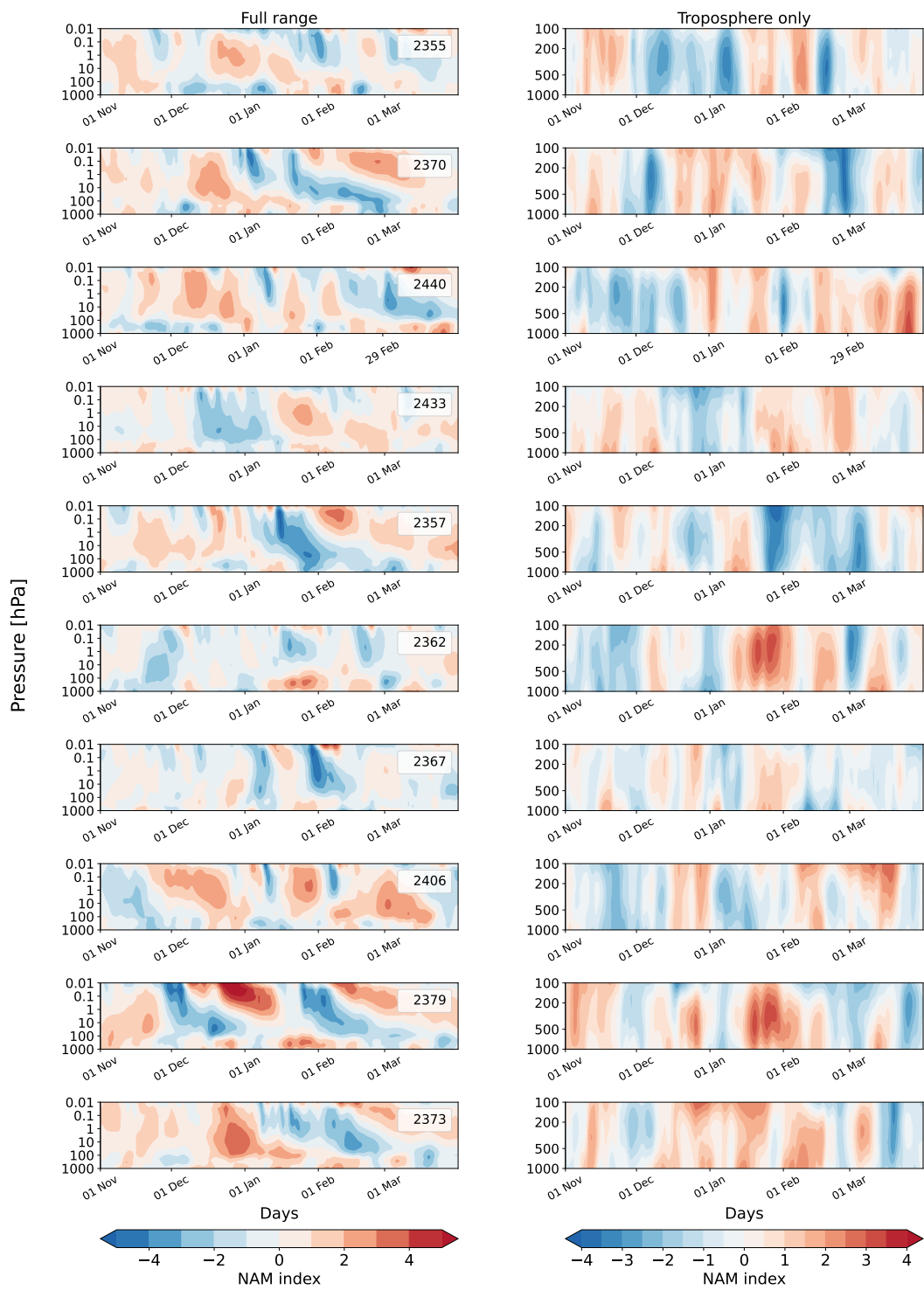Figure A.2: Same as Figure A.1 but for events in the present timeslice.

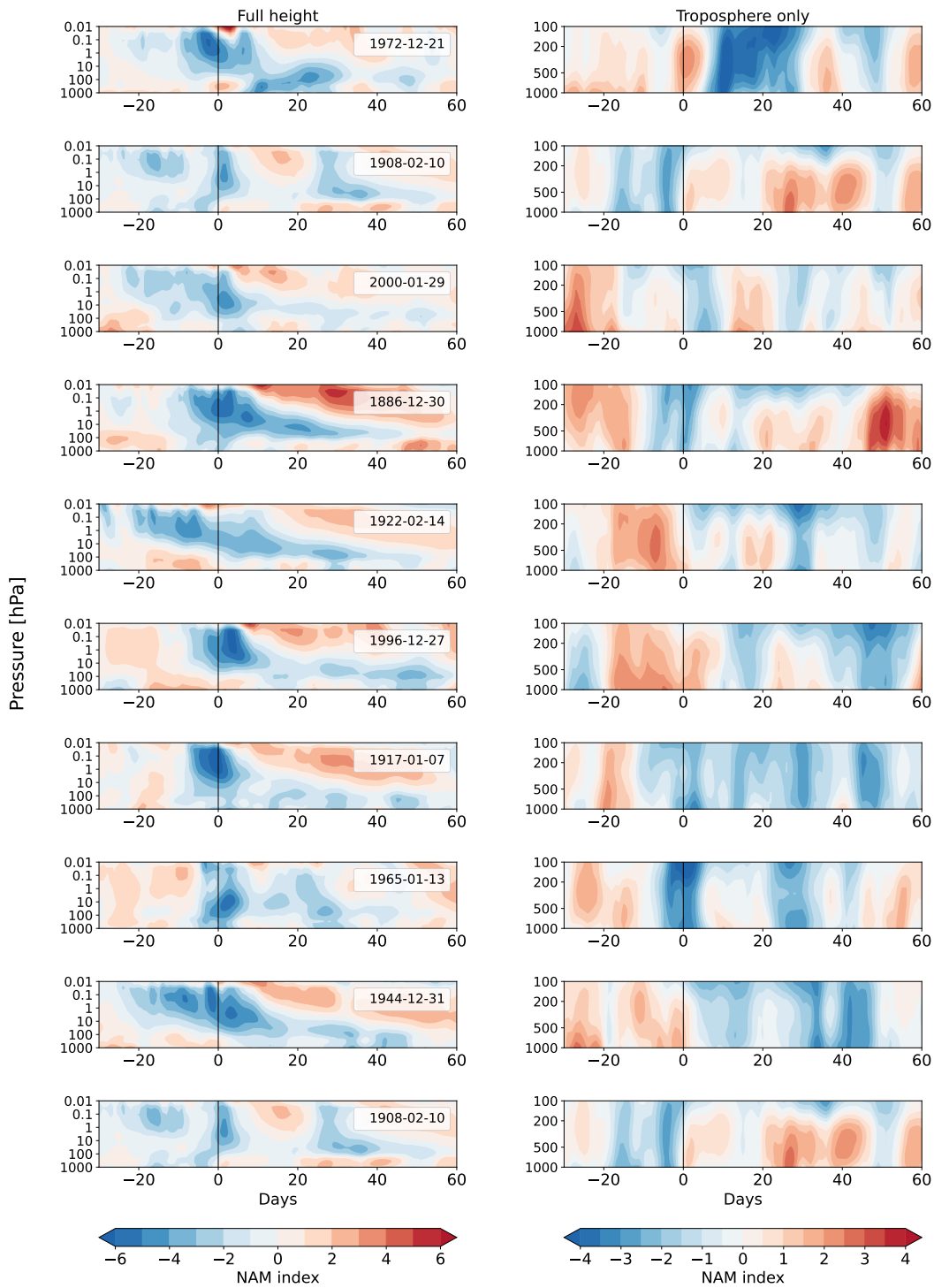Figure A.3: Same as Figure A.1 but for events in the future timeslice.

Figure A.4: NAM index of single SSW events in the EMAC preindustrial simulation. Day 0 marks the SSW onset date, which is indicated in the legend. The troposphere and the middle atmosphere are depicted in the left column. The tropospheric conditions of the respective SSW events are shown on the right. The colour bars have different scaling due to the lower signal magnitude in the troposphere.
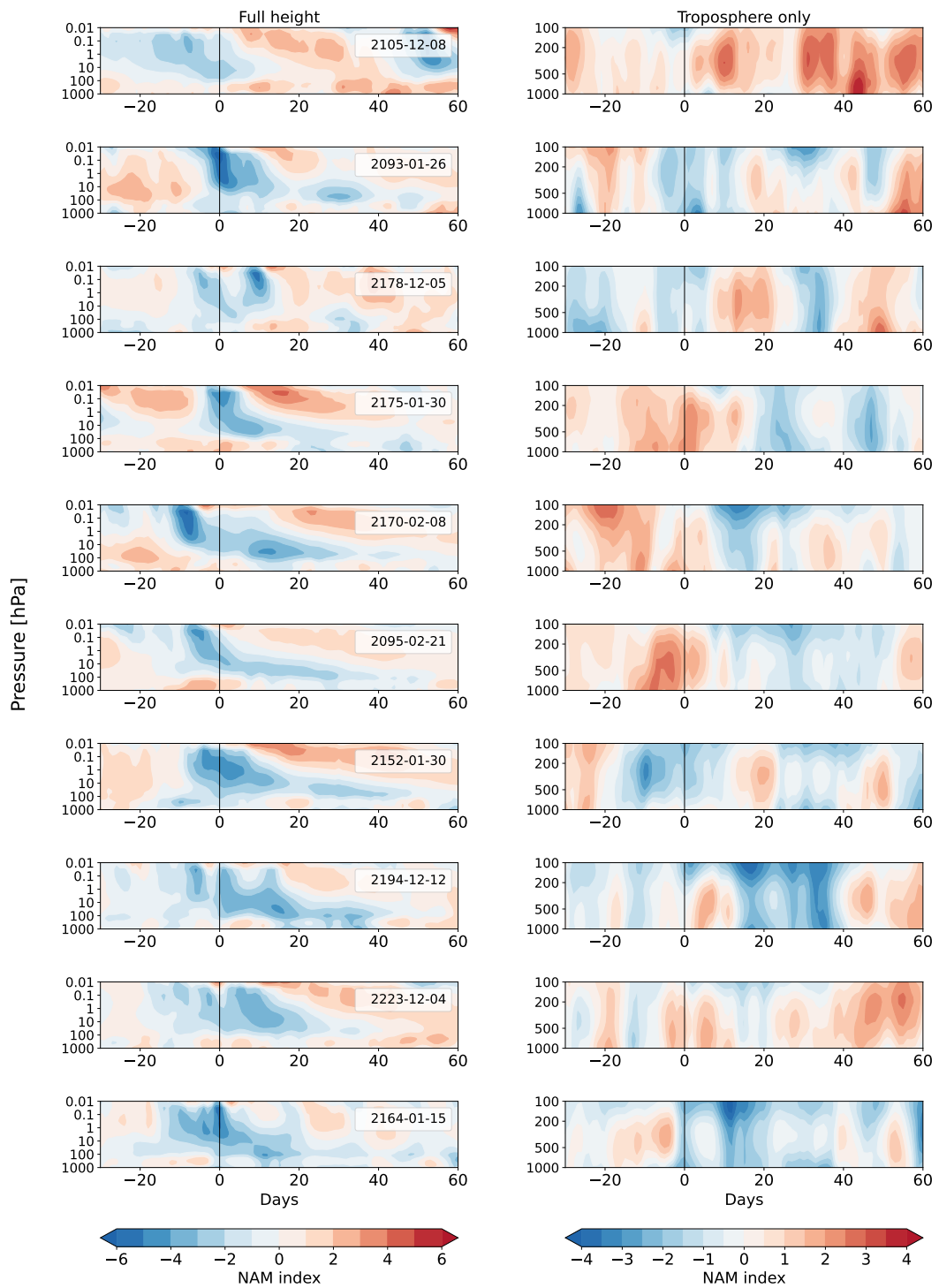
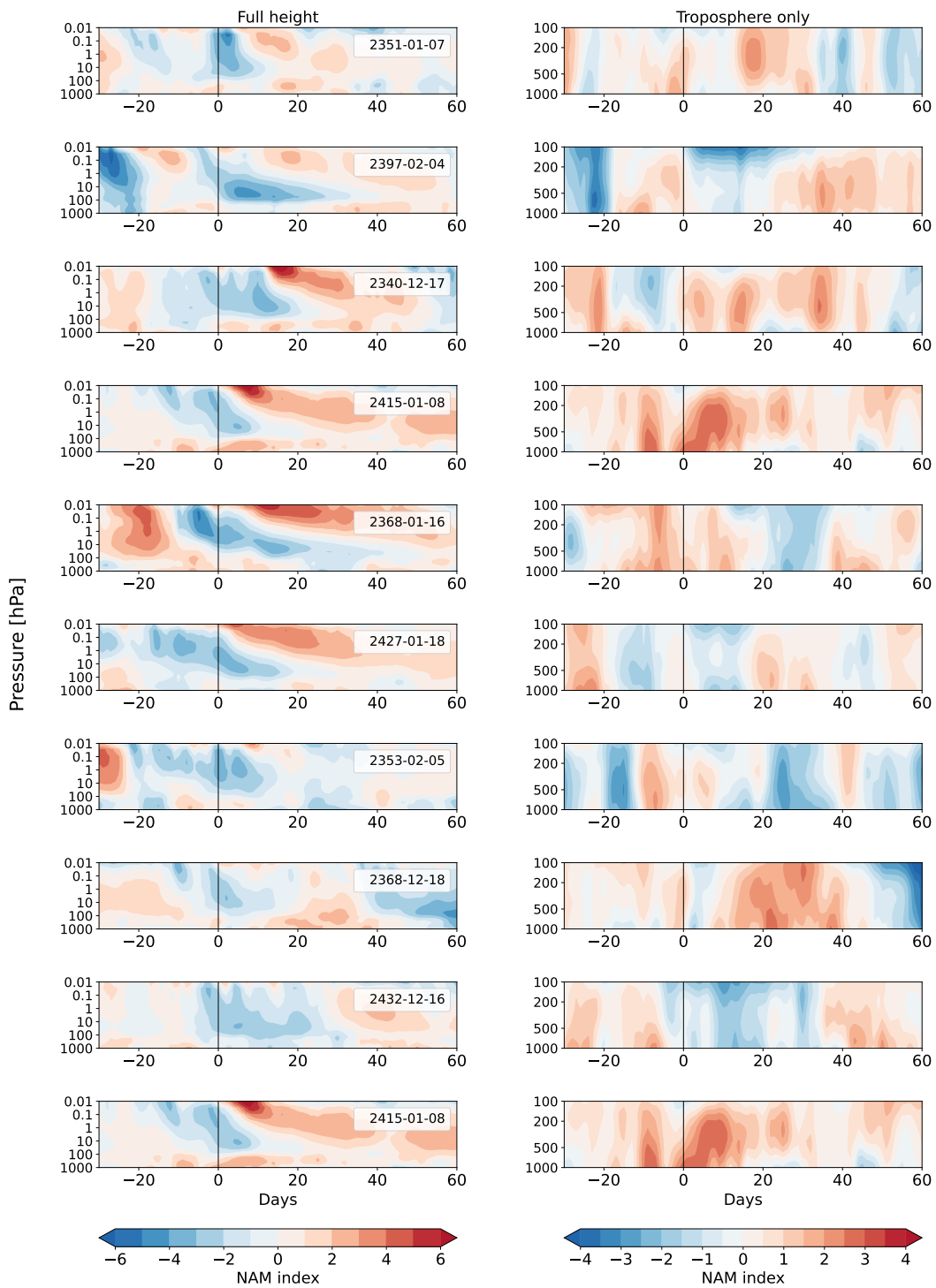Figure A.5: Same as Figure A.4 but for events in the present timeslice.

Figure A.6: Same as Figure A.4 but for events in the future timeslice.

Danksagung

Ich möchte mich bei Prof. Dr. Ulrike Langematz aufrichtig bedanken für die Betreuung dieser Dissertation. Besonders hervorzuheben ist ihr Vertrauen in meine Arbeit und die Unterstützung meine Forschungsergebnisse auf internationalen Konferenzen vorzustellen. Ein besonderer Dank gebührt auch für das uneingeschränkte Verständnis für die ausgedehnte Zeitplanung dieser Promotion, die durch eine Elternzeit und eine Corona-Pandemie mit allen Begleitumständen geführt hat.

Einen besonderen Dank möchte ich Prof. Dr. Stephan Pfahl aussprechen für die Erstellung des Zweitgutachtens und der Ermöglichung die Disputation zügig anzuschließen.

Einen herzlichen Dank geht an Tobias Spiegl für die Unterstützung beim Anfertigen der vielen Simulationen und allen Fragen zum Modell. Trotz einer oftmals räumlichen Distanz, bedanke ich mich für den regen Austausch zu allen technischen und wissenschaftlichen Problemen. Wenn es eine Tonspur für diese Promotion gäbe, wäre es der unermüdliche Klang des Slack-Kanals.

Des Weiteren möchte ich Markus Kunze, Blanca Ayarzagüena und Sophie Oberländer-Hayn für ihre Korrekturen und Diskussionen meinen aufrichtigen Dank aussprechen.

Mein Dank gilt außerdem allen ehemaligen Mitgliedern der AG Atmosphärendynamik für den fachlichen Austausch und ihre Expertise zum Thema Stratosphäre. Die zahlreichen Wetterbesprechungen mit Kollegen haben mein Verständnis für die Stratosphäre vertieft, und ich bin dankbar, dass ich die Gelegenheit hatte, ein so spannendes Forschungsthema bearbeiten zu können.

Ein besonder Dank geht auch an Thomas Bergmann für die technische Unterstützung und der Hilfsbereitschaft bei beharrlichen Problemen mit den Python-Bibliotheken.

Ich bedanke mich für die zur Verfügung gestellte Rechenzeit auf dem Hochleistungsrechner Lise an dem NHR-Zentrum ZIB. Diese werden gemeinsam durch das Bundesministerium für Bildung und Forschung und den am NHR beteiligten Landesregierungen (www.nhr-verein.de/unsere-partner) unterstützt.

Zu guter Letzt, möchte ich meiner Familie für die immerwährende Unterstützung danken. Vielen Dank an meinen Partner Gregor und meine Kinder Hugo und Edith, die meine Abwesenheit vom Familienalltag so selbstverständlich hingenommen haben. Meinen Eltern und meiner Oma danke ich besonders für ihre finanzielle Unterstützung und der Zuversicht in mich und meine Ziele.

Eidesstattliche Erklärung

Hiermit versichere ich, die vorliegende Dissertation selbstständig und ohne unerlaubte Hilfe angefertigt zu haben. Es wurden keine anderen als die im Text aufgeführten Hilfsmittel und Quellen verwendet. Ein Promotionsverfahren wurde zu keinem früheren Zeitpunkt an einer anderen Hochschule oder bei einem anderen Fachbereich beantragt.

Ort, Datum	Franziska Schmidt